Dissertations, Master's Theses and Master's Reports - Open

2005

Filtration and oxidation characteristics of a diesel oxidation catalyst and a catalyzed particulate filter : development of a 1-D 2-layer model

Mohammed Hasan
Michigan Technological University

Follow this and additional works at: https://digitalcommons.mtu.edu/etds

Part of the Mechanical Engineering Commons

Recommended Citation

Hasan, Mohammed, "Filtration and oxidation characteristics of a diesel oxidation catalyst and a catalyzed particulate filter : development of a 1-D 2-layer model", Master's Thesis, Michigan Technological University, 2005.
https://digitalcommons.mtu.edu/etds/371

Follow this and additional works at: https://digitalcommons.mtu.edu/etds

Part of the Mechanical Engineering Commons

THE FILTRATION AND OXIDATION CHARACTERISTICS OF A DIESEL

OXIDATION CATALYST AND A CATALYZED PARTICULATE FILTER:

DEVELOPMENT OF A 1-D 2-LAYER MODEL

By

Mohammed Hasan

A THESIS

Submitted in partial fulfilment of the requirements for the degree of

MASTER OF SCIENCE IN MECHANICAL ENGINEERING

MICHIGAN TECHNOLOGICAL UNIVERSITY

May 2005

This thesis "The Filtration and Oxidation Characteristics of a Diesel Oxidation Catalyst and a Catalyzed Particulate Filter: Development of a 1-D 2-Layer Model" is hereby approved in partial fulfillment of the requirements for the Degree of MASTER OF SCIENCE IN MECHANICAL ENGINEERING

DEPARTMENT: Mechanical Engineering – Engineering Mechanics

Thesis Advisor: John H. Johnson

Department Chair: William W. Predebon

Date:

ABSTRACT

The emissions, filtration and oxidation characteristics of a diesel oxidation catalyst (DOC) and a catalyzed particulate filter (CPF) in a Johnson Matthey catalyzed continuously regenerating trap (CCRT®) were studied by using computational models. Experimental data needed to calibrate the models were obtained by characterization experiments with raw exhaust sampling from a Cummins ISM 2002 engine with variable geometry turbocharging (VGT) and programmed exhaust gas recirculation (EGR). The experiments were performed at 20, 40, 60 and 75% of full load (1120 Nm) at rated speed (2100 rpm), with and without the DOC upstream of the CPF. This was done to study the effect of temperature and CPF-inlet NO_2 concentrations on particulate matter oxidation in the CCRT®.

A previously developed computational model was used to determine the kinetic parameters describing the oxidation characteristics of HCs, CO and NO in the DOC and the pressure drop across it. The model was calibrated at five temperatures in the range of $280 - 465^oC$, and exhaust volumetric flow rates of $0.447 - 0.843$ act-m^3/sec. The downstream HCs, CO and NO concentrations were predicted by the DOC model to within ± 3 ppm. The HCs and CO oxidation kinetics in the temperature range of $280 - 465^oC$ and an exhaust volumetric flow rate of $0.447 - 0.843$ act-m^3/sec can be represented by one 'apparent' activation energy and pre-exponential factor. The NO oxidation kinetics in the same temperature and exhaust flow rate range can be represented by 'apparent' activation energies and pre-exponential factors in two regimes. The DOC pressure drop was always predicted within 0.5 kPa by the model.

The MTU 1-D 2-layer CPF model was enhanced in several ways to better model the performance of the CCRT®. A model to simulate the oxidation of particulate inside the filter wall was developed. A particulate cake layer filtration model which describes particle filtration in terms of more fundamental parameters was developed and coupled to the wall oxidation model. To better model the particulate oxidation

kinetics, a model to take into account the NO_2 produced in the washcoat of the CPF was developed. The overall 1-D 2-layer model can be used to predict the pressure drop of the exhaust gas across the filter, the evolution of particulate mass inside the filter, the particulate mass oxidized, the filtration efficiency and the particle number distribution downstream of the CPF. The model was used to better understand the internal performance of the CCRT®, by determining the components of the total pressure drop across the filter, by classifying the total particulate matter in layer I, layer II, the filter wall, and by the means of oxidation i.e. by O_2, NO_2 entering the filter and by NO_2 being produced in the filter.

The CPF model was calibrated at four temperatures in the range of 280 – 465ºC, and exhaust volumetric flow rates of 0.447 – 0.843 act-m^3/sec, in CPF-only and CCRT® (DOC+CPF) configurations. The clean filter wall permeability was determined to be 2.00E-13 m^2, which is in agreement with values in the literature for cordierite filters. The particulate packing density in the filter wall had values between 2.92 kg/m^3 - 3.95 kg/m^3 for all the loads. The mean pore size of the catalyst loaded filter wall was found to be 11.0 μm. The particulate cake packing densities and permeabilities, ranged from 131 kg/m^3 - 134 kg/m^3, and 0.42E-14 m^2 and 2.00E-14 m^2 respectively, and are in agreement with the Peclet number correlations in the literature. Particulate cake layer porosities determined from the particulate cake layer filtration model ranged between 0.841 and 0.814 and decreased with load, which is about 0.1 lower than experimental and more complex discrete particle simulations in the literature. The thickness of layer I was kept constant at 20 μm. The model kinetics in the CPF-only and CCRT® configurations, showed that no 'catalyst effect' with O_2 was present. The kinetic parameters for the NO_2-assisted oxidation of particulate in the CPF were determined from the simulation of transient temperature programmed oxidation data in the literature. It was determined that the thermal and NO_2 kinetic parameters do not change with temperature, exhaust flow rate or

NO_2 concentrations. However, different kinetic parameters are used for particulate oxidation in the wall and on the wall.

Model results showed that oxidation of particulate in the pores of the filter wall can cause disproportionate decreases in the filter pressure drop with respect to particulate mass. The wall oxidation model along with the particulate cake filtration model were developed to model the sudden and rapid decreases in pressure drop across the CPF. The particulate cake and wall filtration models result in higher particulate filtration efficiencies than with just the wall filtration model, with overall filtration efficiencies of 98-99% being predicted by the model. The pre-exponential factors for oxidation by NO_2 did not change with temperature or NO_2 concentrations because of the NO_2 wall production model. In both CPF-only and CCRT® configurations, the model showed NO_2 and layer I to be the dominant means and dominant physical location of particulate oxidation respectively. However, at temperatures of 280^oC, NO_2 is not a significant oxidizer of particulate matter, which is in agreement with studies in the literature. The model showed that 8.6 and 81.6% of the CPF-inlet particulate matter was oxidized after 5 hours at 20 and 75% load in CCRT® configuration. In CPF-only configuration at the same loads, the model showed that after 5 hours, 4.4 and 64.8% of the inlet particulate matter was oxidized. The increase in NO_2 concentrations across the DOC contributes significantly to the oxidation of particulate in the CPF and is supplemented by the oxidation of NO to NO_2 by the catalyst in the CPF, which increases the particulate oxidation rates. From the model, it was determined that the catalyst in the CPF modeslty increases the particulate oxidation rates in the range of $4.5 - 8.3\%$ in the CCRT® configuration. Hence, the catalyst loading in the CPF of the CCRT® could possibly be reduced without significantly decreasing particulate oxidation rates leading to catalyst cost savings and better engine performance due to lower exhaust backpressures.

ACKNOWLEDGEMENTS

My sincere thanks to my adviser Dr John H. Johnson for his expert advice, thoughtful suggestions and remarkable guidance throughout this research. I would also like to thank Dr Susan T Bagley for her suggestions and assistance during the research. Many thanks to Dr Song-Lin Yang and Dr Jeff Naber for being on my committee and for their suggestions and comments.

I would like to thank Cummins Engine Co. for the financial support they provided for this research. In particular, thanks to Arvind Suresh for his sound technical advice and timely answers to all of our queries.

Special thanks to Michigan Tech and the ME-EM department for providing a quality education and an excellent environment for research. The help of Paul Kilpela, Rob Rowe, Pete 'Buster' Antilla, Gerry Dion and Jesse Nordeng in keeping the Diesel engine and laboratory running is appreciated.

It was a good experience performing experimental research with Ravi. Many thanks to Kiran for working overtime with me to recalibrate the model at such short notice. It was a pleasure to work with the rest of the emissions research group: Antonio, Nishant, Abishek, Anand and Param. Thanks to Brooke for helping calibrate the model. A special note of thanks to all my friends in Houghton and in India who were always there for me.

The special time I had with my infant niece Zoya, no doubt recharged me during my vacation, and helped finish this thesis on time!!! Lastly, because I know they won't mind being mentioned last, a very special thanks to my parents and sisters for their support, love and encouragement. The earnestness with which my parents explained the benefits of a quality high level education motivated me for this masters. I dedicate this thesis to them.

Thanks,

Hasan

Contents

List of Tables

List of Figures

List of Symbols

Abbreviations

DOC: diesel oxidation catalyst,
CPF: catalyzed particulate filter,
DPF: diesel particulate filter,
CRT: continuously regenerating trap,
CCRT: catalyzed continuously regenerating trap,
TPM: total particulate matter,
PM: particulate matter,
CPM: carbonaceous PM: particulate matter,
SOF: soluble organic fraction,
OFA: open fraction area,
CFA: converter frontal area,
BMEP: brake mean effective pressure,
BSFC: brake specific fuel consumption,

Common Symbols

T: absolute temperature,
P: absolute pressure,
Q: Volumetric flow rates,
M_{ex}: exhaust gas molecular weight,
M_c: molecular weight of carbon,
M_{O_2}: molecular weight of oxygen,
M_{NO_2}: molecular weight of NO_2,
$\overline{R}$: universal gas constant,

DOC symbols

a: DOC channel width,
L: DOC monolith length,
K_f: Fanning friction factor,
r: Reaction rates of gaseous species in DOC,
K_i: Adsorption coefficient of gaseous species in DOC,

CPF symbols

α: 'clean' filter wall solidity fraction,

ϵ: filter wall porosity,

b: filter wall unit cell diameter,

k: 'clean' filter wall permeability,

d_{c0}: 'clean' filter wall unit collector diameter,

d_c: 'loaded' filter wall unit collector diameter,

d_{pore}: mean pore size of the filter wall,

d_{aggr}: aggregate size of diesel particles = 0.1μ m,

K: Kuwabara hydrodynamic factor,

Pe: Peclet number in the filter wall,

η_D: particle collection efficiency due to diffusion,

η_R: particle collection efficiency due to direct interception,

v_w: wall flow velocity,

k_B: Boltzmann's constant,

C: Stokes Cunningham slip correction factor,

Kn: Knudsen number in the filter wall,

D_p: particle diffusion coefficient,

μ: dynamic viscosity,

λ: mean free path of the exhaust gas,

R: particle interception parameter,

E: total particle collection efficiency by a packed bed,

m_t: particulate mass collected by a unit collector in the filter wall,

x: distance though wall and particulate,

z: distance along length of the channel,

E_A: Activation energy for oxidation of gaseous species in DOC or of particulate in CPF,

k_{th}: thermal reaction rates of particulate,

k_{cat}: catalytic reaction rates of particulate,

k_{NO_2}: reaction rates of particulate with NO_2,

A_{th}: pre-exponential factor for thermal oxidation of particulate,

A_{cat}: pre-exponential factor for catalytic oxidation of particulate,

A_{NO_2}: = pre-exponential factor for oxidation of particulate by NO_2,

Y_w: Mass fraction of oxygen,

Y_{NO_2}: Mass fraction of NO_2,

$Y_{w,1}$: Mass fraction of oxygen entering layer I,

$Y_{NO_2,1}$ Mass fraction of NO_2 entering layer I,

$Y_{w,2}$: Mass fraction of oxygen entering layer II,

$Y_{NO_2,2}$: Mass fraction of NO_2 entering layer II,

$Y_{w,wall}$: Mass fraction of oxygen entering filter wall,

$Y_{NO_2,wall}$: Mass fraction of NO_2 entering filter wall,

R_{O_2}: oxygen depletion rate,

R_{NO_2}: NO_2 depletion rate,

$R_{O_2,1}$: oxygen depletion rate in layer I,

$R_{O_2,2}$: oxygen depletion rate in layer II,

$R_{NO_2,1}$: NO$_2$ depletion rate in layer I,

$R_{NO_2,2}$: NO$_2$ depletion rate in layer II,

ρ_p: packing density of the particulate cake,

ρ_{pw}: packing density of the particulate in the filter wall,

ψ: percolation factor,

ϕ: partition coefficient,

w: thickness of the particulate cake layer,

w_s: thickness of filter wall,

w_{wall}: thickness of the virtual wall layer,

S: specific area of the particulate,

ρ: density of gas/packing density of particulate,

dh: width of the filter channel,

Δx: discrete unit along the length of the channel,

m_{ij}: mass of particulate present inside each *slab*,

H: heat source term due to particulate reaction,

C_p: specific heat of gas

S_p: specific area of particulate

A_p: surface area of particulate

Subscripts

1: inlet channel,

2: outlet channel,

w: filter wall,

s: wall substrate,

p: particulate,

g: channel gas,

e: layers making up layer I,

cake: properties of the particulate cake layer in particulate cake layer filtration model,

act: standard conditions of temperature and pressure,

Chapter 1

Introduction

Diesel engines power a significant number of heavy-duty trucks, urban buses, off-road vehicles, marine engines and industrial equipment and are increasingly powering new passenger cars due to their high thermal efficiency, reliability, durability and low maintenance cost. Diesel engines without aftertreatment devices have high particulate matter (PM) and nitrogen oxide (NO_X) emissions, which have detrimental effects on the environment and human health. NO_X emissions contribute to atmospheric smog and respiratory illnesses, and diesel particulate emissions are considered to be carcinogenic. While diesel engines emit higher levels of PM and NO_X than their gasoline counterparts, they emit lower levels of hydrocarbons (HC) and carbon monoxide (CO) due of their lean combustion nature.

In the U.S, the driving force for the reduction of PM and NO_X emissions from heavy-duty vehicles has been the EPA mobile source diesel emission standards. The US EPA heavy-duty emission standards of the recent past and near future are shown in Table 1.1, and the emissions standards in Europe are shown in Table 1.2. It can be seen that upcoming *tailpipe* emissions for heavy-duty diesel engines will have to meet very stringent PM and NO_X standards. Tailpipe emissions can be reduced by in-cylinder technologies and exhaust after-treatment devices. During the past 15

Table 1.1: U.S EPA heavy-duty diesel emission standards (g/bhp-hr) [1]

Year	HC	CO	NO$_X$	PM
1990	1.3	15.5	6.0	0.6
1991	1.3	15.5	5.0	0.25
1994	1.3	15.5	5.0	0.1
1998	1.3	15.5	4.0	0.1
2002	0.5	15.5	2.4	0.1
2007	0.14	15.5	0.2	0.01

Table 1.2: European ETC cycle heavy-duty diesel emission standards (g/kWh) [1]

Year (Tier)	HC	CO	NO$_X$	PM
2000 (Euro III)	0.78	5.45	5.00	0.16
2005 (Euro IV)	0.55	4.00	3.50	0.03
2008 (Euro V)	0.55	4.00	2.00	0.03

years, ever more demanding emission standards (Table 1.1 and 1.2), have been met by increasingly complex combustion processes and advanced engine designs. However, meeting the 2007 EPA emission standards will most likely require the use of after-treatment technologies. Simultaneous in-cylinder reduction of PM and NO$_X$ is especially difficult as they tend to 'trade-off' against each other – reducing the emissions of one tends to increase the other. However, this raises the possibility that any after-treatment technology that reduces the emissions of one will allow the other to be reduced by engine design.

One of the technologies currently being developed for reducing particulate emissions are diesel particulate filters (DPFs). DPFs reduce particulate emissions by physically trapping the particles, which they can do with an efficiency greater than 90%. However, the collected PM blocks the pores of the filter and forms particulate cake layers, which obstruct the exhaust flow. This causes the exhaust backpressure to steadily increase, which is detrimental to engine performance and fuel economy. The collected PM has to be *periodically* (or *continuously*) removed from the filter by a process called regeneration. DPFs have been studied for over 25 years, but an efficient, affordable, durable and reliable method of regeneration has yet to be

developed and marketed. Direct means of regeneration employ thermal means to increase the temperature of the exhaust to at least 550^oC. Such temperatures are rarely encountered with engines operating in the city or on the highway. Hence, regeneration by other means, primarily by lowering the temperature of regeneration by using fuel additives, filter catalytic coatings, exhaust catalyst, and oxidant injection have been investigated. Catalyst-assisted regeneration has several advantages over thermal means including lower engine backpressures, energy savings, lower peak temperatures and higher filter material reliability.

An innovative technology uses nitrogendioxide (NO_2) emissions, increased many-fold from engine-out levels by placing a catalyst upstream of the DPF, to continuously oxidize the particulate, at temperatures as low as 275^oC [2]. This system was initially thought to be infeasible due to its requirements of low sulfur diesel fuel (<50 ppm). However, with ultra low sulfur diesel fuel (<15 ppmS) being introduced into the market by mid-2006, as a result of EPA regulations, interest in this technology has been revived. In addition to fuel sulfur requirements, these systems require exhaust temperatures above 275^oC and need minimum NO_X/PM ratios in the range of 8:1 to 20:1 [3, 4]. This system can be used with a suitable EGR strategy so that NO_X and PM standards can be simultaneously achieved. A Johnson Matthey continuously regenerating trap (CRT®) is shown in Figure 1.1.

A continuously regenerating system is a two-stage device and comes as two variants: a CRT® and a catalyzed continuously regenerating trap (CCRT®). Both systems have a diesel oxidation catalyst (DOC), placed upstream of a filter, to oxidize as much of the engine-out NO to NO_2 as possible. In the first generation CRT®, the exhaust exiting the DOC enters an uncatalyzed particulate filter which utilizes the NO_2 to oxidize the PM. In the second generation CCRT®, the exhaust exiting the DOC enters a particulate filter coated with a catalyst which promotes the additional oxidation of NO to NO_2, which is then reused to oxidize PM, thus decreasing
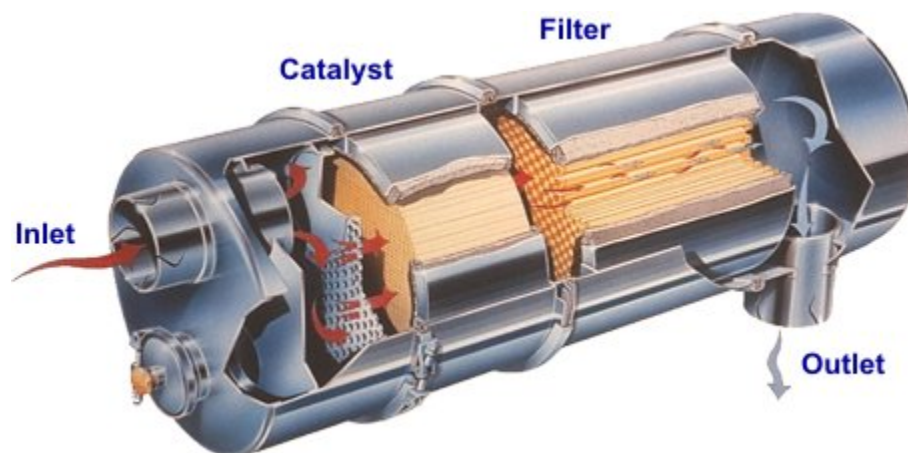
Figure 1.1: A Johnson Matthey CRT® device [5]

minimum NO_X/PM ratios required, making it suitable for use with future low NO_X engines (Tables 1.1 and 1.2). Even if active regeneration systems are eventually used to periodically regenerate filters, passive regeneration systems like the CCRT® are attractive because they ensure reduced PM loading in the filter, and thus do not need to be regenerated as often.

Compared to DOCs, DPFs and catalyzed particulate filters (CPFs), experimental and modeling studies in the literature, with CRTs® and CCRTs® are limited, especially in the case of the latter. Along with experimental research, modeling these complex devices is both a challenging and essential task. Modeling can reduce the number of experimental studies needed to evaluate the device, and expressing performance in terms of fundamental scientific parameters can help the design process, and can also serve as a basis for comparing different configurations of the same device or different devices. Further, modeling parameters can be incorporated into aftertreatment control systems, so that optimal regeneration (and engine) performance, and NO_X and PM control can be obtained.

This thesis is a computational and experimental performance study of a Johnson Matthey CCRT®. The performance of the CCRT® and its components, the DOC and the CPF, have been evaluated. The goal of this study was to perform experiments

and develop models to study the filtration, oxidation and pressure drop characteristics of the CPF and the gaseous emission oxidation and pressure drop characteristics of the DOC. The specific objectives of the research are described below.

1.1   Research Objectives

The experimental work had the following objectives:

- To design steady-state experiments which will provide the necessary data to calibrate the one-dimensional (1-D) DOC and CPF models.

- To perform the necessary experiments and data analysis to study the performance of a CCRT® across a range of exhaust flow rates and temperatures. The effect of CPF-inlet NO_2 concentrations on particulate oxidation were studied by comparing particulate oxidation rates in the CPF with and without the presence of the upstream DOC.

The starting point of the modeling work in this thesis was the following:

- A 1-D model of a DOC developed and validated by reference [6, 7] was used for the DOC modeling studies. The model features a second order kinetic scheme to describe the gaseous emission oxidation characteristics of HC, CO and NO across the DOC, and a model to predict the pressure drop of the exhaust gas across the DOC.

- A 1-D 2-layer model of a CPF, simulating particle filtration by the filter wall, a particulate cake layer oxidation model with a catalyst assisted reaction with O_2 [8] and with NO_2 *entering* the filter from the DOC [7].

Though tested and validated earlier for simpler after-treatment devices[8, 9], the CPF model did not have the capability to model the complex phenomenon occurring

in the CCRT®. Improved sub-models were developed to study the filtration, oxidation and pressure drop characteristics of the CCRT®. The model development and the simulation study thus had the following objectives:

- To develop a model for the oxidation of particulate inside the filter wall. This enabled the model to predict the lower CPF pressure drops due to oxidation of particulate in the wall.

- To develop a particulate cake layer filtration model for the CPF. This model overcame several shortcomings of the previous filtration-oxidation model and described particle filtration in terms of more fundamental parameters. It also properly coupled the wall oxidation model to the particulate cake layer filtration model.

- To develop a model to take into account the oxidation of particulate by the NO_2 *produced* by the catalyst in the CPF. This enabled the modeling of the higher reaction rates caused by the increased availability of NO_2, the primary design feature of the CCRT® as compared to the CRT®.

- To use the DOC model to determine the kinetic parameters describing the gaseous emission oxidation characteristics of the DOC, and predict the pressure drop and gaseous emissions like HC, CO and NO_X (NO and NO_2) downstream of the DOC.

- To use the resulting CPF model to perform a modeling study of the filtration, oxidation and the pressure drop characteristics of the CPF for each of the experimental test conditions. Use the model results to compare the oxidation performance of the CPF with and without the presence of the upstream DOC.

1.2 Thesis Outline

This thesis has six chapters. Chapter 2 is a background study and literature review and discusses relevant studies with DOCs, CPFs, CRTs® and CCRTs®. Chapter 3 contains a review of the MTU 1-D CPF model available at the start of this research, and also describes the improvements made to the model. Chapter 4 is an overview of the experimental test instruments, equipment, procedures, and methods and also discusses the experimental test matrices. Chapter 5 discusses the experimental data obtained, and the results from the CPF and DOC model calibration. Chapter 6 summarizes the conclusions from this research and provides recommendations for future research in this area.

Chapter 2

Background and Literature Review

This chapter is a background study which provides information to better understand the working of DOCs, DPFs and CPFs. It provides a review of particulate oxidation mechanisms in filters, particularly those present in CCRT® devices. A review of experimental studies and relevant findings with CRTs® and CCRTs® is also given.

2.1 Diesel Oxidation Catalysts

DOCs are devices designed to oxidize vapor and gas phase species present in diesel exhaust. They are usually a cellular honeycomb construction, consisting of numerous channels placed axial to the exhaust flow direction. It is a flow-through design, which means that all the channels in the DOC, which are usually square, are open at both ends, causing minimum restriction to exhaust flow. The channel design in a DOC and a schematic of the exhaust flow through a DOC are shown in Figure 2.1

DOCs are usually made of a ceramic called cordierite, $2MgO.2Al_2O_3.5SiO_2$. The function of the cellular honeycomb design is to provide a large surface area to increase contact with the gas phase of the exhaust. The ceramic cordierite itself does not possess any catalyst properties; however, a catalyst is coated onto the walls of
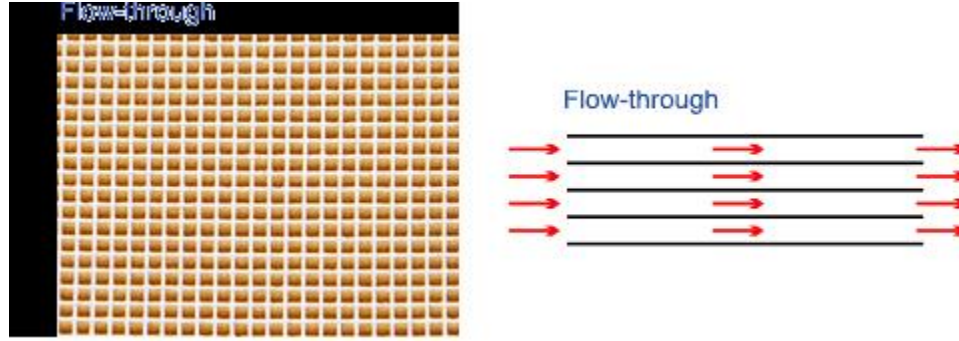
Figure 2.1: Channels in a DOC and a schematic of the flow through it [10]

the DOC. The catalysts, usually noble metals including primarily platinum (Pt), palladium (Pd) or rhodium (Rd), are applied onto a porous, high surface area substance like Al_2O_3, called the washcoat. The main function of the washcoat is to provide a high surface area to be a carrier of the catalyst metals. Washcoats should also possess good thermal stability. Most washcoats like Al_2O_3 are good carriers or promoters of catalytic activity while some like CeO_2 and V_2O_5 display some activity of their own. The Brunauer Emmett Teller surface area of washcoats has been reported to be more than $100 \frac{m^2}{g}$ [10]. The thickness of catalyst washcoats varies from 20μm-100μm, depending on the level of catalyst loading present [10, 11, 12]. The ends of square channels of highly loaded DOCs can get filleted due to the presence of the washcoat, altering the geometrical shape of the channel [11, 13].

As an emissions control device, DOCs oxidize HCs to form water (H_2O) and carbon dioxide (CO_2), and oxidize CO to form CO_2. The following global reactions are assumed to occur at the catalytic sites in the DOC [10, 14].

$$HCs + O_2 \rightarrow H_2O + CO_2 \tag{2.1a}$$

$$CO + \frac{1}{2}O_2 \rightarrow CO_2 \tag{2.1b}$$

Other beneficial effects of the DOC are the oxidation of non-regulated species like aldehydes, polynuclear aromatic hydrocarbons (PAH) and a reduction in the odor of diesel

exhaust [13, 14]. Even though the extent of soluble organic fraction (SOF) presence around particulate at exhaust temperatures (undiluted conditions) is very low [15, 16], DOCs are known to oxidize the HCs present around the particulate [14]. The presence of the DOC hence means that increased initial regeneration rates or stochastic regenerations [17] due to the presence of SOF will be minimal or absent. The mechanism of vapor phase and HC oxidation is believed to be a combination of catalytic cracking of heavy HCs and diffusion of gas phase species and light HCs [13, 14]. Other HCs present in the vapor phase are also known to be oxidized with high efficiency [13, 14]. In addition to temperature, exhaust flow rate (engine speed, turbocharger boost pressure) plays an important role in conversion efficiencies as it affects the residence time of the exhaust in the DOC. DOCs are not known to oxidize the solid phase carbonaceous particles present in the exhaust. Solid particle deposition in a DOC is greatest during transient engine operation by a process called thermophoresis due to the temperature gradient resulting from transient operation [14]. Variables affecting DOC performance include exhaust temperature and flow rate, monolith diameter and length, catalyst formulation and loading, cell density, and channel width.

Due to the small size of the DOC channels, the flow Reynolds numbers are between 10-200 and boundary layer development takes place at the entrance of the DOC and the flow remains laminar for the remaining length of the monolith. The efficiency of HC and CO oxidation by a DOC with a Pt catalyst on a Al_2O_3 washcoat is shown in Figure 2.2. It can be seen that conversion efficiencies become constant after 250^oC for CO and 300^oC for HCs. At low temperatures, the reactions in the DOC are kinetically limited. Under such conditions, the gaseous species diffuse through the laminar boundary layer to the surface of the washcoat, where they can be adsorbed or react at the active catalytic sites. The products of the reaction then diffuse back to the boundary layer. These processes could occur faster, resulting in higher conversions, if the exhaust temperature was higher (kinetically limited). At higher temperatures,
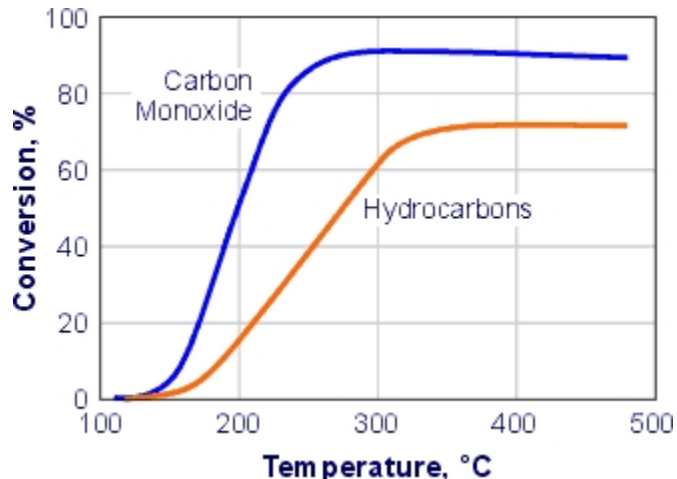
Figure 2.2: Typical HC & CO light-off curves for a DOC [10]

reaction rates increase dramatically, so that kinetics are not a limiting factor anymore. The high reaction rates in fact cause a large concentration gradient to develop between the boundary layer and the washcoat. The result is that reactions are now limited by mass transfer: the faster the gaseous reactants and products can diffuse through the boundary layer and get in and out of the washcoat, the higher the reaction rates. It should be noted that because the flow in the channels is fully developed, the transport of species from the bulk flow to the washcoat, even in the mass transfer limited regime, is still due to diffusion. It should also be noted that diesel exhaust is a complex mixture containing HCs of various molecular weights, and at some intermediate temperature, the reaction can be kinetically limited for light HCs and be mass transfer limited for larger HC molecules [14].

An additional role assumed by modern DOCs is their use to oxidize NO to NO_2, because NO_2 has been discovered to be a better low temperature oxidizer of particulate than oxygen [2, 18, 19, 20, 21, 22]. Fortunately, many catalysts used in DOCs to oxidize HCs and CO, especially Pt, are also known to promote the reaction of NO to NO_2 [2]. The function of the DOC in passive regeneration devices like the CRT® and CCRT®, is to increase the concentration of NO_2 entering the particulate filter.

The global reaction describing this process can be expressed as [23]:

$$NO + \frac{1}{2}O_2 \rightarrow NO_2 \tag{2.2}$$

DOCs oxidize NO keeping the total NO_X approximately constant – no NO_X reduction occurs across the DOC. NO conversion in the DOC depends on exhaust temperature and flow rate, monolith diameter and length, catalyst formulation and loading, cell density, and channel width and the relative concentrations of NO, NO_2 and O_2. A typical NO oxidation curve at different O_2 concentrations is shown in Figure 2.3. Figure 2.4, in contrast, is a NO oxidation curve across a 50 g/ft^3 Pt catalyst at different inlet NO concentrations, with 6% O_2 and 10% H_2O present in the exhaust. Figure 2.5 shows NO oxidation curves at different space velocities. At low temperatures,
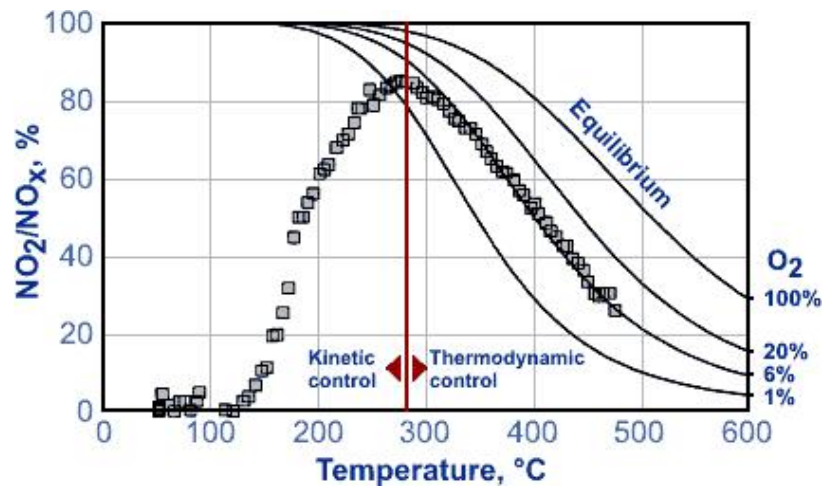
Figure 2.3: NO conversion across the DOC as a function of temperature [13]

before peak conversion, the oxidation of NO is kinetically limited; increasing the temperature or better catalyst formulations, loadings and contact times can all increase the NO conversion. It can be seen that increasing the temperature increases the NO conversion efficiency until a maximum, after which it decreases unlike that of HCs and CO which remain constant after a certain temperature. This suggests that the limiting factor is not mass transfer like in the case of HCs and CO, rather it is due
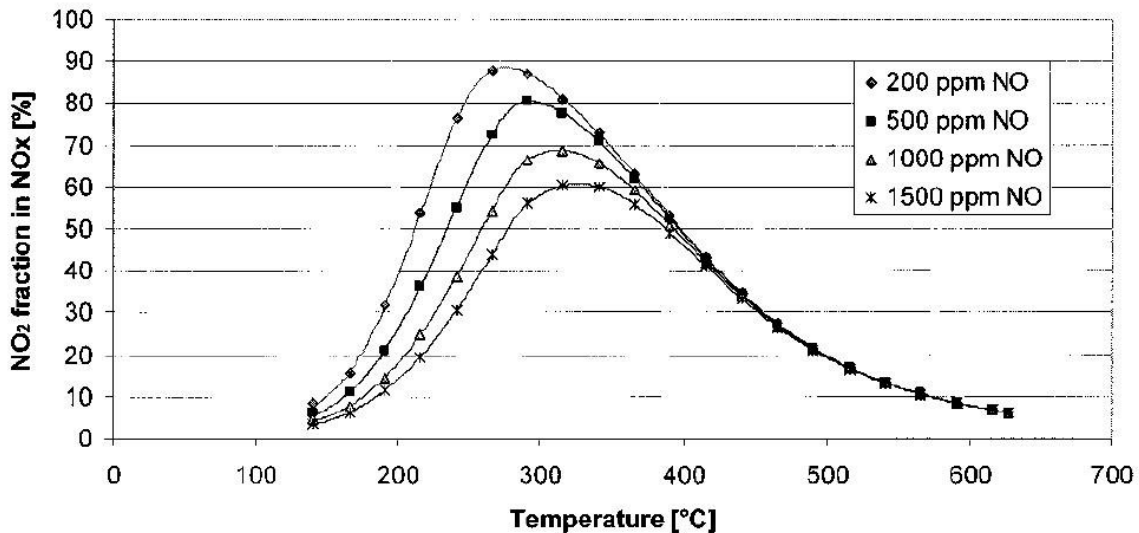
Figure 2.4: NO conversion across the DOC at different NO concentrations (6% O_2 and 10% H_2O) [24]
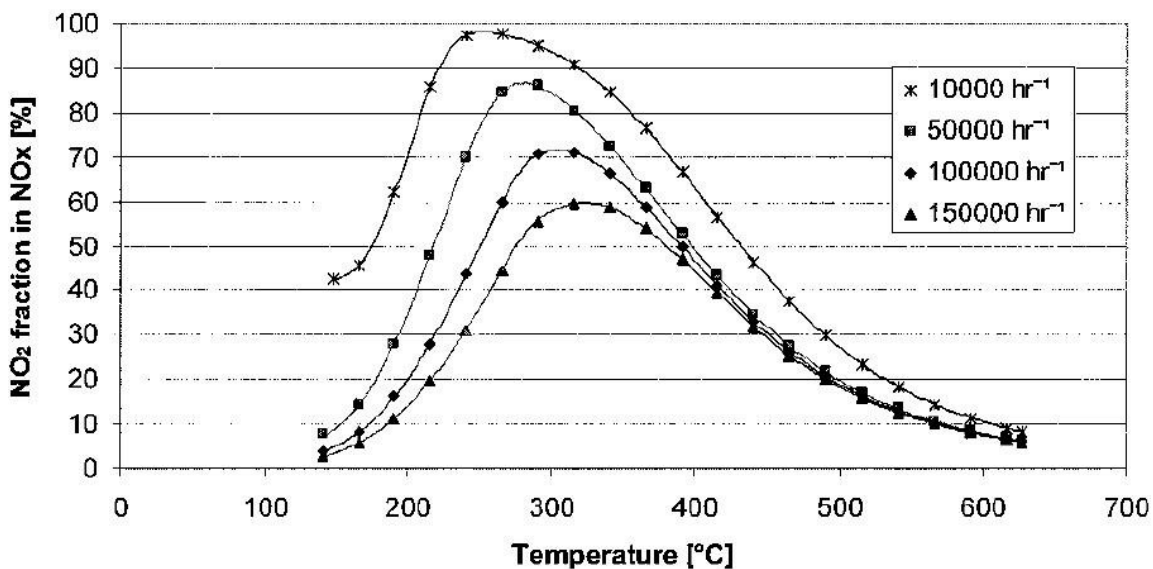
Figure 2.5: NO conversion across the DOC with temperature at different space velocities (270 ppmv NO, 6% O_2, 10% H_2O in N_2) [24]

to thermodynamic limitations, and NO_2 concentrations cannot be increased beyond the point on the equilibrium curve. Similar results have been obtained in other studies [6, 24, 25], although they obtained peak conversions at different temperatures. This makes the DOC most efficient in the temperature range of 330^oC-370^oC, which is suggested by many researchers to be the optimal operating window for passive regeneration [24, 25, 26]. However, it should be noted that although the NO conversion decreases after about 370^oC, total engine-out NO_X concentrations tend to increase with exhaust temperature. By engine calibration, NO_2 levels of about 80-100 ppm can still be made to exit the DOC, in spite of lower conversion efficiencies at temperatures greater than 370^oC. Figure 2.3 shows NO conversion increases with O_2 concentrations due to increased availability of O_2 which increases the rate of Equation 2.2. High NO concentrations at low temperatures result in low conversion efficiencies because of the kinetically limited regime – the kinetics are not strong enough to oxidize the increased concentrations. At high temperatures, beyond peak conversion, all NO concentrations have the same conversion efficiency – because of thermodynamic limitations which limit the NO_2/NO_X and NO/NO_X ratio (Figure 2.4). Low exhaust flow rate (low space velocity) results in a higher residence time in the DOC, which increases the contact time with the catalyst and results in higher NO conversion efficiencies, in both the kinetically limited regime and the thermodynamically limited regime as shown in Figure 2.5.

A major concern with the use of DOCs is that they tend to oxidize sulfur-dioxide present in the exhaust to sulfur-trioxide which can combine with water vapor to form sulfuric acid [10]. This problem is compounded by the fact many of the catalysts active in oxidizing NO→NO_2, HCs and CO, are also active in oxidizing SO_2 [2, 10]. The following global reactions are believed to describe the process [10]:

$$2SO_2 + O_2 \rightarrow 2SO_3 \tag{2.3a}$$

$$SO_3 + H_2O \rightarrow H_2SO_4 \tag{2.3b}$$

Formation of sulfuric acid is undesirable for its adverse impact on health, increase in nuclei-mode particles and total particulate matter (TPM) downstream of the DOC. Further, oxidation of SO_2 to SO_3 involves the use of catalytic sites which decreases the availability of such sites for oxidation of HCs, CO and NO thus decreasing their respective conversion efficiencies. Formation of SO_2 also poisons the catalyst, continuously decreasing catalyst performance with time. Thus, the superiority of a DOC catalyst is demonstrated not only by high conversion efficiencies of HC, CO and NO but also by its inhibition of SO_3 formation. An obvious solution is to limit the SO_2 entering the DOC by the use of low sulfur fuel. Cooper et.al. [2] initially suggested the use of at most 50 ppmS fuel iwith DOCs. However, with ULSF fuel (<15 ppmS) being introduced into the market by mid-2006 as a result of EPA regulations, formation of sulfur-trioxide will be minimal.

2.2   Catalyzed Diesel Particulate Filters (CPFs)

Two problems with particulate oxidation in the exhaust are that it is too dilute in the exhaust, and the residence time in the exhaust line is too short [27]. Hence alternate methods like particulate filters were experimented with to reduce tailpipe-out particulate matter.

The most common design of the particulate filter is the wall-flow monolith. The wall-flow filter has every other channel blocked, forcing the exhaust to flow through porous walls into the outlet channels. Figure 2.6 shows the cell design in wall-flow filters, and a schematic of the exhaust flow through them. Particles in the exhaust are filtered when they flow out of the inlet channels through the particulate cake layer and the filter walls to the four surrounding outlet channels. The channels are usually square although triangular and hexagonal shapes have been reported in the literature.

High particle filtration efficiencies of 90% and above have been obtained with this design, because of low wall porosities(45%-50%), particulate cake layer filtration, and high surface area to volume ratio. Fibrous filters, on the other hand, have lower filtration efficiencies because of higher wall porosities (>60%) and consequently the depth-filtration mechanism involved.
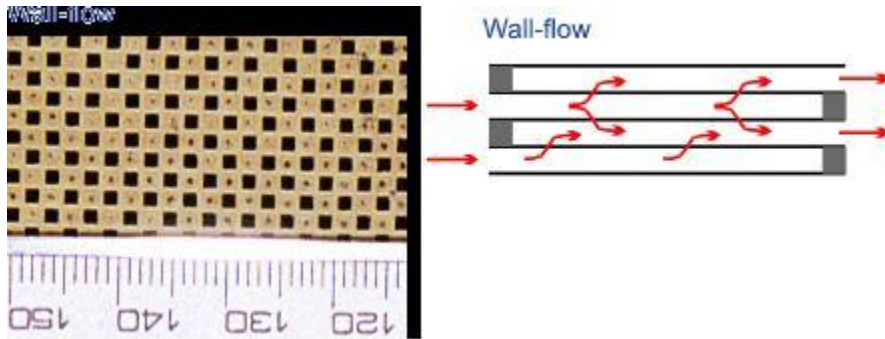
Figure 2.6: CPF channel design and a schematic of the flow through it [28]

2.2.1 Particle Filtration Mechanisms

The two fundamental regimes of particle collection by the filter based on the collection mechanisms are: deep-bed (depth) filtration and particulate cake layer (surface) filtration. Deep-bed filtration occurs when the filter is relatively clean with very little particulate present on the wall, and represents collection in the filter wall. It can be thought to occur when the mean pore size of the filter wall is greater than the mean diameter of the diesel particles, and hence the particles are collected when they flow through the wall. Particle filtration during the particulate cake layer filtration regime occurs when a particulate cake layer has developed and represents filtration by the particulate cake. Filtration by the particulate cake layer can be thought to occur when the mean pore diameter of the cake is less than the mean diameter of the particles. Thus the average particle cannot pass through the passages present in the cake and is collected by *sieving*, with new layers being formed upon existing layers.

Cake filtration is even more efficient than deep-bed filtration, in spite of the cake being much more porous than the wall, because small mean pore sizes of particulate cake deposits, around 0.1μm [17, 29]. Viewing filtration as a phenomenon when pore passages are bigger than mean pore size (or vice-versa) is simplistic because the pore passages in a filter wall are of many diameters and are only represented by an average called a mean pore size. Further, the engine-out particles are themselves composed of an entire range of diameters separated by two orders of magnitude (10-1000nm).

Figure 2.7 is a schematic of particle collection mechanisms in a diesel particulate filter. The filtration processes are Brownian diffusion and direct interception [30, 31]. Brownian diffusion is known to be dominate collection of small particles at low flow rates, when the particles do not follow the streamlines of the flow due to random Brownian motion [31]. Interception occurs when a streamline passes the collection medium at a distance less than the radius of the particle [31]. Other collection

Brownian Diffusion   Inertial Impaction

Interceptional Collection
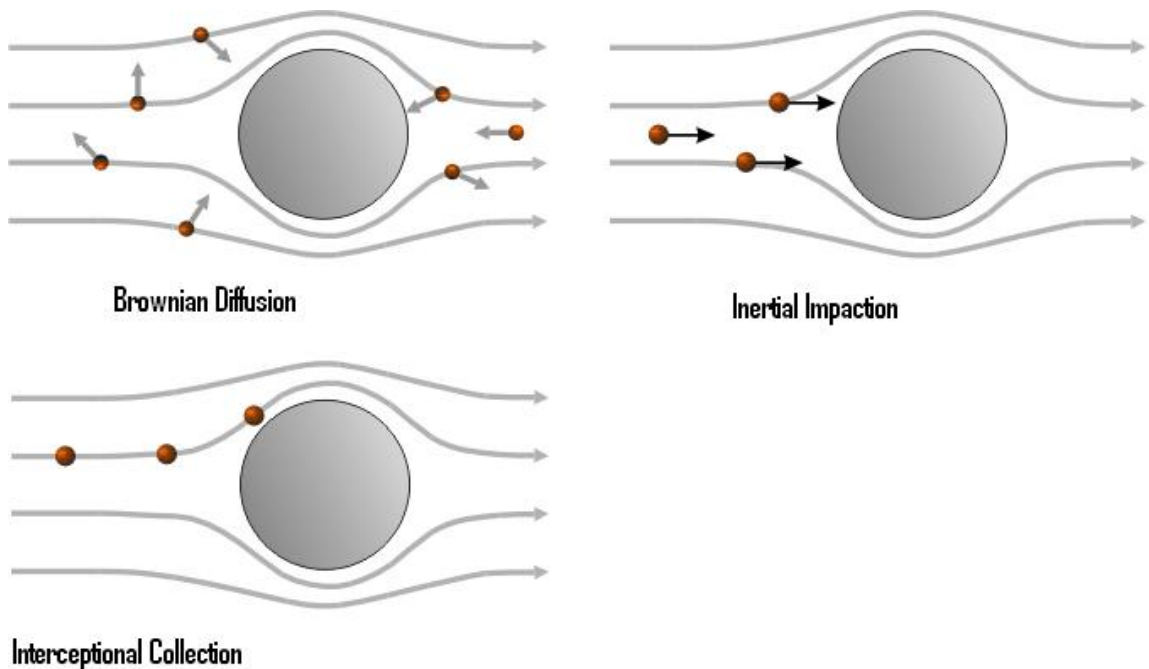
Figure 2.7: Schematic of the filtration mechanisms in a particulate filter [28]

mechanisms like gravitational settling, inertial deposition and thermophoresis are known to be insignificant given the conditions and particle sizes ($< 1\mu$m) of diesel

exhaust[30, 31]. Particles of intermediate size that are too large for collection by Brownian diffusion and too small to be collected by interception, penetrate the filter wall with least filtration.

The biggest engineering problem with regeneration is to design a system that uses passive oxidation and periodic active regeneration of particulate collected by the filter. Regeneration of the collected particulate is essential because it causes flow restriction which leads to an increasing exhaust backpressure, decreasing engine performance. Direct oxidation of particulate requires high temperatures ($> 500^oC$), which are not present during normal engine operation. Hence, alternate means have been investigated, including raising the exhaust temperature or providing energy from other sources (active regeneration), and lowering oxidation temperatures by the use of catalysts or by an active species like NO_2 present in the exhaust (passive regeneration).

Many means of supplying energy to initiate active regeneration have been suggested. Fuel can be injected in the exhaust upstream of a catalyst designed to burn the vaporized hydrocarbons, increasing the exhaust temperature. Another way to raise exhaust temperature is to post-inject fuel in the cylinders during the expansion stroke. Throttling of the intake air, designed to raise exhaust temperatures has also been used.

2.2.2 Thermal Oxidation of Particulate

Thermal oxidation refers to the direct oxidation of the particulate by oxygen. While the actual reaction can be complex involving the formation of intermediates and complexes, a global one step heterogeneous equation can be expressed as:

$$C + (1 - f_{CO}/2)O_2 \rightarrow f_{CO}CO + (1 - f_{CO})CO_2 \qquad (2.4)$$
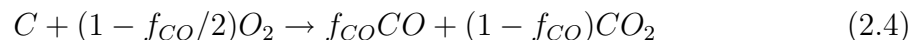
where f_{CO} is the CO selectivity for the particulate oxidation by thermal means. It has a temperature dependence which can be found in references [7, 32, 33, 34].

The major disadvantage with this method is that it requires high temperatures, typically greater than 550^oC, for this reaction to have a significant rate. The reason for the high temperatures required is the high activation energy for direct oxidation of particulate by O_2, around 150-160 kJ/mole [17]. Since such temperatures are not encountered in normal driving conditions, other methods for oxidation of particulate have been investigated.

The thermal oxidation of particulate has a CO/CO_2 fraction of around 1 [17, 35]. Du et.al. [35] postulated that the CO and CO_2 are formed at different sites in the carbon black. They also report that CO is formed across a wide range of activation energies attributed to the complex nature of carbon.

Some studies with diesel particulate have observed reaction rates in the early stages of combustion to be unusually high. This has been attributed to the removal of HCs present around the carbon core [17]. However, levels of HCs present on the particulate particles at engine-out temperatures are unclear, due to the temperatures of the exhaust gas. Konstandpoulos et.al. reported that the particulate deposited in particulate filters above 200^oC are mainly carbonaceous solids[15], while Stratakis et.al. reported that HCs are adsorbed below 200^oC but is only completely desorbed above 400^oC [16]. In any case, the presence of the DOC in continuously regenerating devices will reduce or eliminate such occurrences because of the oxidation of these HCs (Section 2.1). Importantly, Yezerets et.al. found that several particulate samples had high initial reaction rates not related to HCs on the particulates but rather due to initial particulate pre-oxidation [36]. They also found that modeling the pre-oxidation can affect the average kinetic parameters obtained for the entire sample, resulting in lower activation energies. After the particulate pre-oxidation, the reactivities of the remaining particulate samples can be described by first-order Arrhenius kinetics over

a wide range of temperatures from $330^{o}C$–$610^{o}C$ [36].

2.2.3   Catalytic Oxidation of Particulate

Catalysts have been suggested for use in particulate filters to lower the oxidation temperature of particulate by reducing the activation energy. The exact mechanism of oxidation is unclear because of the complex reactions involved in catalytic oxidation of particulate. Mechanisms suggested include enhanced mobility of catalytic oxygen species, adsorption/desorption of oxygen and facilitating reaction with NO_2 by adsorption/desorption. In contrast to thermal oxidation, a characteristic of many catalytic reactions is the very low CO/CO_2 fractions (≈ 0.05) in the products of the reaction [17, 35]. The catalysts are employed by doping of diesel fuel or by coatings on the walls of particulate filters.

Stanmore et.al. report that catalysts that have better contact with particulate have more pronounced effects on oxidation [17]. Further, some catalyst coatings exhibit high activity in 'tight' contact with particulate, but very poor activity in 'loose' contact [17, 37]. This is important because Neeft et.al. showed that for monolithic diesel particulate filters with catalyst coatings, the contact conditions fall into the 'loose' category [37]. Catalyst contact with particulate is accepted to be one of the most important factors determining higher particulate oxidation rates.

The activity of metal oxide catalysts (alkali metals, copper, vanadium, molybdenum, etc.) has been attributed to breaking of C-C bonds and acting as oxygen pumps through redox cycles, involving changes of transition metals valence. It promotes the formation of surface oxygen complexes with low activation energies for desorption. Some have even found carbon oxidation even in the absence of oxygen, indicating that a redox mechanism is active.

Precious metals (like Pt, Pd, Rd) show some low temperature activity because they are partial to HC oxidation which can result in the beneficial after-effect of

carbon oxidation. Pt based catalysts are less active than molten salt based catalysts with oxygen as the oxidant species [19].

Recently Cu-K-V-Cl and Cu-K-Mo-Cl catalysts have been studied that decreased the activation energy of carbon combustion by more than 50%, down to 76 kJ/mol from 157 kJ/mol. Catalyst performance is enhanced when it is dissolved in a eutectic liquid, which expectedly increases the contact between the catalyst and the carbon, due to the *mobility* of the catalytic species. However, some volatile copper chloride catalysts can suffer from evaporative loss of the active species, and further have been linked to formation of hazardous toxins. Newer mobile catalysts, without copper, like $Cs_4V_2O_7$, show significant activity at low temperatures, in fact showing peak activity at 330^oC. It was not found to be suitable for vehicle engines, as this catalyst was found to lose appreciable quantities of active metal ions in water condensate, which can form in engine exhaust lines when the engine is stopped [38]. Molten salt catalysts can reduce the temperature for particulate oxidation, with only O_2 present in the exhaust to about 325^oC [19]. Fino et.al. [39] reported that the liquid mobility of such catalysts made their use with wall-flow filters unsuitable, because the eutectic liquid can plug the small pores (10-15μm) of the filter. This causes high backpressures to develop which can only increase with the particulate cake layer developing on the filter. This makes highly mobile catalysts suitable only for depth-filtration filters, which have larger mean pore sizes. For this reason, wall-flow monoliths might very likely be impregnated with catalysts that remain fairly solid in the temperature range of interest, at a penalty of low temperature performance [39, 40]. For wall-flow filters, perovskite-type catalysts have been suggested which have better stability characteristics, but are less active than molten salt catalysts . These catalysts, compatible with wall-flow filters constructed from cordierite/SiC, oxidize the particulate with α-type weakly chemisorbed suprafacial oxygen species. Some researchers suggest exploiting the formation of α-type weakly chemisorbed suprafacial oxygen species in perovskite

catalysts as the path to develop new active low-temperature catalysts for wall-flow filters [40]. Peak activity temperatures of about $330^{o}C$, underlines the importance, scope and potential of catalysts for enhanced particulate oxidation.

It is clear from this discussion that, although catalytic oxidation of particulate involves adsorption/desorption, formation of intermediates and complex species, it nevertheless involves a reaction with oxygen. A global one step heterogeneous form for the catalytic oxidation of particulate with oxygen is employed for modeling purposes, which is given by:

$$C + (1 - f'_{CO}/2)O_2 \rightarrow f'_{CO}CO + (1 - f'_{CO})CO_2 \qquad (2.5)$$
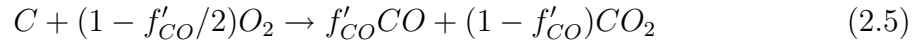
where f'_{CO} is the CO selectivity for the particulate oxidation by catalytic means. It has a form similar to the reaction representing thermal oxidation (equation 2.4) with a temperature and catalyst dependence. References [32, 33, 34] should be conferred for details on the temperature dependency of f'_{CO}.

2.2.4 NO_2 Assisted Oxidation of Particulate

The phenomenon of particulate oxidation by NO_2 present in diesel exhaust in the gaseous phase was first reported by Cooper and Thoss [2]. Since then, studies by other researchers have proven conclusively the beneficial effect of particulate oxidation by NO_2, at temperatures much lower than with reactions with O_2 [18, 22, 41]. This is shown in Figure 2.8, which is a comparison of particulate oxidation rates by O_2 and NO_2, at a constant temperature ramp of $1^{o}C/min$. The particulate oxidation rates with NO_2 can be seen to light-off at temperatures about $200^{o}C$ lower than with O_2. For the NO_2-particulate reaction to work at rates high enough to consume considerable amounts of particulate, the concentration of NO_2 in the exhaust has to be increased from engine-out levels. This is generally done by placing a DOC
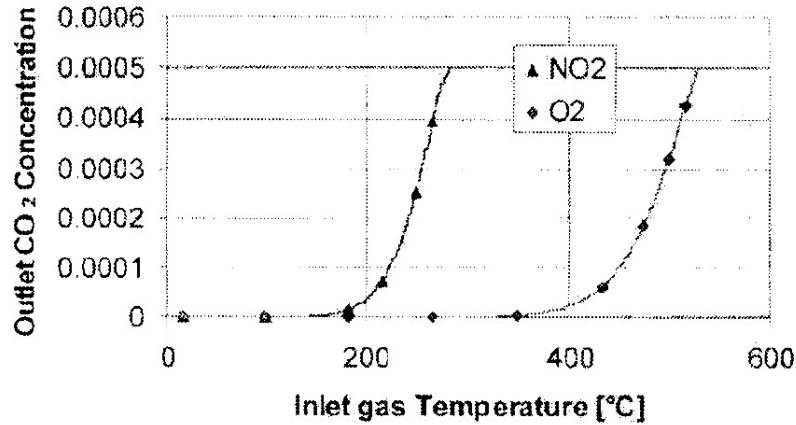
Figure 2.8: Comparison of particulate oxidation rates by O_2 and NO_2 [25]

upstream of the particulate filter (Section 2.1).

NO_2 is directly involved in the chemical reaction oxidation of diesel particulate by adsorbing onto the particulate followed by a reaction which forms CO and NO [2]. No contact with a catalyst, or the presence of oxygen, is required for oxidation of particulate by NO_2. Cooper et.al. originally suggested that the global reactions involved were [2]:

$$NO_2 + C \rightarrow NO + CO \tag{2.6a}$$

$$NO_2 + CO \rightarrow NO + CO_2 \tag{2.6b}$$

However, more recent studies suggest although intermediate species could be formed during the NO_2-particulate reaction, the following global reactions could be assigned to these reactions [18, 22, 42].

$$NO_2 + C \rightarrow NO + CO \tag{2.7a}$$

$$2NO_2 + C \rightarrow 2NO + CO_2 \tag{2.7b}$$
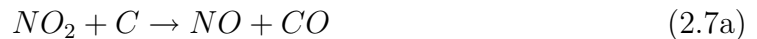
Further, of the two reactions, equation 2.7b is reported to the dominant reaction [18, 22, 42]. This can be said with confidence because the rate of CO_2 formation is much

higher than the rate of CO formation [18].

Activation energies of the NO_2-particulate reaction vary from about 50 kJ/mol [19, 22, 43] to 120 kJ/mol [41]. These results could vary because of the experimental procedures, with some reactors where the supply of the NO_2 is due to diffusion, while in flow-through reactors NO_2 is supplied by convection. In the latter case, the availability of the NO_2 is throughout the particulate cake, not just the top layers, which can affect the *apparent* activation energy of the reaction.

The reaction order of the NO_2-particulate reaction has been reported to be one with respect to the NO_2 concentration, at least at temperatures greater than 300^oC [17, 18, 22]. Andersson et.al. also found that the NO_2-particulate reaction is linear with respect to NO_2 concentration [42]. At temperatures of 300^oC (and below), the NO_2-particulate reactivity is very low, and even greatly increasing the NO_2 concentrations does not increase the oxidation rate. This has been established experimentally by Andersson et.al. [42], and also by computational parametric studies of Triana [7]. This means that at temperatures below 300^oC, the reaction order with respect to NO_2 is zero. In contrast, Mikhno et.al. report that at temperatures below 300^oC and above 200^oC, the reaction order increases to 2, while below 200^oC the reaction order is greater than 2 [22]. The beneficial effect of the presence of water vapor and oxygen on the NO_2-particulate reaction was first also reported by Copper and Thoss [2]. Jacquot el. al. reported that the presence of oxygen and water not only increases the rate of the NO_2-particulate reaction, but that their effect is cumulative [18]. Water vapor and O_2 increase the reaction rate due to two very different reasons. The increase in reaction rate due to the presence of oxygen is attributed to the reaction between O_2 and intermediate species. Water vapor does not participate in the NO_2-particulate reaction, but rather acts like a catalyst: an oxygen balance reveals that oxygen atoms of water are not consumed during the NO_2-particulate reaction. In fact, the reaction between the intermediate species and NO_2, O_2 is catalyzed by water vapor [18]. These

effects are shown in Figures 2.9 and 2.10, where the increase in particulate oxidation rates with NO_2 due to the presence of oxygen and water vapor can be seen.
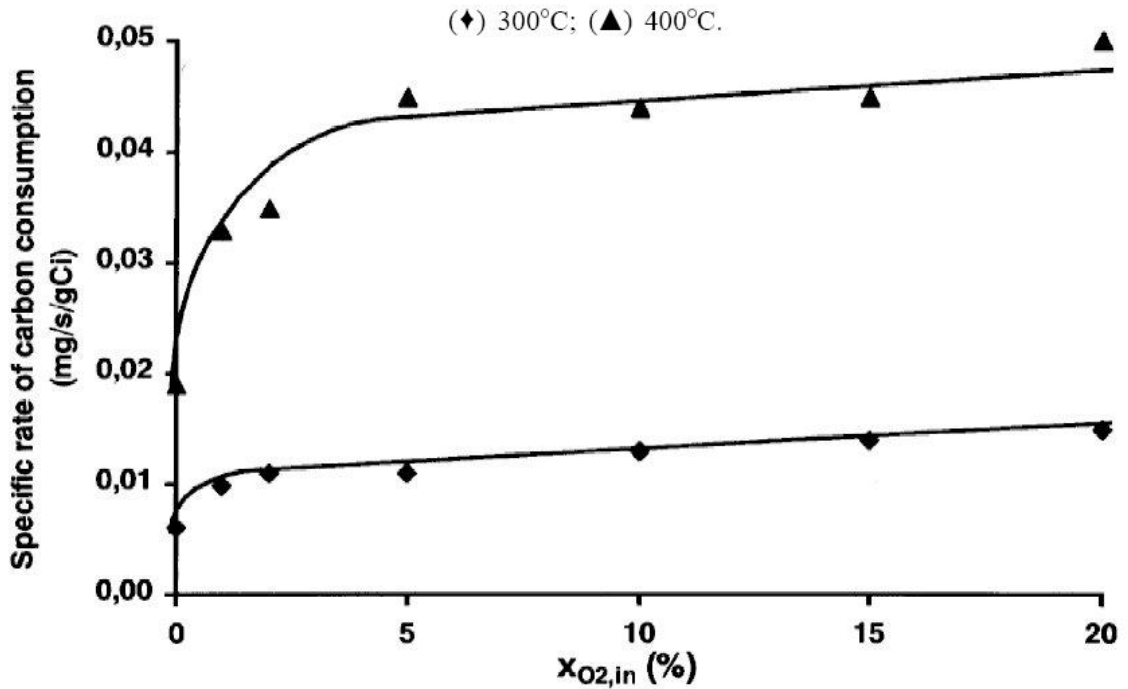
Figure 2.9: Effect of O_2 on particulate oxidation rates with NO_2 (NO_2=437ppmv) [18]

CRT® devices, patented by Johnson Matthey, use NO_2 emissions increased many-fold from engine-out levels by placing a DOC upstream of a DPF, to continuously oxidize the particulate deposited inside the filter at temperatures much lower than by O_2 (Figure 2.8). CRT® devices can be integrated with an appropriate EGR strategy to achieve simultaneous reduction in PM and NO_X levels. Chatterjee et.al. have used the CRT® with low pressure EGR, achieving a 40%-60% reduction in NO_X and a 90%-plus reduction in HCs, CO and PM [44]. For optimal operation, the engine has to be calibrated to achieve mass based NO_2/PM ratios of at least 8-10 downstream of the DOC. Triana found that the CRT® devices had good oxidation rates at limited conditions when used with EGR, than when used without EGR [7]. Triana also reported that the NO_2-assisted regeneration showed significant benefits
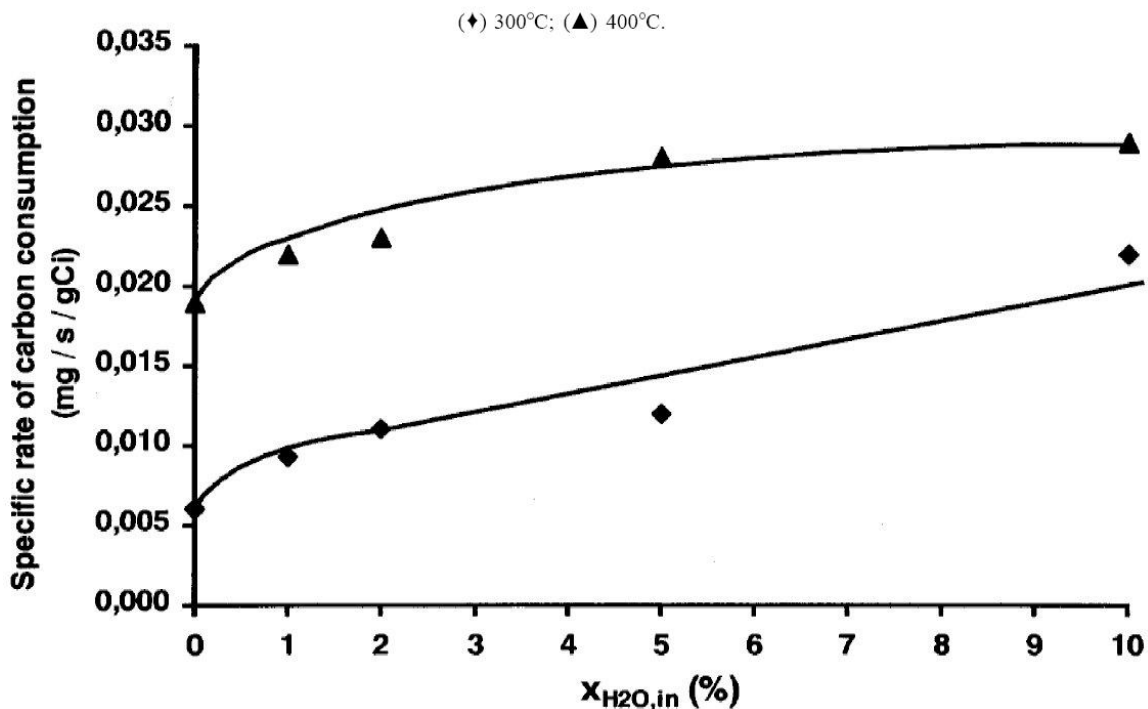
Figure 2.10: Effect of H_2O on particulate oxidation rates with NO_2
(NO_2=437ppmv) [18]

at temperatures of about 360^oC, with mass based NO_2/PM ratios of at least 8 and NO_2 concentrations above 100 ppm. Walker et.al. achieved NO_X reductions of 92% along with a 90% plus reduction in HCs, CO and PM by using a combined CRT®-SCR system[45]. They demonstrated that this system achieved the EURO V and possibly the EPA heavy-duty 2007 (subject to PM verification) emission standards. The advantage of having a NO_X treatment device downstream of a CRT® is that much lower EGR levels can be used, thus greatly increasing the NO_2/PM ratios by simultaneously increasing NO_X and decreasing PM concentrations.

Recently, Triana verified that the pressure drop across the DPF in CRT® devices and DPF-only configurations can be very different at optimal NO_2-assisted regeneration conditions [7]. Triana also reported that at some conditions a relatively high particulate mass can be deposited inside the filter while still having a low pressure drop across the filter. Pressure drop is thus not always a reliable indicator of partic-

ulate mass in the filter. This has implications for after-treatment control models for such devices, which have traditionally used the filter pressure drop as an indicator of the particulate mass in the filter. It could be that oxidation by small amounts of NO_2 (ppm), could be a highly localized phenomenon, occurring in pockets, resulting in increased particulate cake permeabilities due to lower flow restriction [7, 46]. Maly et.al. reported that oxidation by NO_2 can be highly non-uniform, and can lead to high regeneration rates in some locations, depleting the particulate cake locally, and decreasing the pressure drop due to increased exhaust flow through these depleted sections of the filter [47]. The spatially non uniform phenomenon reported by Maly et.al could also occur in several channels with different degrees of oxidation, further complicating the picture. In CRT® devices, the pressure drop across the filter can drop below the balance point at some operating conditions ([7, 46] and chapter 5). This could be due to oxidation inside the wall of the filter. Unlike catalyst coatings, NO_2 being a gaseous species, can have a higher penetration into the filter wall and could 'reach' the particulate inside the wall readily. This can lead to oxidation in the pores of the wall, which can decrease the pressure drop across the DPF.

For modeling purposes, a global one step heterogeneous form for the reaction, involving all the available NO_2 is employed.

$$C + (2 - g_{CO})NO_2 \rightarrow g_{CO}CO + (1 - g_{CO})CO_2 + (2 - g_{CO})NO \qquad (2.8)$$
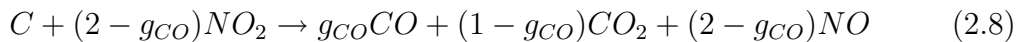
where g_{CO} is the CO selectivity for the particulate oxidation by NO_2. It has a form similar to the reactions representing thermal and catalytic oxidations (equations 2.4 and 2.5), and a temperature dependence which can be found in references [7, 41]. The fact that Equation 2.7b is the dominant reaction means that g_{CO} can be assumed to be equal to zero (or close to zero) without any adverse impact on model results. Jacquot el. al. [18] have published kinetic parameters of a more complex model taking into

account the concentrations of water and oxygen in the exhaust. However, it is not been used as a basis for the NO_2 based regeneration in the MTU 1-D model as it is different from the regeneration framework of Bisset [48] and Konstandopoulos [41] upon which the MTU CPF model is based.

Activity of molten salt-based catalysts, which are used as active catalysts for the oxidation of particulate with oxygen, is not affected by the presence of NO in the exhaust. These catalysts also do not promote the oxidation of NO to NO_2 when exhaust flows over them. Hence, oxidation of particulate takes place only when NO_2 is present in the exhaust [19]. The particulate oxidation with NO_2 *present in the exhaust* thus remains the the same irrespective of the presence of the molten salt-based catalyst present on the particulate filter.

The rate of the reaction in the presence of Pt based catalysts increases if NO_X is present in the exhaust. This has been attributed to the catalytic oxidation of NO to NO_2, over the Pt catalyst, followed by the reaction of NO_2 with particulate [3, 19, 20, 21, 49]. Such behavior only happens with a catalyst in a washcoat , doping platinum catalysts with diesel fuel does not increase the oxidation rate of particulate due to the reoxidation of NO to NO_2. The authors report a 'recycling' effect of NO_2, whereby NO_2 reduced to NO due to reaction with the particulate, is catalytically oxidized back to NO_2, which oxidizes the particulate again. This happens a number of times, possible even greater than 3. This 'recycling' effect was found to be significant, only at temperatures greater than about 340^oC [19]. It is possible that at temperatures below 350^oC, when the NO-NO_2 reaction is kinetically limited, the production of NO_2 in the catalyzed filter will be insignificant compared to that of a upstream DOC, due to the longer contact time of the gas with the DOC than in a filter. At higher temperatures, the NO-NO_2 reaction kinetics could be high enough to cause multiple oxidations of NO to NO_2 and their subsequent reaction with particulate. The presence of HCs and CO in the exhaust can increase the NO_2-particulate reaction over Pt

based catalysts. It was also found that the HCs and CO components of the simulated exhaust, are completely oxidized over the Pt based catalysts [19]. This serves an additional function of the CPF catalyst when used with an active regeneration system – to oxidize the HCs that have slipped past the DOC during fuel injection in the exhaust.

Second generation CCRT® devices are based on the principle of increased particulate regeneration rates by the NO_2 'recycling' effect, by coating the filter with a catalyst which promotes the oxidation of NO. Such a device has been found to have increased oxidation rates at low exhaust temperatures, and lower balance temperatures as compared to a CRT® device[3, 49]. Maly et.al. too found that the CCRT® device had the highest oxidation rates compared with CRT® and CPF-only systems[47]. This means that for the same inlet NO_2 concentrations, the CCRT® has a higher particulate oxidation rate compared to a CRT®, and for the same particulate oxidation rate, the CCRT® will require lower inlet NO_2 concentrations. In CCRT® devices, the catalyst loading in the CPF is paramount not only because of the NO-NO_2 dependence but also to keep costs down by decreasing overall catalyst loadings. Lower catalyst loadings also decrease the engine back pressure because catalyst coatings decrease the porosity (and permeability) of the filter substrate [50]. Allanson et.al. found that reducing the catalyst loading in the CPF of the CCRT® to 25% of its original loading did not decrease the particulate oxidation rates significantly [49].

It is known that only some of the NO_2 present in the exhaust, reacts with the particulate deposited on the walls of the filter, while the remaining NO_2 leaves without reacting. This phenomenon is called NO_2-slip. This is probably why NO_2/PM ratios needed for continuously regenerating the particulate are much greater than 1, in fact they are reported to be at least 8 (or 16), depending on which reaction is assumed to be dominant (Equations 2.7a and 2.7b). This could also be because of insufficient time for the NO_2-particulate reaction, as Cooper et.al. reported that the reaction

proceeds by the NO_2 first adsorbing onto the particulate [2]. This is supported by Jacquot et.al. whose studies show a transient regime in NO_2 outlet concentrations and nitrogen balance even in steady state conditions [18, 22]. The 'recycling' effect of NO_2 is thus important, because it better utilizes the available NO_2. Further, with stricter upcoming standards for NO_X, now being achieved by high pressure cooled EGR technology, the 'recycling' effect of NO_2 will become even more important, because of its more efficient utilization of available NO_2 (and NO). Under these conditions, the CCRT® device can be expected to perform better than a CRT®.

Chapter 3

1-D DOC, CPF Models and Improvements

This chapter reviews the 1-D DOC and CPF models used in this research. A brief review of the DOC model is presented with a discussion of its salient features. A detailed review of the CPF model which was available at the start of this research is given followed by a description of the the various sub-models added to the model, including oxidation inside the wall, a particulate cake layer filtration sub-model and an oxidation sub-model to account for the NO to NO_2 oxidation in the CPF.

3.1   Overview of the 1-D DOC Model

An overview of the DOC gas phase oxidation and pressure drop models is presented in this section. The model was developed and validated by Triana [6, 7], and no modifications were made to the code.

The DOC model is a single channel representation of the DOC and is based on the work of reference [51]. A schematic of this representation is shown in Figure 3.1 (taken from [7]). In the Figure, 'L' is the length of the DOC and 'x' is the coordinate in the axial direction.

Some of the important assumptions in the DOC model are as follows. The model is a quasi steady-state representation of the DOC considering the short residence time of the exhaust gases in the DOC. The temperatures, gaseous species concentrations and flow velocities are channel cross section averaged properties, and any radial variation in these properties is neglected. Heat transfer between the channel and the surroundings is neglected. The chemical reactions shown in Equation 3.1, are the only reactions taking place and they take place at the DOC wall temperature.

DOC Single Channel Schematic
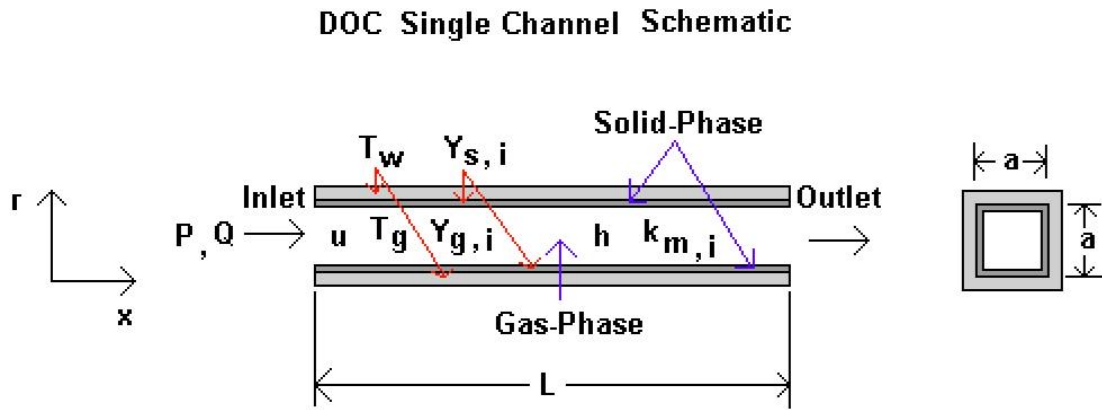
Figure 3.1: A schematic of the DOC single channel representation [7]

The kinetic scheme in the model can be used to predict the concentrations of HCs, CO and NO downstream of the DOC, assuming that the following reactions take place in the DOC:

$$CO + \frac{1}{2}O_2 \rightarrow CO_2 \tag{3.1a}$$

$$C_3H_6 + \frac{9}{2}O_2 \rightarrow 3CO_2 + 3H_2O \tag{3.1b}$$

$$NO + \frac{1}{2}O_2 \rightarrow NO_2 \tag{3.1c}$$
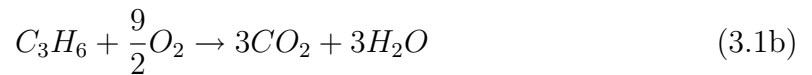
HC oxidation is represented using propylene (C_3H_6) although actual HC concentrations consists of a range of C_1 to C_{40}. Note that the model assumes complete oxidation of the HC's to CO_2 and H_2O, without formation of CO. The effect of sulfur oxidation

was neglected as ULSF fuel was used in the experiments. It is assumed that total NO_X concentrations do not change across the DOC. The kinetic schemes assumed are second order reactions, with an inhibition term (G) to take into account the relative concentrations of CO, C_3H_6 and NO present in the exhaust. The reaction rates are given by:

$$r_{CO} = K_{CO}Y_{CO}Y_{O_2}/G \tag{3.2a}$$

$$r_{C_3H_6} = K_{C_3H_6}Y_{C_3H_6}Y_{O_2}/G \tag{3.2b}$$

$$r_{NO} = K_{NO}Y_{NO}Y_{O_2}/G \tag{3.2c}$$

where, Y_i is the concentration of species 'i' in the exhaust. K_{CO}, $K_{C_3H_6}$ and K_{NO} are adsorption constants modeled using Arrhenius type functions of type,

$$K_i = A_i.exp(-E_i/\overline{R}T) \tag{3.3}$$

where, A_i and E_i are the pre-exponential and activation energies for any of the reactions in Equation 3.2.

The pressure drop across the DOC is modeled using Darcy's equation for friction losses in laminar flows in channels. The final form of the equation for the DOC pressure drop can be written as [6, 7, 51]:

$$\Delta P = \frac{2.\mu.K_f.L.Q}{CFA.a^2.OFA} \tag{3.4}$$

where, μ is the dynamic viscosity of the exhaust gas, K_f is the Fanning friction factor and has a value of 14.23 for square channels, L is the length of the channel, Q is the actual volumetric flow rate, a is the channel width and CFA is the converter frontal area, OFA is the open fraction area. Equation 3.4 represents the major pressure loss in the DOC and does not include the losses due to the inlet channel contraction and

outlet channel expansion as the exhaust flows in and out of the DOC and losses in
the DOC channels before the flow becomes laminar.

3.2   Transient 1-D CPF Filtration/Oxidation Model

This section contains a review of the 1-D CPF model which was available at the
beginning of this research. The reader should use this section along with the thesis
of Triana [7] for a complete mathematical description of the model.

The CPF model is a single channel representation of the entire filter. According
to this view, a single inlet and outlet channel pair are representative of the behavior
of all the channels in the filter. The model solves the flow, filtration, heat transfer,
and regeneration equations along the length of the filter. The axial length of the filter
wall is discretized for computational purposes, and the flow, filtration temperature
and regeneration equations are solved at each node of the discretized filter wall. The
thickness of the filter wall 'w$_s$', is divided into layers called 'slabs' for computational
purposes. A schematic of the co-ordinate system used in the model development is
shown in Figure 3.2. The 'z' coordinate is the distance along the axial length of the
filter, and the 'x' coordinate is the distance through the particulate cake layer and
the filter wall.
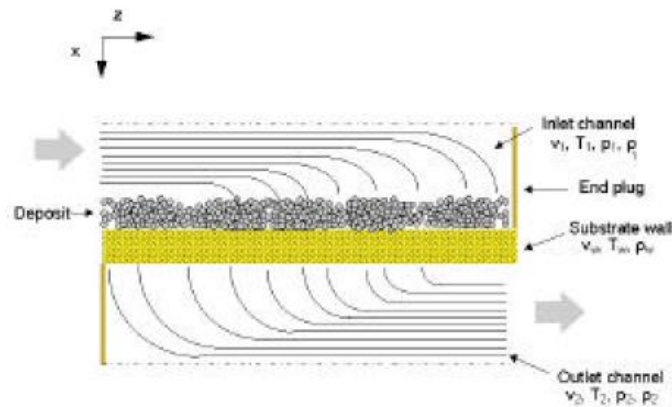
Figure 3.2: Definition of co-ordinates used in the CPF model [41]

3.2.1   Wall Filtration Model

Particulate matter filtration in filters made of extruded ceramics like cordierite can be modeled by the theory of filtration of particles by packed beds [30]. According to this view, the granular micro-structure of the ceramic filter wall can be represented by spherical unit cells, each of which contain a unit collector which filters the particles present in the exhaust gas [31, 41]. In formulating the theory of filtration by packed beds, the presence of particles on the fluid flow is neglected, the individual collectors are closely packed together and the mutual interference effects of neighboring collectors on the flow field are considered [31, 52]. The flow field model is the Kuwabara-Happel flow, which is a solution of creeping flow in a system of spheres based on the unit cell model.

By drawing an imaginary spherical boundary at a certain arbitrary distance around the unit collector, the volume fraction α (solidity fraction), related to clean porosity (ϵ_0) and the unit cell diameter (b) by [31]:

$$\alpha = 1 - \epsilon_0 = \left(\frac{d_{c0}}{b} \right)^3 \tag{3.5}$$

ϵ_0 is the 'clean' filter wall porosity, and d_{c0} is the diameter of the 'clean' spherical unit collector.

The diameter of the clean unit collector, d_{c0}, is related to the filter wall mean pore size, d_{pore}, and filter wall clean porosity, ϵ_0, by [30, 31, 41]:

$$d_{c0} = 1.5 \left(\frac{1 - \epsilon_0}{\epsilon_0} \right) d_{pore} \tag{3.6}$$

d_{pore} is the mean pore size of the filter wall. The relation is obtained by assuming that all the void fraction is distributed over cylindrical pores of diameter d_{pore} and that the external area of the collectors matches the area of the surface of these pores [31, 41].

Small particles at low flow rates are primarily collected by Brownian diffusion [31]. As particle size increases, direct interception and gravitational settling become increasingly important. If particle size and flow rates are further increased, particle collection by inertial impaction eventually dominates for particle sizes larger than $1\mu m$ [31]. In the current model, only diffusional and direct interception collection mechanisms have been considered, given that diesel exhaust particles are generally less than $1\mu m$ in size.

The single collector collection efficiency due to diffusional deposition is defined as the ratio of the rate at which particles diffuse to the sphere surface to that at which particles approach a surface with the cross-sectional area of the sphere [31, 41]. In the Kuwabara-Happel flow field this is given by:

$$\eta_D \approx 3.5 \left(\frac{\epsilon}{K} \right)^{\frac{1}{3}} Pe^{\frac{-2}{3}} \tag{3.7}$$

ϵ is the porosity of the filter wall containing particulate ('loaded' porosity). K is Kuwabara's hydrodynamic factor given by [31, 41]:

$$K = 2 - \epsilon - \frac{9}{5} (1 - \epsilon)^{\frac{1}{3}} - \frac{1}{5} (1 - \epsilon)^2 \tag{3.8}$$

The Peclet number (Pe) is a dimensionless number quantifying the relative magnitudes of convective and diffusive deposition effects as a particle flows around a unit collector. It is given by [31, 41]:

$$Pe = \frac{v_i d_c}{D_p} \tag{3.9}$$

where, d_c is the diameter of the 'loaded' unit collector, v_i is the undisturbed flow velocity approaching the unit collector, which is related to the wall flow velocity, v_w, by:

$$v_i = \frac{v_w}{\epsilon} \tag{3.10}$$

D_p is the particle diffusion coefficient given by [41]:

$$D_p = \frac{k_B T C}{3\pi \mu d_p}$$ (3.11)

where k_B is Boltzmann's constant, T is the absolute temperature of the gas, μ is the dynamic viscosity of the exhaust gas and d_p is the size of the diesel particle. C is the Stokes-Cunningham slip correction factor employed to take into account slip conditions present when gas flows through small passages of low porosity media. Slip flow conditions become important when the mean free path of the gas is equal to or higher than the mean pore diameter of the filter wall. It is related to the local Knudsen number by [41]:

$$C = 1 + Kn \left(1.257 + 0.4 e^{\frac{-1.1}{Kn}} \right)$$ (3.12)

with the Knudsen number (Kn) defined as,

$$Kn = \frac{2\lambda}{d_{pore}}$$ (3.13)

where λ is the mean free path of the gas molecules, and d_{pore} is the mean pore size of the filter wall,

$$\lambda = \frac{\mu}{P} \sqrt{\frac{\pi \overline{R} T}{2 M_{ex}}}$$ (3.14)

In equation 3.14, P is the absolute pressure of the exhaust gas, T is the absolute temperature of the gas, $\overline{R}$ is the universal gas constant and M_{ex} is the molecular weight of the exhaust gas.

The efficiency of particle collection by a unit collector in a packed bed due to interception, taking into account the interference effect due to surrounding collectors,

is given by [31, 41, 52]:

$$\eta_R = 3.5 \left(\frac{\epsilon}{K}\right) \frac{R}{(1 + R^m)} \tag{3.15}$$

where R is the particle interception parameter given by (ratio of diameters) [31, 52],

$$R = \frac{d_p}{d_c} \tag{3.16}$$

and the exponent m is given by [31, 52],

$$m = \frac{3 - 2\epsilon}{3\epsilon} \tag{3.17}$$

Assuming that the diffusional and interception mechanisms are independent of each other, the overall collection efficiency of a single collector can then be given as [31, 41]:

$$\eta_{DR} = \eta_D + \eta_R(1 - \eta_D) = \eta_D + \eta_R - \eta_D\eta_R \tag{3.18}$$

Equations (3.7), (3.15) and (3.18) represent the diffusional, interception and total collection efficiency of a single collector. The total particle collection efficiency of the packed bed/filter wall of thickness Δx is related to the total collection efficiency of a single sphere by [31, 41]:

$$E = 1 - exp\left(\frac{-3\left(1 - \epsilon\right)\eta_{DR}\Delta x}{2\epsilon d_c}\right) \tag{3.19}$$

For numerical purposes, equation 3.19 is not applied to the entire thickness of the filter wall at once. Rather, the thickness of the filter wall is divided into a number of layers called 'slabs' of thickness Δx, and the total filtration efficiency is related to the filtration efficiencies of the 'slabs', as shown in Figure 3.3.

The exhaust gas is filtered by the wall, according to the local filtration efficiency, given by equation (3.19) and which causes the local filter wall properties to change. It
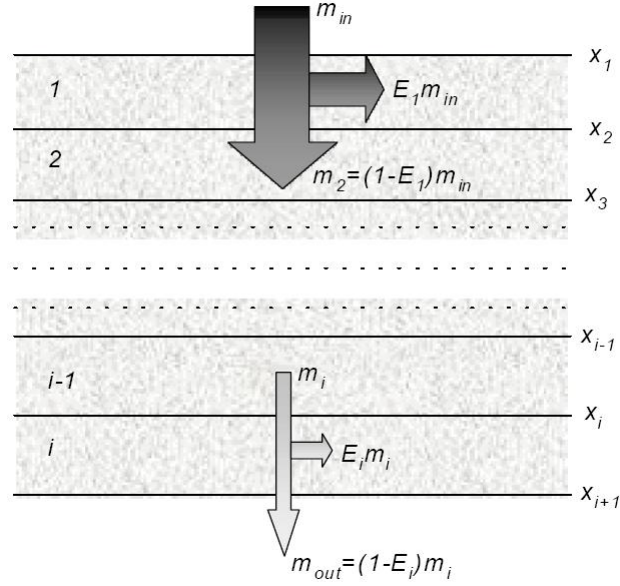
Figure 3.3: Division of the filter wall into 'slabs' [41]

is assumed that the mass of the particles collected by the filter wall forms a uniform layer around the unit collector causing it to grow in size, but keeping its spherical shape intact. This is done by defining a 'density' of particulate in the wall, ρ_{pw} [41]. The total diameter of the particulate loaded spherical unit collector can be easily derived by considering the increase in volume of a unit collector by mass m$_t$ packed uniformly around it with density ρ_{pw} [41]:

$$d_c = \left[\left(\frac{d_{c0}}{2} \right)^3 + \frac{3}{4\pi} \cdot \frac{m_t}{\rho_{pw}} \right]^{\frac{1}{3}} \tag{3.20}$$

where, d_c is the diameter of the 'loaded' unit collector at time t, m_t is the mass around the unit collector at time t and ρ_{pw} is the packing density of particulate in the filter wall. Thus it can be seen that ρ_{pw} is not a real particulate packing density, but rather a means by which particulate filtered by the collector is uniformly distributed around the collector, in order to keep its spherical shape intact for theoretical purposes. This is an important observation which will later be used during the development of the wall oxidation model. It is easy to show using Equations (3.5) and (3.20) that the

'loaded' porosity of the filter wall, ϵ, changes according to the equation:

$$\epsilon = 1 - \left(\frac{d_c}{d_{c0}} \right) \cdot (1 - \epsilon_0) \tag{3.21}$$

With the 'loaded' unit collector' diameter and 'loaded' porosity known from equations 3.20 and 3.21 respectively, the loaded mean pore size of the wall can be computed by rearranging the terms present in equation 3.5, to obtain:

$$d_{pore} = \frac{2}{3} \left(\frac{\epsilon}{1 - \epsilon} \right) d_c \tag{3.22}$$

If k_0 is the permeability of the clean filter wall, then the permeability of the 'loaded' filter wall, k_t, is given by [31, 41]:

$$\frac{k_t}{k_0} = \left(\frac{d_{c,t}}{d_{c0}} \right)^2 \cdot \left(\frac{K(\epsilon_t)}{K(\epsilon_0)} \right) \cdot \left(\frac{1 - \epsilon_0}{1 - \epsilon_t} \right) \tag{3.23}$$

K is the Kuwabara hydrodynamic factor defined in equation 3.8. The term $\frac{K(\epsilon_t)}{K(\epsilon_0)}$ controls the rapidly decreasing permeability of the filter wall during the depth filtration phase due to a decrease in porosity of the filter wall.

During the depth filtration phase, most of the particles are collected inside the filter wall. Eventually, most of the particles are collected by the particulate cake layer. On the filter wall, the particulate is not dispersed as it is inside the wall and forms a cake like structure. A partition coefficient $\phi(0 \leq \phi \leq 1)$ has been defined to determine the fraction of total upstream filter particles entering the filter wall. It is thus used as a filtration parameter for the particulate cake layer itself. The definition can be expressed mathematically as:

$$\phi_t = \frac{d_{c,t} - d_{c0}}{\psi.b^2 - d_{c0}^2} \tag{3.24}$$

where, $\psi(0 < \psi < 1)$ is a dimensionless 'percolation' factor which determines how close the diameter of a loaded collector can approach that of a unit cell before filtration is completely by the particulate cake layer. The percolation factor is used as a control variable to determine the amount of loading (time length of depth-filtration phase) inside the filter wall. A deficiency of this model is that the partition coefficient, which is based on filter wall parameters, is used as a filtration parameter for the particulate cake layer even when the particulate cake layer itself becomes a filter for the particles.

3.2.2 Particulate Cake Layer Loading Model

A large fraction of the diesel particles entering the filter is deposited on the filter wall [34, 41]. Some of the remaining particles are deposited inside the wall while the rest leave the filter. Under steady state inlet conditions, the particulate deposited on the wall are assumed to increase the width of the particulate cake layer with the packing density (cake bed porosity) and permeability of the particulate cake layer remaining constant. A brief overview of this particulate cake layer loading model is given in this section. For a detailed discussion on the relevant calculations involved, see reference [7].

The packing density, ρ_p, and porosity (ϵ_p) of the particulate cake layer depend on the mechanics of particulate growth on the wall. These mechanisms can be random diffusive motions which lead to open and porous cake structures, or convective effects which would form more compact beds. These effects can be characterized by a dimensionless Peclet number for the particulate cake layer [53]:

$$Pe = \frac{v_w d_{prim}}{D_p} \tag{3.25}$$

Here d_{prim} is the primary particle diameter and lies between 25nm-40nm [53]. D_p is

the aggregate particle diameter based diffusion coefficient, defined as [53]:

$$D_p = \frac{k_B T C}{3\pi \mu d_{aggr}}$$ (3.26)

d_{aggr} is the aggregate particle diameter with a representative value of 100 nm (0.1 μ m) [53, 54]. Since mean pore sizes of the particulate cake layer are much smaller than those for the ceramic wall, slip flow effects are much stronger, and are taken into account by the Stokes-Cunningham factor C, which is defined using an aggregate size based Knudsen number [53, 55].

$$Kn = \frac{2\lambda}{d_{aggr}}$$ (3.27)

Using this approach, Konstandopoulos et.al. [53] found that a good approximation to experimentally determined values of particulate cake layer porosities (or packing densities) and permeabilities could be obtained. This is important because the pressure drop across the particulate cake layer can be described sufficiently with the knowledge of packing density (to determine cake thickness) and permeability. Values of particulate cake layer packing densities and permeabilities determined from this theory have been used with some success by [9, 34] for O_2 based catalytic oxidation rates for exhaust temperatures up to 450°C. The effect of higher oxidation rates with NO_2 and O_2 on these correlations is unclear. Indeed, it may be that particulate cake layer properties, especially the permeability, change considerably with oxidation, and values determined from this simple Peclet number based model may be very different from the true values, as found by Triana [7]. Some researchers have suggested that while both packing densities and permeabilities can change with oxidation, their product remains fairly constant [7, 55].

The thickness of the particulate cake layer changes due to particle deposition and oxidation. Some studies have tried to include a migration effect, according to which,

drag forces due to flow in the inlet channel cause the particulate deposited in the front of the channel to be transported toward the end of the channel [56]. This effect, though present, should be negligible, and might be of significance at very high flow rates or under active regeneration conditions. Presently, it is assumed that particle deposition and oxidation adequately describe the evolution of particulate cake layer thickness with time.

3.2.3 Mass, Momentum and Energy Balance

A brief overview of the mass, momentum and energy equations of the exhaust gas in the filter channels is given in this section. The interested reader should refer to references [7, 48, 57] for detailed derivations and explanations.

The mass balance equation in the inlet and outlet channels can be described by [48]:

$$\frac{\partial(\rho_1 v_1)}{\partial z} = -\frac{4}{D}\rho_w v_w \tag{3.28a}$$

$$\frac{\partial(\rho_2 v_2)}{\partial z} = \frac{4}{D}\rho_w v_w \tag{3.28b}$$

D is the width of the channel, v is the velocity of the exhaust gas, ρ is the density of the exhaust gas with subscripts 1, 2 and w referring to the inlet channel, outlet channel and the filter wall respectively. Note that the left hand side (L.H.S) of the continuity equation is not equal to zero due to flow of exhaust gas through the porous walls.

The momentum equation of the gas in the inlet and outlet channels can be described by [48]:

$$\frac{\partial p_1}{\partial z} + \frac{\partial(\rho_1 v_1^2)}{\partial z} = \frac{-\mu v_1}{D^2} \tag{3.29a}$$

$$\frac{\partial p_2}{\partial z} + \frac{\partial(\rho_2 v_2^2)}{\partial z} = \frac{-\mu v_2}{D^2} \tag{3.29b}$$

p is the pressure and μ is the dynamic viscosity of the exhaust gas with subscripts 1,

2 and w referring to the inlet channel, outlet channel and the filter wall respectively. The term on the right hand side (R.H.S) represents the viscous drag loss along the length of the channel since the gas velocity at the wall in that direction is equal to zero. A numerical solution to these equations are used to determine the friction losses in the inlet and outlet channels.

An energy balance of the exhaust gas in the inlet and outlet channels results in [48]:

$$C_{p,g}\rho_1 v_1 \frac{\partial T_1}{\partial z} = \frac{4}{D}h_1\left(T_w - T_1\right) \tag{3.30}$$

$$C_{p,g}\rho_2 v_2 \frac{\partial T_2}{\partial z} = \frac{4}{D}\left(T_w - T_2\right)\left[h_2 + C_{p,g}\rho_2 v_w\right] \tag{3.31}$$

$C_{p,g}$ is the specific heat and T is the absolute temperature of the exhaust gas with subscripts 1, 2 and w referring to the inlet channel, outlet channel and the filter wall respectively. The equations are obtained by an energy balance of the channel gas with convection from/to the wall (energy transfer coefficient h_i) and the enthalpy loss/gain by way of flow through the particulate cake layer and wall. Equations (3.30) and (3.31) are somewhat different from those originally proposed by Bisset [48]. Bisset assumed that the temperature of the gas entering and leaving the wall is equal to the wall temperature. This caused the local convective energy gain/loss of the walls from the inlet channel to exactly balance the loss/gain to the outlet channel. Our view is that the temperature of inlet channel gas entering the wall should be at the temperature of the inlet channel gas, T_1. The exhaust gas can be assumed to reach thermal equilibrium with the wall as it passes through the wall, given the high thermal Peclet numbers. It thus leaves the wall and enters the outlet channel at the wall temperature, T_w as Bisset and Shadman [57] reported that typical length scales over which the gas temperature adjusts to differences with the wall temperature is several times smaller than typical particulate cake layer thicknesses. In most cases, the impact should be minimal due to the presence of the term v_w, which in most cases

has a maximum of about 0.05 m/sec.

3.2.4   Kinetics of Particulate Oxidation

The MTU 1-D CPF oxidation model is based on the 2-layer theory of Konstandopoulos et.al. [32], which is based on the framework of Bisset [48]. The 2-layer model can describe the regeneration of particulate matter by thermal oxidation and by a catalyst present in the washcoat of the filter wall. Konstandopoulos et.al. [41], and later Triana [7] extended this framework to particulate oxidation by NO_2 as in the case of the CRT® [41].

The catalyst effect can be expected to be confined to about (10μm-30μm) of the particulate layer deposited on the walls of the filter[9, 32, 33, 34] and is assumed to be the thickness of layer I. Thus the particulate in layer I, which is closest to the catalyst coating on the filter wall can be oxidized by both thermal and catalytic means. Particulate deposited over this layer, forms layer II, and can be thought of as being 'out of range' for catalytic oxidation. A schematic of the division of the particulate cake layer into layer I and layer II is shown in Figure 3.4. Particulate present in both layers I and II can be oxidized by NO_2 as the NO_2 in the exhaust gas passes through both of the layers.
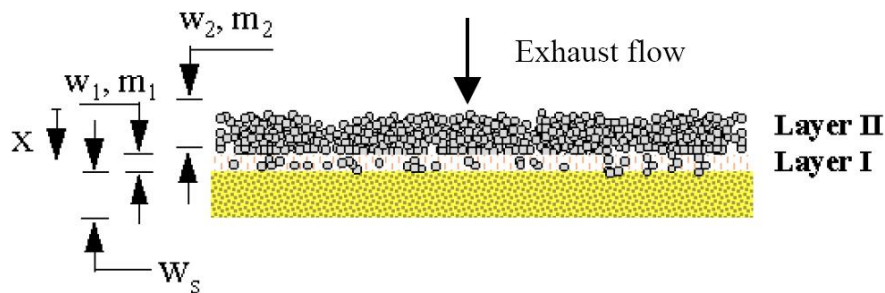
Figure 3.4: Division of the particulate cake layer into layer I and layer II [41]

The oxygen mass fraction, Y_w, entering layer II (if layer I reaches its maximum), or layer I when it is forming, is balanced by convective transport through the layer

and reaction kinetics in the layer. Assuming that the oxygen-particulate reaction is first-order heterogeneous oxidation of the particulate, and that diffusion of the oxidant species is negligible compared to convection, the following oxygen balance equation results for layer II [32, 48]:

$$\frac{\partial}{\partial x}(\rho_w v_w Y_w) = -S_p \rho_w Y_w k_{th}(T_w)(1 - \frac{f_{co}}{2}) \tag{3.32}$$

f_{CO} is the CO selectivity for the particulate oxidation by thermal means (section 2.2). k_{th} is a rate constant for thermal oxidation defined later in equation 3.37a. S_p is the specific area of the particulate related to the surface area and particulate cake layer packing density (ρ_p) of diesel particulate by:

$$S_p = A_p . \rho_p \tag{3.33}$$

The surface area of diesel particulate, A_p, is around 100 m^2/g [17, 27, 32, 33].

Some researchers have used models where the concentration of gaseous species (especially the oxidant species) decreases along the inlet channel due to diffusion [56] into the particulate cake layer. The transport of gaseous species in the exhaust gas along the length of the channel is expected to be dominated by convective effects and not diffusion [48]. Hence, there should be minimal species concentration gradient along the length of the inlet channel. In our view, such mathematical treatment is unnecessary, adds further complexity to the model, and serves no readily apparent purpose.

Assuming that the gas density and wall flow velocity remain constant as it flows through the particulate cake layer (a good assumption), and integrating equation 3.32 across layer II, gives the following depletion rate for O$_2$ across layer II [32, 48].

$$R_{O_2,2} = \rho_w v_w Y_w . \left(1 - exp\left(\frac{-S_p k_{th}(1 - \frac{f_{co}}{2})w_2}{v_w}\right)\right) \tag{3.34}$$

where, w_2 is the thickness of layer II. The O_2 mass fraction exiting layer II and entering layer I, $Y_{w,1}$, can be obtained from equations 3.32 and 3.34.

$$Y_{w,1} = Y_w \cdot exp\left(\frac{-S_p k_{th}(1 - \frac{f_{co}}{2})w_2}{v_w}\right) \qquad (3.35)$$

The O_2 concentration entering layer I is assumed to follow two reaction paths: a catalytic path (β) and a thermal path (1-β). Accordingly, the O_2 balance equation for layer I can be written as [32]:

$$\frac{\partial}{\partial x}(\rho_w v_w Y_{w,1}) = -S_p \rho_w Y_{w,1}\left(k_{th}(T_w)\left(1 - \frac{f_{co}}{2}\right)(1 - \beta) + k_{cat}(T_w)\left(1 - \frac{f_{co'}}{2}\right)\beta\right)$$
$$(3.36)$$

where $f_{CO'}$ is the CO selectivity for the particulate oxidation by catalytic means (section 2.2.2). The terms k_{th} and k_{cat} refer to the rate constants for particulate oxidation by thermal and catalytic oxidation respectively. They are assumed to be modified Arrhenius-type functions of the form [32, 33, 48]:

$$k_{th}(T_w) = A_{th}T_w exp\left(-E_{th}/(\overline{R}T_w)\right) \qquad (3.37a)$$

$$k_{cat}(T_w) = A_{cat}T_w exp\left(-E_{cat}/(\overline{R}T_w)\right) \qquad (3.37b)$$

A_{th} and A_{cat} are pre-exponential factors for the oxidation of particulate by thermal and catalytic means respectively. They are determined by fitting the model results to the experimental data. Note that k_{th} and k_{cat} both depend on the wall temperature, T_w, as it is assumed that the wall and the particulate are at the same temperature.

Integrating equation 3.36 in a fashion similar to 3.32 gives the total depletion rate of O_2 in layer I ($R_{O_2,total,1}$). This O_2 depletion equations in layer I are somewhat

different than the ones used by references [9, 34].

$$R_{O_2,total,1} = \rho_w v_w Y_{w,1} \cdot \left(1 - exp\left(\frac{-S_p k^* w_1}{v_w}\right)\right) \tag{3.38a}$$

$$k^* = k_{th}(T_w)\left(1 - \frac{f_{co}}{2}\right)(1 - \beta) + k_{cat}(T_w)\left(1 - \frac{f_{co'}}{2}\right)\beta \tag{3.38b}$$

where, w_1 is the thickness of layer I. The contributions of thermal ($R_{O_2,th,1}$) and catalytic ($R_{O_2,cat,1}$) oxidation paths are given by [32, 33]:

$$R_{O_2,th,1} = R_{O_2,total,1} \cdot \left(\frac{k_{th}(T_w)\left(1 - \frac{f_{co}}{2}\right)(1 - \beta)}{k^*}\right) \tag{3.39a}$$

$$R_{O_2,cat,1} = R_{O_2,total,1} \cdot \left(\frac{k_{cat}(T_w)\left(1 - \frac{f_{co'}}{2}\right)\beta}{k^*}\right) \tag{3.39b}$$

Assuming that oxidation takes place so that the particulate cake packing density, ρ_p, and the particulate specific area, S_p, remain constant, the evolution of particulate cake layer thickness with time can be described by the following equations [32, 33, 48].

$$\frac{\partial}{\partial t}(\rho_p w_2) = -\frac{M_c}{M_{ox}}\left(\frac{R_{O_2,2}}{1 - f_{co}/2}\right) \tag{3.40a}$$

$$\frac{\partial}{\partial t}(\rho_p w_1) = -\frac{M_c}{M_{ox}}\left(\frac{R_{O_2,th,1}}{1 - f_{co}/2} + \frac{R_{O_2,cat,1}}{1 - f_{co'}/2}\right) \tag{3.40b}$$

This assumption is not believed to be valid strictly, but is used nevertheless for two reasons: one, lack of detailed data on the nature of change in particulate properties with different rates of oxidation; and secondly, for computational simplicity. Palotas et.al. reported that increasing oxidation rates changes the particulate properties, such as increased ordering of the carbon structure, and this changes rate of oxidation in turn [58]. Du et.al. found that thermal oxidation depends strongly on the carbon structure of the deposit, while for the catalytic reaction, the catalytic contact and loading matters most [35, 37].

Konstandopoulos et.al. [41] extended the regeneration framework of references [32, 48] to the oxidation of particulate by NO_2 entering the particulate filter. Other researchers have also studied NO_2-assisted particulate oxidation with similar computational models [24, 25, 26]. More recently, Triana [7] developed and used a similar model to study NO_2-assisted regeneration, across a wide range of engine loads and speeds, in a CRT® system. Triana [7] found that regeneration behavior across a wide range of temperatures and flow rates can be satisfactorily described by a single set of kinetic parameters: an activation energy of 1.218E+08, pre-exponential factor 100, and a temperature order of 1.0. References [7, 41] have detailed mathematics on the development and integration of this framework into the 2-layer oxidation model. A review of the NO_2 assisted particulate cake layer oxidation developed by Triana [7] for a CRT®, was modified to work with a 2-layer model and is presented here. The model will be improved in section 3.5 to take into account the NO_2 produced by the catalyst present in the CPF.

The NO_2 mass fraction, Y_{NO2}, entering layer II is balanced by convective transport and reaction kinetics. Assuming that the NO_2 assisted oxidation is first-order heterogeneous, the following NO_2 balance equation results for layer II [7, 41]:

$$\frac{\partial}{\partial x}(\rho_w v_w Y_{NO2}) = -S_p \rho_w Y_{NO2} k_{NO2}(T_w)(2 - g_{CO}) \tag{3.41}$$

Here, g_{CO} is the CO selectivity for the particulate oxidation by NO_2 (section 2.2.4). The reaction rate for the NO_2 assisted oxidation is assumed to be a modified Arrhenius-type function:

$$k_{NO2}(T_w) = A_{NO_2}.T_w.exp\left(-E_{NO_2}/(RT_w)\right) \tag{3.42}$$

where A_{NO_2} and E_{NO_2} are the pre-exponential factor and activation energy for the NO_2 assisted oxidation of particulate respectively.

Assuming that the exhaust gas density and wall flow velocity remain constant as

it flows through the particulate cake layer and integrating equation 3.41 across the thickness of layer II gives the following NO_2 depletion rate in layer II [7, 41].

$$R_{NO_2,2} = \rho_w v_w Y_{NO2}. \left(1 - exp\left(\frac{-S_p k_{NO2}(2 - g_{CO})w_2}{v_w}\right)\right) \tag{3.43}$$

The NO_2 mass fraction exiting layer II and entering layer I, $Y_{NO2,1}$, can be obtained from Equations 3.32 and 3.34.

$$Y_{NO2,1} = Y_{NO2}.exp\left(\frac{-S_p k_{NO2}(2 - g_{CO})w_2}{v_w}\right) \tag{3.44}$$

The NO_2 conservation equation in layer I is:

$$\frac{\partial}{\partial x}(\rho_w v_w Y_{NO2,1}) = -S_p \rho_w Y_{NO2,1} k_{NO2}(T_w)(2 - g_{CO}) \tag{3.45}$$

Integrating equation 3.45 across the thickness of layer I yields the NO_2 depletion rate in layer I.

$$R_{NO_2,1} = \rho_w v_w Y_{NO2,1}. \left(1 - exp\left(\frac{-S_p k_{NO2}(2 - g_{CO})w_1}{v_w}\right)\right) \tag{3.46}$$

From equations 3.45 and 3.46, the NO_2 mass fraction exiting layer I, and entering the filter wall can be determined to be:

$$Y_{NO2,wall} = Y_{NO2,1}.exp\left(\frac{-S_p k_{NO2}(2 - g_{CO})w_1}{v_w}\right) \tag{3.47}$$

The evolution of the thicknesses of layer II (w_2) and layer I (w_1), due to oxidation by NO_2 and O_2 can be described by the following equations [7, 41].

$$\frac{\partial}{\delta t}(\rho_p w_2) = -\left(\frac{M_c}{M_{ox}}\left(\frac{R_{O_2,2}}{1 - f_{co}/2}\right) + \frac{M_c}{M_{NO2}}\left(\frac{R_{NO_2,2}}{(2 - g_{CO})}\right)\right) \tag{3.48a}$$

$$\frac{\partial}{\partial t}(\rho_p w_1) = -\frac{M_c}{M_{ox}}\left(\frac{R_{O_2,th,1}}{1 - f_{co}/2} + \frac{R_{O_2,cat,1}}{1 - f_{co'}/2}\right) - \frac{M_c}{M_{NO2}}\left(\frac{R_{NO_2,1}}{(2 - g_{CO})}\right) \qquad (3.48b)$$

Equations 3.48a and 3.48b describe the evolution of particulate cake layer, with oxidation by thermal, catalytic and NO_2 assisted means. Both equations are solved in the model by a Runge-Kutta numerical scheme of 4th order.

3.2.5 Energy Equation for the Wall

The rate of energy accumulation in the wall is equal to the rate at which energy is transported from the inlet channel, minus the rate of energy loss to the outlet channel, plus the rate of energy production due to particulate oxidation, minus the rate of energy conduction in the axial direction [48]. Even though energy due to the reaction is produced in the particulate cake layer, conduction in the ceramic wall is so large that wall temperature can be taken to be the same was the particulate temperature [48, 57]. A careful consideration of these contributions leads to the following equation for the energy balance in the wall which is solved for the temperature in the wall.

$$(\rho_p C_{pp} w + \rho_s C_{ps} w_s)\frac{\partial T_w}{\partial t} = -h_1(T_1 - T_w) - h_2(T_2 - T_w) + H_{react} + H_{cond} + C_{pg}\rho_w v_w(T_1 - T_w)$$

$$(3.49)$$

C_{pp}, C_{ps} and C_{pg} are the specific heats of the particulate, filter wall substrate and the exhaust gas respectively, w and w_s are the thickness of the particulate and filter wall substrate, ρ_s is the density of the filter wall substrate and H_{react} and H_{cond} refer to the heat of combustion of particulate oxidation and axial conduction in the wall respectively. The contribution due to conduction in the axial direction is given by [48]:

$$H_{cond} = -\lambda_p\frac{\partial}{\partial z}\left(w\frac{\delta T_w}{\delta z}\right) - \lambda_s w_s\frac{\partial^2 T_w}{\partial z^2} \qquad (3.50)$$

λ_p and λ_s are the thermal conductivities of the particulate and filter wall substrate respectively.

The heat of combustion of particulate oxidation is dependent on the oxygen depletion in layers I and II due to particulate oxidation [32, 48]:

$$H_{react} = \frac{\Delta H^{th}}{M_c}\left(\frac{M_c}{M_{ox}}\frac{1}{1-f_{co}/2}R_{O_2}^{th}\right) + \frac{\Delta H^{cat}}{M_c}\left(\frac{M_c}{M_{ox}}\frac{1}{1-f_{co'}/2}R_{O_2,cat,1}\right) \quad (3.51)$$

$R_{O_2}^{th}$ is the total oxygen depletion due to thermal oxidation given by the sums of equations 3.34 and 3.39a. That is,

$$R_{O_2}^{th} = R_{O_2,2} + R_{O_2,th,1} \quad (3.52)$$

The thermal and catalytic heats of reaction depend on their respective CO selectivities, f_{CO} and $f_{CO'}$ [32]:

$$\Delta H^{th} = f_{CO}\Delta H_{CO} + (1-f_{CO})\Delta H_{CO_2} \quad (3.53a)$$

$$\Delta H^{cat} = f_{CO'}\Delta H_{CO} + (1-f_{CO'})\Delta H_{CO_2} \quad (3.53b)$$

The term $C_{pg}\rho_w v_w(T_1 - T_w)$ present in equation 3.49 was absent in Bisset's original formulation of the equation. It appears because convective energy loss/gain of the walls from the inlet and outlet channels do not exactly cancel each other out as discussed in Section 3.2.3.

3.2.6   Pressure Drop Model

The presence of the inlet and outlet channels, particulate cake layer and the filter wall act as a restriction in the path of the exhaust gas flow. The restriction of the exhaust gas manifests itself as a drop in pressure across the filter. It is an important parameter because the total pressure drop across the filter can be expressed in terms of variables of interest such as the filter wall permeability, particulate cake layer

thickness (mass) and permeability.

The total pressure drop across the filter is a sum of many contributions: inlet channel contraction losses, inlet and outlet channel frictional losses, pressure drop due to presence of the particulate cake and wall and outlet channel expansion losses.

Inlet channel contraction and outlet channel expansion losses are inertial losses which scale with the square of the inlet gas velocity. The total pressure drop due to contraction and expansion according to the following equation [41, 59, 60].

$$\Delta P_{contr+exp} = \frac{2\zeta Q^2 \rho (a + w_s)^4}{V_{trap}^2 a^2} \left(\frac{L}{a}\right)^2 \tag{3.54}$$

Konstandopoulos et. al. [41, 59] reported that the expansion losses are approximately two times those of the contraction losses (ratio). ζ is the contraction/expansion inertial loss coefficient and can have values ranging from 0.2 to 0.8 depending on the open fraction area of the trap and the Reynolds number. They are however known to be significant only at very high exhaust flow rates, with relative contributions of order 10^{-2} and thus can be neglected [41, 59].

Friction losses take place in the filter as the gas flows along the inlet and outlet channels. The small width of the inlet and outlet channels means that typical Reynolds numbers are less than 1000 which means viscous effects will dominate the flow and that the flow will be laminar. The total frictional losses can be calculated by the following equation [41, 60]:

$$\Delta P_{friction} = \frac{4}{3} \frac{\mu Q (a + w_s)^2 F L^2}{V_{trap}^2 a^4} \tag{3.55}$$

In this equation, $F = 2c_f Re$, and $c_f Re$ has a value of 14.227. The friction losses can be obtained from the above equation, or can be determined from a solution of the momentum equations (Equations 3.29 a and b) as in the MTU 1-D 2-layer model.

The pressure drop across the porous ceramic wall is approximated as fluid flow

through a porous medium and can be described by Darcy's law and a Forchheimer term [30, 41, 60, 61]:

$$\Delta P_{wall} = \frac{\mu}{k_t} v_w w_s + \beta \rho v_w^2 w_s \qquad (3.56)$$

where, μ is the dynamic viscosity of the gas, v_w is the local wall flow velocity, k_t is the permeability of the filter wall (equation 3.23) and w_s is the thickness of the filter wall. Thus the pressure drop across the wall depends on the thickness of the wall and its permeability, and viscosity and velocity of the exhaust gas. The wall permeability, k_t, is an intensive property of the substrate and is independent of the fluid passing through the material. It depends on properties of the material such as porosity and pore size distribution. The first term in Equation 3.56 is a viscous term and pressure losses due to viscous forces exerted on the fluid. The Forscheimer coefficient is called the inertia term, and is only significant for high porosity filters like foam filters operated at high flow rates. For relatively low porosity (50%) cordierite particulate filters at normal operating flow rates, it has been shown that the inertial(Forscheimer) term is very small and can be neglected [59, 60].

The pressure drop across the particulate layer is also assumed to be given by a Darcy-like formulation [32, 48, 60]:

$$\Delta P_{cake} = \frac{\mu}{k_p} v_w w = \frac{\mu}{k_p} v_w (w_1 + w_2) \qquad (3.57)$$

where, k_p is the permeability of the particulate cake. The filter wall and the particulate cake can be viewed as two resistances in series, and the total pressure drop, ΔP_{total}, across both of them is given by the sum of equations 3.56 and 3.57. More complex treatments are available which take into account the decreasing width of the inlet channel due to the loaded particulate cake. However, for most cases, the

following equation should suffice:

$$\Delta P_{total} = \Delta P_{cake} + \Delta P_{wall} = \frac{\mu}{k_p} v_w w + \frac{\mu}{k_t} v_w w_s \qquad (3.58)$$

3.3 Oxidation in the Wall Model

The filtration-oxidation model developed by Bisset [48] and Konstandopoulos et.al. [32, 41] does not oxidize particulate present inside the filter wall. Some of the pressure drop data obtained during the experimental phase of this research (chapter 5 and reference [46]), especially in CCRT® configuration, suggested that oxidation in the wall was causing the rapid decrease in pressure drop across the CPF. Thus for modeling purposes, it was necessary to develop a CPF sub-model that oxidizes particulate inside the filter wall. The approach to particulate oxidation inside the filter wall should not only incorporate the oxidation process as it actually occurs, it must also be consistent with the filtration model. Early in the development process, it was also found to be necessary to add and couple a particulate cake filtration model as describe in Section 3.4.

Figure 3.5 is a schematic of the discretization of the filter wall in the computational domain (adapted from [7]) (also see Figure 3.3). The length of the wall (L) is
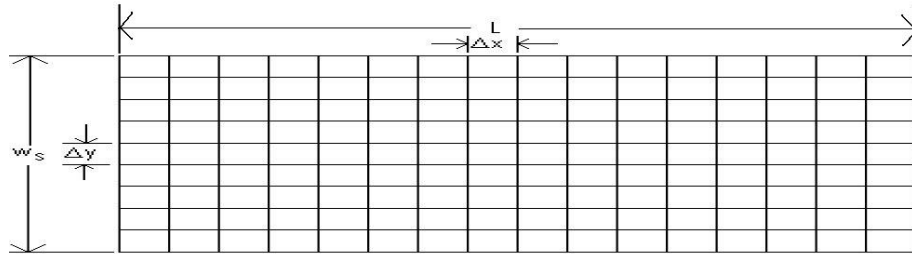
Figure 3.5: Schematic of the discretization of the filter wall [7]

discretized by dividing it into a number of elements of length Δx. The thickness of the wall, w_s, is divided into a number of 'layers' called 'slabs' in the filtration sub-

model. Thus the discretization in the axial direction and division into 'slabs' in the transverse direction results in a computational domain of 'cells' as shown in Figure 3.5. Each of the resulting cells contain a number of unit collectors (for details cf. [7]). The mass collected by the collectors in each slab is related to the mass exiting the previous slab and the filtration efficiency given by equation 3.19. Each of the cells has a different amount of particulate collected, resulting in different local porosities and permeabilities. Further, the physical structure of particulate deposits in the filter wall are not well-defined. However, it is known that the deposits are small [9, 34], and scattered with 'percolation' properties [41], so that small amounts of particulate rapidly decrease the porosity (and permeability) of the wall which initially is about 52% porous. Model simulations show that during typical operating conditions in the Peclet number range of 0.6 to 1.5, there is less than 3 grams of particulate deposited inside the filter wall [7, 9, 34]. Because the entire filter wall is divided into 'slabs' and 'cells', the particulate mass present in each 'slab' will be lesser, and particulate mass present in each cell will be even less. This means that any oxidation technique which oxidizes the particulate cell by cell, inside the filter wall, might not be stable due to the possible generation and propagation of numerical errors. Such a technique is also thought to be unfeasible because oxidation of particulate cell by cell would be computationally intensive.

The O_2 and NO_2 depletion equations apply to particulate in the form of a cake (equations 3.32 and 3.41). However, inside the filter wall, the particulate is dispersed and it is assumed that the mass of the collected particles form a uniform layer around the unit collector causing it to grow in size, but keeping its spherical shape intact [41]. One of the objectives during the development of the wall oxidation model was to be able to use a framework compatible with that of Bisset and Konstandopoulos [32, 41, 48] (Equations 3.32 and 3.41). This brings up the question of the value of the specific area of the particulate, S_p (Equation 3.33), inside the filter wall . This is an open

question because there are no data in the open literature, to the authors knowledge, detailing the physical structure or morphology of the particulate inside the filter wall.

Given the complexities of the stated problem, it is clear that simplifying assumptions have to be made. It is reasonable to assume that even though there are different amounts of particulate in each computational cell of the wall, they have the same oxidation rates. However, the total mass oxidized will be related to the initial amount of particulate mass present. The approach adopted is *to determine reaction rates in the wall such that if a similar amount of particulate were present on the wall under the same conditions, they would both deplete by the same amounts.* To ensure integration with the regeneration framework of Layer I and II, the following solution was formulated: For each axial discretization, collect all the particulate present in each of the 'slabs' in the filter wall (Figure 3.5) and form a *virtual* wall layer. This ensures that rate depletion of the forms in equations 3.32 and 3.41 can be applied. Such an approach ensures short computational time and is less likely to propagate numerical errors due to 'bulk' oxidation of all particulate present in the wall.

The mass of the *virtual* wall layer, present at every discretized location in the axial direction can be computed by,

$$M_{wall} = \sum_{i=1}^{nlayer} m_i \tag{3.59}$$

where, m_i is the particulate mass present in the ith 'slab' (Figures 3.3 and 3.5).

To determine the thickness of the virtual wall layer, a particulate density is needed. Here it should be realized that the particulate density inside the wall used in the filtration model, ρ_{pw} is not a true density, but rather a tool by which all the particulate collected by the unit collector is made to uniformly distribute around the unit collector keeping its spherical shape intact for theoretical purposes. This is the reason for the considerable difference in relative magnitudes of particulate cake density (ρ_p) and

particulate 'density' in the wall (ρ_{pw}) [7, 9, 34, 41]. Keeping this in mind, and also the aim of keeping oxidation rates in the wall of the same magnitude as on the wall, under the same conditions, the particulate cake packing density, ρ_p, was used to calculate the thickness of the virtual wall layer.

$$w_{wall} = \frac{M_{wall}}{\rho_p dh \Delta x} \tag{3.60}$$

dh is the CPF channel width, and Δx is the discretization length in the axial direction. The physical meanings of both 'densities', ρ_p and ρ_{pw}, should be clearly understood to appreciate the seemingly odd selection of ρ_p to calculate the *virtual* cake thickness.

Selection of ρ_p for the density for the *virtual* cake thickness means that one can use ρ_{cake} in the calculation of S_p. S_p, inside the filter wall, is defined as (same as equation 3.33):

$$S_p = A_p.\rho_p \tag{3.61}$$

The O$_2$ conservation equation for oxidation in the wall can now be written as,

$$\frac{\partial}{\partial x}(\rho_w v_w Y_{w,wall}) = -S_p \rho_w Y_{w,wall} k_{th}(T_w)(1 - \frac{f_{co}}{2}) \tag{3.62}$$

where Y$_{w,wall}$ is the mass fraction of oxygen entering the wall. It is computed by considering the filter inlet O$_2$ mass fraction, Y$_w$, and the depletion in layers I and II (Equations 3.34 and 3.38):

$$Y_{w,wall} = Y_w * exp\left(\frac{-S_p k_{th}(1 - \frac{f_{co}}{2})w_2}{v_w}\right) * exp\left(\frac{-S_p k^* w_1}{v_w}\right) \tag{3.63a}$$

$$k^* = k_{th}(T_w)\left(1 - \frac{f_{co}}{2}\right)(1 - \beta) + k_{cat}(T_w)\left(1 - \frac{f_{co'}}{2}\right)\beta \tag{3.63b}$$

The O$_2$ depletion equations inside the wall can be obtained from an integration of

equation 3.62 across the virtual wall layer thickness,

$$R_{O2,wall} = \rho_w v_w Y_{w,wall} \left(1 - exp\left(\frac{-S_p k_{th}\left(1 - \frac{f_{co}}{2}\right)w_{wall}}{v_w}\right)\right) \tag{3.64}$$

In a similar fashion, the NO$_2$ conservation equation inside the wall can now be written as,

$$\frac{\partial}{\partial x}(\rho_w v_w Y_{NO2,wall}) = -S_p \rho_w Y_{NO2,wall} k_{NO2}(T_w)(2 - g_{CO})) \tag{3.65}$$

where $Y_{NO2,wall}$ is the mass fraction of NO$_2$ entering the filter. It is related to the NO$_2$ mass fraction entering the filter, Y_{NO2}, and the NO$_2$ depletion in layers I and II and is defined by equation 3.47. It is reproduced below for convenience.

$$Y_{NO2,wall} = Y_{NO2,1} exp\left(\frac{-S_p k_{NO2}(2 - g_{CO})w_1}{v_w}\right) \tag{3.66}$$

The NO$_2$ depletion equations inside the wall can be obtained from an integration of Equation 3.65 across the virtual wall layer thickness,

$$R_{NO2,wall} = \rho_w v_w Y_{NO2,wall} \left(1 - exp\left(\frac{-S_p k_{NO2}(2 - g_{CO})w_{wall}}{v_w}\right)\right) \tag{3.67}$$

The evolution of the the virtual wall layer thickness due to particulate oxidation by O$_2$ and NO$_2$ can be described by the following equation.

$$\frac{\partial}{\partial t}(\rho_p w_{wall}) = -\frac{M_c}{M_{ox}}\left(\frac{1}{1 - f_{co}/2}R_{O2,wall}\right) - \frac{M_c}{M_{NO2}}\left(\frac{1}{(2 - g_{CO})}R_{NO2,wall}\right) \tag{3.68}$$

The depletion rate of the virtual wall layer thickness is given by Equation 3.68. To determine the rate of particulate mass depletion in each of the cells present in the computational domain (Figure 3.5), a method of ratio and proportion is adopted.

The specific depletion rate of the virtual wall layer, in each iteration, is given by:

$$\Delta w_{wall} = \left((w_{wall})_{n-1} - (w_{wall})_n\right) / (w_{wall})_{n-1} \qquad (3.69)$$

where, the subscript n refer to the iterations at the nth time step. By ratio and proportion, assuming that all the cells in the wall have the same reaction rates,

$$(m_i)_n = (m_i)_{n-1} * (1 - \Delta w_{wall}) \qquad (3.70)$$

This simple approach of ratio and proportion can easily be verified to conserve mass.

The density of the exhaust gas and the wall flow velocity in the wall, ρ_w and v_w, are assumed to be the constant through the virtual wall layer, just as in the particulate cake layer as assumed in the original model. The kinetic pre-exponential factors, A_{th} and A_{NO_2} for the wall ((equations 3.64 and 3.67) can be assumed to be the same as those of the particulate cake layer (equations 3.37a and 3.42), or can be tuned independently to calibrate the model. Like equations 3.48a and 3.48b, equation 3.68 is solved by a Runge-Kutta numerical scheme of 4th order for accuracy and stability.

Using the technique outlined above, it is possible to include in a similar fashion, catalytic oxidation by O_2 in the wall. However, this was chosen not to be implemented due to a lack of data in the literature on the extent of catalyst penetration inside the wall. The extent of penetration varies with the physical properties of the wall, type and loading of catalyst and the catalyst application technique. The catalyst penetration (about 10 μm-30 μm) and is hence expected to be confined to the first few 'slabs' in the filter wall. This means that a more complex approach to wall oxidation, with highest oxidation rate in the first 'slab' and progressively lesser oxidation rates in the lower 'slabs' might be needed. In the present formulation, any O_2 based catalyst effect in the filter wall, will show up as higher NO_2 pre-exponential factors in the wall.

Results with this model, used in conjunction with a particulate cake filtration model described in the next section will be presented in Chapter 5. Some results of using this wall oxidation model with only the wall filtration model are presented by Triana [7], for a CRT® system. It was found that using this model results in low particle filtration efficiencies. This is because the 1-D model uses the partition coefficient (equation 3.24) to determine the fraction of engine-out particles entering the filter wall. Since the partition coefficient is defined based on 'loaded' unit collector diameters in the wall, which decrease due to particulate oxidation in the wall, the wall oxidation model adversely affects the filtration process. This improper coupling between the filtration and oxidation models also affects the predicted pressure drop because the filtration process directly affects the amount of particulate entering the filter wall. Higher filtration efficiencies, more accurate pressure drop prediction, and the larger problem of proper coupling between the filtration and oxidation models can be obtained with the development of particulate cake filtration model described in the next Section.

3.4   Particulate Cake Layer Filtration Model

A filtration model for the particulate cake layer was developed and coded in this research. A need to develop it arose to model large and rapid decreases in pressure drop taking place when high oxidation rates on and apparently inside the filter wall were present with high filtration efficiencies. Also, as pointed out in Section 3.3, use of the wall oxidation model with the wall filtration model resulted in low filtration efficiencies as reported by Triana [7], which also affects the pressure drop calculations. The reason for this was traced to the use of the partition coefficient (equation 3.24), which decreases due to oxidation inside the filter wall. Since the partition coefficient is used to filter the engine-out particles before they enter the filter wall, it decreases

the filtration efficiency, which also effects the pressure drop across the filter wall. Thus an improper coupling can be seen when the new wall oxidation model (Section 3.3) is combined with the old wall filtration model (Section 3.2.1). In addition, there has always been a deficiency in the wall filtration model in that physically, as soon as the particulate cake forms on the wall, it should become the filtering material above the first slab of the wall. Further, using the partition coefficient, which is based on parameters of the wall (equation 3.24), as a filtration parameter is weak reasoning, as it is known that the particulate cake is a highly efficient filter medium. A more realistic way to model filtration by the particulate cake will be to determine its filtration efficiency based on the properties of the particulate cake itself. Secondly, in a wall oxidation model without a particulate cake filtration model, the particulate in the first 'slab' of the filter wall is oxidized, but is immediately refilled completely because the decreased partition coefficient allows more particles to enter the filter wall. Thus the permeability of the first filter wall 'slab' does not decrease in spite of oxidation in the filter wall. This means that large and rapid decreases in pressure drop due to wall oxidation cannot be modeled properly, because the first filter wall 'slab' continues to be highly impermeable due to the particulate mass collected by it. In reality, the particulate mass in the first 'slab' can be oxidized but not be completely refilled, if the particulate cake layer is thick enough to filter out most of the inlet particulate.

A model which uses the developing particulate cake for filtration can make the partition coefficient redundant by combining particulate cake filtration with the already developed theory of wall filtration. Thus, the overall filtration will be the sum of the particulate cake and filter wall filtration. This also means that there is now no need for a percolation factor defined in the wall filtration model, as the filtration efficiency of the particulate cake would determine the amount of particulate entering the filter wall (depth filtration phase). The particulate cake filtration model was de-

veloped to address these issues and is based on the idea of modeling the particulate cake in a manner similar to the filter wall. This was thought suitable because the structure of the particulate cake is granular and porous, which means that it can be modeled by unit collector theory. This approach also lends itself to easy integration with the current code based on filtration by the unit collector theory.

Many studies on the physical and micro-structure of diesel particulate have been performed on carbon blacks instead of the particulate itself. Before extending their properties to diesel particulate, a comparison of their physical structure is essential. Clague et.al. [62] reported that there are significant differences between the particulate and carbon blacks in the chemical composition, surface chemistry and presence of adsorbed lubricants. However, diesel particulate, exhaust particulate and typical carbon blacks have very similar primary particle sizes and physical structure [62]. Clague et.al. [62] also report that carbon blacks and diesel particulate have differences in surface area, particle aggregate sizes and aggregate porosities. Diesel aggregate particles themselves are porous and made up of primary particles [17, 53, 62], which for diesel particle size distributions can be taken to be between 20μm and 40μm [53, 62]. The physical structure of diesel particulate is known to be granular and highly porous [53, 62, 63], similar to ceramic filter substrates, and suggests that a filtration model based on unit collector theory can be applied to particulate cakes. Although the spherule density of carbon,ρ_{soot} is taken to be 2000 kg/m^3 [17, 53], it could be higher due to the presence of adsorbed materials such as iron, lubricant or other wear related material [63]. The spherule density of particulate,ρ_{soot}, is related to the particulate cake packing density,ρ_p by [17, 53]:

$$\rho_p = \rho_{soot}(1 - \epsilon_p) \qquad (3.71)$$

where, ϵ_p is the porosity of the particulate cake.

To model the filtration by the particulate cake based on unit collector theory, representative values of mean pore size and porosity for the particulate cake are needed. Some authors have reported that the mean pore size of particulate cakes is close to 0.1μm [29]. If this is taken to be the mean pore size, then equation 3.6 could be used to calculate the collector diameter by using the porosity as a model fitting parameter to adjust the filtration efficiency of the cake, thus determining the amount of particulate mass going into the wall. However, assuming that the mean pore size remains the same across different exhaust flow conditions is incorrect, as it is known that particulate cake porosities and permeabilities which are mathematically related to the mean pore size decrease with Peclet number ([53] and Equation 3.6). Hence, a more fundamental approach was adopted to develop a particulate cake filtration model. The primary particles mentioned earlier, do not exist independently, but cluster together to form aggregate particles which are the stable particles found in particulates [62]. The particle aggregate diameter is related to the average diameter of the accumulation mode of the diesel particle size distribution and can be assumed to remain constant across engine operating conditions. Although the shape of the aggregate size is not spherical [62], rather ill-defined in fact, it can be assumed to be spherical, and such an approach was used with success by Konstandopoulos et.al. in correlating particulate cake properties to the Peclet number. Konstandopoulos et.al. report that a representative value for the diesel aggregate particle diameter can be taken to be 100 nm (0.1μm) [53]. Shadman reports that the loading of particles from a diesel engine onto a filter provided a deposit of particles with a very narrow size distribution [54, 57] with an average diameter determined by scanning electron microscopy of 0.1μm [54]. Thus the diesel aggregate diameter can be assumed to be the fundamental particle size making up particulate cakes. Assuming that the diesel aggregate particle is solid, and that it acts as a unit collector in a porous particulate cake layer of other such aggregate sized collectors filtering out particles of

the diesel exhaust makes it possible to develop a filtration model for the particulate cake. With the collector diameter being assumed to be equal to the aggregate particle diameter, the particulate bed porosity can be used as a model fitting parameter during calibration of the model.

The particulate cake filtration model can now be formulated as follows. The mean collector diameter, $d_{c,cake}$, is assumed to be equal to the mean aggregate size of diesel particulate, d_{aggr}. This is shown schematically in Figure 3.6 and defined in Equation 3.72.
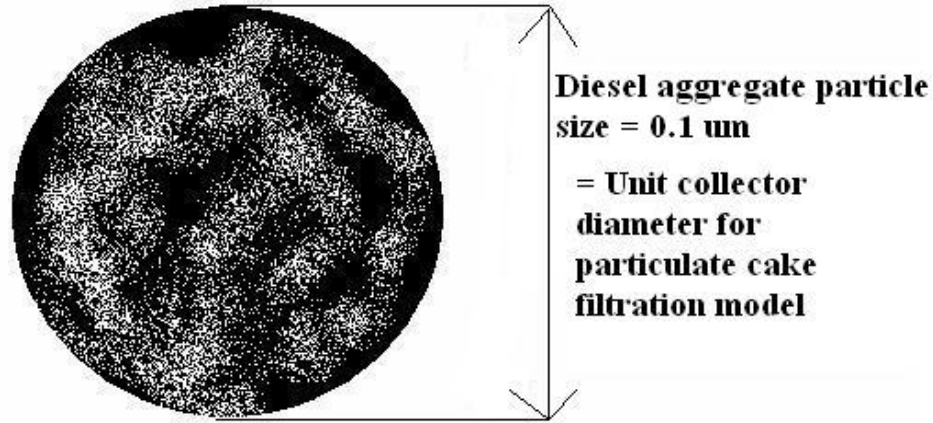
Figure 3.6: A schematic of the aggregate particle and collector diameters

$$d_{c,cake} = d_{aggr} = 100nm = 0.1\mu m \tag{3.72}$$

The particles comprising the diesel particle range are filtered by the unit collectors of diesel particles themselves. The particle collection mechanisms, just as the filter wall, can be assumed to be by diffusion and direct interception. The collection efficiency by diffusion can be expressed as (similar to equation 3.7):

$$\eta_{D,cake} \approx 3.5 \left(\frac{\epsilon_p}{K}\right)^{\frac{1}{3}} Pe_{cake}^{\frac{-2}{3}} \tag{3.73}$$

Just as in the filter wall (equation 3.9), the Peclet number can be used to quantify the relative magnitudes of convective and diffusive effects as a particle flows around a unit collector. It is defined in a fashion similar to equation 3.9:

$$Pe_{cake} = \frac{v_w d_{aggr}}{\epsilon_p D_p} \qquad (3.74)$$

where, v_w is the wall flow velocity. K is Kuwabara's hydrodynamic factor (equation 3.8) defined in a manner similar to the filter wall [31, 41]:

$$K = 2 - \epsilon - \frac{9}{5}(1-\epsilon)^{\frac{1}{3}} - \frac{1}{5}(1-\epsilon)^2 \qquad (3.75)$$

D_p is the particle diffusion coefficient, defined similarly to equation 3.11 [34, 41]:

$$D_p = \frac{k_B T C}{3\pi \mu d_p} \qquad (3.76)$$

It is worthwhile here to examine the term d_p, which defines the relevant scale of the diffusion coefficient. In the wall filtration model, it refers to the individual particle sizes present in diesel exhaust and thus the filtration efficiencies are calculated for individual particles across the entire size range (section 3.2.1). For the particulate cake filtration, it is assumed that particle deposition is approximated with the mean aggregate diameter. Hence d_p can be assumed to be equal to d_{aggr}, i.e. $d_p = d_{aggr}$. The physical interpretation is that particles of aggregate diameter act as unit collectors, filtering out engine-out particles of the same aggregate diameter, thus increasing the width of the particulate cake. That is why d_{aggr} is used in the numerator of equation 3.74 and not $d_{primary}$. In the same equation, C is the Stokes-Cunningham slip correction factor. Because of the small passages (mean pore size) present in particulate cakes compared to filter wall substrates [29], slip flow conditions are more important for particulate cakes. For particulate cakes, it can be related to the local

Knudsen number and particle aggregate diameter by [53]:

$$C = 1 + Kn_{cake} \left(1.257 + 0.4 e^{\frac{-1.1}{Kn_{cake}}} \right) \tag{3.77}$$

with the Knudsen number (Kn_{cake}) being defined based on a scale relative to the mean aggregate diameter of diesel particles,

$$Kn_{cake} = \frac{2\lambda}{d_{aggr}} \tag{3.78}$$

where λ is the mean free path of the gas molecules defined by,

$$\lambda = \frac{\mu}{P} \sqrt{\frac{\pi \overline{R} T}{2M}} \tag{3.79}$$

In this equation, P, $\overline{R}$, M, and T refer to the absolute pressure, universal gas constant, molecular weight and absolute temperature of the exhaust gas respectively.

The efficiency of particle collection by a unit collector due to interception is given by [31, 41, 52]:

$$\eta_{R,cake} = 3.5 \left(\frac{\epsilon_p}{K} \right) \frac{R}{(1 + R^m)} \tag{3.80}$$

where R is the particle interception parameter defined by a ratio of diameters, which as per the discussion above reduced to 1.0:

$$R = \frac{d_p}{d_{c,cake}} = \frac{d_{aggregate}}{d_{aggregate}} = 1.0 \tag{3.81}$$

and the exponent m is given by:

$$m = \frac{3 - 2\epsilon_p}{3\epsilon_p} \tag{3.82}$$

Assuming that the diffusional and interception mechanisms are independent of each

other, the overall collection efficiency of a single collector in the particulate cake can then be given as [31, 41]:

$$\eta_{DR,cake} = \eta_{D,cake} + \eta_{R,cake}(1 - \eta_{D,cake}) = \eta_{D,cake} + \eta_{R,cake} - \eta_{D,cake}\eta_{R,cake} \quad (3.83)$$

The total particle collection efficiency by the particulate cake layer, with layer thickness w_{cake} is related to the total collection efficiency of a single collector by [31, 41]:

$$E_{cake} = 1 - exp\left(\frac{-3\left(1 - \epsilon_p\right)\eta_{DR,cake}w_{cake}}{2\epsilon_p d_{aggr}}\right) \quad (3.84)$$

Equation 3.84 is a relation to calculate the filtration efficiency for the particulate cake layer based on the thickness of the particulate cake layer, w$_{cake}$, itself. Particulate cake layer porosity, ϵ_p, can be used as a model fitting parameter, thus making the percolation factor redundant, as discussed earlier. However equation 3.84 cannot be used with a 'clean' filter, because in such a case the particulate cake layer thickness w$_{cake}$ is equal to zero. Hence the filtration efficiency of the particulate cake E$_{cake}$ will be equal to zero. Hence, an initial starting solution for computational purposes is needed. A good approximation of the clean filtration efficiency is the partition coefficient (equation 3.24) discussed earlier. With a clean filter, it is logical to assume that the filtration efficiency depends on the size of the collectors in the filter wall as in the partition coefficient. Thus equation 3.24 is used for the first few, typically 10, time iterations until the thickness of the particulate cake layer, w$_{cake}$, has a non-zero numerical value following which equation 3.84 can be used.

Equation 3.84, thus makes the filtration by the particulate cake layer independent of the oxidation in the filter wall. Thus filtration and oxidation in the particulate layer is independent of the oxidation in the filter wall. The filtration processes are coupled because engine-out particles are filtered by the particulate cake layer according to equation 3.84, and the remaining enter the filter wall, which collects a fraction of the

particles based on the slab collection efficiency (Equation 3.19).

3.5 NO$_2$ Produced by the CPF Model

Research clearly demonstrating the beneficial effect of NO$_2$ on particulate oxidation is well documented [2, 18, 22, 41]. More recent research has also firmly established that particulate filters coated with appropriate catalysts can oxidize NO to NO$_2$ as the exhaust flows through the washcoat of the filters. In these conditions, the rate of particulate oxidation can be accelerated due to the re-oxidation of NO→NO$_2$. This 'recycling' process can happen more than once, possible even greater than 3 [3, 19, 20, 49]. Oxidation of NO→NO$_2$ in the CPF of the CCRT®, in both CPF-only and CCRT® configurations, was measured during the steady state characterization experiments. Modeling the higher particulate oxidation rates with a kinetic scheme that only accounts for particulate oxidation by NO$_2$ entering the filter, as in a CRT®, can result in the model kinetic parameters being different than their true values. It can also result in the attribution of particulate oxidation by NO→NO$_2$ oxidation, to a 'catalyst' effect due to O$_2$. While such a 'catalyst' effect due to O$_2$ may actually be present, its effect will be overestimated due to the lack of a NO→NO$_2$ production model. To study this effect on particulate oxidation, a model to take into account the oxidation of particulate by NO$_2$ produced by the catalyst washcoat in the CPF was developed.

In the original 1-D 2-layer CPF regeneration model framework of Konstandopoulos et.al, the 'catalyst' effect due to O$_2$ was limited to layer I [32, 33]. Extending this to filters with catalysts promoting the oxidation of NO→NO$_2$ in the washcoat, the production of NO$_2$ can be said to be occurring in layer I which is influenced by the presence of the catalyst. The kinetic effect describing this can be expressed by the

following general expression [2, 41]:

$$\frac{dy_{NO_2}}{dt} = k_{NO} y_{O_2}^{\gamma} y_{NO}^{n} \tag{3.85}$$

Use of Equation 3.85 to describe the NO→NO$_2$ oxidation reaction in the CPF and to thus take into account the higher reaction rates was first proposed by Konstandopoulos et.al. [41]. However, equation 3.85 also has to be integrated with the particulate oxidation framework presented in Section 3.2.4. The solution procedure described by Konstandopoulos et.al. [41] is complicated and relies on numerical integration of the resulting O$_2$ and NO$_2$ mass conservation equations. A simpler method was devised and implemented in this research.

Cooper and Thoss reported that the exponents n and γ, representing reaction orders vary with space velocity [2]. These exponents are reproduced below. The authors do not explicitly state the threshold value of space velocity, above which the flow can be said to have high space velocity, but figures in the same reference suggest 42,000 hr^{-1} and 373,000 hr^{-1} as being 'low' and 'high' space velocities respectively.

$$\gamma = 0.22, AllSpaceVelocities \tag{3.86a}$$

$$n = 0.5, LowSpaceVelocity \tag{3.86b}$$

$$n = 1.4, HighSpaceVelocity \tag{3.86c}$$

k$_{NO}$ is the frequency factor for the NO→NO$_2$ oxidation reaction assumed to follow a modified Arrhenius function given by[41]:

$$k_{NO}(T_w) = A_{NO}.T_w^n.exp\left(\frac{-E_{NO}}{RT_w}\right) \tag{3.87}$$

where, n is the temperature order for the reaction and A$_{NO}$ and E$_{NO}$ are the pre-

exponential frequency factor and activation energy for the for NO→NO$_2$ oxidation reaction respectively. The value of E$_{NO}$ can be taken to be 0.906E+08 determined experimentally by Konstandopoulos et.al. [41] and also used by Triana in modeling the same NO→NO$_2$ reaction in the DOC [6, 7]. This reaction is assumed to be the same as in the DOC, given by equation 2.2. The value of E$_{NO}$ is then known and A$_{NO}$ can then be determined from calibration of the model to fit the experimental data. It should be noted that the model used here is a general kinetic expression, and hence A$_{NO}$ can vary with exhaust conditions.

Use of equation 3.87 in layer I causes the concentrations of NO$_2$, NO and O$_2$ to change through the thickness of layer I, due to which a gradient of NO$_2$ concentrations is formed through the thickness of layer I. Any change in O$_2$ or NO$_2$ concentrations affects the particulate oxidation rates by thermal, catalytic and NO$_2$ means. However, the change in O$_2$ concentrations is expected to be minimal due to the low concentrations of NO and NO$_2$ relative to O$_2$ (ppm as compared to %Vol.). Thus the complexity in layer I kinetics is due to simultaneous depletion and production of NO$_2$ by the particulate and catalyst respectively. The following numerical solution was devised to solve the problem. To use equation 3.85 in the regeneration framework of the 1-D 2-layer CPF model, the thickness of the particulate in layer I was discretized into a number of *layers* of equal thickness, rather like the division of the filter wall into 'slabs'. This is shown schematically in Figure 3.7. Depletion of NO$_2$ (and O$_2$) takes place within these particulate layers which results in a depletion of each of the layers. This results in a decrease in NO$_2$ (and O$_2$) concentrations and an increase in NO concentrations exiting the particulate layers. The consumption (depletion) rates of O$_2$ and NO$_2$ in layer I is defined by equations 3.38 and 3.46 respectively. Between these layers occurs an increase in NO$_2$ concentrations (due to NO→NO$_2$ oxidation) and a corresponding decrease in NO and O$_2$ concentrations. Thus the particulate layers closer to the filter wall have progressively higher inlet NO$_2$ concentrations resulting
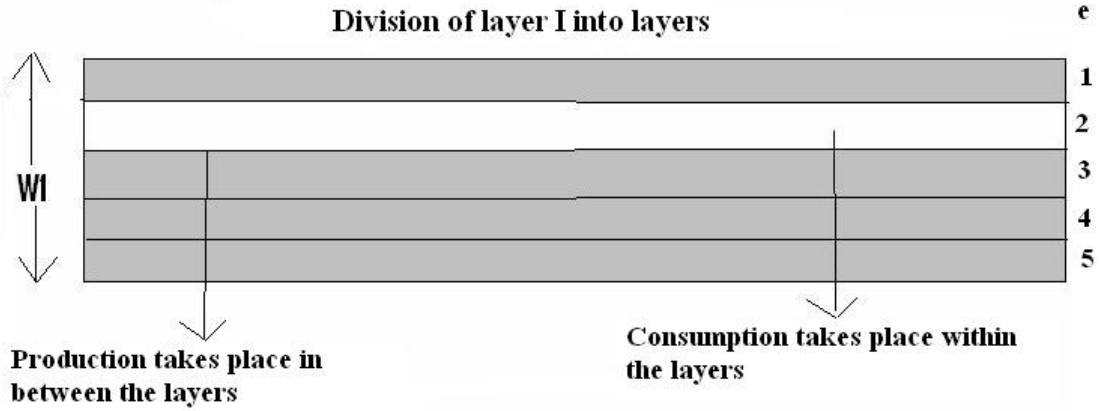
Figure 3.7: A schematic of the discretization of layer I

in higher particulate depletion rates due to increased availability of NO$_2$.

The concentrations of O$_2$ and NO$_2$ leaving layer II and entering layer I are calculated using engine-out concentrations and the depletion in layer II given by equations 3.35 and 3.44. For the first layer, the model calculates the rate of particulate depletion using concentrations of O$_2$ and NO$_2$ leaving layer II and entering layer I. The particulate layer thickness shrinks due to depletion of particulate by NO$_2$ and O$_2$. The evolution can be described by (similar to equation 3.48b):

$$\frac{\partial}{\partial t}(\rho_p w_e) = -\frac{M_c}{M_{ox}}\left(\frac{1}{1 - f_{co}/2}R_{O_2,th,e} + \frac{1}{1 - f_{co'}/2}R_{O_2,cat,e}\right) - \frac{M_c}{M_{NO2}}\left(\frac{1}{(2 - g_{CO})}R_{NO_2,e}\right)$$

(3.88)

where, the subscript e refers to the particulate layers.

The thermal, catalytic and NO$_2$ depletion rates in the particulate layer are given by (similar to equations 3.39a, 3.39b and 3.43 respectively):

$$R_{O_2,th,e} = R_{O_2,total,e} * \left(\frac{k_{th}(T_w)\left(1 - \frac{f_{co}}{2}\right)\beta}{k^*}\right)$$

(3.89a)

$$R_{O_2,cat,e} = R_{O_2,total,e} * \left(\frac{k_{cat}(T_w)\left(1 - \frac{f_{co'}}{2}\right)(1 - \beta)}{k^*}\right)$$

(3.89b)

$$R_{NO_2,e} = \rho_w v_w Y_{NO2,1} * \left(1 - exp\left(\frac{-S_p k_{NO2}(2 - g_{CO})w_e}{v_w}\right)\right) \tag{3.89c}$$

where, the total oxygen depletion rate due to thermal and catalytic means, $R_{O_2,total,1}$, is given by (similar to equation 3.38):

$$R_{O_2,total,e} = \rho_w v_w Y_{w,1} \left(1 - exp\left(\frac{-S_p k^* w_e}{v_w}\right)\right) \tag{3.90}$$

Equations 3.88 to 3.90 can be used to determine the depletion in the thickness of the particulate layers due to oxidation of particulate by NO$_2$ and O$_2$.

The NO$_2$ and O$_2$ concentrations (mass fractions), $Y_{NO_2,e}$ and $Y_{w,e}$ leaving the particulate layer can be given by (similar to equations 3.35 and 3.44 respectively):

$$Y_{NO_2,e} = Y_{NO2,1} \left(1 - exp\left(\frac{-S_p k_{NO2}(2 - g_{CO})w_e}{v_w}\right)\right) \tag{3.91a}$$

$$Y_{w,e} = Y_{w,1} \left(1 - exp\left(\frac{-S_p k^* w_e}{v_w}\right)\right) \tag{3.91b}$$

where, subscript 'e' refers to the mass fractions exiting the particulate layers. Note that these decreases in NO$_2$ and O$_2$ concentrations are due to consumption of these species by the carbon in the particulate layer.

Due to the production of NO$_2$ from NO (equation 3.85) by the catalyst in the CPF, the concentrations of NO$_2$ increase while the O$_2$ and NO concentrations decrease. These changes are assumed to happen in between the particulate layers. The particulate layer outlet NO mole fraction is calculated from a conservation of nitrogen atoms equation [41],

$$y_{NO,e} = y_{NO} + y_{NO_2} - y_{NO_2,e} \tag{3.92}$$

where, y_{NO} and y_{NO_2} are the mole fractions of NO and NO$_2$ entering the entering the particulate layers. They can also be taken to be equal to the engine-out NO and NO$_2$ mole fractions as total nitrogen atoms are always conserved. $y_{NO_2,e}$ is the mole

fraction of NO$_2$ leaving the layer and is related to equation 3.91a by the basic equation relating mass to moles for a species: Mass Fraction = Mole Fraction*Molecular Weight. Using the same basic equation, the individual particulate layer outlet O$_2$ and NO$_2$ mole fractions can be calculated from equations 3.91b and 3.91a respectively, and are then inserted in equation 3.85 to calculate the production of NO$_2$ from NO. Solution of equation 3.85 causes the NO$_2$ mole fraction entering the next particulate layer to increase, while the O$_2$ and NO mole fractions decrease and can calculated by a conservation of O$_2$ atoms, relative to equation 2.2 as follows:[*]

$$y_{O2} = y_{w,e} - 0.5 * (y_{NO2,gen} - y_{NO2,e}) \tag{3.93}$$

where, $y_{w,e}$ and $y_{NO2,e}$ are the mole fractions of oxygen and NO$_2$ exiting the particulate layer, and are related to equations 3.91b and 3.91a. $y_{NO2,gen}$ is the increased mole fraction of NO$_2$ in between the particulate layers after NO$_2$ generation by equation 3.85. The application of equation 3.93 in the code is not essential as the decrease in O$_2$ concentrations is of order O(10^{-4}) because NO$_2$ concentrations are much smaller than O$_2$ concentrations but was nevertheless implemented in the MTU 1-D 2-layer model.

For the solution of the NO$_2$ production equation 3.85, layer I was divided between 5 to 10 particulate layers, depending on the thickness of layer I. The thickness of layer I is related to the thickness of the catalyst washcoat which is generally between 10μm and 30μm. During coding, an easy and simple method to determine the optimum number of particulate layers is to keep increasing their number until it converges to the solution. Further increases in the number of particulate layers will only slow down the computation process. For the solution of equation 3.85, a first-order difference technique was found to be sufficient in accuracy. More complicated solvers

---

[*] Implementation of equation 3.93 should be exercised with care because the O$_2$ mole fraction is generally expressed in %Vol. while NO and NO$_2$ concetrations are expressed in ppm

like the Runge-Kutta 4th order scheme are unnecessary because of the linear nature of equation 3.85.

This procedure described above is repeated for each of the particulate layers. The total depletion of layer I is obtained by summing up the depleted thicknesses of the each of the layers making up layer I.

$$w_{1,dep} = \sum_{i=1}^{e-layers} w_{e,dep} \tag{3.94}$$

w$_{1,dep}$ is the total thickness of layer I after depletion, and w$_{e,dep}$ is the depleted thicknesses of the particulate layers. The particulate layers deplete by progressively increasing rates because the NO$_2$ concentrations entering each of these layers is progressively higher.

Chapter 4

Experimental Setup and Procedures

This chapter describes the experimental setup used and procedures followed during the course of the experimental work performed. It also contains a description of of the test matrices devised and the purpose of the experiments with the CCRT®. Details are provided of the engine, fuel, dynamometer, engine controls, particle size instruments, gaseous emission analyzer and particulate sampling setup. A brief description of how the experiments were conducted is also provided. The experiments were carried out in conjunction with Lakkireddy [46], and the experimental setup and procedures are described in more detail in his M.S thesis [46].

4.1 Experimental Setup

The engine used in this research was a Cummins ISM 2002 heavy duty engine. Details of the engine are provided in the Table 4.1. Important changes affecting emissions in this engine are: an automatically controlled high pressure cooled EGR system, variable geometry turbocharging (VGT) with infinite adjustment which provides the exact amount of boost at any engine speed. The engine is designed to

Table 4.1: Details of the Cummins ISM 2002 heavy-duty Engine

Model	Cummins ISM 2002
Type	4-Stroke
Cylinders	6, inline
Aspiration	Variable geometry turbocharger, aftercooled
Displacement (L)	10.8(125mmX147mm)
Rated Power (kW)	246kW@2300rpm
Rated Speed (rpm)	2100
Peak Torque (Nm)	1697Nm@1200rpm
Timing	Variable (electronic)
EGR	Auto, high pressure, aftercooled

meet the 2.5 grams NO_X+NMHC* emissions requirement for 2002. High pressure EGR systems recirculate the exhaust to the engine manifold via a restriction to increase its pressure above the intake manifold pressure. This results in a substantial fuel penalty [13, 64, 65]. With the use DPFs, cooled low pressure EGR systems are now being developed, in which the exhaust is recirculated from downstream of the particulate filter to upstream of the compressor where the pressure is close to ambient.

A schematic of the test cell is shown in Figure 4.1, adapted from reference The engine was coupled to an eddy current dynamometer manufactured by Eaton Corporation. It has a rating of 500 hp at speeds between 1750 rpm and 7000 rpm. A Digalog 1022A controller was used to control the load and speed on the engine. The air supply to the engine came from the test cell. The pressure drop across a laminar flow element and the temperature of the supply air was used to calculate the mass flow rate of air to the engine. Relative humidity was measured before the start of each experiment using a sling psychrometer. The pressure in the test cell during the experiment was measured using a mercury barometer. [46].

---

*Non-Methane Hydrocarbons
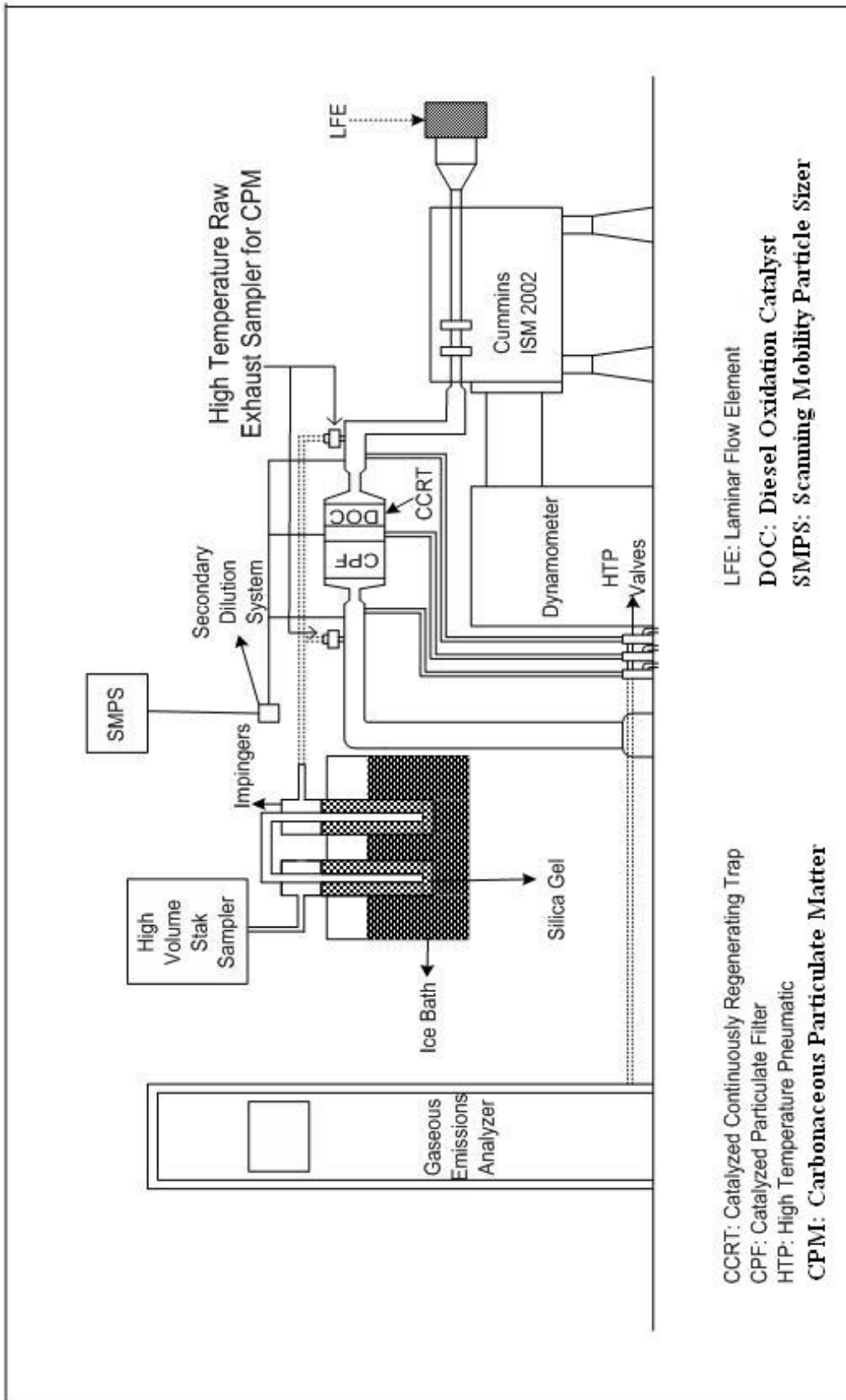
Figure 4.1: A schematic of the experimental setup (not to scale) [46]

CCRT: Catalyzed Continuously Regenerating Trap
CPF: Catalyzed Particulate Filter
HTP: High Temperature Pneumatic
CPM: Carbonaceous Particulate Matter

LFE: Laminar Flow Element
DOC: Diesel Oxidation Catalyst
SMPS: Scanning Mobility Particle Sizer

The fuel mass flow rate to the engine was measured using an AVL fuel weigher. The instrument allowed measurements of the time taken for the engine to consume 0.4 kg of diesel fuel, which, when divided, provided the average fuel mass flow rate during that period. The diesel fuel used in this research was ultra low sulfur diesel fuel (ULSF), with less than 1 ppmS present to 1) avoid catalyst poisoning in the DOC and CPF [2], 2) decrease sulfate formation downstream of the catalysts thus keeping TPM levels low [46] and 3) keeping the NO→NO$_2$ oxidation efficiency to a maximum [2]. An overview of the properties of the ULSF diesel fuel are shown in Table 4.2.

Temperatures in the DOC, CPF and ambient were measured using K-type thermocouples from Omega Engineering Inc., which were connected to a junction box in the test cell. Temperatures in the engine were measured using E-type thermocouples supplied by Cummins Inc., but were not connected to the junction box. The pressure drop across the DOC and CPF were measured using 13.8 kPad and 68.9 kPad differential pressure transducers respectively. %EGR was calculated by measuring the temperatures before after the recirculated exhaust mixes with the compressed aftercooled air supply to the engine (for derivation see reference [46]). Two SCXI modules, provided by National Instruments Inc., were used for signal processing and were linked to a data acquisition board and the data were recorded using Labview software by National Instruments Inc on a personal computer (PC). The recorded data were analyzed using Microsoft's Excel® spreadsheet software.

Particle size distributions were measured by a scanning mobility particle sizer (SMPS) model 3077 made by TSI. The SMPS instrument uses an electric mobility detection technique. An electrostatic classifier charges particles to a known charge distribution and then classifies them according to their ability to pass through an electrical field and a condensation particle counter (CPC) measures their concentration. The SMPS instrument was calibrated before use with the help of a manual

Table 4.2: Properties of the ULSF diesel fuels used

Property	ASTM No.	Batch 2 (2/04-8/04)	Batch 3 (8/04-10/04)
API gravity	D-1298	39.1	39.4
Cetane index	D-976	51.1	51.7
Sulfur content (ppm)	D-4045	0.30	0.20
Distillation Profile			
T10 (^{o}C)	D-86	207	209
T50 (^{o}C)	D-86	253	254
T90 (^{o}C)	D-86	318	313
Fuel analysis (% Vol.)			
Parafins & Napthenes	D-1319	69.7	74.2
Olefins	D-1319	3.0	0.8
Aromatics	D-1319	27.3	25.0

provided by TSI. The measurements were made upstream of the DOC, downstream of the DOC and downstream of the CPF in the size range of 13.6nm to 763.5nm. Three sets of particle size measurements were made at every location in the following order: upstream of the DOC, downstream of the DOC and downstream of the CPF, since only one location can sampled at any given time. A thermodenuder which removes the volatile and vapor contents in the sample lines prior to sampling [34], could not be used because it was being repaired by the manufacturer. A two-stage dilution system was used to dilute the sample exhaust so that near ambient particle concentrations enter the SMPS. It consists of a critical flow orifice in each stage of the device to assist in obtaining iso-kinetic sampling conditions and fixing the dilution ratio. In the absence of a thermodenuder a high total dilution ratio of 72.3 was used during the experiments to prevent particle nucleation and formation in the nuclei mode range [66, 67, 68]. For a details of the dilution system, orifice calibration and performance with pressure of supply air see the thesis of Lakkireddy [46]. To ensure that the SMPS drew the sample at the required rate, a T-section was connected when sampling upstream of the DOC and upstream of the CPF, as the back pressure at these locations forced excess air through the particle sample lines which made the SMPS lose its calibration (see [46] for setup). This was not necessary when sampling

downstream of the CPF due to the absence of any backpressure. Prior to the start of each experiment, the particle size sample lines were cleaned with propanol and water and compressed air was blown through the lines to clean them. This was especially important for the downstream CPF sample line due to the low concentrations present that are reduced even further due to dilution. Once it was known that the CCRT® had very high filtration efficiencies, particle size measurements were first made downstream of the CPF to determine the downstream particle size distribution, so that the filtration efficiency could be calculated as a function of time. The sampling can be started using a PC and data obtained was converted to size distribution data using software provided by TSI Inc.

Gaseous emissions were measured with a Pierburg AMA 400 emissions analyzer at the following locations: upstream of the DOC, downstream of the DOC and downstream of the CPF. The analyzer can simultaneously measure the concentrations of HCs, NO_X (or NO), CO, CO_2 and O_2 present in the sampled exhaust. Each set of readings taken at each location were carried out in the NO and NO_X modes so that the approximate NO_2 concentrations could be obtained by subtraction. The Pierburg AMA 400 analyzer uses a flame ionization detector to measure HCs, a non dispersive infra red analyzers to measure CO and CO_2 concentrations, a chemiluminescence analyzer to measure NO_X and NO and an O_2 sensor to measure O_2 concentrations. The analyzer reports the concentrations of CO_2 and O_2 on a dry fraction basis. The sampling locations were connected to the emissions analyzer by means of a heated line, which is maintained at 185^oC by the analyzer when measuring emissions in 'diesel' mode. The switching between the sampling locations is done by means of fast acting pneumatically operated valves whose compressed air supply is from an air compressor in the test cell. This system and its design are described in the thesis of Lakkireddy [46]. Prior to the start of each experiment an internal leak check was performed to ensure that no leaks were present in the heated line or the instrument. The

analyzer was controlled by a PC and the data recorded was analyzed using Microsoft's Excel® software.

Carbonaceous particulate matter (CPM) samples were measured upstream of the DOC and downstream of the CPF. CPM concentrations measured upstream of the DOC were taken to be the concentrations entering the CPF as it can be assumed that CPM concentrations do not change across a DOC [14]. The sampling train, made by Anderson Instruments Inc., draws exhaust through a six-hole probe inserted in the exhaust line. CPM are collected on 47mm glass fiber filters (Pall Corporation), supported on an under drain disk and a screen to prevent the filters from damage. For a detailed description on the design of the sampling system see references [46, 69], and a schematic of the setup is reproduced in Figure 4.1 (from reference [46]) . The flow rate through the 47 mm filters was between 17-29 std-liters/min with a high volume stak sampler, maintained by keeping a constant pressure drop across a calibrated orifice. However, since the exhaust temperature varies with engine load, face velocities on the 47 mm filters during CPM collection were different during the experiments. The samples were drawn through two tubes full of silica gel kept in an ice bath to absorb the moisture present in the sample exhaust. The 47 mm filters were weighed on a micro-balance manufactured by Metler Toledo Inc, with a maximum capacity of 2 g and an accuracy of 0.1 μg, before and after the experiment, to determine the increase in weight of the 47mm filters due to the deposited CPM. Prior to weighing, all the 47mm filters were conditioned in a humidity controlled chamber for 24 hours to provide a constant mass of water on each filter. Immediately after the experiments, the exposed 47mm filters were placed in an ammoniation chamber to convert the hygroscopic $H_2SO_4.7H_2O$ to the less hygroscopic ammonium sulfate $(NH_4)_2SO_4$, thus avoiding an increase in weight of the samples due to pick up of moisture. Corrections to the weight, due to the samples being kept in the humidity controlled chamber were taken into account by also weighing a 47mm 'control' filter which is always present
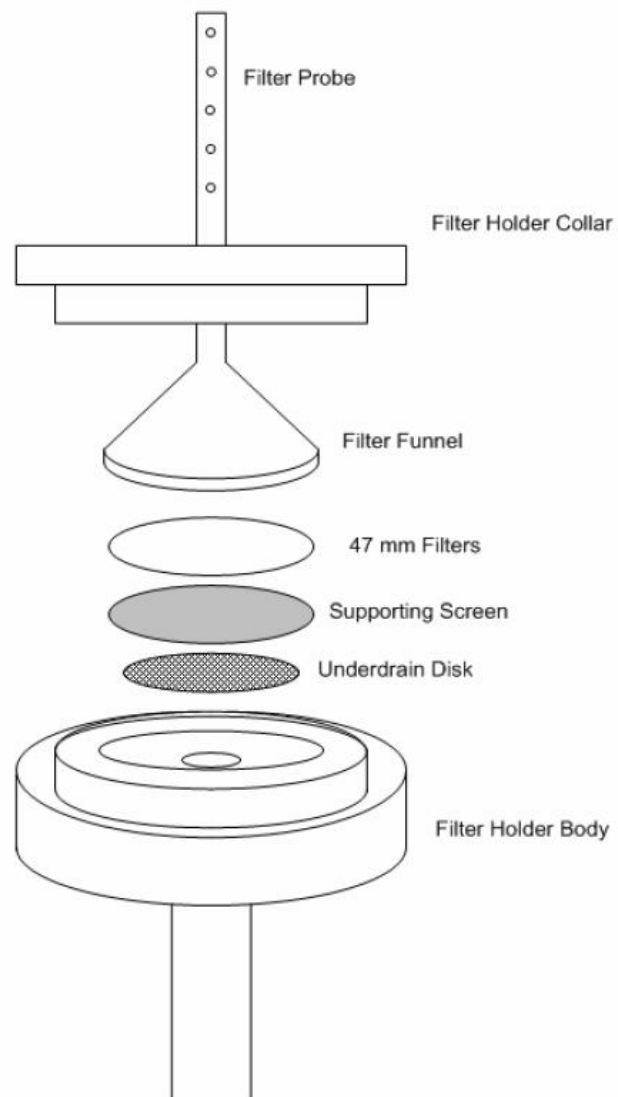
Figure 4.2: A schematic of the CPM sampling system [46]

in the humidity controlled chamber.

The CCRT® used in this research was supplied by Johnson Matthey. The DOC and CPF specifications are shown in Table 4.3. For both the DOC and the CPF, catalyst formulations and loadings were not revealed due to their proprietary nature. It was made known in a private communication with Cummins Inc. that the catalyst in the CPF is optimized to oxidize particulate by reoxidizing NO to NO_2, rather than catalyzing a reaction of particulate with oxygen [70].

4.2 Modeling Data Required and Test Matrices

The purpose of the experimental part of this research was to provide data to calibrate the MTU 1-D DOC and 1-D CPF models, so that model parameters describing the CPFs filtration, oxidation and loading characteristics could be determined. Initially it was thought that the CPF model developed by references [7, 34] which were also validated by reference [9] would be used for the calibration. However, during and after the experiments, several improvements deemed necessary to study the CCRT® were made, which are described in Chapter 3.

The CPF model needs the following parameters: clean filter wall permeability, average filter wall mean pore diameter, particulate packing density in the wall, percolation factor, permeability of particulate cake layer, packing density of particulate cake layer, pre-exponential and activation energies for thermal, catalytic and NO_2-assisted particulate oxidation. These are parameters of the original MTU 1-D CPF model [9, 34]. With the new model described in chapter 3, the NO_2 pre-exponential factor in the filter wall, porosity of the particulate cake layer and the NO_2 production factor by the catalyst in the CPF would need to be determined. The percolation factor used in the original model, is not used in the new model.

The aim of the DOC characterization experiments was to obtain the following pa-

Table 4.3: Properties of Johnson Matthey DOC and CPF

Property	DOC	CPF
Material	Cordierite	Cordierite
Cell Geometry	Square, both ends open	Square, alternate ends plugged
Diameter (m)	0.2667	0.2667
Length (m)	0.1524	0.3048
Porosity	0.35	0.52*
Permeability (m^2)	N/A**	15.0E-12*
Mean pore size (m)	N/A**	13.0E-6*
Channel width (mm)	1.092	1.498
Channel thickness (mm)	0.1752	0.3048
Cell density (cpsi)	400	200
Wall density (kg/m^3)	N/A**	1130
Thermal Conductivity(W/m-K)	N/A**	1.0
Specific Heat(kJ/kg-K)	N/A**	1.0
Catalyst	Proprietery	Proprietery
Catalyst Loading	Proprietery	Proprietery

*: properties of uncatalyzed filter
**: not available

rameters for the DOC model: 'apparent' activation energies of the DOC catalyst with respect to the oxidation of HCs, CO and NO, and their respective pre-exponential factors. The DOC model also has a model to predict the pressure drop across the DOC. Since the model is a steady state model, steady state measurements of the exhaust temperature at DOC inlet, exhaust mass flow rate, pressure drop across the DOC and HCs, CO and NO concentrations upstream and downstream of the DOC are needed to calibrate the DOC model. Since these data could be obtained during CCRT® characterization experiments, no separate DOC characterization experiments were needed.

For a proper meaningful study of the oxidation characteristics of the CCRT®, the temperature range should be one in which particulate oxidation by NO_2 is considerable. Not only should the exhaust temperature be conducive for particulate oxidation by NO_2, NO_2 concentrations in the exhaust should be high ($\approx$ 100 ppm [7]), for significant particulate oxidation rates. Since NO_2 oxidation begins at temperatures of

about 275°C, a lower limit of 275°C was imposed. Secondly, since 'catalytic' oxidation is generally significant at temperatures above 400°C [9, 34], some experiments at these temperatures were also needed. Exhaust temperatures around 450°C are also needed for determination of kinetic parameters in the 1-D model which would help modeling of future active regeneration experiments at MTU [71]. Loads at rated speed were selected for the characterization experiments since engines typically operate a significant portion of their running time at this speed. With these considerations in mind, the following engine conditions were selected after studying the then available data of the Cummins ISM 2002 engine from the emission characterization experiments of Lakkireddy [46]: loads at 20, 40, 60 and 75 % of full load (1120 Nm) at rated speed were in the range of the temperatures and NO_2 concentrations needed. When the experimental plan was being devised, it was thought that the catalyst in the CPF is optimized to oxidize particulate by 'catalytic' reaction of particulate with oxygen in addition to reoxidizing NO to NO_2*. To study the independent effects of the 'catalytic' and NO_2 effects, the plan called for steady state characterization experiments to be conducted at every load and speed in both CCRT® (DOC+CPF) configuration and in a CPF-only configuration. Characterization experiments in the CPF-only configuration would yield the kinetic parameters of the 'catalytic' reaction. With the kinetic paramters of the 'catalytic' reaction known, modeling of the data in CCRT® configuration would yield the kinetic parameters of the NO_2-assisted oxidation. The experimental test matrices for the CPF-only and CCRT® characterization experiments are shown in Table 4.4. Table 4.5 describes the most important experimental data needed to determine the relevant CCRT® model parameters.

Prior to the start of each experiment, the CCRT® and baked in an oven at about 560°C for about 8 hours. After the baking, it was taken out of the oven and reweighed when still hot to prevent moisture from influencing the weight, to check for

---

*Subsequently, it was found that the CPF catalyst is only optimized to oxidize NO→NO_2 [70]

Table 4.4: Test matrices for CPF-only and CCRT® characterization experiments

Experiments in CPF-only configuration				
% load at rated speed	20	40	60	75
Speed (rpm)	2100	2100	2100	2100
Torque (Nm)	224	448	672	840
Exhaust Temp. (^{o}C)	280	340	415	460
Oxidation Mechanism	Catalytic	Catalytic	Catalytic	Catalytic
Experiments in CCRT® (DOC+CPF) configuration				
% load at rated speed	20	40	60	75
Speed (rpm)	2100	2100	2100	2100
Torque (Nm)	224	448	672	840
Exhaust Temp. (^{o}C)	280	340	415	460
Oxidation Mechanism	NO_2, Catalytic	NO_2, Catalytic	NO_2, Catalytic	NO_2, Catalytic

Table 4.5: Determination of CCRT® model parameters from experimental data

Model Parameter	Relevant data
Filter wall clean permeability	Clean pressure drop
Wall packing density	Depth filtration ΔP
Percolation factor	Depth filtration ΔP
Particulate cake density	Cake filtration ΔP
Particulate cake permeability	Cake filtration ΔP
Particulate cake kinetics	CPM, CPF mass retained
Filter wall mean pore size	Filtration efficiency, ΔP
New 1-D model parameters	
Wall oxidation kinetic factors	Entire ΔP curve
Particulate cake porosity	Depth filtration ΔP
NO_2 generation factor	CPF mass retained, outlet NO_2 conc.

proper baking. For details refer the thesis of Lakkireddy [46]. The experiments were performed as follows.

- Install the clean CPF or CCRT® in the exhaust trap line with all the thermocouples properly installed and verified to be working correctly. The engine was started in the base line and after warm-up it was ramped up to the desired load and speed. The engine was run at one of the target loads and speeds in Table 4.4, until it reached steady state conditions, i.e. engine temperatures, air and fuel mass flow rates did not change with time.

- The exhaust was switched from the base line to trap line. The exhaust temperatures at DOC inlet, DOC outlet and CPF outlet were carefully recorded. At this time, the pressure drop across the DOC and CPF were also recorded.

- During the first half hour, two to three particle size measurements downstream of the CPF were taken to measure the filtration efficiencies during the depth filtration phase.

- Raw CPM samples were taken upstream of the DOC and downstream of the CPF. The upstream DOC samples were taken for a period of 5 minutes, while the downstream CPF samples were taken for at least 1 hour due to the low CPM concentrations exiting the CPF. CPM concentrations entering and leaving the CPF are necessary to model the particulate oxidation rates and filtration efficiencies of the CPF. At least three samples were taken at the two locations. More samples were taken upstream of the DOC to reduce the scatter in the CPM measurements.

- Gaseous emissions measurements were taken upstream of the DOC, downstream of the DOC and downstream of the CPF. At least two sets of measurements were taken at every location, with each set having data in both NO and NO_X modes to determine the approximate NO_2 concentrations.

- Particle size measurements were taken upstream of the DOC, downstream of the DOC and downstream of the CPF. These measurements along with the particle size measurements taken during the depth filtration phase provides data on the evolution of CPF filtration efficiency with time. At least three samples were taken at every location.

- After at least 5 hours of running or when all the above mentioned measurements were completed the engine was stopped. The CPF was removed carefully while still hot and weighed on a balance. The increase in mass of the CPF from its clean value was taken to be the particulate mass deposited in the filter.

- Immediately after the experiments, the 47 mm sampled filters were placed in an ammoniation chamber for an hour. Prior to reweighing, all the 47mm filters were conditioned in a humidity controlled chamber for 24 hours.

Chapter 5

Results and Discussion

This chapter presents the experimental results obtained from the CPF-only and CCRT® characterization experiments carried out to obtain data to calibrate the 1-D DOC and CPF models. The results from the calibration of the DOC model kinetics and pressure drop model are presented. The results from the calibration of the 1-D CPF model are presented along with a discussion of the model parameters and their interpretation.

5.1 Characterization Experimental Results

A review of the CPF-only and CCRT® characterization experimental results is given in this section. For a more detailed presentation, the reader should also refer the thesis of Lakkireddy [46].

The A/F ratio and %EGR measured during the experiments are shown in Figure 5.1. The A/F ratio decreases at higher loads as a result of higher fuel consumption and increased inlet air boost due to the turbocharger. It can also be seen that this engine has been calibrated to decrease EGR rates with load at rated speed. Reference [46] describes the derivation of the equation used to calculate EGR rates from the temperatures of the recirculated exhaust, fresh air intake and the manifold

temperatures. EGR calibration strategies for engines designed to be used with passive regeneration systems are limited by the particulate emission rates and the NO_X/PM ratio [42]. Use of high EGR rates can result in a substantial decrease in oxidation rates in the filter, due to a reduction in NO_X levels and simultaneous increase in particulate concentrations, thus considerably decreasing the NO_X/PM ratios [42]. A summary of the engine data collected during the characterization experiments is shown in Table 5.1. A discussion and analysis of engine data from the characterization experiments and initial runs with the Cummins ISM 2002 engine are shown in Appendix A.
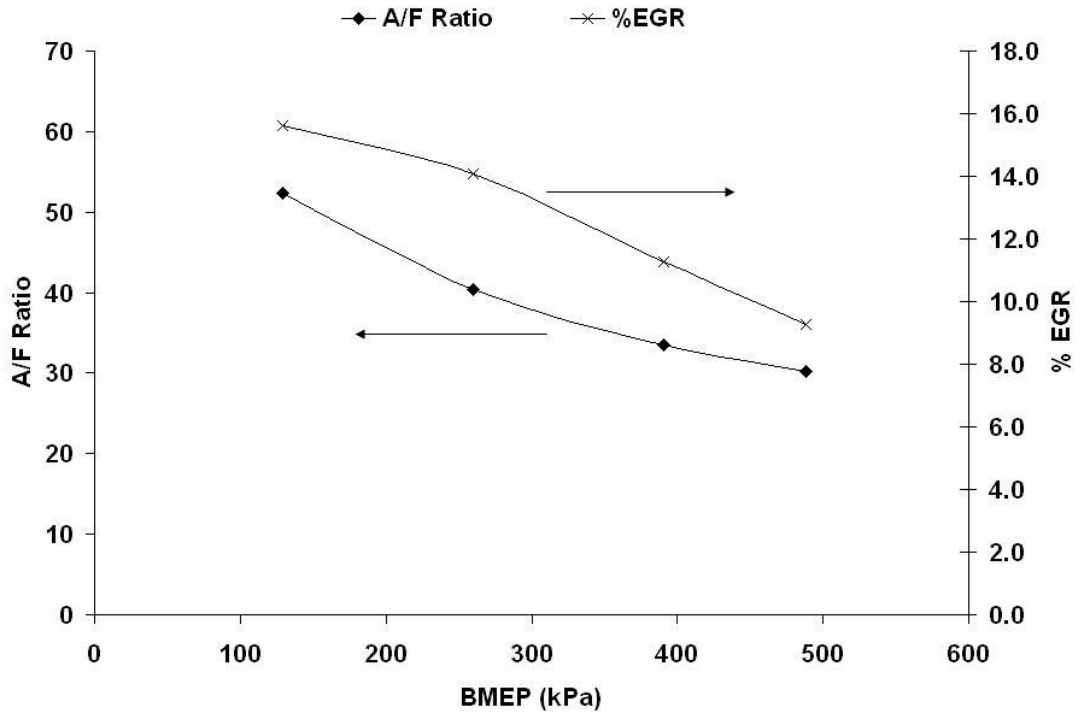

Figure 5.1: A/F ratios and %EGR as a function of BMEP during characterization experiments

Table 5.1: Engine data during the CPF-only and CCRT® characterization experiments

% Load at rated speed →		20		40		60		75	
Parameter ↓	Units ↓	CCRT®	CPF	CCRT®	CPF	CCRT®	CPF	CCRT®	CPF
Load	N-m	223	223	446	446	671	671	840	840
Speed	rpm	2100	2100	2100	2100	2100	2100	2100	2100
Power	kW	49	49	98	98	148	148	185	185
Air flow rate	kgs/sec	0.280	0.282	0.322	0.325	0.360	0.354	0.392	0.392
Fuel flow rate	kgs/sec	0.005	0.005	0.008	0.008	0.010	0.010	0.013	0.013
A/F ratio	kgs air/kgs fuel	52.3	51.8	40.3	40.7	33.5	32.5	30.2	30.2
BSFC	g/kWh	393	401	292	293	261	265	253	253
CPF inlet temp.	^oC	279	277	340	337	414	408	460	466
EGR	$\frac{exhaustrate*100}{air\;flowrate}$, %	15.6	16.0	14.1	14.2	11.3	11.7	9.3	9.3

The pressure drops measured across the DOC during all the experiments are shown in Figure 5.2. During the first few minutes after switching the exhaust from the baseline to the trap line, the pressure drop across the DOC rises rapidly because the temperature of the exhaust at the DOC inlet slowly increases to a steady state value as the exhaust trap line is heated up to the exhaust temperature. A discussion on how the transient temperature affects the pressure drop across the DOC is given in Appendix E. The pressure drop across the DOC becomes constant with time because the primary component of the pressure drop is the friction loss due to laminar flow in the square channels [6, 7, 61], which is constant for a given temperature and actual exhaust volumetric flow rate (Equation 3.4). For modeling purposes, a time averaged DOC pressure drop was calculated for each load and is shown in Table 5.2.
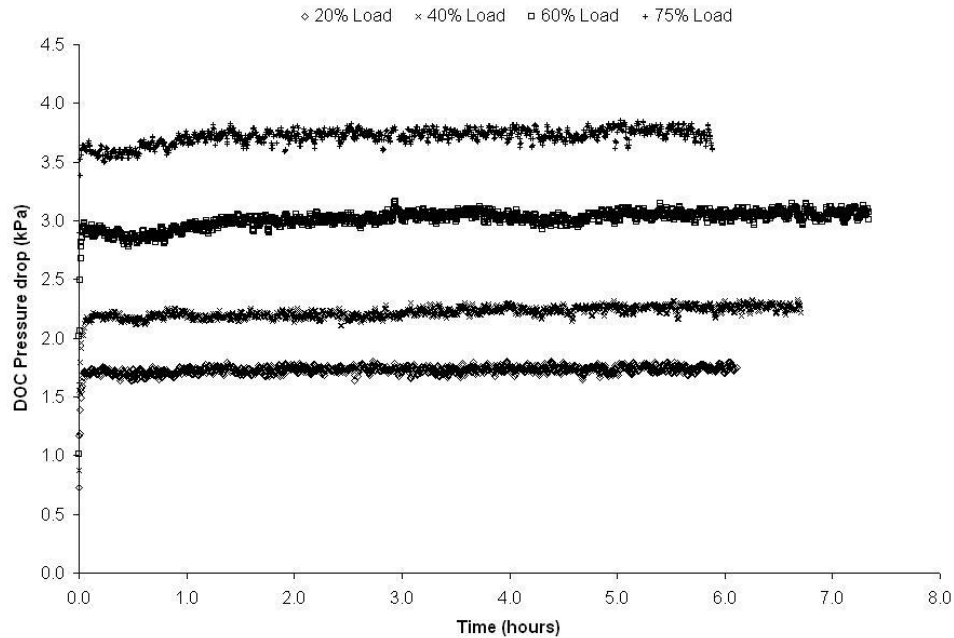

Figure 5.2: DOC pressure drop during the CCRT® characterization experiments

A comparison of the pressure drop measured across the CPF in CPF-only and CCRT® configurations during the experiments are shown in Figures 5.3 through 5.6. The non-linear pressure drop across the CPF when starting from 'clean' is called the depth filtration phase and signifies particle collection by the filter wall. Subsequently,

Table 5.2: Time averaged pressure drop across the DOC

% Load	Average DOC ΔP (kPa)
20	1.8
40	2.3
60	3.1
75	3.8

the pressure drop becomes linear and signifies particle collection by the particulate cake layer. This phase is called the cake layer filtration phase. The legend key 'CPF-only' refers to the pressure drop across the CPF when loading the CPF without the DOC, 'CPFinCCRT' refers to the pressure drop across the CPF when loading the CPF downstream of the DOC, and 'EntireCCRT' refers to the sum of the pressure drop across the DOC and the CPF in CCRT® configuration. These figures should be used with Table 5.3 which shows the particulate mass retained in the filter at the end of the experiments. For all the experiments, the particulate mass retained in the CPF in CCRT® configuration was lower than in CPF-only configuration due to the higher concentrations of NO_2 entering the CPF in the CCRT® configuration.
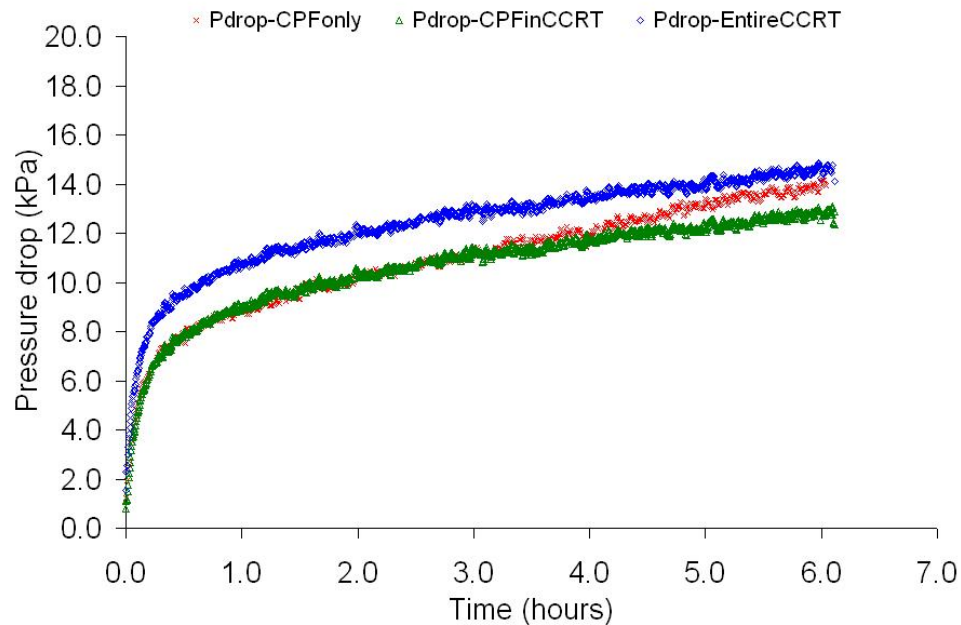

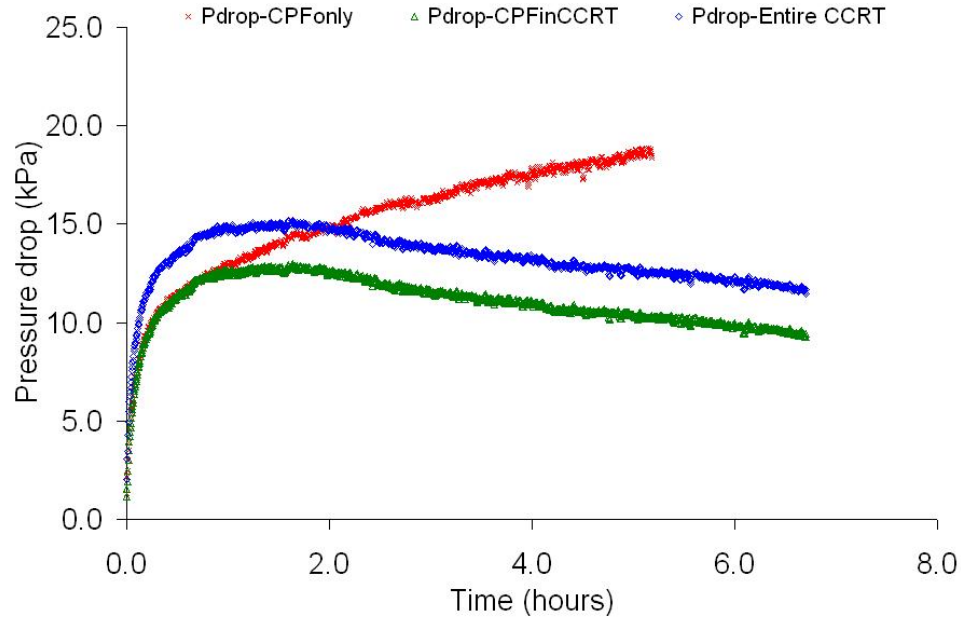Figure 5.3: Pressure drop across the CPF and entire CCRT® at 20% load

Figure 5.4: Pressure drop across the CPF and entire CCRT® at 40% load

Table 5.3: PM mass retained in the CPF at the end of characterization experiments

%Load	CPF-only configuration		CCRT® configuration	
	Time (hrs)	Mass retained (gms)	Time (hrs)	Mass retained (gms)
20	5.93	85	6.11	65
40	5.18	99	6.70	66
60	5.93	52	7.34	13
75	7.05	25	5.88	7

At 20% load condition, the pressure drop profiles are very similar, and begin to diverge after about 3.5 hours of loading. Both the CPF-only and CCRT® configuration experiments were run for similar lengths of time, but the particulate mass retained in CPF configuration was 20 grams higher. This suggests that the divergence of the pressure drops after about 3.5 hours is due to increased particulate oxidation rates in CCRT® configuration. The pressure drop profiles at all other conditions, 40, 60 and 75% loads at rated speed, are distinctively dissimilar from each other (Figures 5.4 - 5.6) demonstrating the beneficial effect of increased NO_2 concentrations at the CPF inlet. Even though the pressure drop profile for the 40% CCRT® configuration
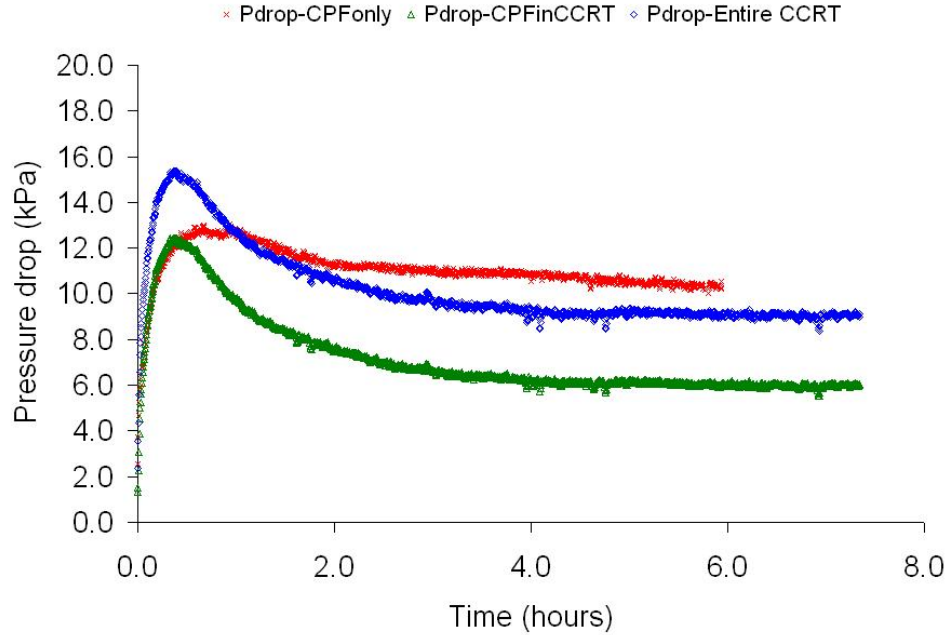
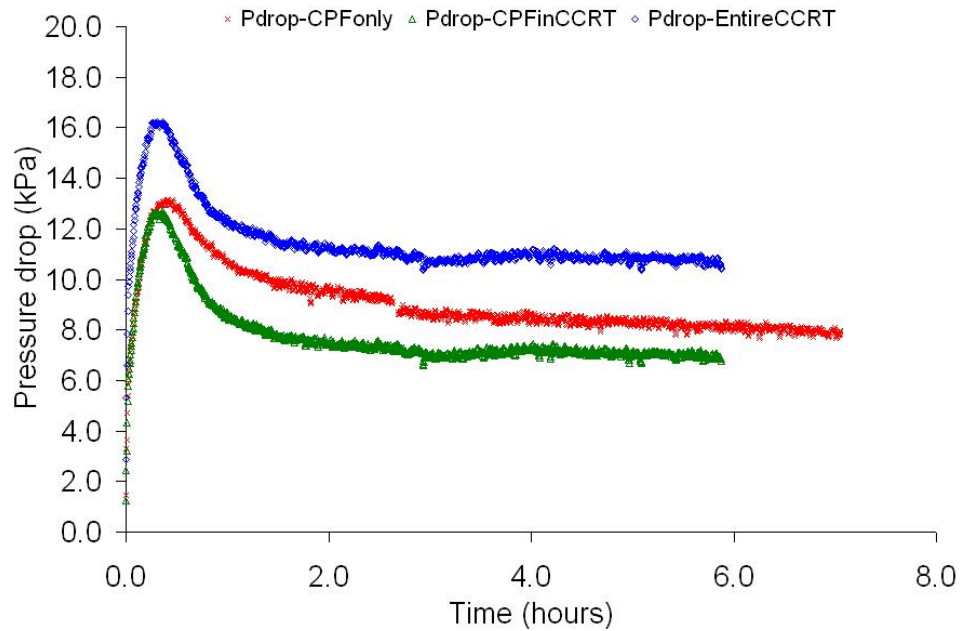Figure 5.5: Pressure drop across the CPF and entire CCRT® at 60% load

Figure 5.6: Pressure drop across the CPF and entire CCRT® at 75% load

is decreasing with time, 66 grams of particulate were retained in the filter. It is clear that 66 grams of particulate could not have entered the trap before the pressure drop started to decrease in the 40% CCRT® configuration. Hence, if the pressure drop started to decrease with the particulate mass in the filter increasing, then it can be concluded that the filter pressure drop is not a reliable indicator of the particulate mass in the filter. Hence control models for such devices need to take this behavior into account in their strategies for active regeneration. The 60% CCRT® pressure drop profile shows a rapidly decreasing pressure drop after the depth filtration phase and near complete oxidation of the particulate mass, with only 13 grams retained in 7.34 hours. The 60% CPF pressure drop profile, just like the 40% CCRT® pressure drop, shows a decreasing profile with time, while still having a relatively high particulate mass of 52 grams retained in the filter. Thus, the behavior of decreasing pressure drop with increasing particulate mass in the trap can occur at both high and low NO_2 concentrations (with and without the DOC).

The 75% CPF-only, 60% CCRT® and 75% CCRT® pressure drop profiles show a rapid and sudden decrease in pressure drop after an initial rise in pressure drop during the depth filtration phase. Such behavior can be attributed to oxidation of particulate inside the filter wall. Just as particulate deposition of a few grams inside the filter wall can significantly increase the pressure drop across the filter wall [7, 9, 34, 41], likewise particulate oxidation of a few grams inside the wall can cause the pressure drop to rapidly decrease. To verify if particulate oxidation in the wall can explain Figures 5.4 - 5.6, the wall oxidation model described in Section 3.3 was developed. It is interesting to note that the pressure drop characteristics of the CPFs used in references [9, 34] did not show particulate oxidation inside the filter wall even at exhaust temperatures of 460^oC, while the DPF in a CRT®, used in reference [7] showed characteristics of oxidation inside the filter wall. This suggests that particulate oxidation in the wall is due to NO_2 in the exhaust stream, which being a gaseous species has a greater 'reach'

to particulate deposited in the pores of the filter wall, compared with an immobile catalyst washcoat which is only present on the surface of the filter wall.

An interesting observation is that the pressure drop across the entire CCRT® is higher than across CPF-only at the 20 and 75% load conditions only. At 40 and 60% load conditions, the pressure drop across the entire CCRT® is actually lower than across CPF-only after 2.1 and 1.1 hours respectively. Thus, although the particulate oxidation rate in the CCRT® configuration is always higher than in CPF-only, it translates into a backpressure advantage to the engine only at the 40 and 60% load conditions. The reasons for the 20 and 75% load conditions to be in the same category together are very different though. At 20% load, the pressure drop profiles in CPF-only and CCRT® configuration are very similar so that the DOC causes additional backpressure with no *apparent* advantage in particulate oxidation rates due to increased NO_2 concentrations (Figure 5.3). At 75% load, the DOC causes additional backpressure with no *significant* advantage in particulate oxidation rates, because NO_2-assisted oxidation rates in the 75% CPF-only condition are already very high (Figure 5.6).

A summary of the CPM concentrations measured upstream of the DOC are shown in Figure 5.7. The CPM concentrations tended to decrease with load and is related to the engine fuel system characteristics and prevalent EGR rates. For all the measurements, the mean CPM values were different at the same load in CPF-only and CCRT® configurations, but were within the 95% confidence interval (mean $\pm$2S.D.), which makes the separate measurements indistinguishable. Because CPM concentrations are directly related to CPF inlet particulate mass flow rates, it is a good idea to use concentrations averaged across all measurements made at a particular load (load-averaged). Also shown in Figure 5.7 are the load-averaged CPM concentrations. Since air and fuel flow rates, A/F ratios and EGR rates at a particular load were very similar (Table 5.1), the engine-out particulate concentrations of the Cum-
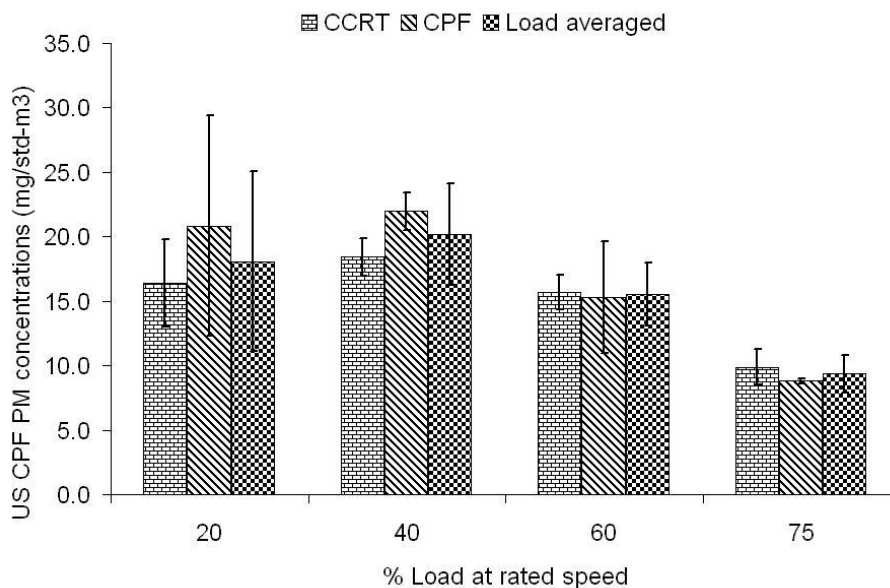
Figure 5.7: CPM concentrations measured during characterization experiments

mins ISM 2002 engine should have been very nearly the same. Using load-averaged
CPM values also has the advantage of decreasing the standard deviations by increas-
ing the number of measurements*. CPM measurements made downstream of the
CPF turned out to be negative in most cases and were taken to be zero. To increase
the chances of positive measurement by taking advantage of the fact that particulate
filters have lower filtration efficiencies when 'clean', exhaust sampling was begun im-
mediately after the exhaust flowed through the filter. However, these were negative
too. It turned out that 47mm fiber glass filters were losing mass due to exposure to
the high temperature environment of diesel exhaust. Further, the filter mass loss was
proportional to temperature, which meant that measurements at high loads would be
particularly skewed. These were the same kind of filters used previously by Huynh [34]
and Shende [9]; it is possible that they did not encounter this problem because the
100 cpsi filters these researchers experimented with could have had a lower filtration
efficiencies than the 200 cpsi filter used in this research. The experiments and results

---

*S.D^2=$\frac{1}{n-1}\sum_{i=1}^{n}(y_i - \overline{y})^2$, n is the number of measurements,y_i is the i$^t h$ measurement and $\overline{y}$ is
the sample mean

of the investigation to determine the characteristics of filter mass loss are described by Lakkireddy [46]. A result of this investigation was the recommendation that the 47mm filters be temperature-conditioned before use.

The gaseous emissions data measured during all of the CPF-only and CCRT® characterization experiments are shown in Tables 5.4 and 5.5 respectively. A comparison of HC and CO concentrations upstream and downstream of the DOC is shown in Figure 5.8. Downstream of the DOC, CO concentrations were too low to be measured by the Pierburg AMA 4000 emissions analyzer, and were taken to be 0 ppm, leading to apparent CO oxidation efficiencies of 100%. Even though engine-out CO concentrations were always higher than the HCs, CO concentrations were lower downstream of the DOC. This suggests that the catalyst in the DOC oxidizes CO more efficiently than it does HCs. Similar behavior of a DOC in a CRT® system was reported by Triana [6, 7]. The NO and NO_2 concentrations upstream and downstream of the DOC and the NO conversion efficiency are shown in Table 5.6 and Figure 5.9 respectively. Even though EGR is effective in reducing NO_X emissions particularly at low A/F ratios, NO_X concentrations in heavy duty engines increase with decreasing A/F ratios due to increasing combustion temperatures [65]. NO conversion *appears* to peak around 340°C (40% load) at 54%, although more data points are needed to determine the temperature where NO conversion is a maximum. The conversion decreases at temperatures greater than about 400°C due to thermodynamic NO/NO_X ratio limitations as discussed in Section 2.1. Even though the NO conversion efficiency decreases at high temperatures, the NO_2 concentrations leaving the DOC don't quite decrease in the same proportion due to the increase in engine-out NO concentrations with load, as seen in Figure 5.9. This is summarized in Table 5.6, and has important implications for passive regeneration especially in a CCRT® system where the NO_2 can be 'recycled' a number of times.

Table 5.4: Gaseous emission measurements in CPF-only configuration

% Load ↓	Location ↓	HCs (ppmC)	CO (ppm)	NO_X (ppm)	NO (ppm)	NO_2 (ppm)	CO_2 (% Vol.)	O_2 (% Vol.)
20, Mean (S.D)	US CPF	84 (1)	94 (2)	179 (2)	146 (2)	35 (3)	4.56 (0.08)	14.51 (0.11)
	DS CPF	4 (2)	0 (0)	177 (2)	106 (1)	71 (2)	4.52 (0.06)	14.56 (0.08)
40, Mean (S.D)	US CPF	68 (2)	163 (4)	205 (3)	183 (3)	22 (3)	5.82 (0.06)	12.7 (0.07)
	DS CPF	8 (2)	0 (0)	203 (3)	108 (7)	96 (10)	5.71 (0.05)	12.8 (0.08)
60, Mean (S.D)	US CPF	66 (2)	148 (3)	283 (3)	257 (1)	24 (3)	6.98 (0.05)	11.0 (0.07)
	DS CPF	6 (2)	0 (0)	275 (3)	164 (3)	111 (5)	6.83 (0.06)	11.1 (0.08)
75, Mean (S.D)	US CPF	53 (2)	130 (3)	312 (4)	299 (4)	13 (5)	7.81 (0.04)	10.0 (0.08)
	DS CPF	4 (1)	0 (0)	305 (3)	214 (4)	90 (4)	7.68 (0.06)	10.1 (0.10)

Table 5.5: Gaseous emission measurements in CCRT® configuration

% Load ↓	Location ↓	HCs (ppmC)	CO (ppm)	NO_X (ppm)	NO (ppm)	NO_2 (ppm)	CO_2 (% Vol.)	O_2 (% Vol.)
20, Mean (S.D)	US DOC	75 (3)	185 (2)	182 (3)	146 (4)	36 (3)	4.57 (0.06)	14.4 (0.13)
	DS DOC	17 (2)	0 (0)	182 (3)	77 (1)	105 (2)	4.60 (0.07)	14.3 (0.14)
	DS CPF	7 (1)	0 (0)	181 (3)	68 (3)	113 (2)	4.60 (0.06)	14.3 (0.15)
40, Mean (S.D)	US DOC	67 (4)	160 (3)	229 (3)	200 (2)	29 (3)	5.77 (0.03)	12.9 (0.05)
	DS DOC	15 (3)	0 (0)	227 (3)	92 (2)	136 (3)	5.78 (0.04)	12.8 (0.06)
	DS CPF	6 (1)	0 (0)	229 (4)	97 (3)	132 (3)	5.73 (0.04)	12.9 (0.06)
60, Mean (S.D)	US DOC	61 (2)	151 (3)	259 (4)	239 (6)	21 (5)	7.11 (0.06)	11.0 (0.07)
	DS DOC	10 (2)	0 (0)	257 (4)	154 (4)	103 (4)	7.12 (0.04)	11.0 (0.05)
	DS CPF	5 (1)	0	255 (3)	141 (2)	113 (4)	7.03 (0.05)	11.1 (0.07)
75, Mean (S.D)	US DOC	56 (6)	145 (3)	281 (7)	264 (4)	17 (6)	7.91 (0.08)	9.78 (0.14)
	DS DOC	11 (4)	0 (0)	279 (10)	216 (4)	63 (10)	7.93 (0.07)	9.69 (0.13)
	DS CPF	9 (3)	0 (0)	273 (6)	187 (3)	86 (6)	7.81 (0.08)	9.74 (0.13)
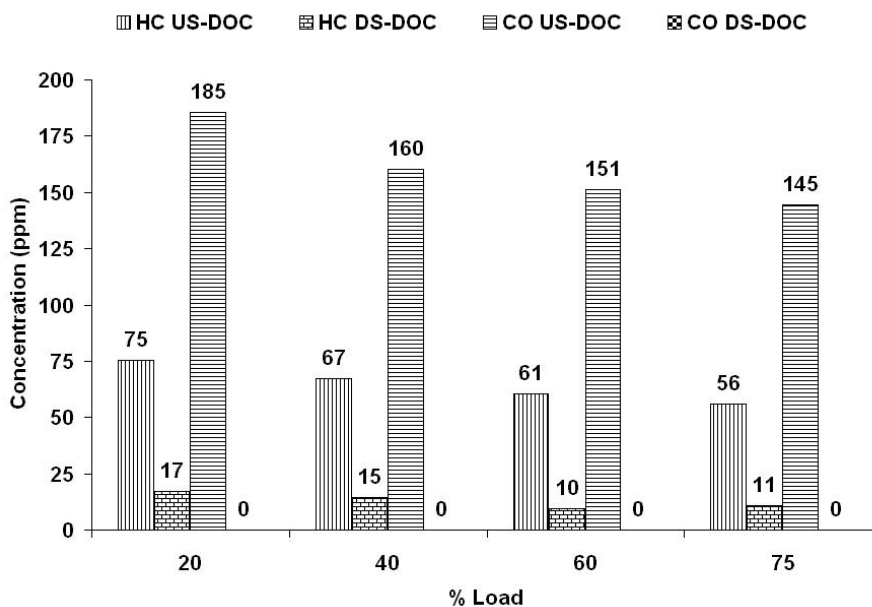
Figure 5.8: HC and CO concentrations upstream and downstream of the DOC

Table 5.6: NO conversion efficiency across the DOC

% Load	US DOC NO (ppm)	DS DOC NO (ppm)	NO conv. eff. (%)
20	146	77	48
40	200	92	54
60	239	154	35
75	264	216	18

A comparison of the HC,CO and NO oxidation efficiencies across the DOC, CPF and the entire CCRT® is shown in Figures 5.10, 5.11 and 5.12, respectively. The HC conversion efficiency appears to become constant after 415^oC (60%load), possibly due to mass transfer limitations, as discussed in section 2.1. Both the DOC and the CPF are very efficient in oxidizing CO (Figure 5.11) suggesting that the activation energy for CO oxidation is relatively low and/or that CO adsorbs onto the catalyst very well, indicating that many more active catalyst sites are available for CO than for the HC's. Figure 5.10 shows that the DOC is less efficient in oxidizing HCs at all 4 loads compared to the CPF.

The gaseous emissions measurement confirmed a design feature of the CCRT®
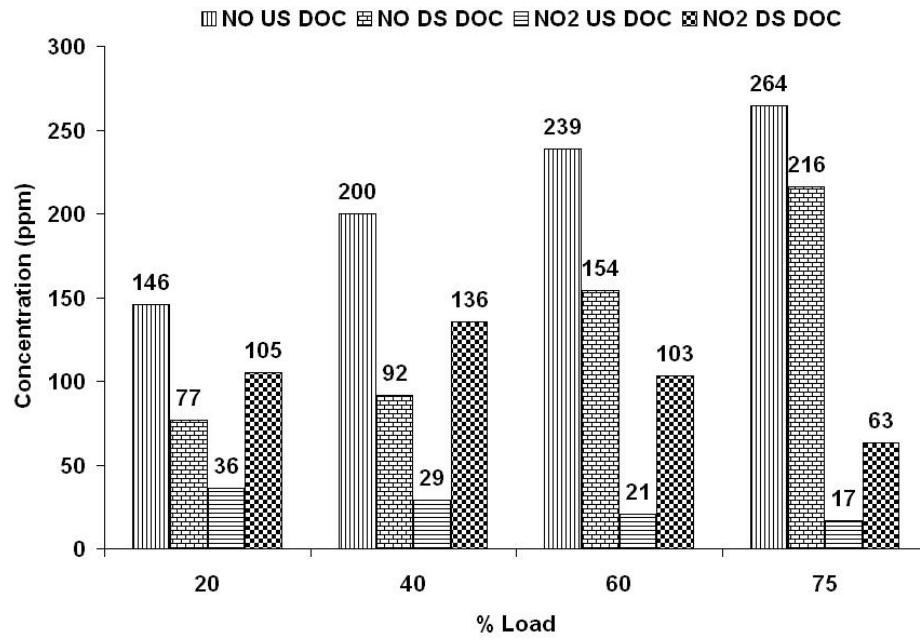
Figure 5.9: NO concentrations upstream and downstream of the DOC
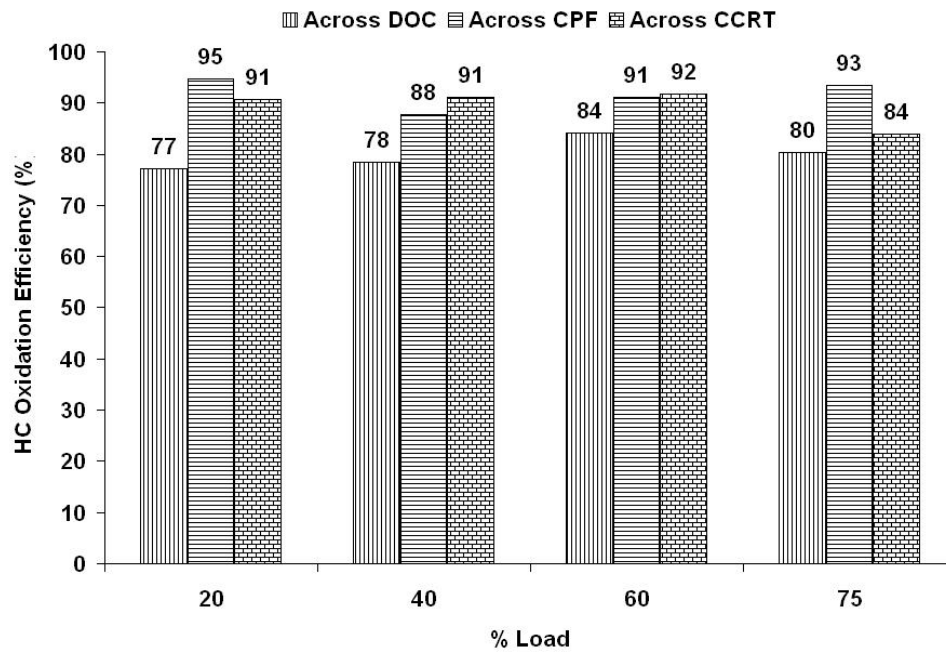
Figure 5.10: HC conversion efficiency across the DOC, CPF and CCRT®
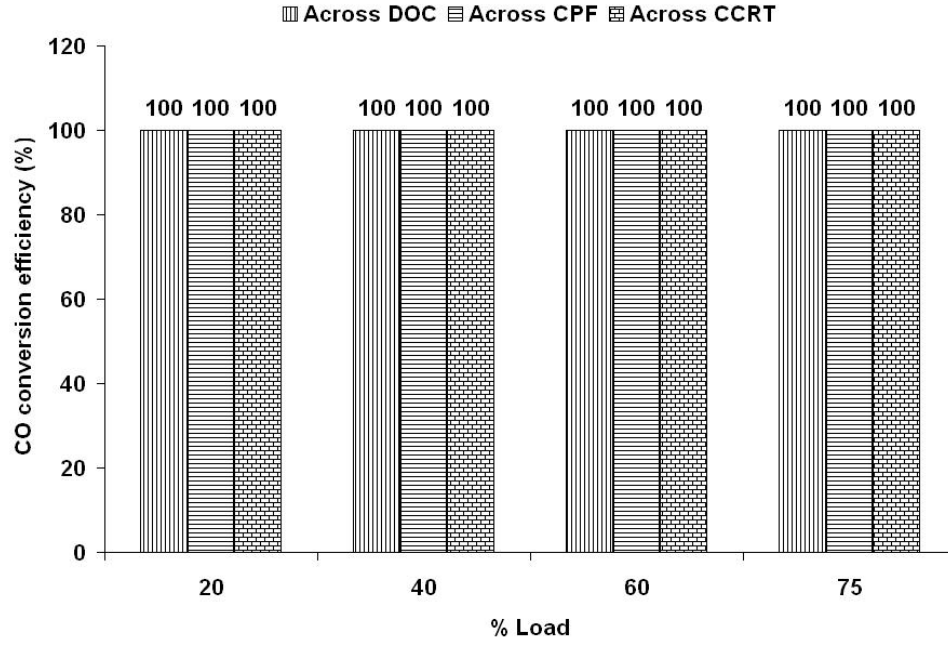
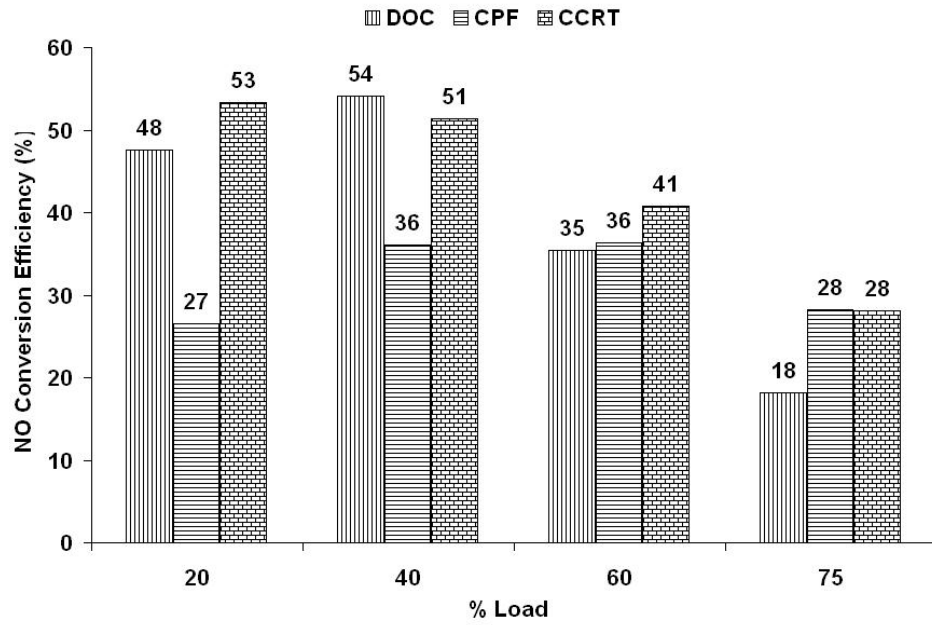Figure 5.11: CO conversion efficiency across the DOC, CPF and CCRT®

Figure 5.12: NO conversion efficiency across the DOC, CPF and CCRT®

i.e., oxidation of NO→NO_2 by the catalyst in the CPF. Table 5.7 summarizes the increase in NO_2 concentrations across the the CPF in both CPF-only and CCRT® configurations. The increase in NO_2 concentrations in the CCRT® configuration is not as large as in the CPF-only configuration because the NO_2/NO_X ratio exiting the DOC and entering the CPF is already close to equilibrium (Figures 2.3-2.5). An apparent decrease in concentrations is seen at the 40% CCRT® condition, but the small difference of 4 ppm practically indicates parity in consumption and production of NO_2 in the CPF. These data indicate that in CCRT® configuration, the production of NO_2 in the CPF is at least equal to NO_2 consumed due to particulate oxidation, while in CPF-only configuration, the production of NO_2 vastly exceeds NO_2 consumption in the filter.

Table 5.7: Increase in NO_2 concentrations across the CPF

	CCRT® configuration, Mean (S.D)		CPF-only configuration, Mean (S.D)	
% Load	US-CPF,	DS-CPF	US-CPF	DS-CPF
20	105 (2)	113 (2)	35 (3)	71 (2)
40	136 (3)	132 (3)	22 (3)	96 (10)
60	103 (4)	113 (4)	24 (3)	111 (5)
75	63 (10)	86 (6)	13 (5)	90 (4)

It is worthwhile to try and explain why the CPF is more efficient than the DOC in oxidizing HCs and in some conditions NO, even though the exhaust flows through the entire length of the catalyst coated DOC and only through the particulate covered catalyst washcoat in the CPF, which is typically only 10μm-30μm. One possible explanation is that as the exhaust flows through the micrometer sized pores of the catalyst washcoat in the CPF, the HCs, CO and NO molecules are in much closer contact with the catalyst than in a DOC where the molecules have to diffuse back and forth through the laminar boundary layer (section 2.1). For NO oxidation at low temperatures, contact time with the catalyst would matter most because the reaction is kinetically limited, however at high temperatures the reaction rate increases exponentially and better contact with the CPF catalyst washcoat (albeit for shorter time

period) might be sufficient to obtain higher conversion efficiencies. The other possibility is that the outlet channels of the CPF are also coated with the catalyst. Thus, at least a part of the HC, CO and NO oxidation by the CPF could take place in the outlet channels of the CPF. Keeping in mind that the samples of gaseous emissions were taken at various times during the loading phase, an important observation is that the gaseous oxidation activity remains the same irrespective of particulate mass in the filter. This means that many of the active catalyst sites participating in the oxidation of the gaseous emission species are apparently unaffected by the presence of the particulate matter. This suggests that the outlet channels of the CPF are indeed also coated with the catalyst. The 200 cpsi CPF would presumably be less efficient than the 400 cpsi DOC considering the larger channel width and decreased surface area, however the fact that the CPF is twice as long as the DOC could compensate for that (Table 4.3).

Particle size measurements made upstream of the DOC, downstream of the DOC and downstream of the CPF during the characterization experiments are shown in Figures 5.13 through 5.16. Particles with a mean diameter of 50 nm or less are called nuclei-mode particles while those greater than 50 nm and less than 1 μm are called accumulation-mode particles. The DOC was seen to have little effect on the particle number distribution as has been reported by [14], with particle numbers falling by less than 10% at all the conditions tested. The reduction in particle size numbers across the CPF in both nuclei and accumulation mode range was seen be about two orders of magnitude. The thermodenuder, which is used to remove the HCs and sulfates present as nuclei mode particles [34], could not be used since it was being repaired. The upstream CPF exhaust samples were sampled at a dilution ratio of 72.3 to lower the sample temperature and reduce the concentration of particles entering the SMPS instrument to near ambient. For consistency, the downstream CPF samples, though already reduced by almost two orders of magnitude due to filtration, were

also sampled at a dilution ratio of 72.3. Although particle formation depends on many factors such as dilution ratio, residence time, humidity, temperature etc., rapid dilution to a high dilution ratio tends to freeze particle formation due to homogeneous nucleation of nanoparticles [66, 67, 68, 72]. The use of catalyzed filters with modern engines with high injector pressures has raised concerns that, while particulate mass emissions can reduce, the number emissions actually increase. However, all particle size measurements downstream of the CPF showed that the distribution is unimodal, which can be attributed to the use of ULSF fuel. The highest particle concentrations, at all the loads, were particles of diameter 100nm (0.1μm), which is related to the mean aggregate size of diesel particles, as explained in the development of the cake filtration model in Section 3.4.
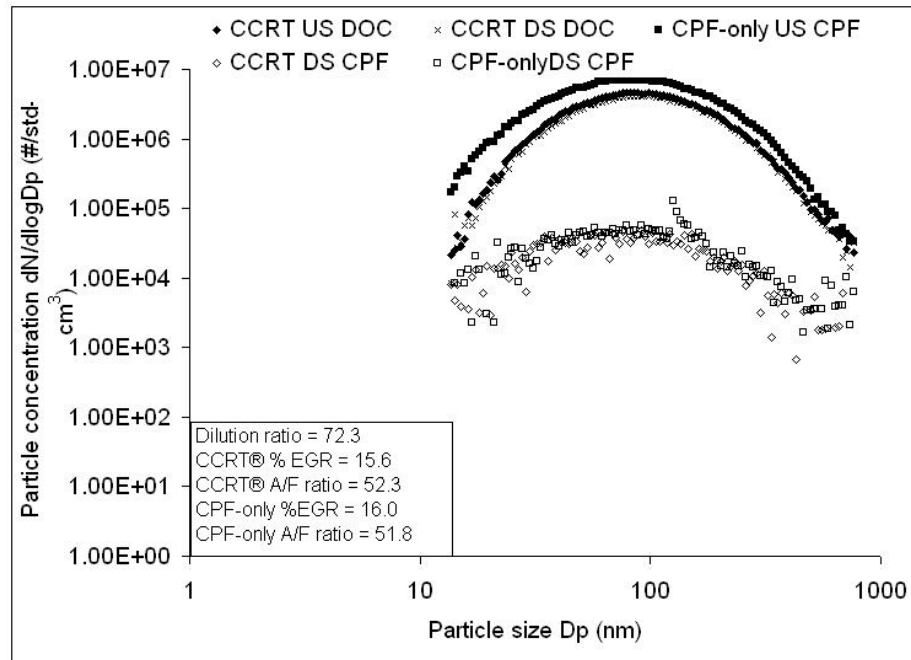
Figure 5.13: Raw particle size distribution during experiments at 20% load
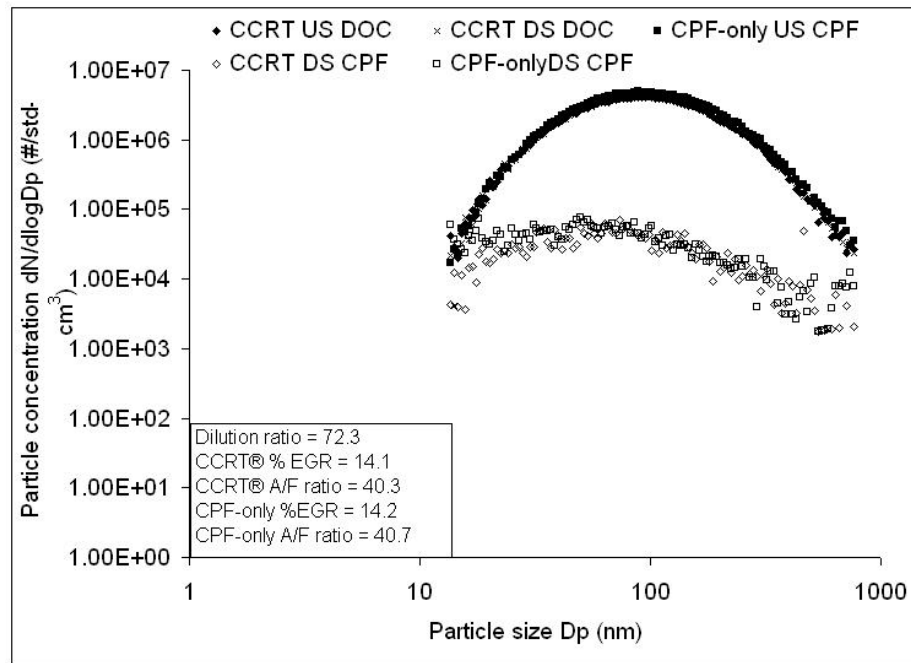
Figure 5.14: Raw particle size distribution during experiments at 40% load
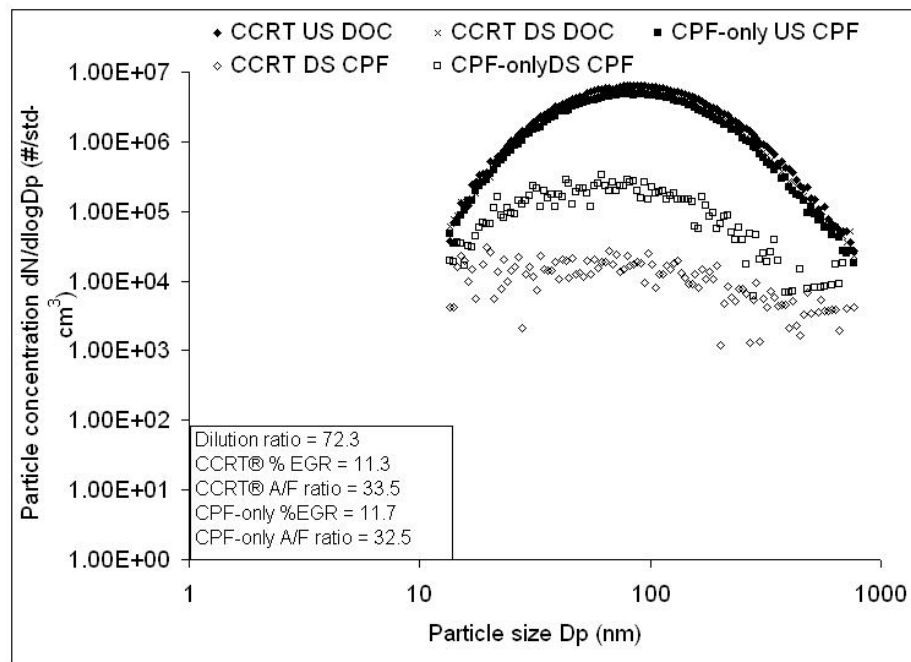
Figure 5.15: Raw particle size distribution during experiments at 60% load
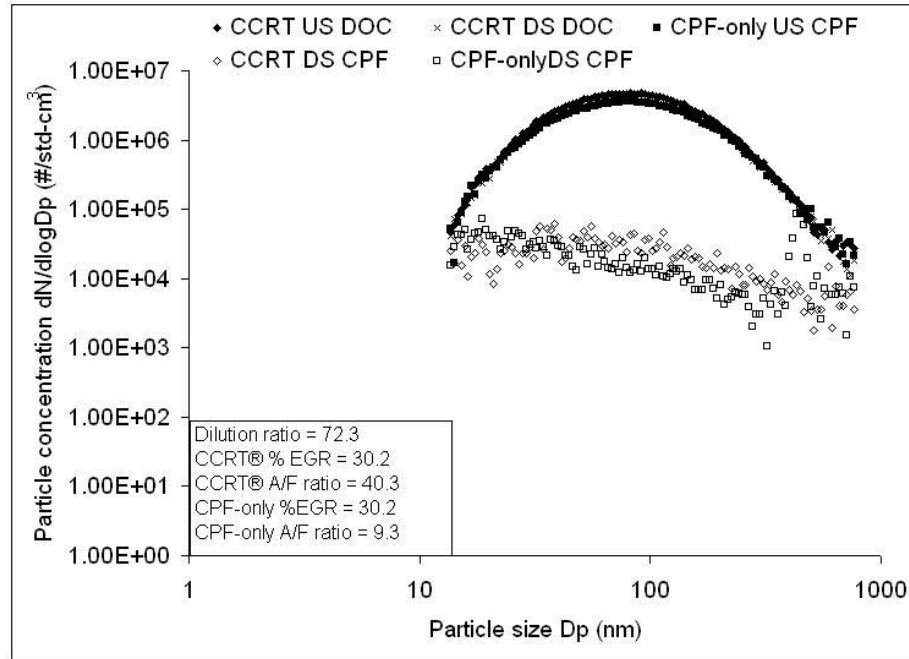
Figure 5.16: Raw particle size distribution during experiments at 75% load

5.2   DOC Modeling Results

In this section, results from the calibration of the DOC model are presented. The 20, 40, 60 and 75% load at rated speed (2100 rpm) data from the raw gaseous emission characterization experiments were used for the calibration of the model. In addition, data from a 25% load at rated speed experiment from the dilute emission characterization experiment of reference [46] were also used.

The DOC model kinetics can be calibrated by tuning the pre-exponential factors and activation energies for the oxidation of HCs, CO and NO. With the oxidation of the HCs, CO and NO (ppm levels) in the gas phase, there is a corresponding change in O_2, CO_2 and H_2O (%vol. levels) concentrations across the DOC, but these are two low to be measured and their depletion is not considered by the model. The DOC model can also be used to predict the drop in pressure of the exhaust as it flows through the DOC.

The data describing the input data to the DOC model are shown in Appendix

C. The DOC model takes the temperature, actual volumetric flow rate, pressure and concentrations of O_2, H_2O, CO_2, N_2, NO, NO_2, HCs, and CO entering the DOC as input. The concentrations of HCs, CO, NO and NO_2 and the pressure drop across the DOC are the model output data.

The results from the DOC pressure drop model are shown in Table 5.8. The model predicts the pressure drop within 0.5 kPa. The DOC pressure drop model calculates the pressure drop of the exhaust gas due to friction by laminar flow through the channels in the DOC (equation 3.4). However, this is only the major component of the total pressure loss across the DOC. This model does not include the losses due to inlet channel contraction and outlet channel expansion as the exhaust flows in and out of the DOC, losses in the DOC channels before the flow becomes laminar. This is the reason the DOC model always under predicts the pressure drop. Since these losses generally increase with exhaust flow rate, the error in prediction increases with load.

Table 5.8: DOC pressure drop model results

% Load	Model predicted (kPa)	Avg. expt. (kPa)	Difference (kPa)
20	1.5	1.8	0.3
40	2.0	2.3	0.3
60	2.7	3.1	0.4
75	3.3	3.8	0.5

The results of the gaseous emission oxidation calibration along with a comparison with the experimentally measured concentrations of HCs, NO, NO_2 and CO upstream and downstream of the DOC are shown in Table 5.9. All concentrations were predicted within 3 ppm of the experimentally measured values. Since CO concentrations downstream of the DOC were too low to be measured by the Pierburg emissions analyzer, the model was calibrated to predict CO concentrations within 1 ppm downstream of the DOC.

To calibrate the model kinetics, activation energies for oxidation of HCs, CO and

NO were adopted from the work of Triana [6, 7] which were also used previously by references [41, 51]. The activation temperatures and the pre-exponential factors used to calibrate the kinetics of the DOC model are shown in Table C.3 of Appendix C. The activation energies are assumed to be constant with exhaust temperature (load) and the pre-exponential factors were changed with load to calibrate the model kinetics.

Table 5.9: DOC model gaseous emission kinetics calibration results

% Load	Location	HC (ppmC)	NO (ppm)	NO$_2$ (ppm)	CO (ppm)
20	US DOC (Expt.)	75	146	36	185
	DS DOC (Expt.)	17	77	105	0
	DS DOC (Model)	17	75	107	0.2
25	US DOC (Expt.)	81	161	39	177
	DS DOC (Expt.)	18	77	122	0
	DS DOC (Model)	17	77	123	0.3
40	US DOC (Expt.)	67	200	29	160
	DS DOC (Expt.)	15	92	136	0
	DS DOC (Model)	16	91	138	0.3
60	US DOC (Expt.)	61	239	21	151
	DS DOC (Expt.)	10	154	103	0
	DS DOC (Model)	10	155	105	0.2
75	US DOC (Expt.)	56	264	17	145
	DS DOC (Expt.)	11	194	83	0
	DS DOC (Model)	10	199	82	0.3

To unify the model kinetics, so that one apparent activation energy and pre-exponential factor can be used for each gaseous emission species, Arrhenius plots are used. The mathematical basis of the construction of Arrhenius plots is given in Appendix B. The activation temperatures and pre-exponential factors shown in Table C.3 are used to calculate the model reaction rates and then plotted versus the inverse of the absolute DOC channel wall temperature shown in Table C.1. A linear regression fit for each species then yields an 'apparent' activation energy and pre-exponential factor for that species. These apparent kinetics are different from real parameters because of the influence of diffusion and mass transfer effects of this DOC on the apparent kinetics determined from Arrhenius plots. The results from

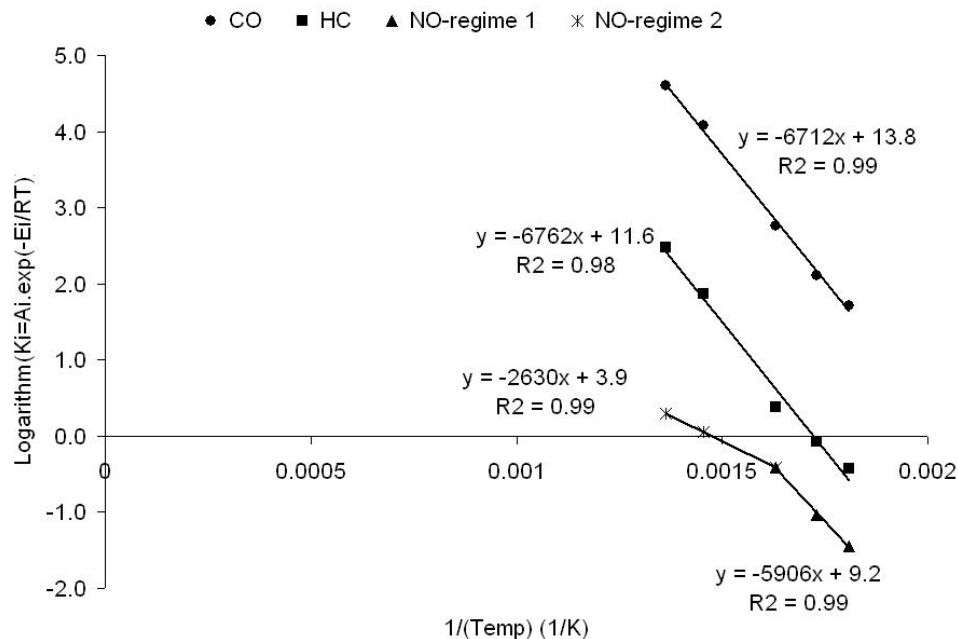such an analysis is shown in Figure 5.17. The HCs, CO and NO kinetics were fit

Figure 5.17: Arrhenius plots of HCs, CO and NO kinetic data for the DOC

with an R^2 value of 0.99. For the entire temperature range of 280^oC-460^oC, the HCs and CO kinetics can be described by one apparent activation energy and pre-exponential factor, while the NO kinetics are best described by apparent activation energies and pre-exponential factors in two regimes as shown in Figure 5.17. The two regimes in the NO calibration result could possibly be the result of the transition from kinetically limited oxidation at low temperatures to thermodynamically limited oxidation at high temperatures (section 2.1). The fact that the the two regimes separate at a temperature of about 350^oC lends credence to this interpretation. Such behavior of best fits in different temperature and flow rate windows was also reported by Triana [6, 7] in the calibration of a DOC in a CRT®. A comparison of the gaseous emission oxidation kinetics of the DOC used in this research with that used by Triana [6, 7] in a CRT® is given in Appendix D.

A summary of the 'apparent kinetic' parameters is shown in Table 5.10. The apparent kinetic parameters determined from the DOC model, shown in Figure 5.17

and Table 5.10, can be used to predict the HC, CO and NO emissions downstream of this DOC. These parameters do not change in the temperature range of 280^oC-460^oC and flow rate range of 0.44-0.85 act-m^3/sec.

Table 5.10: Summary of reported and apparent DOC kinetic parameters

Parameter	Units	HC	CO	NO$_{regime1}$*	NO$_{regime2}$†
Act. temp. – reported	K	14556	12556	10900	10900
Act. temp. – apparent	K	6762	6712	2630	5906
Pre-exp. factor–apparent	(mol-K/cm^2-s)	1.09E+05	9.85E+05	4.94E+01	9.90E+03

5.3 CPF Modeling Results

In this section, the results of using the 1-D CPF model described in Chapter 3 are presented. The approach to calibrate the model and determine the model parameters is described. The detailed model results at 20 and 75% load in CPF-only and CCRT® configurations are presented with a comparison to the experimental data. The detailed model results at 40 and 60% load and associated figures are shown in Appendix G. A comparison of the pressure drop, particulate mass retained and the downstream CPF particle size distribution with the experimental data is provided. A discussion of the CPF modeling results is also given.

5.3.1 Calibration and Determination of Constants in Model

Table 5.11 shows the parameters defining the state of the exhaust gas, flow rate and gaseous species concentrations as input to the CPF model. For the 'clean' pressure drop calculation, the atmospheric pressure was assumed to be 101.3 kPa‡. For all model calculations, the time varying pressure drop upstream of the CPF was used

---

†Regime 1: 340^oC-460^oC

†Regime 2: 280^oC-340^oC

‡The atmospheric pressure in the test cell was not measured during all the experiments. Hence, it was assumed to be equal to 101.3 kPa

to calculate the volumetric flow rate and physical properties of the exhaust gas. The equation used was

$$V_{act} = m\overline{R}T_{act}/(P_{ref} + \Delta P)$$

where, m is the sum of the air and fuel flow rates and P_{ref} is the pressure downstream of the exhaust and equal to 100.3 kPa (101.3 - 4" H_2O*). This detail was not considered by previous MTU researchers [7, 9, 34], but it is important to implement this as reference [60] points out that incorrect model parameters can be obtained if the actual upstream CPF pressure is not used in the model. This is because the higher pressure upstream of the CPF increases the density of the exhaust gas. As mentioned earlier, CPM concentrations used were the load-averaged concentrations in Figure 5.7. However, to ensure that the total CPM inlet to the filter was greater than the PM mass retained in the filter at the end of the experiment, the mean±2S.D. of the load-averaged CPM concentrations in Figure 5.7 was sometimes used. The sum of mole fractions of N_2, O_2, H_2O and CO_2 for each of the conditions add up to 1.0 in Table 5.11. Thermodynamic properties of these species were used to calculate the properties of the exhaust gas, while properties of HCs, NO and NO_2 were not considered as their concentration levels were typically in ppm (as compared to %Vol.). The concentrations of O_2, NO_2 are input as the oxidant species in the exhaust gas, while the concentrations of NO are also required in this 1-D CPF model to compute the production of NO_2 in the catalyst washcoat of the filter (Section 3.5).

---

*Downstream of the CPF, a suction of 4" H_2O is maintained

Table 5.11: Exhaust gas parameters input to the CPF model as a function of % load at rated speed

Parameter ↓	Units	Input in CCRT® configuration				Input in CPF-only configuration			
		20	40	60	75	20	40	60	75
Temperature	^oC	287	340	416	460	287	340	416	466
Exhaust flowrate*	std-m^3/sec	0.241	0.279	0.313	0.341	0.245	0.279	0.313	0.341
CPF inlet PM conc.†	mg/std-m^3	16.4	20.2	15.5	10.8	17.9	23.5	14.0	10.8
y_{O_2}	%vol.	13.48	11.94	10.09	8.85	13.67	11.89	10.10	9.10
y_{NO_2}	ppm	105	136	103	83	33	22	25	13
y_{NO}	ppm	77	92	154	194	146	183	257	299
y_{CO_2}	%vol.	4.32	5.38	6.53	7.23	4.30	5.42	6.43	7.14
y_{H_2O}	%vol.	5.85	6.89	8.04	8.84	5.83	6.94	7.93	8.65
y_{N_2}	%vol.	76.35	75.79	75.34	75.18	76.20	75.75	75.54	75.11

†Assumed standard pressure and temperature of 101.3 kPa and 25^oC respectively.

To determine the clean wall permeability of the CPF, accurate measurements of the 'clean' pressure drop, CPF-inlet temperature and volumetric flow rate of the exhaust are needed. An assumption is that the filter is clean and free of particulate and ash at the beginning of the experiment. 'Clean' pressure drop data obtained during the experiments suggested that the filter baking procedure might have been incomplete, which meant that the filter permeability was not always the same at the start of the experiments. The basis for this conclusion, and its influence on the determination of the clean filter permeability is described in Appendix E. Hence, model calibration was done so that all 'clean' pressure drops were predicted within ± 0.2 kPa of the experimentally determined value, using one value of the clean filter wall permeability. The variation assumed in the 'clean' pressure drop, ± 0.2 kPa, is low enough to be a source of experimental error and is not expected to skew the filter wall permeability calibration. Using this approach, a 'clean' filter permeability of 2.00E-13 m^2 was determined and agrees well with the findings of references [7, 9, 34, 41] for filters of cordierite. This value is the effective filter wall permeability, which is an intensive property of the cordierite filter wall coated with the catalyst.

A comparison of the model predicted and experimentally measured 'clean' CPF pressure drop is shown in Table 5.12. The 60% load CCRT® clean pressure drop was predicted with an error of -0.8 kPa, because the CPF inlet temperature could not be be ascertained due to a thermocouple error. The values of the 'clean' pressure drops in Table 5.12 were calculated using CPF-inlet exhaust temperatures a few seconds after the exhaust was diverted from baseline to trapline. These values are lower than their steady state values due to heat transfer. With the clean filter wall permeability known, the model was used to predict the 'clean' pressure drop across the CPF, for the exhaust temperature at CPF inlet being equal to the steady state exhaust temperature and and the temperature of the CPF filter walls equal to 25°C. These results are shown in Table 5.13. The slight difference in the ΔP values in CPF-

only and CCRT® configurations is due to a difference in steady state CPF-inlet temperatures.

Table 5.12: Model predicted and experimental 'clean' pressure drops

	CPF-only configuration (kPa)				CCRT® configuration (kPa)			
% Load	Expt.	Model	Diff.	% Error	Expt.	Model	Diff.	% Error
20	0.79	0.87	0.08	10.1	1.13	1.02	-0.11	-9.7
40	1.30	1.10	-0.20	-15.4	1.15	1.04	-0.11	-9.6
60	1.35	1.14	-0.21	-15.6	2.50	1.70	-0.80	-32.0
75	1.24	1.36	0.12	9.7	1.46	1.65	0.19	13.0

Table 5.13: Model predicted 'clean' CPF pressure drop at steady state CPF-inlet temperature

% Load	$\text{Temp}_{CPF-only}$ (^oC)	$\Delta P_{CPF-only}$ (kPa)	Temp_{CCRT} (^oC)	ΔP_{CCRT} (kPa)
20	287	1.87	285	1.84
40	340	2.39	340	2.39
60	416	3.14	416	3.14
75	466	3.83	460	3.79

The experimental data shows that the pressure drop rises very rapidly from 'clean' pressure drop values of about 1.0 kPa, between the exhaust flow rates of $0.447 - 0.843$ act-m^3/s, to values in the deep bed filtration of greater than 8 kPa (Figures 5.3 and 5.6). From the experimental data, it was concluded that a part of this large pressure rise can be attributed to a transient increase in temperature of the exhaust at the CPF inlet, which happens because the exhaust trap line takes time to be heated up to the exhaust temperature. The basis for this conclusion and supporting data are shown in Appendix E. The model was therefore calibrated in a transient mode, with a variable CPF-inlet temperature taken from the LabVIEW data acquisition system.

After determining the value of the filter wall permeability, the entire 1-D CPF model was calibrated to obtain agreement with the experimental data. The kinetics of particulate oxidation by NO_2 were not determined from the experimental data, but rather from the calibration of a transient temperature programmed oxidation (TPO) reactor study of reference [21]. The reason for this approach is that significant

NO_2 production occurs in the CPF (Table 5.7), in both CPF-only and CCRT® configurations, which meant that the particulate is oxidized by the NO_2 entering the filter and by the NO_2 being produced in the filter. Since both these mechanisms are active in both configurations, their independent effects cannot be separated without knowing the effect of either one *a priori*. A description and results of the calibration of the TPO results of reference [21] are shown in Appendix F. Oxidation due to PM oxidation by O_2 was assumed to be thermal, and the relevant kinetic parameters were adopted from the work of Triana [7], who used a similar kinetic scheme for direct oxidation of PM by O_2. Any further oxidation needed to make the model agree with experimental results was attributed to NO_2 production by the catalyst in the CPF, with the limitation that model predicted CPF-outlet NO_2 concentrations do not exceed the experimentally measured concentrations. If any oxidation activity, in addition to thermal, CPF-inlet NO_2 and NO_2 produced in the CPF, was required to make the model and experimental results agree, then it was assigned to an O_2 based 'catalytic' reaction with particulate.

The kinetic parameters of the 1-D model for the particulate cake layer oxidation are shown in Table 5.14. The particulate cake layer is the dominant physical location of particulate oxidation, and these kinetic parameters did not change with load or with CPF-only and CCRT® configurations, where the CPF-inlet NO_2 concentrations are very different due to the presence of the DOC. The kinetic parameters of the 1-D model for the particulate oxidation in the filter wall, and the NO_2 production factor in the CPF are shown in Table 5.15. The NO_2 production factor varied with load and configuration, because the NO_2 production model used is a general kinetic expression, which means that the pre-exponential factor can vary with exhaust conditions (Section 3.5). The temperature order, n, for the NO_2 production (equation 3.86) was taken to be equal to 3 to reduce the order of magnitude of the pre-exponential factor. The kinetic parameters for oxidation in the wall increased with load and NO_2

concentrations, indicating increased activity in the wall with temperature and NO_2 concentrations (Table 5.15). Arrhenius plots of the kinetic parameters in the wall showed that the oxidation kinetics can be represented by a single set of parameters. The procedure of deriving these parameters is described in Appendix H, and the result is shown in Table 5.16. The derived model parameters represent oxidation kinetics by a simple Arrhenius equation, as opposed to modified Arrhenius forms used earlier.

Table 5.14: Kinetic parameters for particulate oxidation by NO_2

Oxidation Mechanism	Act. Energy (J/kmole)	Temp. Order	Pre-exp factor
Thermal Oxidation	1.497E+08	1.0	1.0 (m/s-K)
NO_2 oxidation	0.73E+08	0.5	1.0 (m/s-$K^{0.5}$)

Table 5.15: Kinetic parameters for oxidation in the wall and the NO_2 production factors

	Wall NO_2 pre-exp. factor (m/s-$K^{0.5}$)		CPF NO_2 production factor (1/s-K^3)	
% Load	CPF-only	CCRT®	CPF-only	CCRT®
20	1.0	0.2	40000	28000
40	0.1	0.15	3000	3500
60	0.12	0.38	400	750
75	0.30	0.55	145	175

Table 5.16: Apparent NO_2 kinetics in the wall

Configuration	Activation Energy (J/kmole)	Pre-exponential factor (m/s)
CCRT® – all loads	1.02E+08	1603.6
CPF-only – all loads	0.93E+08	184.9

It should be realized that a difference between the model predicted and experimentally measured particulate mass retained in the CPF at the end of the experiment, can arise due to two reasons: first, the error in measuring the weight of the CPF by the balance, and secondly, the more important effect of imprecise measurements of CPF-inlet CPM concentrations entering the filter. Since the total particulate mass entering the filter is the $CPM_{conc.}$*$\dot{V}_{exhaust}$*$Time_{expt}$, with $Time_{expt}$ usually between

5-8 hours*3600 seconds, a small error in measurement of C_{in} can multiply to a large difference in total mass inlet and thus affect the mass retained/oxidized calculation. To reduce the variability in CPM concentrations from affecting the model parameters, the model predicted and experimentally measured PM mass retained in the filter were fit to within ± 5 grams. Using this approach, the CPF model kinetics were calibrated (Tables 5.14 and 5.15) without resorting to the use of a 'catalytically' aided PM oxidation with O_2 as used by references [9, 32, 33, 34].

The packing density of the particulate cake layer, (ρ_p), was determined from the Peclet number correlation of reference [53], which is shown in Figure 5.18. The values for ρ_p determined from Figure 5.18 are shown in Table 5.17. Since this model assumes that ρ_p is independent of oxidation activity, these values were the same in CPF-only and CCRT® configurations, and only varied with load.

Table 5.17: Packing density of the particulate cake layer, ρ_{soot}, with load [53]

	NO$_2$ pre-exp. factor for wall (m/s-K$^{0.5}$)		NO$_2$ production factor in CPF (1/s-K^3)	
% Load	CPF-only	CCRT®	CPF-only	CCRT®
20	0.1	0.16	40000	28000
40	0.13	0.18	3000	3500
60	0.14	0.42	400	750
75	0.30	0.55	145	175

The remaining parameters determined from the calibration of the model are: PM cake porosity (ϵ_{cake}), PM cake permeability (k_{soot}), packing density of particulate in the filter wall (ρ_{pw}), packing density of the particulate cake (ρ_p), mean pore size of the filter wall (d_{pore}), PM cake collector diameter $(d_{coll,cake})$ and the thickness of layer I. The sequence in the determination of model constants and model calibration was as follows:

- Determine clean filter wall permeability, k_0, using clean pressure drop measurements so that the 'clean' pressure drops at all the loads can be predicted with one value of filter permeability.
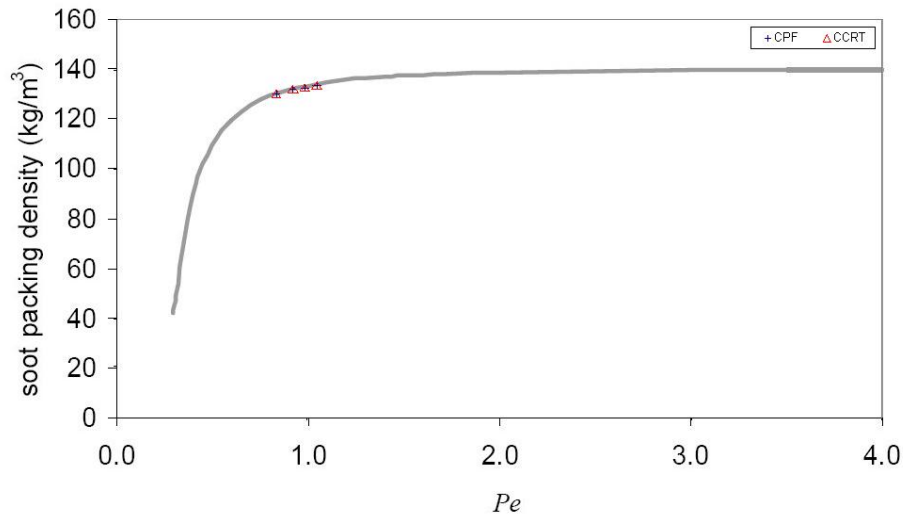
Figure 5.18: Particulate cake layer packing density with Peclet number [53]

- Adjust ρ_{pw} and ϵ_{cake} to make the model predicted and experimental depth filtration phase pressure drops agree.

- Determine the NO_2 and O_2 kinetic parameters for the particulate cake layer from model calibration of other studies (Appendix F).

- If significant wall oxidation is present, adjust the NO_2 pre-exponential factor in the wall, in addition to ρ_{pw} and ϵ_{cake}, in the depth filtration phase to get agreement between the model predicted and experimental pressure drops. If significant wall oxidation is not present, use the NO_2 pre-exponential factor to adjust the entire model predicted pressure drop curve.

- Adjust the NO_2 production factor in the CPF to get agreement with the experimentally determined particulate mass remaining in the filter at the end of the experiment. This should be done with the limitation that model predicted CPF-outlet NO_2 concentrations do not exceed the experimentally measured concentrations.

- Determine the values of packing density of the particulate cake (ρ_p) for each

load from the Peclet number correlation of reference [53], which is also shown in Figure 5.18.

- With ρ_p known, adjust the permeability of the particulate cake, k_{soot}, to adjust the model predicted pressure drop in the particulate cake filtration regime.

- If experimentally measured PM concentrations downstream of the CPF are unavailable, adjust the mean pore size of the filter wall to make the downstream particle size distributions agree.

Table 5.18: Experimental and model predicted NO_2 concentrations downstream of the CPF

Configuration →	CPF -only (ppm)		CCRT® (ppm)	
% Load↓	Expt. (Mean±2S.D.)	Model	Expt. (Mean±2S.D.)	Model
20	74±4	74	113±4	116
40	96±20	45	132±6	130
60	111±10	52	113±8	122
75	90±8	52	86±12	99

The values of these parameters are shown in Table 5.19. The model calibration was performed with an objective of varying as few parameters as possible with loads, and also with CPF-only and CCRT® configurations at a particular load. By permitting some difference between model predicted and experimental results, less variation in parameters like the packing density in the wall, particulate cake porosity (compared to percolation), particulate cake layer packing density and model kinetics was seen. Table 5.19 has two parts, the top segment has two parameters which varied at every load and the bottom segment has parameters which were either constant, or variable but known before the calibration. The experimentally measured and model predicted NO_2 concentrations downstream of the CPF are shown in Table 5.18. The experimental values shown are the 95% confidence interval given by the mean±2.S.D, taken from Tables 5.4 and 5.5 respectively.

Table 5.19: Filtration and particulate cake layer parameters from CPF model calibration as a function of % load

Parameter	Units	20%		40%		60%		75%	
		CPF-only	CCRT®	CPF-only	CCRT®	CPF-only	CCRT®	CPF-only	CCRT®
ϵ_{cake}	-	0.841	0.838	0.834	0.837	0.828	0.828	0.810	0.814
k_{soot}	m^2	0.50e-14	0.42e-14	0.43e-14	2.00e-14	1.15e-14	1.80e-14	1.02e-14	0.91e-14
ρ_{pw}	kg/m^3	3.95	3.95	3.51	3.48	3.30	3.28	3.07	2.92
ρ_p	kg/m^3	131	131	133	133	133	133	134	134
d_{pore}	μm	11.0	11.0	11.0	11.0	11.0	11.0	11.0	11.0
$d_{coll,cake}$	μm	0.1	0.1	0.1	0.1	0.1	0.1	0.1	0.1
Layer I	μm	20	20	20	20	20	20	20	20

5.3.2 Modeling Results

Figures 5.19, 5.20, and 5.22 show the experimental and model predicted pressure drops at 20 and 75% load in CPF-only and CCRT®, configurations respectively. The model results at 40% and 60% load at rated speed are shown in Appendix G. The deviation of the model from the experimental measured pressure drop, in the particulate cake layer regime, are shown in Figures 5.21 and 5.23 for the 20 and 75% loads, respectively. Good agreement of the model with the experimental data, with a maximum deviation of about 0.5 kPa can be seen. A comparison was not made in the depth filtration phase because further model development for that regime is needed, as explained later. A good fit between the experimental and model predicted pressure drops can be seen for the 75% CPF-only and CCRT® configurations, which have significant PM oxidation inside the filter wall, lending support to the wall oxidation model described in Chapter 3. For the 20% load curves, allowing some overshoot during the depth filtration phase made it possible to fit the particulate cake filtration regime. The pressure drop at 20% load, before the onset of the particulate cake filtration regime, was more 'rounded' compared to the pressure drop profiles of [7, 9, 34]. Better fits in this region can be obtained with an equation which allows a more gradual and 'rounded' profile to the filter wall permeability with particulate deposition (equation 3.23). It is also possible that a more complex model for wall oxidation than the one devised in Chapter 3 will be needed better predict the pressure drop in this region.
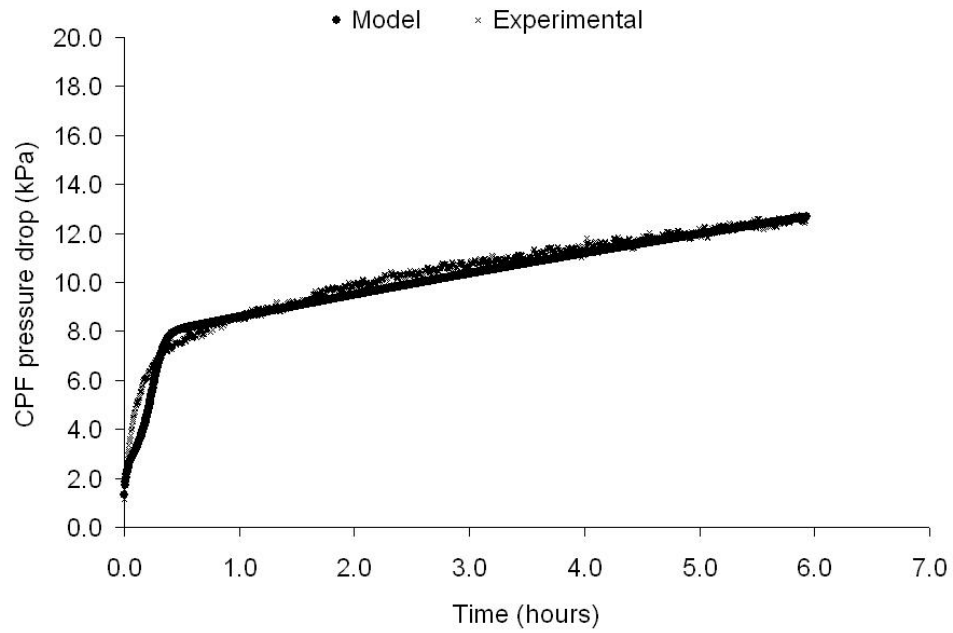
Figure 5.19: 20% CPF-only pressure drop: experimental and model results
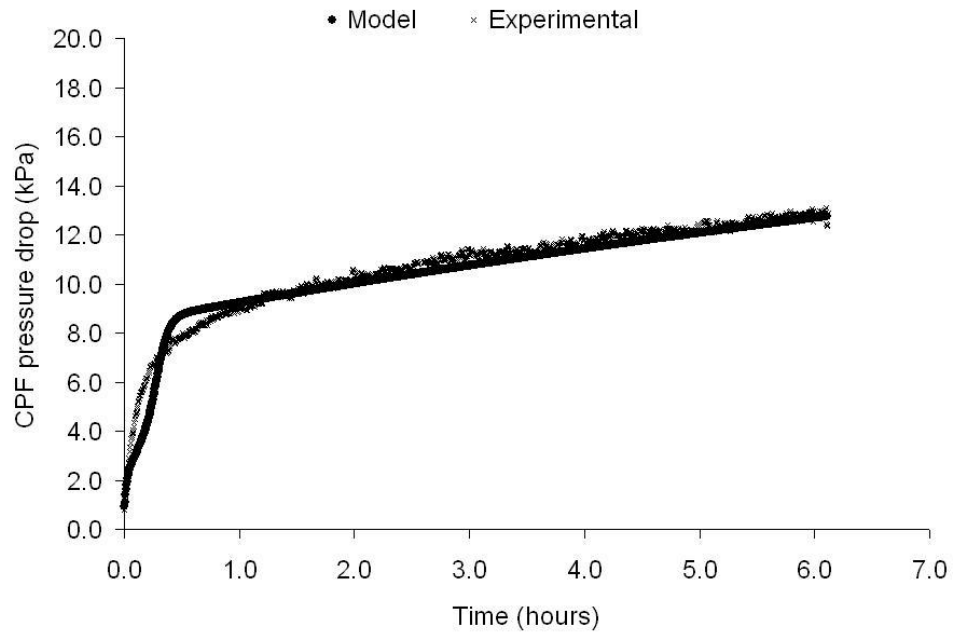
Figure 5.20: 20% CCRT® pressure drop: experimental and model results
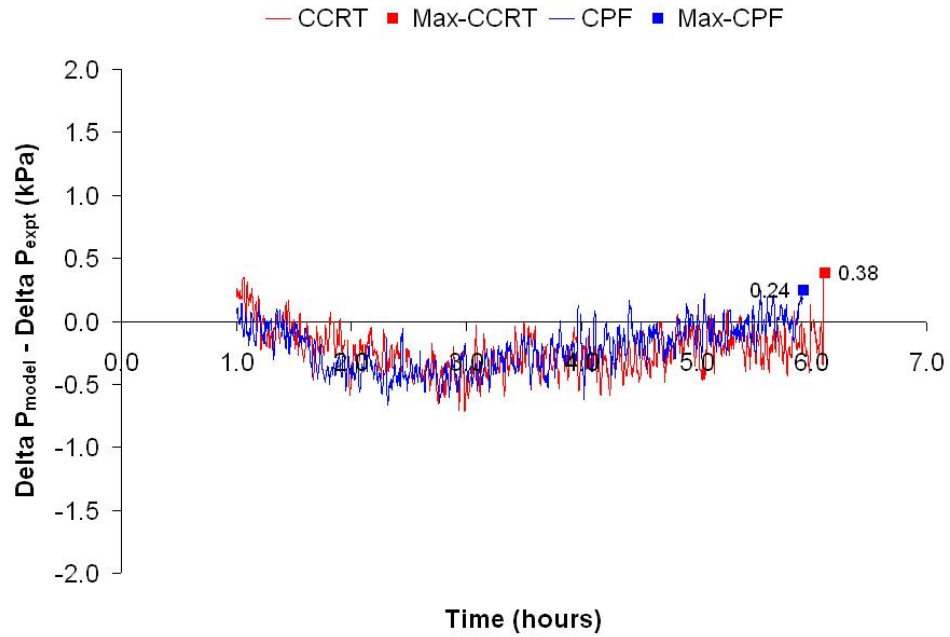
Figure 5.21: 20% load: Deviation of the model from the experimental measured pressure drop
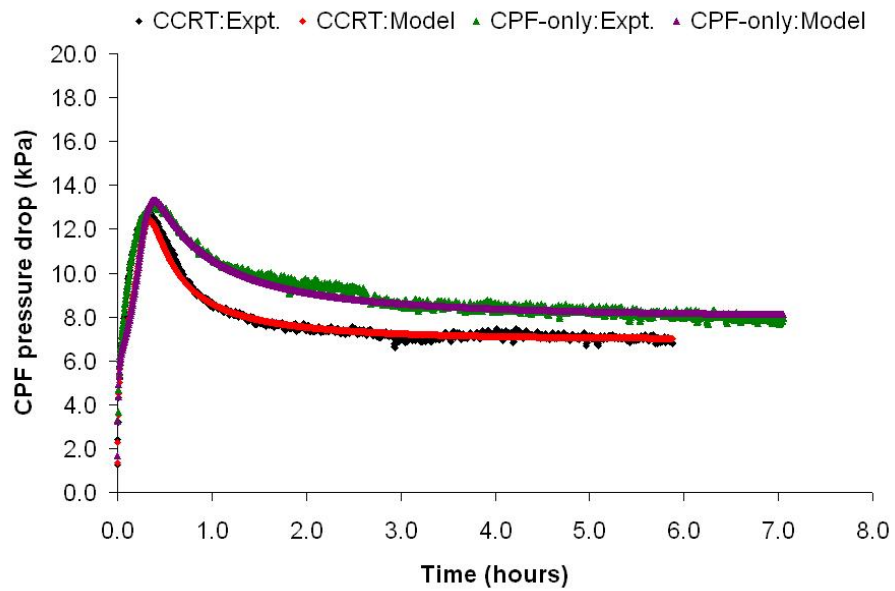
Figure 5.22: 75% load pressure drop: experimental and model results
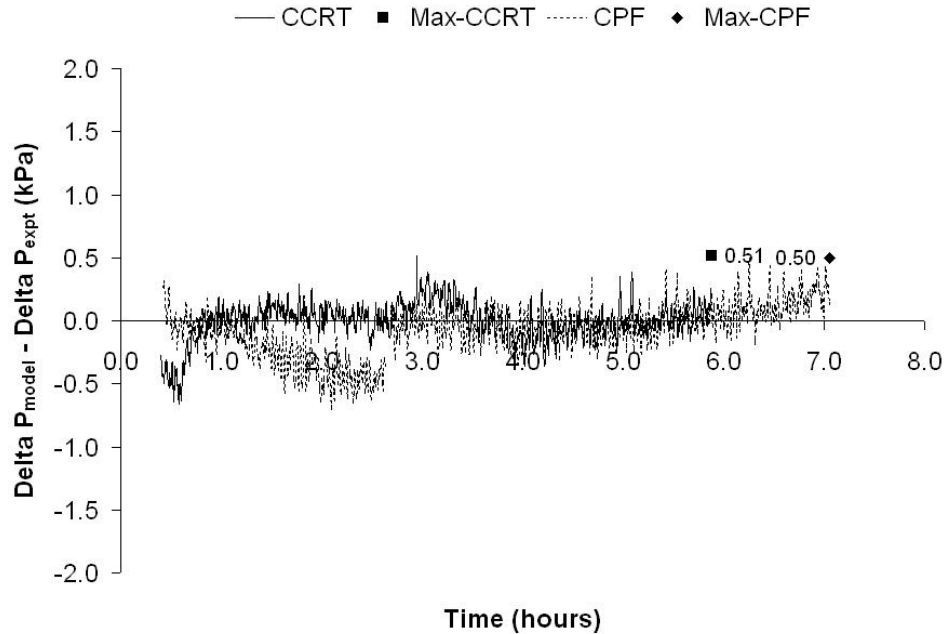
Figure 5.23: 75% load: Deviation of the model from the experimental measured pressure drop

Using the calibrated model, the individual components of the total pressure drop across the CPF were determined and are shown in Figures 5.24 - 5.27 for the 20 and 75% load in CPF-only and CCRT®, configurations respectively. The different contributions to the total pressure drop, discussed in Section 3.2.6 are the friction losses in the channels (equation 3.29), pressure drop across the wall and the particulate cake layer (equation 3.58). Even at the 20% load condition, there is oxidation in the filter wall as seen by the negative slope of the wall pressure component of the total pressure drop, in Figures 5.24 and 5.25. Figures 5.26 and 5.27 show that the rapid decrease in pressure drop at the 75% load condition, is due to the decreasing pressure drop across the filter wall, which is a consequence of particulate oxidation in the filter wall. A comparison of the pressure drop components at 20 and 75% load conditions, after five hours of loading is given in Figure 5.28. Differences in component contributions to the total pressure drop are evident at 75% load where the pressure drops in CPF-only and CCRT® configurations are not quite the same.

The difference between the total pressure drop and the sum of the contributions of the filter wall and PM cake is constant at any condition, and is equal to the friction losses in the inlet and outlet channels. Using the model pressure drop breakdown, it is interesting to compare the pressure losses due to friction in the channels of the DOC and the CPF. The comparison is shown in Table 5.20. The friction losses in the CPF, which is twice as long as the DOC, are lower than in the DOC.
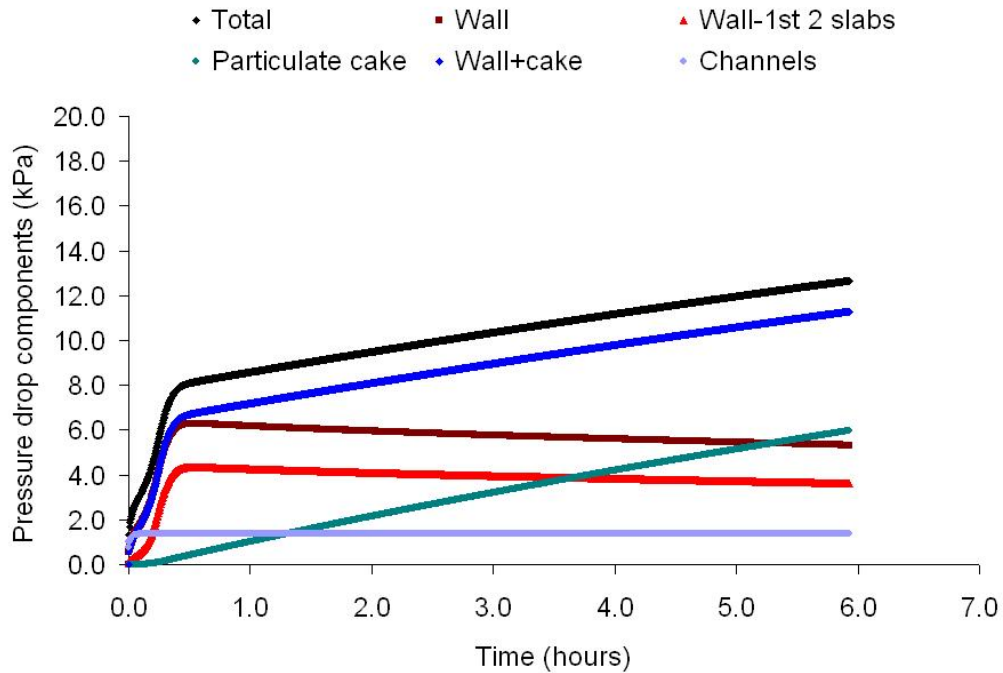
Figure 5.24: 20% CPF-only pressure drop components

Table 5.20: Comparison of channel friction losses in the DOC and CPF

% Load	ΔP in DOC channels (kPa)	ΔP in CPF channels (kPa)
20	1.8	1.3
40	2.3	1.8
60	3.1	2.7
75	3.8	3.3
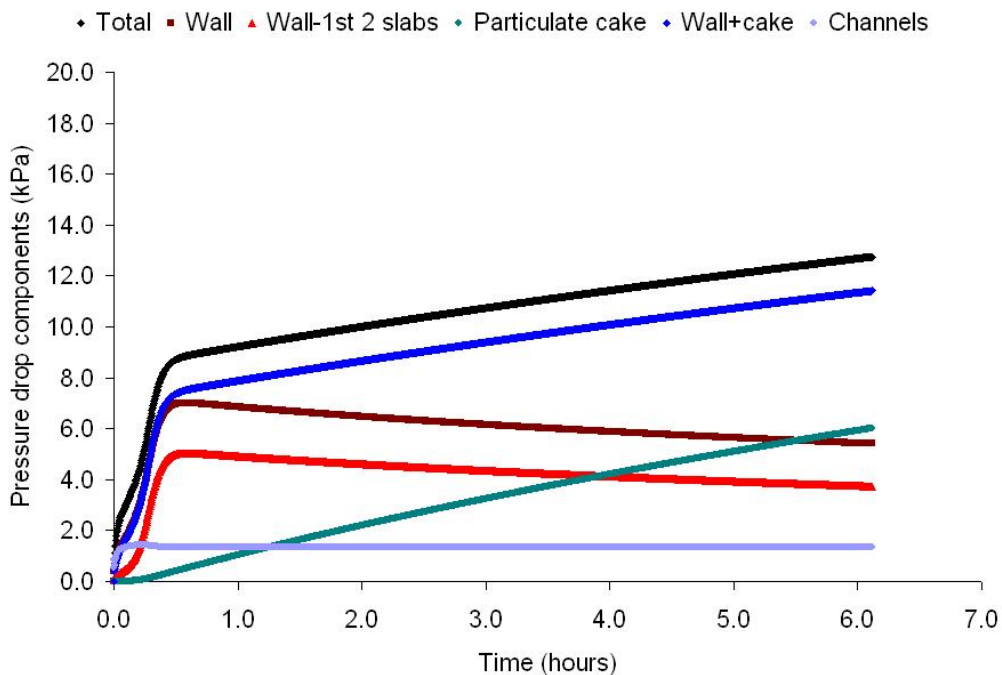
Figure 5.25: 20% CCRT® pressure drop components
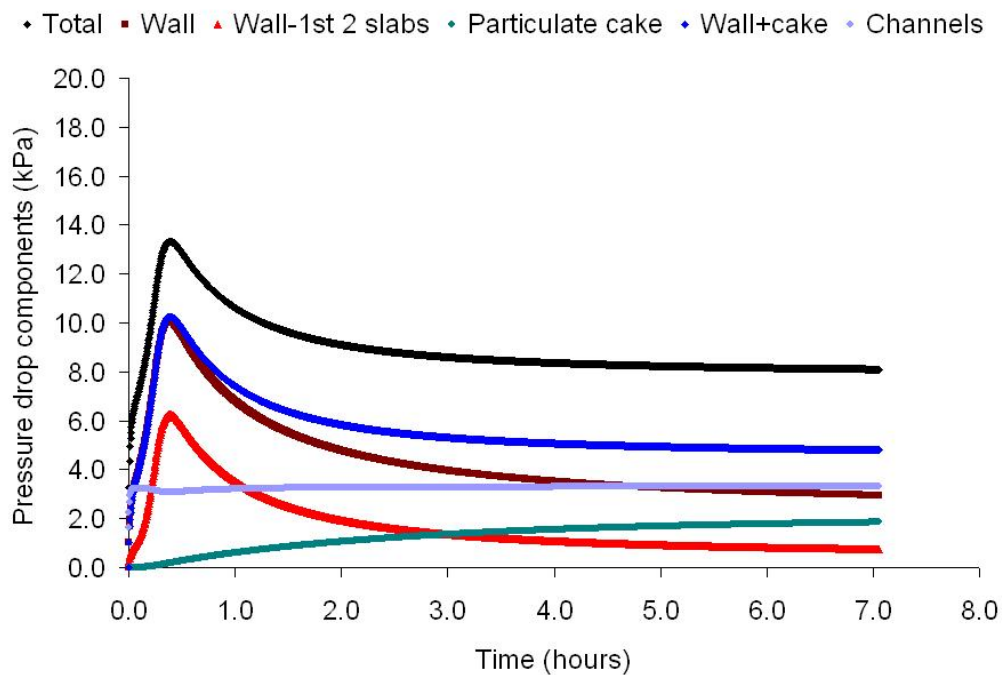
Figure 5.26: 75% CPF-only pressure drop components
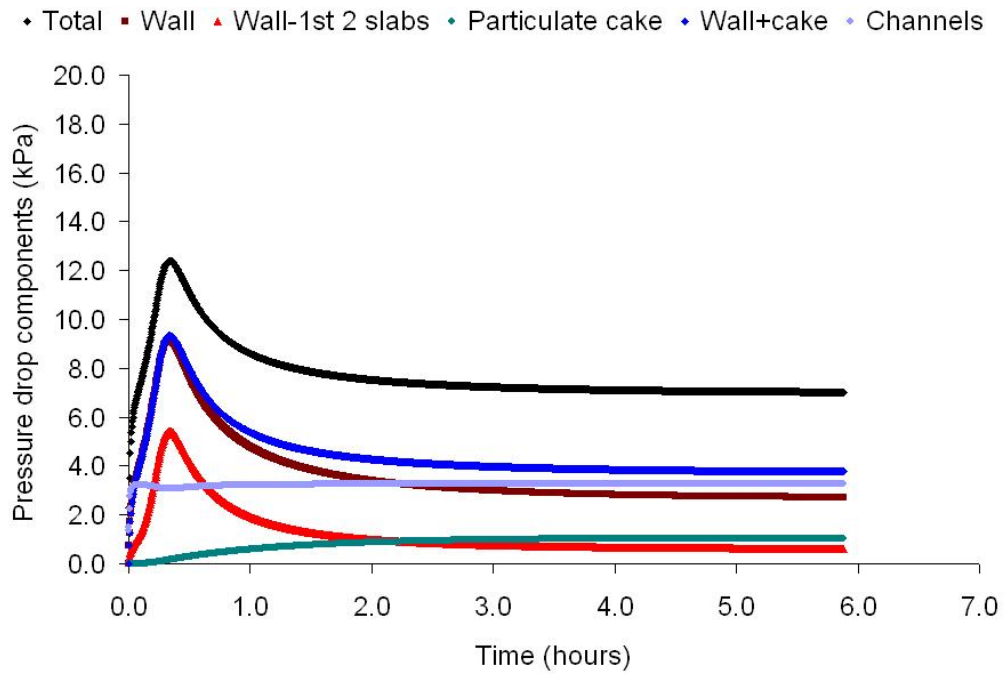
Figure 5.27: 75% CCRT® pressure drop components
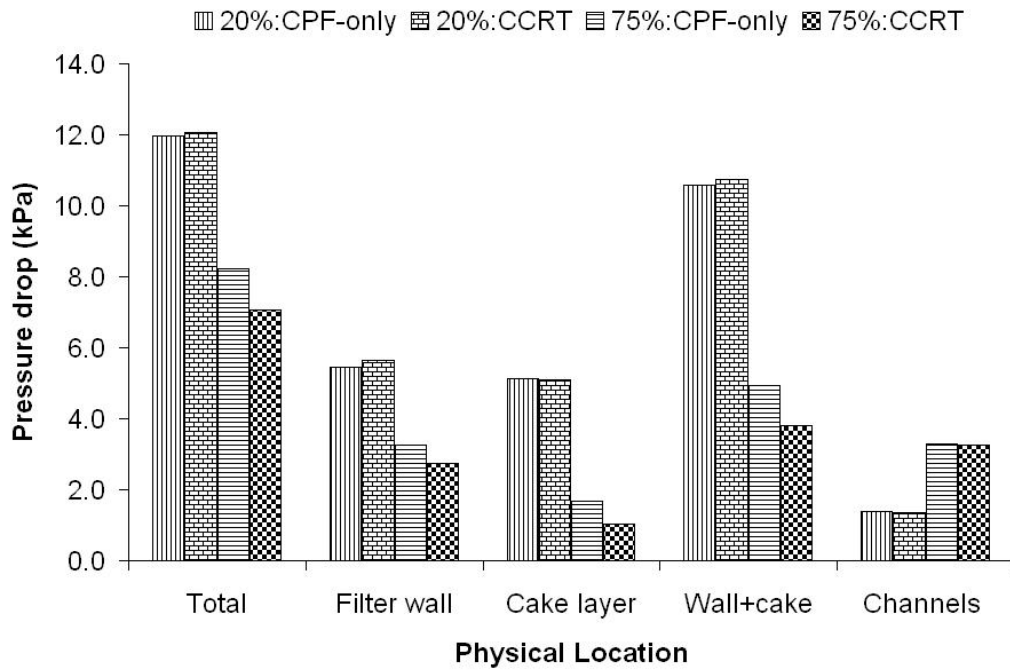
Figure 5.28: 20 and 75% loads: pressure drop components after 5 hours of loading

A comparison of the relative filtration efficiencies of the filter wall and particulate cake layer, for the 20 and 75% load conditions, can be made using Figures 5.29 and 5.30, respectively. The filtration efficiency of the particulate cake layer exceeds that of the filter wall after one hour at 20% load. The filtration efficiency of the wall reaches a maximum and constant value of 76%, while that of the PM cake keeps increasing with time. The reason is that the efficiency of the filter wall depends on the efficiency of its unit collectors, as the thickness of the filter wall is constant (equation 3.19). The efficiency of the unit collectors in the filter wall reaches a maximum when the size of the unit collector loaded with PM equals that of the unit cell. When this happens the unit collectors in the wall cannot grow further in size and thus their efficiency peaks at this stage. On the other hand, the efficiency of the particulate cake layer, in addition to depending on the efficiency of the unit collectors in the particulate cake layer, also depends on its own thickness (equation 3.84). Thus if the thickness of the particulate cake layer increases, so does its filtration efficiency, as Figures 5.29 and 5.30 show. Note that the filtration efficiency of both the filter wall and particulate cake layer in the 75% load configuration are lower than those in the 20% load configuration because of the higher oxidation rate in the wall and a lower particulate cake layer thickness.
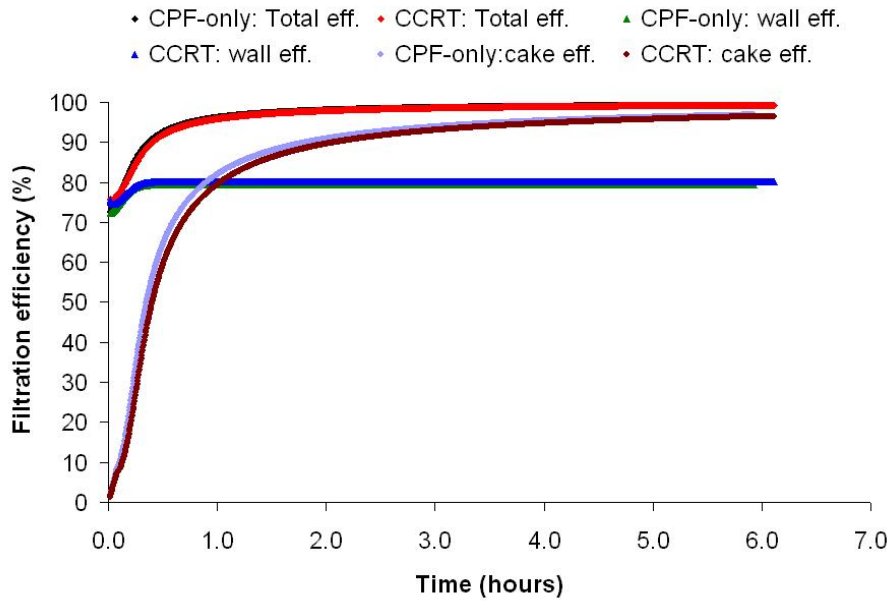
Figure 5.29: 20% load: Comparison of filtration efficiencies in CPF-only and CCRT® configurations
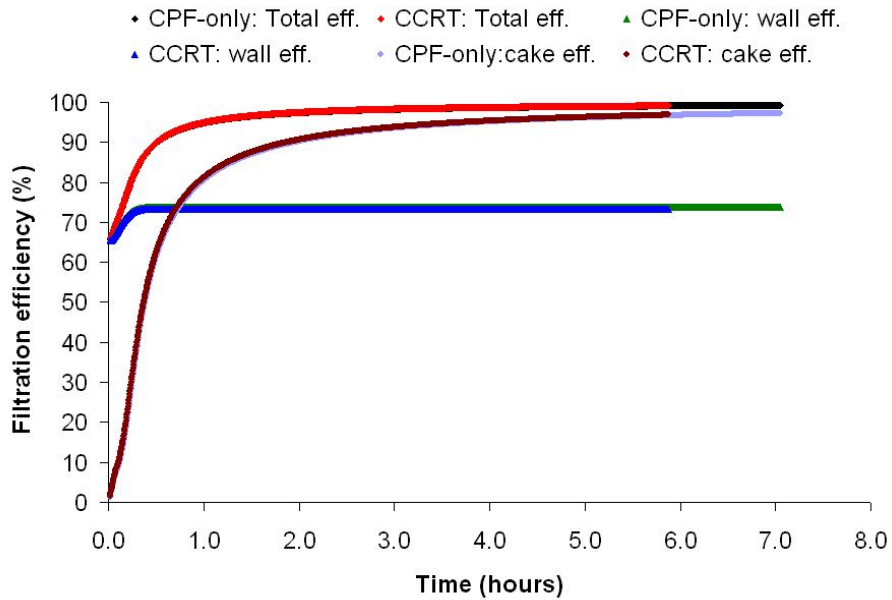
Figure 5.30: 75% load: Comparison of filtration efficiencies in CPF-only and CCRT® configurations

The model predicted particulate mass evolution with time for the 20 and 75% load conditions are shown in Figures 5.31 - 5.34 respectively. It can be see that most of the particulate mass deposited is on the filter wall i.e. the particulate cake layer. Also shown in Figures 5.32 and 5.35 are the CPF outlet PM and PM mass in the filter wall for the 20 and 75% load conditions respectively. It can be seen that the filter in CPF-only configuration is slightly better collector than the CCRT® configuration, because of its higher particulate cake layer filtration efficiency. The outlet concentrations are higher initially because of the lower filtration efficiency of the filter wall and particulate cake layer when the wall is clean. Figure 5.35 shows that there is near complete oxidation of the total particulate mass in the filter wall at the 75% load condition at 6 hours.
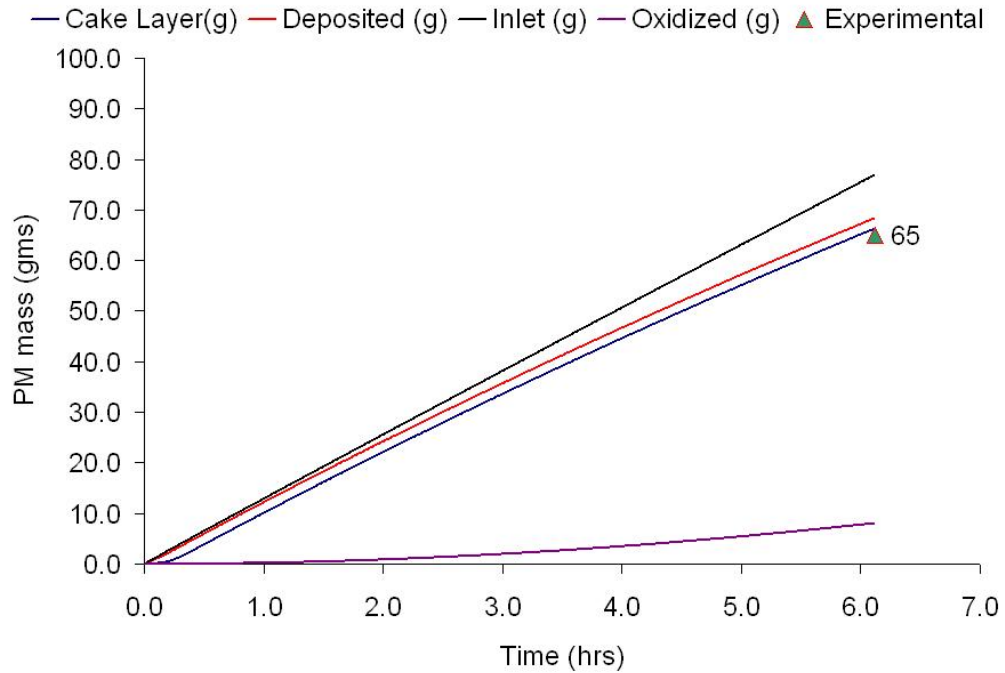
Figure 5.31: 20% CCRT®: PM mass evolution with time
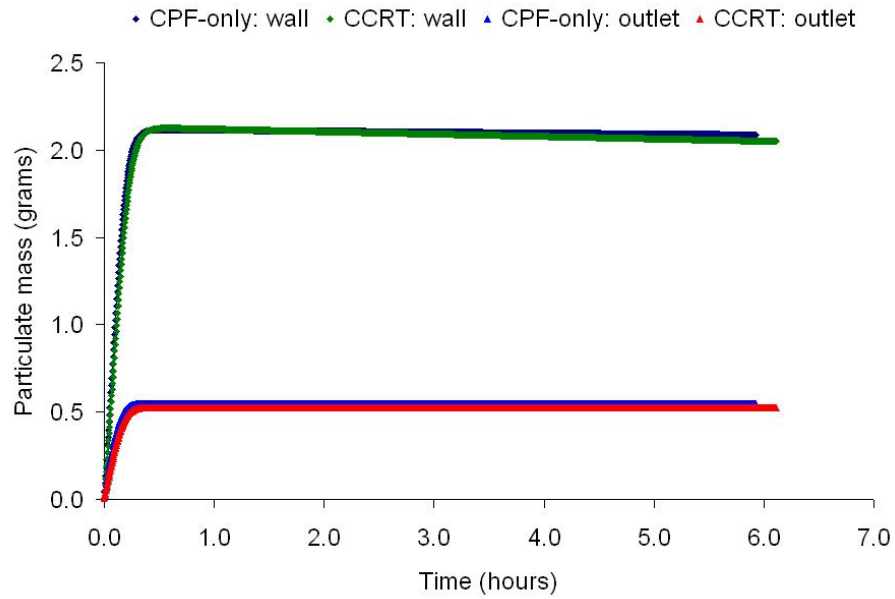
Figure 5.32: 20% load: comparison of outlet PM and mass in filter wall
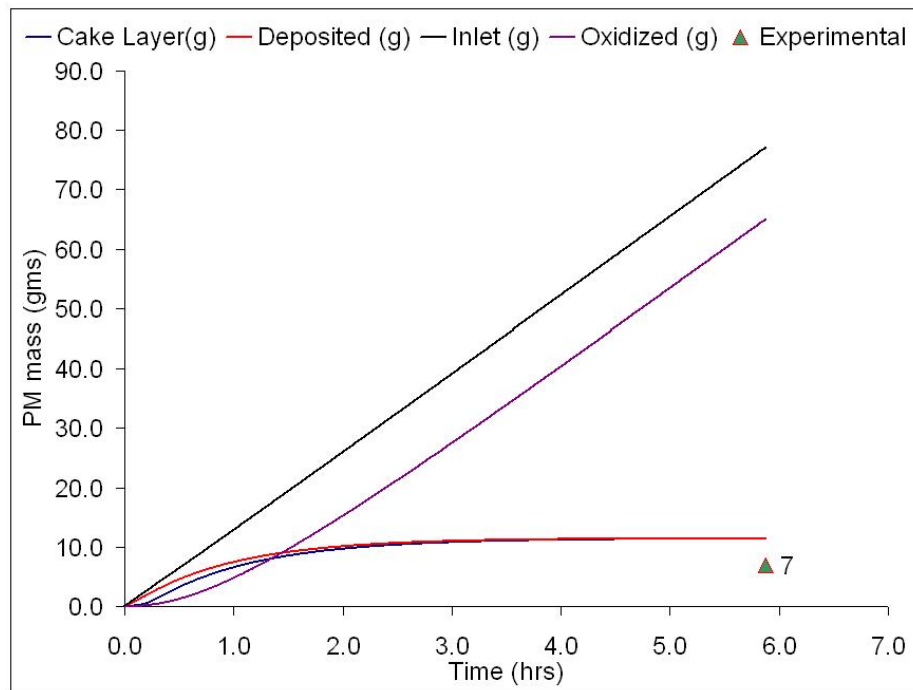
Figure 5.33: 75% CCRT®: PM mass evolution with time
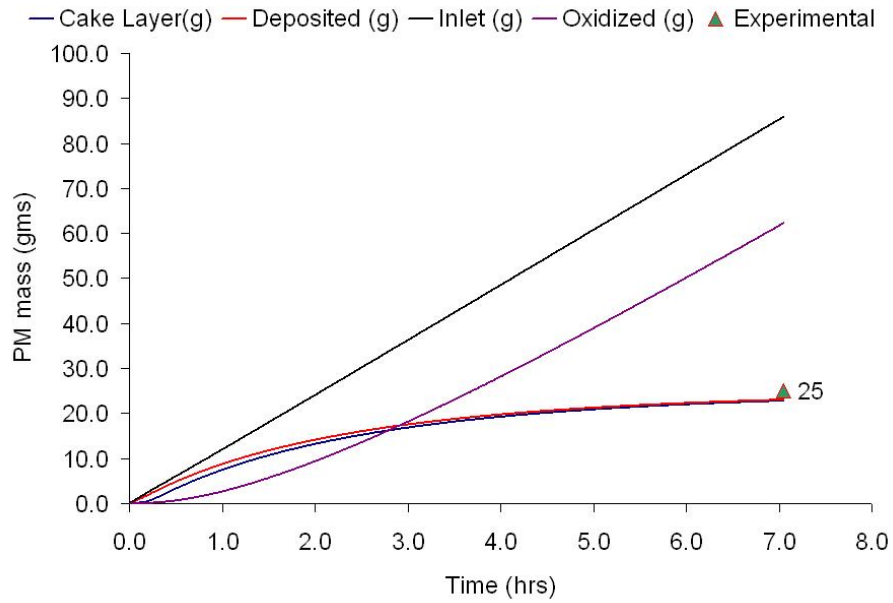
Figure 5.34: 75% CPF-only: PM mass evolution with time
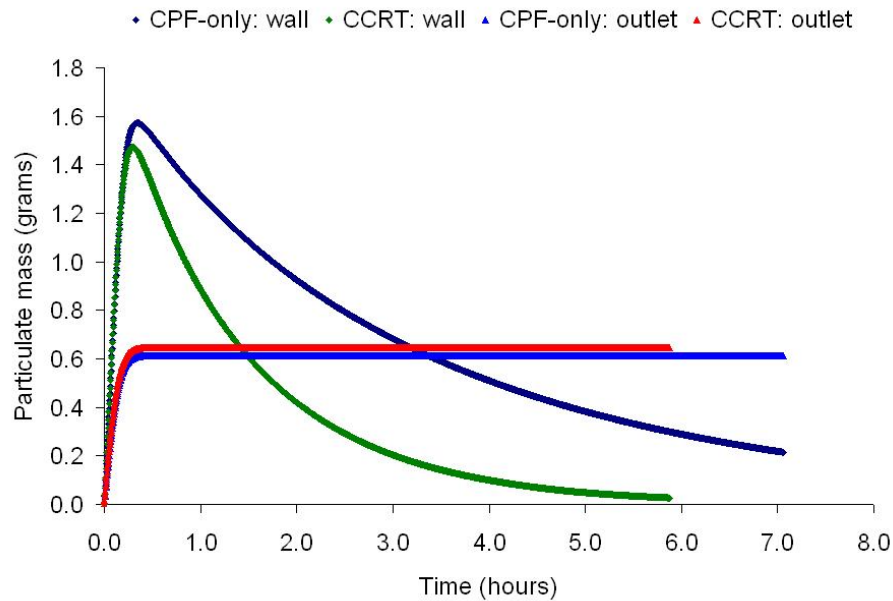
Figure 5.35: 75% load: comparison of outlet PM and mass in filter wall

A comparison between the experimental and model-predicted particulate mass retained in the filter at the end of the experiment is shown in Table 5.21. All model predictions are within 5 grams of the experimentally determined value, except the 60% CCRT® condition which agreed within 10 grams of the experimental value. As mentioned earlier, all of these calibrations were performed without resorting to the use of a 'catalytically' aided PM oxidation with O_2, thus predicting the PM mass oxidation in the CPF in terms of NO_2-assisted and thermal oxidation at both 'high' and 'low' concentrations of NO_2 entering the filter (with and without the DOC).

A comparison of the pressure drop across the CPF for a given particulate mass in the filter is shown in Figure 5.36 for the 20 and 75% load conditions. At the same load, with the same particulate cake layer properties (packing density and permeability) shown in Table 5.19, the pressure drop versus particulate mass in the filter is seen to be quite dissimilar. The reason is that there is always more particulate oxidation in the filter wall in the CCRT® configuration, because of the higher concentrations of NO_2 at CPF-inlet. This is confirmed by the parameters in Table 5.14, where the pre-exponential factors for the filter wall, at every load, are higher in the CCRT® configuration. However, since there is very little particulate mass in the wall, it does not decrease the total particulate mass in the filter appreciably, although the pressure drop decreases substantially as discussed earlier. When comparing across loads, actual volumetric flow rates differ, and thus the same particulate mass will have a higher pressure drop for higher volumetric flow rates (Equation 3.58). However, after wall oxidation begins, the 75% load still has a lower pressure drop than at 20%, in spite of the higher actual volumetric flow rates, because of oxidation of the particulate matter in the filter wall.

Table 5.21: Experimental and model predicted particulate mass retained in the filter

| % Load | Time (hrs) | | Expt. mass (g) | | Model mass (g) | | Error (g) | | % Error | |
	CPF-only	CCRT®	CPF-only	CCRT®	CPF-only	CCRT®	CPF-only	CCRT®	CPF-only	CCRT®
20	5.93	6.11	85	65	89	68	4	3	4.7	4.6
40	5.18	6.7	99	66	94	69	-5	3	-5.1	4.5
60	5.93	7.34	52	13	48	22	-4	9	-7.7	69.2
75	7.05	5.88	25	7	23	11	-2	4	-8.0	57.1

Figures 5.37 and 5.38 show the particulate mass in the 'slabs' of the filter wall with time for the 20 and 75% CCRT® configurations respectively. Slab 1 is the slab closest to the particulate cake layer and contains the most particulate amongst all the slabs as the only filter before it is the particulate cake layer. On the other hand, slab 9 is the last slab in the filter wall after which the exhaust exits the filter and hence contains the least mass as most of the particles are filtered by the particulate cake layer and slabs before it. The effect of oxidation in the wall is clearly demonstrated in Figure 5.38 at the 75% load condition. It is instructive to understand why the particulate mass in the wall increases during approximately the first 0.3 hours and then decreases. During the initial loading period, the total particulate mass oxidized in the filter wall is less than the total particulate inlet into the filter wall because of the low filtration efficiency of the particulate cake layer (Figures 5.29 and 5.30). Once the particulate oxidation rate in the wall is greater than the rate of particulate inlet into the filter wall, the pressure drop across the filter wall decreases due to a 'net' decrease in particulate mass in the filter wall. In Figures 5.37 and 5.38, note the decrease in particulate mass in all the slabs in the filter wall which is a result of the particulate cake layer filtration model. If the wall oxidation model was used without the particulate cake filtration model, the particulate mass in the first slab would be oxidized but be immediately refilled as the results of Triana [7] show, and the model predicted pressure drop would not decrease as rapidly as the experimental data.
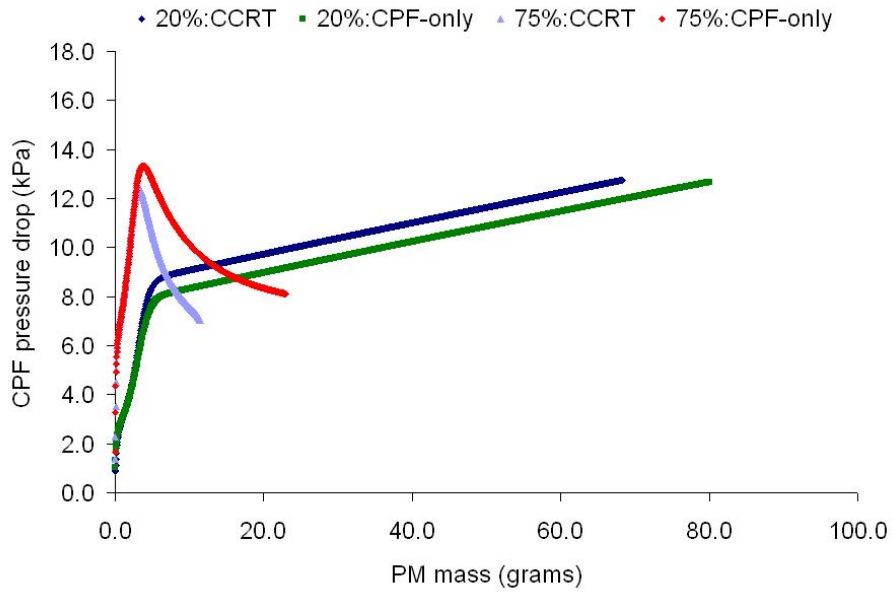
Figure 5.36: 20 and 75% loads: pressure drop versus particulate mass
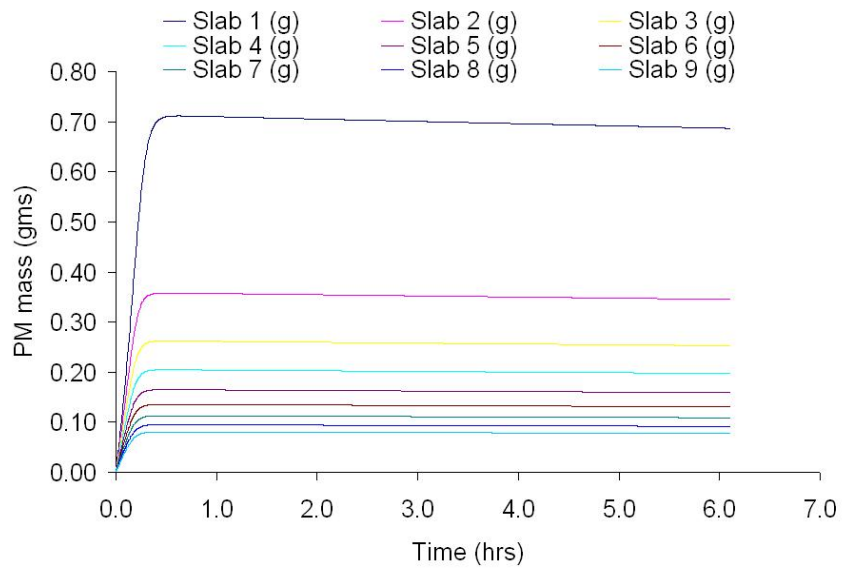
Figure 5.37: 20% CCRT®: particulate mass in the wall with time
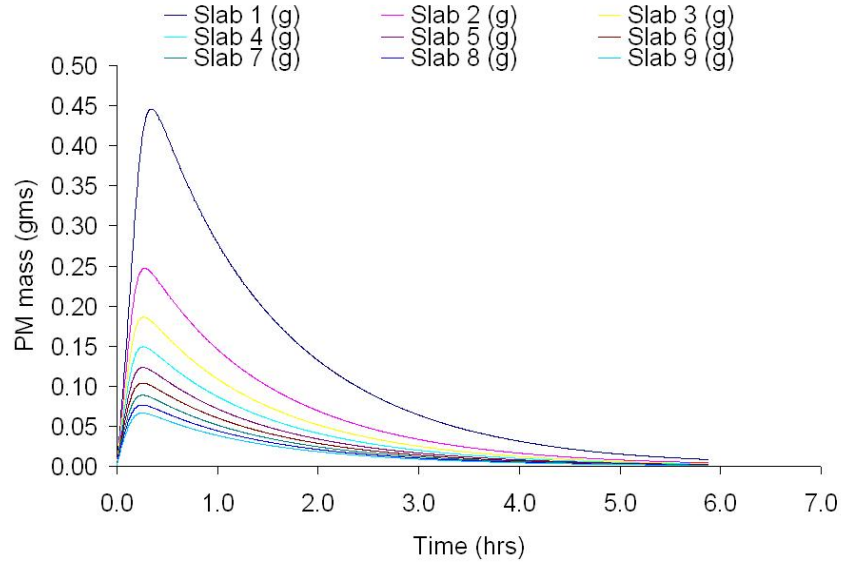
Figure 5.38: 75% CCRT®: particulate mass in the wall with time

A comparison of the thicknesses of layer I and layer II for the 20 and 75% load conditions are shown in Figures 5.39 and 5.40 respectively. For both the 20 and 75% load conditions, because of the higher concentrations of NO_2 entering the filter in CPF-only configuration compared to CCRT® configuration, layer I and II form in a shorter time in CCRT® configuration. For the same reason, the thickness of the particulate layer in CCRT® configuration, at any given instant, is less than the the thickness of the particulate layer in CPF-only configuration. The high oxidation rates at 75% load result in all the particulate matter being confined to layer I with no formation of layer II (Figure 5.40). Even with only 15 ppm NO_2 entering the filter in the 75% CPF-only configuration, the high oxidation rates result in a non-linear evolution of the layer I thickness as shown in Figure 5.40.

The particulate cake layer and the wall filtration models can be used to predict the particle size distribution downstream of the filter. The result for the 20% CPF-only and 75% CCRT® experiments are shown in Figures 5.41 and 5.42 respectively. Good agreement with the experimentally measured downstream particle size distribution can be seen. The reader should be cautioned that not much should be read into the
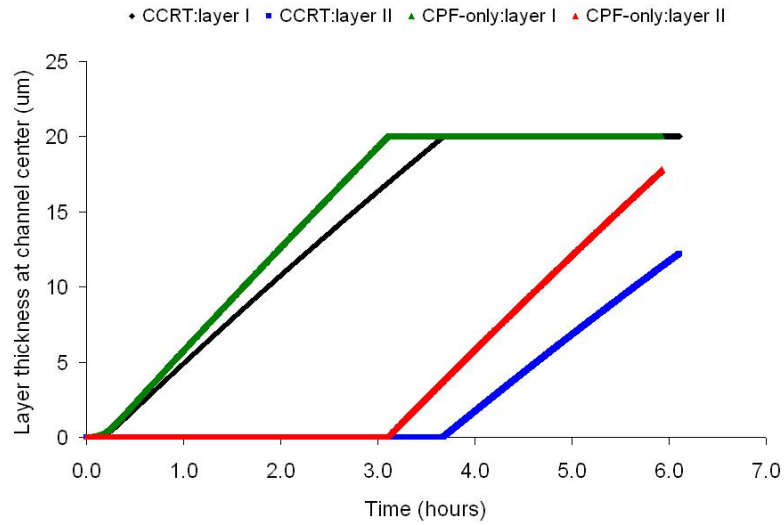
Figure 5.39: 20% Load: comparison of particulate layer thickness with time
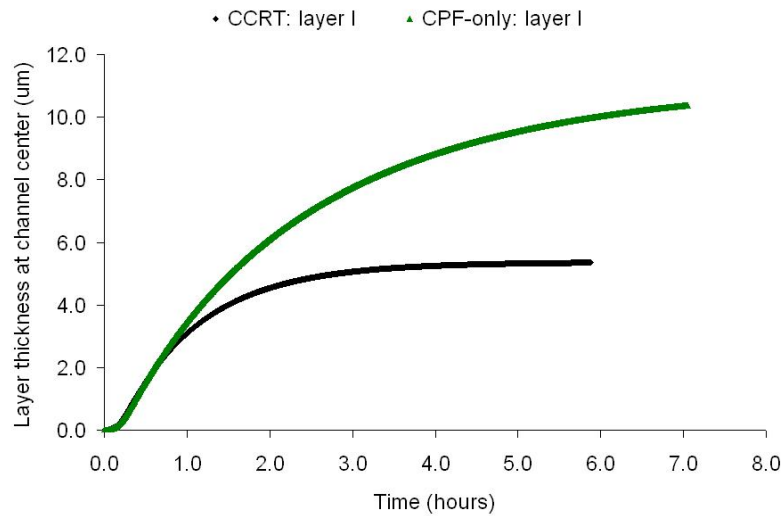
Figure 5.40: 75% Load: comparison of particulate layer thickness with time

comparison between the model predicted and experimentally measured downstream particle size distribution, because the measured downstream particle size distribution of CPFs include some particle formation due to sulfates and losses during sampling, which is not accounted by the CPF model.

It can be seen that the model can predict the 98%+ total filtration efficiencies [46] in spite of the high oxidation rates in the filter wall, especially for the 75% CCRT® condition. Thus, the particulate cake layer filtration model developed in section 3.4, along with the wall filtration model, can model high PM oxidation rates in the wall while still maintaining high filtration efficiencies which were experimentally measured. This was not possible if one uses the wall oxidation model with only the wall filtration model, as found by Triana [7].
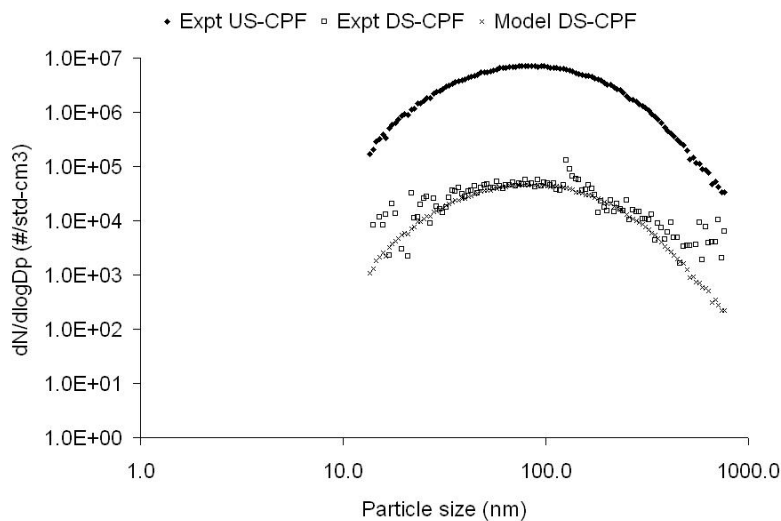
Figure 5.41: 20% CPF-only: particle size distribtion comparison

Using the calibrated model, the particulate oxidation rates by physical location, i.e., layer I, layer II and filter wall, and by type of oxidation, thermal and NO_2, were determined. Figures 5.43 - 5.46 show these results for the 20 and 75% load conditions respectively. These results should be used in conjunction with Figures 5.39 and 5.40 for a complete understanding of the physics involved. At 20% load, all the oxidation
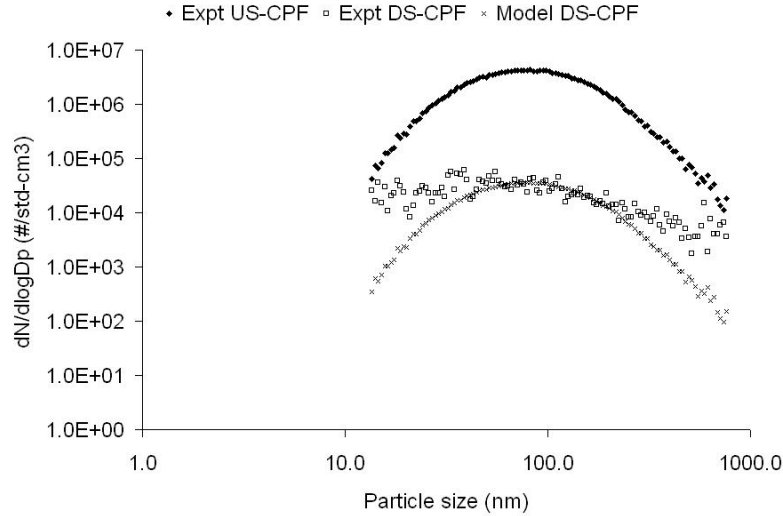
Figure 5.42: 75% CCRT®: particle size distribtion comparison

is due to NO_2, with thermal oxidation rates equal to zero, because of the low exhaust temperatures of 280^oC. However, at 75% load, the thermal oxidation rates, though finite due to exhaust temperatures of 460^oC, are one order of magnitude lower than oxidation rates due to NO_2. Further, there is no significant difference between the oxidation rates in CPF-only and CCRT® configurations at 20% load. At 75% load, because of exhaust temperatures of 460^oC and the NO_2 concentrations, oxidation rates in layer I and in the wall are higher in CCRT® configurations compared to CPF-only configuration. At both 20 and 75% loads, the oxidation rate in layer I is greater than in layer II due to the production of NO_2 in layer I of the CPF, which is part of the sub-model discussed in Section 3.5. The oxidation rates at 20% load are about one order of magnitude lower than at 75% due to the difference in exhaust temperatures (280^oC compared to 460^oC).
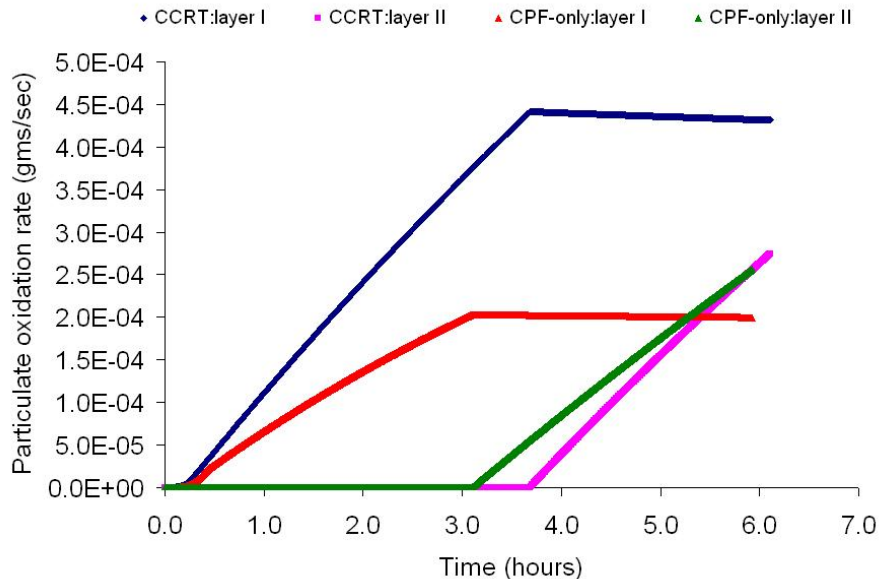
Figure 5.43: 20% Load: comparison of particulate oxidation rate by location
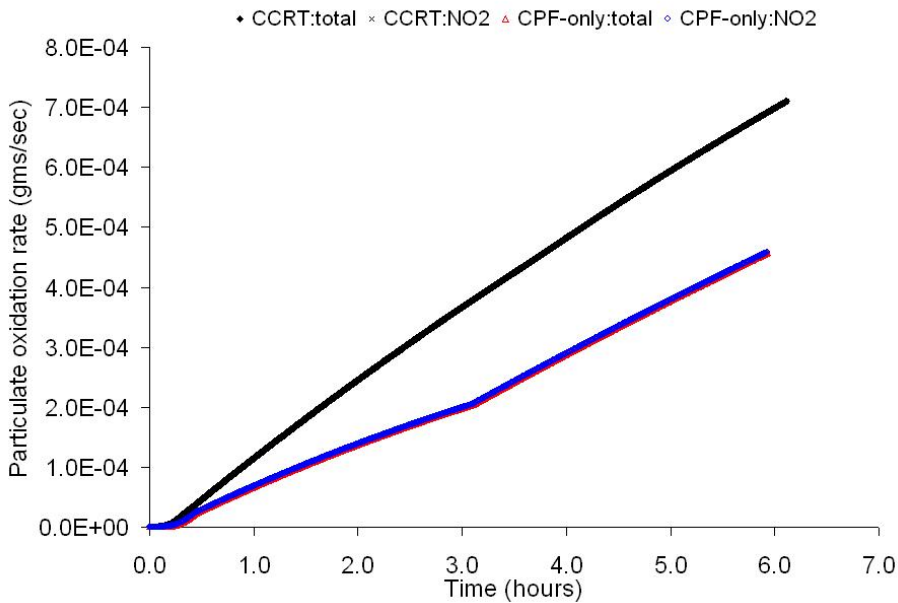
Figure 5.44: 20% Load: comparison of particulate oxidation rate by type
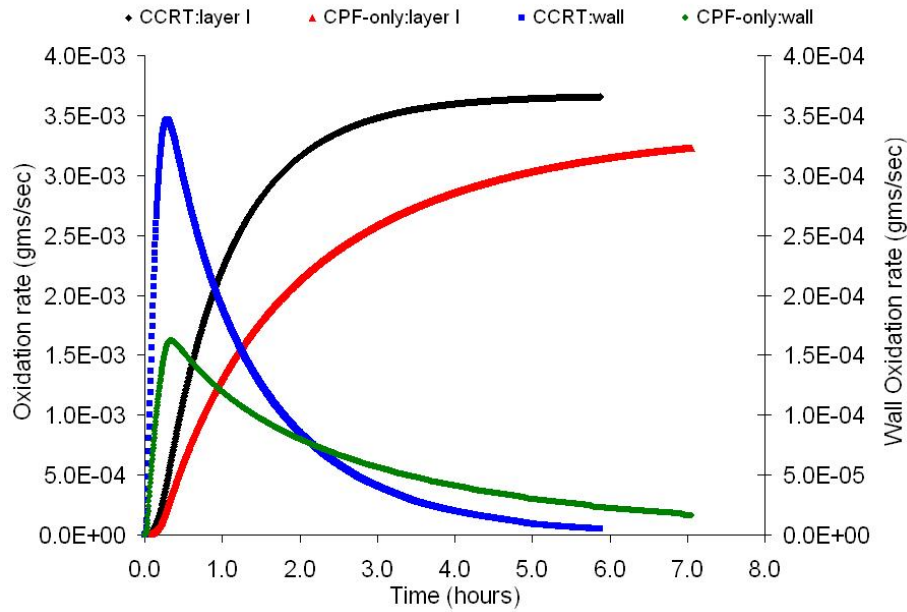
Figure 5.45: 75% Load: comparison of particulate oxidation rate by location
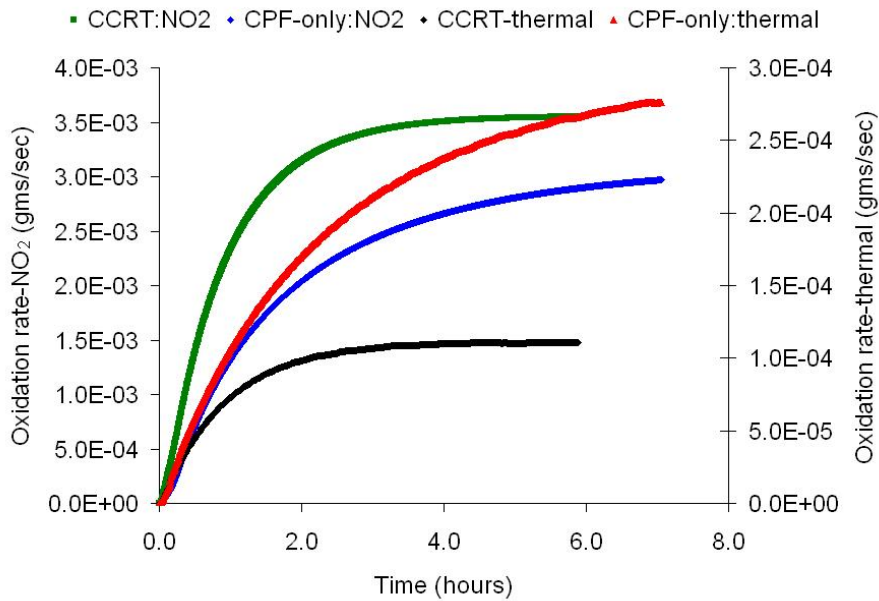
Figure 5.46: 75% Load: comparison of particulate oxidation rate by type

From the calibrated model, the time-integrated total particulate mass oxidized, classified by physical location and type of oxidation mechanism was determined, for all the loading conditions and configurations. Figures 5.47 – 5.50 summarize the particulate oxidized on an individual load basis, for the 20, 40, 60 and 75% loads, while Figures 5.51 and 5.52 summarize the same data as a function of load based on configuration. The total particulate mass into the CPF, the particulate mass retained, particulate oxidized and the % oxidation efficiency are shown in Table 5.22. The simulated data shown are for a total run time of 5 hours for all of the loads and configurations. The figures confirm that, for the same loading time, more particulate is oxidized in CCRT® configuration compared to CPF-only configuration. The figures also show that NO_2 and layer I are the dominant means and physical location of particulate oxidation for the complete temperature range of 280-460°C. It can be seen that most of the PM oxidized is in layer I, much more than in layer II. This is for two reasons: first, the production of NO_2 in the CPF which increases the particulate oxidation rates due to increased availability of NO_2, and secondly, particulate oxidation in layer II can begin only after it forms. As seen in Figure 5.39, layer II does not form until about 3 hours after the start of loading. Also, sometimes layer II may not form at all and hence all the oxidation will be in layer I, as in the 60 and 75% CCRT® configurations respectively.
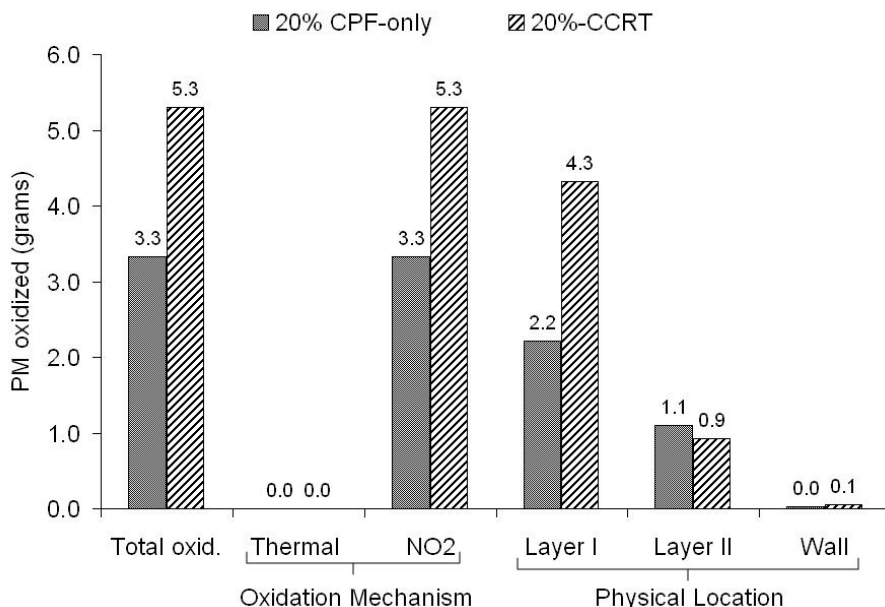
Figure 5.47: 20% Load: total particulate oxidized after 5 hrs by type and physical location
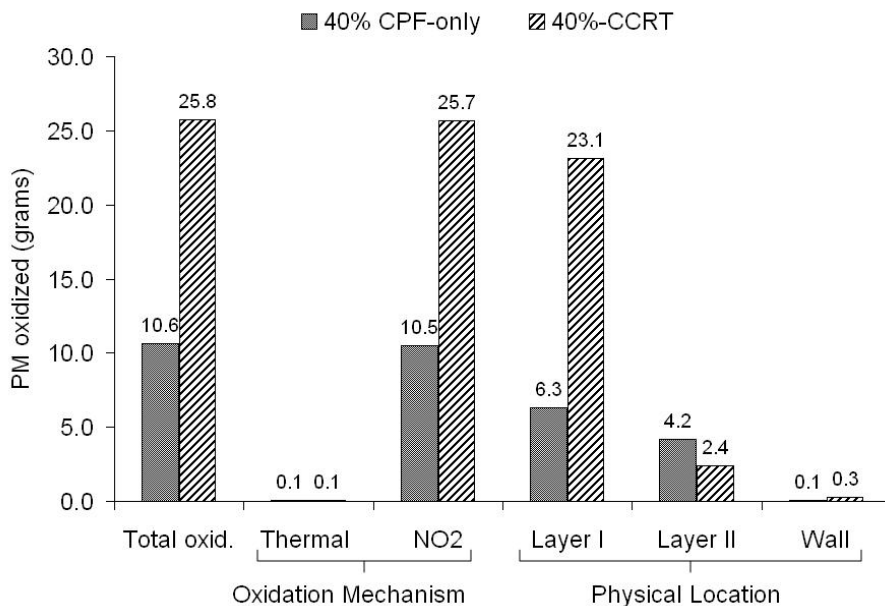

Figure 5.48: 40% Load: total particulate oxidized after 5 hrs by type and physical location
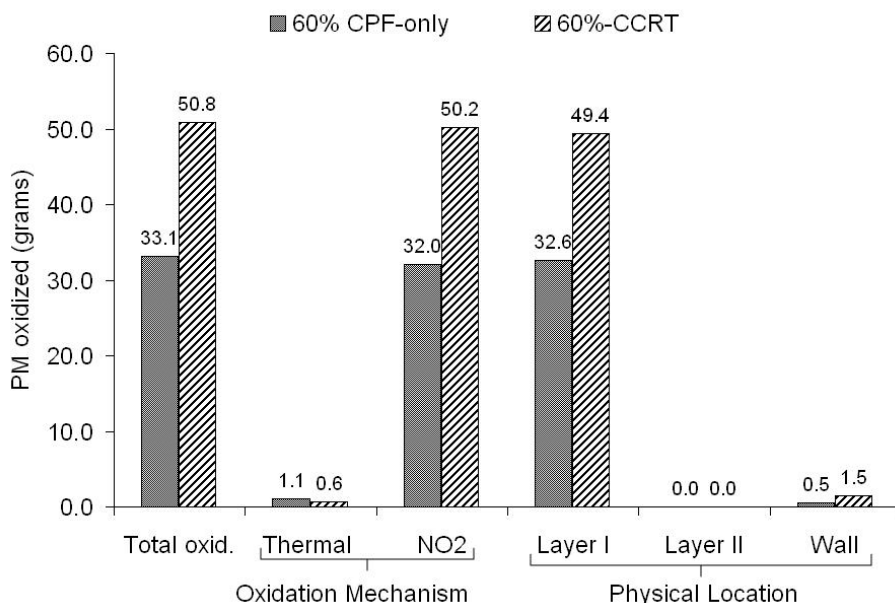
Figure 5.49: 60% Load: total particulate oxidized after 5 hrs by type and physical location
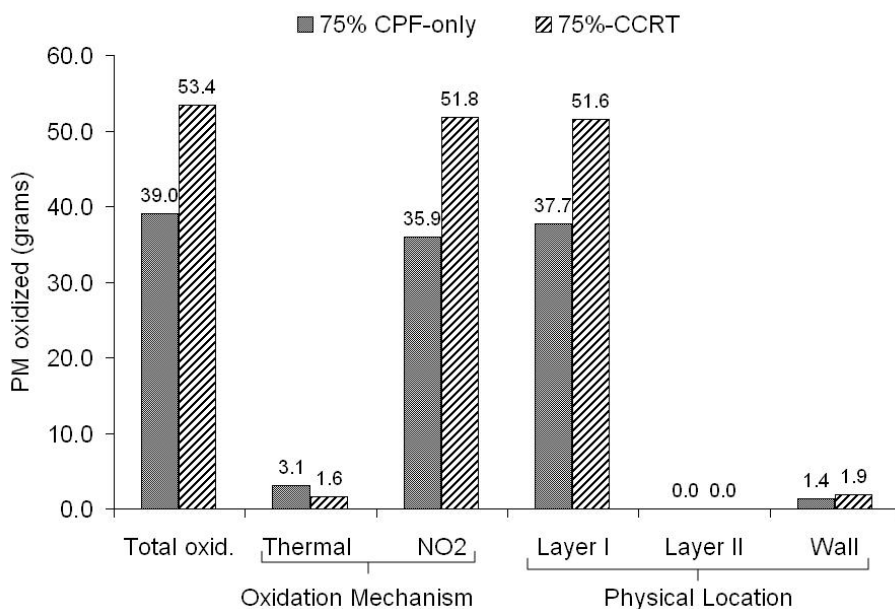

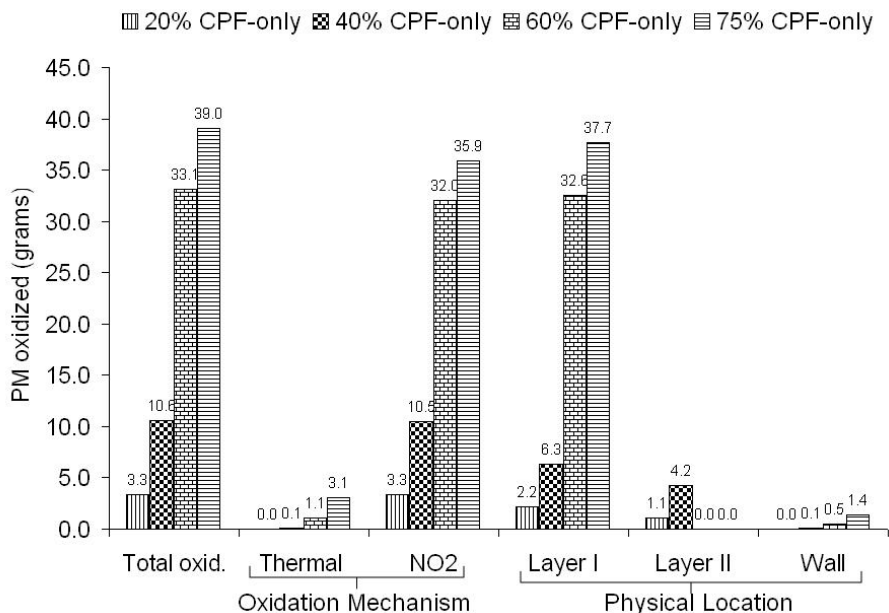Figure 5.50: 75% Load: total particulate oxidized after 5 hrs by type and physical location

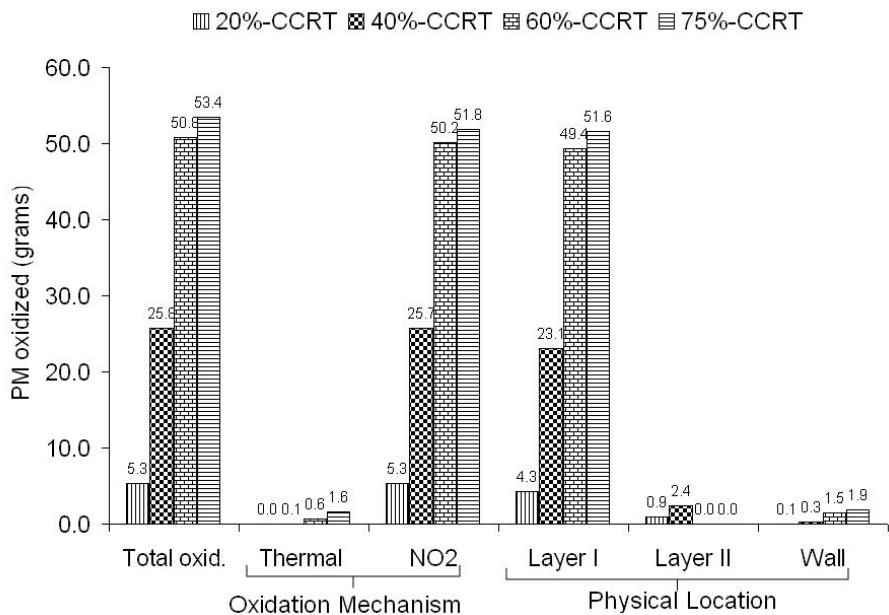Figure 5.51: CPF-only configuration: total particulate oxidized after 5 hrs by type and physical location

Figure 5.52: CCRT® configuration: total particulate oxidized after 5 hrs by type and physical location

Table 5.22: Particulate mass inlet, retained, oxidized and oxidation efficiency in CPF-only and CCRT® configuration

Configuration↓	PM Inlet (g)	PM Retained (g)	PM Oxidized (g)	PM Oxidation Eff. (%)
20: CPF-only	72.9	69.1	3.2	4.4
20: CCRT®	71.8	65.1	6.2	8.6
40: CPF-only	88.5	79.0	8.9	10.0
40: CCRT®	91.2	61.6	29.1	31.9
60: CPF-only	78.6	47.0	31.0	39.5
60: CCRT®	81.3	23.1	57.6	70.1
75: CPF-only	52.2	17.8	33.8	64.8
75: CCRT®	53.0	9.0	43.3	81.7

From the NO_2 production model (section 3.5), an estimate of the particulate mass oxidized by NO_2 entering the CPF and by NO_2 being produced in the CPF was obtained. These data are shown in Table 5.23. The data suggests that the presence of the catalyst in the CPF only modestly increases the total particulate oxidized in the CCRT® configuration. In fact, the maximum % increase is only 8.3% at a temperature of 416^oC. However, in CPF-only configuration, the catalyst in the CPF makes a vast difference with increases from 40.6 to 60.5%. This suggests that the catalyst loading in the CPF of the CCRT® could possibly be reduced with no significant reduction in the passive regeneration performance of the CCRT®, leading to catalyst cost savings, reduced back pressure and better engine performance. A similar finding, based on experimental measurements, has been reported by Allanson et.al [49], who found that reducing the platinum catalyst loading in the CPF of a CCRT® to 25% of its original value did not significantly decrease the oxidation of particulate matter. The reason for this behavior could be as follows: in the CCRT® configuration, the NO_2 concentrations entering the CPF are high enough so that the NO_2 produced in the CPF does not greatly increase the particulate oxidation rates. In CPF-only configuration, the NO_2 concentrations entering the CPF are low, so that additional oxidation due to NO_2 produced in the CPF makes a considerable difference to the total mass oxidized.

Table 5.23: Particulate matter oxidized by NO_2 entering the filter and NO_2 generated in the filter

Configuration↓	Total oxid. (gms)	PM oxid. by inlet NO_2 (gms)	PM oxid. by NO_2-gen (gms)	% PM oxid. by NO_2-gen
20:CPF-only	3.2	1.9	1.3	40.6
40:CPF-only	8.8	5.0	3.8	43.2
60:CPF-only	29.9	16.6	13.3	44.5
75:CPF-only	31.2	11.7	19.5	62.5
20:CCRT®	6.2	5.8	0.4	6.5
40:CCRT®	29.0	27.7	1.3	4.5
60:CCRT®	56.9	52.2	4.7	8.3
75:CCRT®	42.0	38.9	3.1	7.4

5.3.3   Discussion of Modeling Results

A discussion of the modeling results and also the parameters shown in Table 5.19 is given in this section.

An important conclusion of this modeling study is that model kinetics can be calibrated without resorting to the use of a 'catalytically' aided PM oxidation with O_2 as used by various references. This is possible for both CPF-only and CCRT® configurations, thus making the kinetic parameters independent of inlet NO_2 concentrations. The independence of the NO_2 pre-exponential factor with CPF-inlet NO_2 concentrations, is also due to the use of the NO_2 production model in the CPF. Without this model, particulate oxidation especially in CPF-only configuration would have been too 'weak' because of the low CPF-inlet NO_2 (≤ 25 ppm), and a 'catalytic' reaction with O_2 would have had to be assigned to model the oxidation activity. This is evident from Table 5.23, where the NO_2 production model is able to increase the particulate oxidation rates in CPF-only configuration by about 41-63%. Further, the model NO_2 kinetics did not vary with temperature (load), showing that calibration of reactor studies can be used to extract kinetic parameters. Some of the error in model prediction of mass retained in the filter could be due to measurements of CPM upstream of the filter.

The variation of the NO_2 pre-exponential factor for particulate oxidation in the wall, shown in Table 5.15, with load and configuration could be because of the wall oxidation model is a simple representation of the complex phenomenon of particulate oxidation in the pores of the filter. Another reason is that particulate oxidation in the wall also depends on the extent of catalyst penetration inside the filter wall, which is not taken into account in the present formulation due to its complex nature. By using Arrhenius plots, a single set of kinetic parameters for the filter wall were obtained, with a correlation coefficient of 0.98 (Table 5.16 and Appendix H).

The kinetic NO_2 production factor in Table 5.15, was found to vary with load

and configuration, and as noted in Section 3.5, this is because the NO_2 production model is a general kinetic expression which means that the pre-exponential factor can vary with exhaust conditions. It cannot, for example, take into account the fact that the $NO \rightarrow NO_2$ oxidation is thermodynamically limited at high temperatures, and hence inhibition factors like those present in the DOC model [6, 7] would be needed. The exponents for the NO_2 production model in equation 3.86, are taken to be those representing high space velocities from reference [2] and are also reproduced in section 3.5. The temperature order, n, for the NO_2 production in the CPF (equation 3.86) was taken to be equal to 3 to reduce the magnitude of factor.

The particulate cake layer porosities varied with load and in particular had a decreasing trend with increasing exhaust flow rates, which is in accordance with the Peclet number correlation of reference [53]. The range of porosity values were 0.81-0.84 which is on average 0.1 lower than the values determined from the Peclet number correlation of reference [53], possibly due to deviation of unit collector filtration theory from the more accurate discrete particle simulations of reference [53]. A comparison of the determined porosities with those of [53] is shown in Figure 5.53. Particulate cake layer porosities shown in Table 5.19, were fairly constant at any particular load in both CPF-only and CCRT® configurations, validating the use of the particulate cake porosity as a filtration parameter.

The magnitudes of particulate cake layer permeabilities agrees well with reported data in the literature [7, 9, 34, 53]. A comparison of the determined particulate cake layer permeabilities with the more accurate discrete particle simulations of reference [53] is shown in Figure 5.54. It can be seen that the values agree within 10-20% of the discrete particle simulations of reference [53]. The determined particulate cake layer permeabilities shown in Table 5.19, varied with load in general, but remained the same for both CPF-only and CCRT® configurations in the 20 and 75% load cases . For the 40 and 60% load cases, the particulate cake layer permeabilities also

varied between CPF-only and CCRT® configurations, because the 40% CCRT® and 60% CPF-only cases had decreasing pressure drop profiles with simultaneous particulate mass accumulation. As explained earlier, such conditions were modeled by particulate oxidation in the wall and unusually high values of the particulate cake layer permeabilities (equation 3.58). This effect can be explained as follows: the oxidation of particulate by NO_2 could be occurring in small pockets near the filter wall where it is more likely to be adsorbed to both the particulate and the active sites on the catalyst, causing the cake permeability to increase, which decreases the resistance of the cake to the flow. The particulate oxidation rates can be low enough to cause a net accumulation on the wall while the resultant high cake permeability and oxidation inside the wall causes the cake pressure drop component to be obscured compared to the total pressure drop. The 'rounded' pressure drop profiles, mentioned earlier, could also be the result of particulate cake permeabilities increasing with time, which is not considered in the current model. The increase in permeability could be related to the NO_2 oxidation causing channeling in the particulate layer and hence causing less resistance to the flow.

The packing density in the filter wall only varied between 2.92 and 3.95 kg/m^3, and was constant in CPF-only and CCRT® configurations at every load. This variation with load is fairly minimal, with an average of 3.43 and a standard deviation of 0.37, as shown in Figure 5.55.

The packing density of the particulate cake increased with load but were determined from the Peclet number correlation of reference [53]. These values remain the same in both CPF-only and CCRT® configurations at every load. Before model calibration, PM cake packing densities were determined from Figure 5.18, and hence even though the parameter varied, it was deterministic and known *a priori*.

The mean pore size of the catalyst loaded filter wall was constant and was determined to be 11.0 μm. The mean pore size of the cordierite filter wall before the
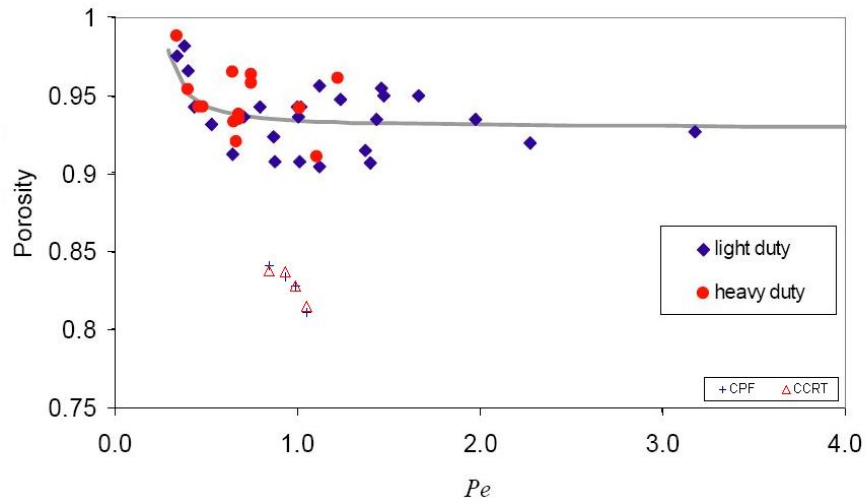
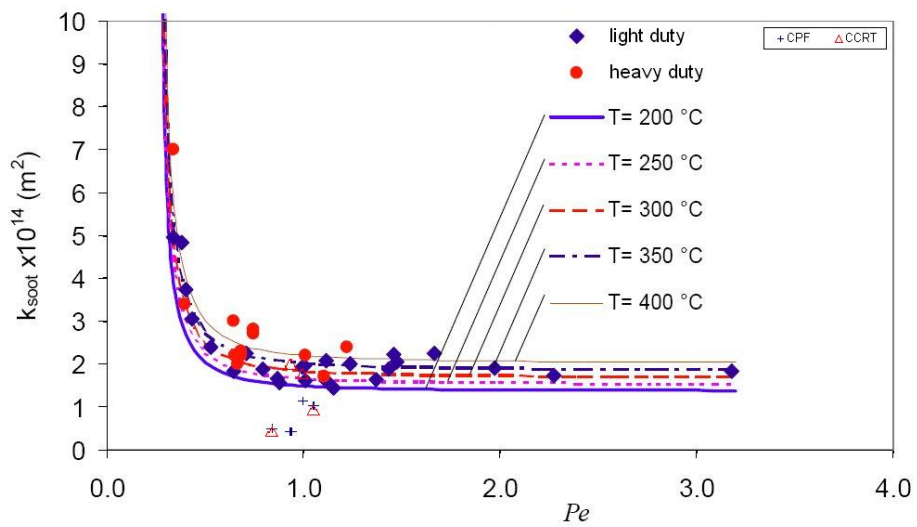Figure 5.53: Comparison of particulate cake layer porosities with reference [53]

Figure 5.54: Comparison of particulate cake layer permeabilities with reference [53]
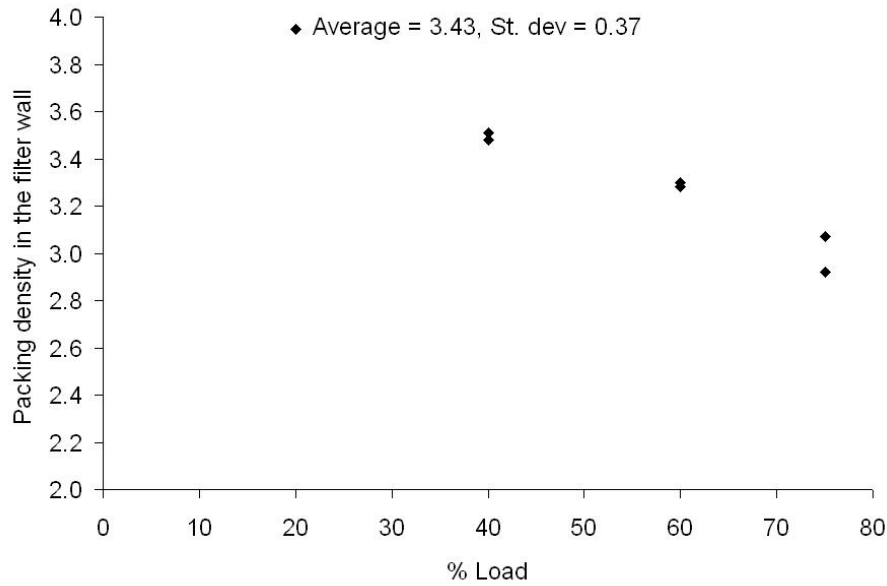
Figure 5.55: Variation in packing density in the filter wall with load

catalyst was loaded onto it was 13.0 μm (Table 4.3 and [73]).

The thickness of layer I was held constant at 20.0 μm and the mean collector diameter in the PM cake filtration sub-model was set equal to 0.1 μm [53, 54], which is equal to the mean aggregate size of diesel particulate particles.

From the model parameters shown in Tables 5.14 to 5.19, it is clear that the performance of this CCRT® in steady state conditions can be characterized by calibration of model parameters of which two are unknown: the particulate cake layer porosity (ϵ_{cake}) and the particulate cake layer permeability (k_{soot}). All other parameters (Tables 5.19, 5.14 and 5.15) are either constant or are known *a priori*. This is a very important result from the use of the new CPF model to characterize a modern device like the CCRT®. This can be appreciated when one compares these results to the number of parameters varied by [7, 9, 34] to model devices simpler in functioning compared to the CCRT®.

From the model results, it was determined that the presence of the catalyst in the CPF does not significantly increase the total particulate oxidized in the CCRT®

configuration. However, in CPF-only configuration, the presence of the catalyst makes a vast difference, greatly increasing the particulate matter oxidized. This suggests that the catalyst loading in the CPF of the CCRT® could possibly be reduced with no significant reduction in the passive regeneration performance of the CCRT®.

Chapter 6

Summary, Conclusions and Recommendations

This chapter provides a summary of the experimental and computational research carried out. Important conclusions from this research are reviewed and directions for future research projects are recommended.

6.1 Summary

Steady state CCRT® characterization experiments were performed with and without the DOC upstream of the CPF to study the filtration, loading and particulate oxidation characteristics of the CPF with a Cummins ISM 2002 diesel engine. A previously developed computational model [6] was used to determine the kinetic parameters describing the gaseous emission (HCs, CO, NO) oxidation characteristics in the DOC and also predict the pressure drop across it. The model was calibrated using experimental data at five loads at rated speed in the temperature range of 280 – 465°C, and actual exhaust volumetric flow rates of 0.447 – 0.843 act-m^3/sec. The 1-D 2-layer CPF model previously developed [7] was further developed to 1) include particulate oxidation inside the filter wall to study decreasing pressure drop profiles

with time, 2) model the particle filtration by the particulate cake layer in the CPF and couple it to the wall oxidation and filtration models, 3) model the NO_2 produced in the catalyst washcoat of the CPF. The kinetic parameters for the NO_2-assisted oxidation of particulate in the CPF were determined from the simulation of transient temperature programmed oxidation (TPO) data in the literature. The CPF model was used to predict the pressure drop with time, particulate mass evolution in and on the filter wall, particulate mass oxidized, particle filtration efficiency, outlet particulate concentrations and the downstream particle size distribution. From the CPF modeling study, using the experimental data for calibration, the following parameters were determined: clean filter wall permeability, filter wall mean pore size, particulate packing density in the filter wall, packing density, porosity, and permeability, of the particulate cake layer, and kinetic parameters for thermal and NO_2-assisted oxidation of the particulate cake layer and in the filter wall.

6.1.1   Experimental Summary

The following items summarize the experimental research.

- The DOC oxidizes engine-out NO to NO_2 with a peak conversion efficiency of 54% at 340ºC. The DOC had a 100% CO oxidation efficiency* at all loads, and HC conversion efficiencies in the range of 77 and 84%. Total NO_X concentrations remained nearly constant across the DOC. The DOC does not significantly affect the particle size distribution of diesel exhaust. The pressure drop across the DOC remains constant during steady state operation and scales linearly with actual exhaust volumetric flow rate.

- The increased NO_2 concentrations out of the DOC contributed significantly to the oxidation of particulate in the CPF, as seen from a comparison of CPF loading experiments performed with and without the DOC.

---

*Within the measurement capability of the gaseous emission analyzer

- The CPF without the DOC and the CCRT® is a highly efficient reducer of diesel particulate emissions, with mass reductions of over 90%. The CPF alone, like the DOC, has a 100% CO oxidation efficiency* at all loads, and was more efficient than the DOC in oxidizing HCs with efficiencies between 88% and 95% respectively. At temperatures below 340°C, the DOC had a higher NO conversion efficiency than the CPF, while above 340°C the CPF was more efficient. Disproportionate decreases in filter pressure drop with respect to particulate loading in the filter occur at temperatures above 340°C. Above 415°C, the CCRT® oxidizes over 71% of the particulate matter entering the device.

6.1.2 Modeling Summary

The following items summarize the modeling research.

- The pressure drop across the DOC was always predicted within 0.5 kPa by the model. The DOC model predicted the downstream HCs, CO and NO to within ±3 ppm. The HCs and CO oxidation kinetics in the entire temperature range of 280°C - 465°C and an exhaust actual volumetric flow rate range of 0.447 - 0.843 act-m^3/sec can be represented by one 'apparent' activation energy and pre-exponential factor. The NO oxidation kinetics in the same exhaust flow rate range can be represented by 'apparent' activation energies and pre-exponential factors in two temperature regimes – 280°C - 340°C and 340°C - 465°C.

- The 'clean' CPF wall permeability was determined to be 2.00E-13 m^2, which is in agreement with the results of references [7, 9, 34, 41] obtained for cordierite filters. During the depth filtration and cake filtration phases only three parameters, the particulate cake porosity, particulate cake permeability and packing density in the filter wall varied with all other model parameters remaining con-

---

*Within the measurement capability of the gaseous emission analyzer

stant or known *a priori* before model calibration. The particulate packing density in the filter wall was fairly constant with values between 2.92 kg/m^3 - 3.95 kg/m^3, which is in agreement with the results of references [7, 9, 34, 41, 74]. The particulate cake layer permeabilities varied between 0.42E-14 m^2 and 2.00E-14 m^2, which is in agreement with the results of references [7, 9, 34, 41, 53, 74]. Particulate cake layer porosities determined from the cake layer filtration model were always higher than 0.8, and decreased with load, which is only about 0.1 lower and in trend wise agreement with experimental and more complex computational studies of reference [53]. The activation energies and pre-exponential factors for the thermal and NO$_2$ assisted oxidation of particulate were determined to be 1.5E+08 (J/kmole), 0.73E+08 (J/kmole), 1.0 m/(s-K) and 1.0 m/(s-K$^{0.5}$) respectively. The kinetic parameters did not change with temperature, exhaust flow rate or NO$_2$ concentrations. However, separate kinetic parameters are required for particulate oxidation in and on the filter wall, and the variation in kinetic parameters in the filter wall was eliminated by using Arrhenius plots. The mean pore size of the catalyst loaded filter wall was found to be 11.0 μm. The particulate cake packing densities, in the Peclet number range of 0.84 – 1.05, ranged from 131 kg/m^3 - 134 kg/m^3, and were determined from the model of reference [53].

- The pressure drop due to viscous losses in the fluid stream in the DOC was more than the pressure drop due to friction in the CPF. Particle filtration in the deep bed phase can be decribed by the particulate cake porosity, which is a more fundamental parameter than the 'percolation' factor used previously. The model showed that the single channel homogeneous effect of oxidation in the filter wall, along with the particulate cake layer filtration model can predict the complex pressure drop profiles of the CCRT®. The decreasing CPF pressure drops with time with simultaneous accumulation of particulate

mass was due to particulate oxidation in the filter wall and high particulate cake layer permeability. The pre-exponential factors for oxidation by NO_2 did not change with temperature or NO_2 concentrations because of the NO_2 production model. The kinetics parameters for particulate oxidation in the filter wall are different from the particulate cake layer and increased with temperature and NO_2 concentrations.

6.2 Conclusions

From the experimental and modeling research, the following conclusions were made:

1. The particulate oxidation kinetics modeling of the model in CPF-only and CCRT® configurations didnt require any 'catalyst effect' with O_2 to be present. All particulate oxidation kinetics were described by thermal and NO_2-assisted oxidation of particulate.

2. The model showed that NO_2 is the dominant means of particulate oxidation in the temperature range of 280^oC – 460^oC. Layer I was the dominant physical location of particulate oxidation.

3. The wall oxidation model coupled to the particulate cake layer filtration model shows that oxidation in the pores of the filter wall explains the disproportionate decrease in the pressure drop across the filter with respect to particulate mass.

4. The filtration model developed for the particulate cake layer showed that it is a very efficient filter of particles in the exhaust, even more than the filter wall, and overall filtration efficiencies of 98-99% were predicted.

5. The catalyst in the CPF significantly increases particulate oxidation rates in the CPF-only configuration. However, the CPF catalyst does only modestly

increases the particulate oxidation rates in the CCRT® configuration. Hence, the catalyst loading in the CPF could possibly be reduced without significantly decreasing the passive regeneration performance of the CCRT®.

6. The DOC and CPF modeling was an effective tool in developing a physical and chemical understanding of the performance of the CCRT®.

6.3 Recommendations for Future Research

The following recommendations are made for future experimental and computational research:

- The 47mm glass fiber filters used in the CPM sampling measurements should be temperature conditioned, just as they are humidity conditioned, so that more accurate upstream CPM concentrations and positive downstream CPM concentrations can be obtained. This is very important, as the upstream CPM concentrations affects the modeling of the kinetics, filter wall and the particulate cake layer properties.

- An ideal way to perform the characterization experiments will be to perform DOC-DPF (uncatalyzed filter) experiments and then DOC-CPF experiments on the same engine, to truly isolate model kinetic parameters. By this method, the reliance on TPO studies to extract kinetic parameters will be eliminated. This method also eliminated the need for performing CPF-only characterization experiments.

- Characterization experiments should be performed with an engine with cooled low pressure EGR to assess the passive regeneration performance of the CCRT® system at lower NO_2/PM ratios. If EGR rates are varied, passive regeneration in

the CCRT® could be studied at different NO_2/PM ratios at the same temperature and flow rate, and also provide a validation for model parametric studies where the NO_2/PM ratios are varied.

- Steady-state experiments should be performed at more than one speed in addition to load variation. A test matrix that has variation of temperature at one exhaust flow rate (and vice versa), will help isolate the independent effects of flow rate and temperature on particulate oxidation and particulate cake layer properties.

- The following modeling recommendations are made for steady-state studies. The NO_2 production model in the CPF, developed in this research, could be improved by having inhibition parameters similar to the DOC model. The improvement will make the model take into account the change in NO oxidation efficiencies with HC and CO concentrations and temperature. A sub-model should be developed for the transition from the deep bed to the particulate cake filtration regimes, as has also been suggested by reference [55], to model the more 'rounded' pressure drop profiles in this region. The particulate cake filtration model should be further developed to take into account transient effects. The key modeling issue here is to determine how the particulate cake porosity changes during transient operation. Shadman's shrinking spheres model [54] can be used to develop a better model of the depletion in layer thickness due to oxidation. This is important because the shrinking spheres model (uniform oxidation) of Shadman is an exact opposite of the current surface oxidation model (uniform packing density) and the true representation will lie in between. This might be especially important at the high temperatures encountered in active regeneration.

- A model for active regeneration studies should be developed. The DOC model

should be improved to model oxidation during active regeneration conditions, with high DOC-inlet HC concentrations, and the subsequent decrease in NO oxidation, as determined by Singh [71]. The CPF model should be improved to consider multi-channel effects, this is particularly important because of higher heat transfer during active regeneration, which can significantly affect the temperature and consequently particulate mass distribution in the CPF. The implementation is fairly straightforward as the only variable that changes is the temperature, which can be accounted for by the inclusion of a radial heat transfer term, as references [75, 76] show. The oxidation of particulate in the exhaust stream, before it is deposited in the filter wall or the particulate cake, which can happen during the high temperatures involved during active regeneration, should be modeled. A shrinking spheres model, for example Shadman's model [54] used in wall flow filters could be modified or models used in in-cylinder combustion studies could be used. Another area for improvement is to model the oxidation of HCs in the CPF during active regeneration, as the high concentrations of HCs can augment the regeneration process. The scheme used can be similar to the one used in the DOC model.

References

[1] Diesel Net Online Resource. `http://www.dieselnet.com/standards.html`.

[2] Barry J. Cooper and James E. Thoss. Role of NO in Diesel Particulate Emission Control. *SAE:890404*, 1989.

[3] Andrew P. Walker, Ronny Allansson, Phil G. Blakeman, Barry J. Cooper, Howard Hess, and Peter J. Silcock. Optimizing the Low Temperature Performance and Regeneration Efficiency of the Continuously Regenerating Diesel Particulate Filter (CR-DPF) System. *SAE:2002-01-0428*, 2002.

[4] Diesel Net Online Resource. `http://www.dieselnet.com/tech/dpf_crt.html`, 2002.

[5] Johnson Matthey Catalysts Website. `http://www.jmcsd.com/CRT.pdf`.

[6] Antonio P. Triana, John H. Johnson, Song L. Yang, and Kirby J. Baumgard. An Experimental and Numerical Study of the Performance Characteristics of a Diesel Oxidation Catalyst in a Continuously Regenerating Particulate Filter. *SAE:2003-01-3176*, 2003.

[7] Antonio P. Triana. *Development of Models to Study the Emissions, Flow, Kinetic Characteristics from a Diesel Oxidation Catalyst and Particulate Filter.* PhD thesis, Michigan Technological University, 2005.

[8] T.C. Hunyh, J.H. Johnson, S.L. Yang, S.T. Bagley, and James R. Warner. A One Dimensional Computational Model for Studying the Filtration and Regeneration Characteristics of a Catalyzed Wall Flow Diesel Particulate Filter. *SAE:2003-01-0841*, 2003.

[9] Anand S. Shende. A Study of the Filtration and Particulate Matter Oxidation Characteristics of Two Catalyzed Wall Flow Diesel Particulate Filters: Experimental and 1-D 2-layer Model Results. Master's thesis, Michigan Technological University, 2003.

[10] Diesel Net Online Resource. `www.dieselnet.com/tech/catdoc.html`, 2002.

[11] Manuel Presti, Lorenzo Pace, Jan Hodgson, Gino Bella, and Alessandro De Maio. A Computational and Experimental Analysis for Optimization of Cell Shape in

High Performance Catalytic Converters. *SAE:2002-01-0355*, 2002.

[12] Yasuyuki Banno, Takashi Hihara, Makoto Nagata, and Yasushi Tanaka. Pre-Filter Diesel Oxidation Catalyst Development for DOC-CSF System . *SAE:2004-01-1430*, 2004.

[13] Diesel Net Online Resource. `www.dieselnet.com`.

[14] Jon E. Johnson and David B. Kittleson. Physical Factors Affecting Hydrocarbon Oxidation in a Diesel Oxidation Catalyst. *SAE:941771*, 1994.

[15] A. G. Konstandopoulos, L. D. Gratz, J. H. Johnson, S. T. Bagley, and D. G. Leddy. Ceramic Particulate Traps for Diesel Emissions Control–Effects of a Manganese-Copper Fuel Additive. *SAE:880009*, 1988.

[16] G. A. Stratakis and A. M. Stamatelos. Thermogravimetric Analysis of Soot Emitted by a Modern Diesel Engine Run on Catalyst-Doped Fuel. *Combustion and Flame*, 132:157–169, 2003.

[17] B.R. Stanmore, J.F. Brilhac, and P. Gilot. The Oxidation of Soot: A Review of Experiments, Mechanisms and Models. *Carbon*, 39:2247–2268, 2001.

[18] F. Jacquot, V. Logie, J.F. Brilhac, and P. Gilot. Kinetics of the Oxidation of Carbon Black by NO_2: Influence of the Presence of Water and Oxygen. *Carbon*, 40:335–343, 2002.

[19] Agus Setiabudi, Barry A.A.L. van Setten, Michiel Makkee, and Jacob A. Moulijn. The Influence of NO_X on Soot Oxidation Rate: Molten Salt versus Platinum. *Applied Catalysis B: Environmental*, 35:159–166, 2002.

[20] Agus Setiabudi, Michiel Makkee, and Jacob A. Moulijn. An Optimal NO_X Assisted Abatement of Diesel Soot in an Advanced Catalytic Filter Design. *Applied Catalysis B: Environmental*, 42:35–45, 2003.

[21] Agus Setiabudi, Michiel Makkee, and Jacob A. Moulijn. The Role of NO_2 and O_2 in the Accelerated Combustion of Soot in Diesel Exhaust Gases. *Applied Catalysis B: Environmental*, 50:185–194, 2004.

[22] B.A. Lur'e and A.V. Mikhno. Interaction of NO_2 with Soot. *Kinetics and Catalysis*, 38(4):335–343, 1997.

[23] W.A. Majewski, J.E. Ambs, and Kenneth Bickel. Nitrogen Oxides Reactions in a Diesel Oxidation Catalyst. *SAE:950374*, 1995.

[24] I.P. Kandylas and G.C. Koltsakis. NO_2-Assisted Regeneration of Diesel Particulate Filters: A Modeling Study. *Ind. Eng. Chem. Res.*, 41:2115–2123, 2002.

[25] I.P. Kandylas and G.C. Koltsakis. Simulation of Continuously Regenerating Diesel Particulate Filters in Transient Driving Cycles. *Proc. Inst. Mech. Eng. Part D J. Automob. Eng.*, 216(7):591–606, 2002.

[26] I.P. Kandylas, O.A. Haralampous, and G.C. Koltsakis. Diesel Soot Oxidation with NO_2: Engine Experiments and Simulations. *Ind. Eng. Chem. Res.*, 41:5372–5384, 2002.

[27] M.J. Murphy, L.J. Hillenbrand, D.A. Trayser, and J.H. Wasser. Assessment of Diesel Particulate Control-Direct and Catalytic Oxidation. *SAE:810112*, 1981.

[28] Diesel Net Online Resource. `http://www.dieselnet.com/tech/dpf_top.html`, 2002.

[29] Olivier Solvat, Patrice Marez, and Gerard Belot. Passenger Car Serial Application of a Particulate Filter System on a Common Rail Direct Injection Diesel Injection. *SAE:2002-01-1015*, 2002.

[30] Athanasios G. Konstandopoulos and John H. Johnson. Wall-Flow Diesel Particulate Filters-Their Pressure Drop and Collection Efficiency. *SAE:890405*, 1989.

[31] Kyoo Won Lee and James A. Gieseke. Collection of Aerosol Particles by Packed Beds. *Environmental Science and Technology*, 13(4):466–470, 1979.

[32] A.G. Konstandopoulos and M. Kostoglou. Periodically Reversed Flow Regeneration of Diesel Particulate Traps. *SAE:1999-01-0469*, 1999.

[33] Athanasios G. Konstandopoulos and M. Kostoglou. Reciprocating Flow Regeneration of Soot Filters. *Combustion and Flame*, 121:488–500, 2000.

[34] Cuong T. Hunyh. A Study of the Filtration and Regeneration Characteristics of a Catalyzed Wall Flow Diesel Particulate Filter: One Dimensional Model Calibrated and Validated with Experimental Data. Master's thesis, Michigan Technological University, 2002.

[35] Zhiyou Du, Adel F. Sarofim, and John P. Longwell. Kinetic Measurement and Modeling of Carbon Oxidation. *Energy and Fuels*, 5:214–221, 1991.

[36] Aleksey Yezerets, Neal W. Currier, and Heather A. Eadler. Experimental Determination of the Kinetics of Diesel Soot Oxidation by O_2 – Modeling Consequences. *SAE:2003-01-0833*, 2003.

[37] J.P.A. Neeft, O.P. van Pruissen, M. Makee, and J.A. Moulijn. Catalysts for the Oxidation of Soot from Diesel Exhaust Gases II. Contact between Soot and Catalyst under Practical Conditions. *Applied Catalysis B: Environmental*, 12:21–31, 1997.

[38] Debora Fino, Guido Saracco, and Vito Specchia. Filtration and Catalytic Abatement of Diesel Particulate from Stationary Sources. *Chemical Engineering Science*, 57:4955–4966, 2002.

[39] Debora Fino, Paolo Fino, Guido Saracco, and Vito Specchia. Innovative Means for the Catalytic Regeneration of Particulate Traps for Diesel Exhaust Cleaning.

Chemical Engineering Science, 58:951–958, 2003.

[40] Debora Fino, Nunzio Russo, Guido Saracco, and Vito Specchia. The Role of Suprafacial Oxygen in Some Perovskites for the Catalytic Combustion of Soot. *Journal of Catalysis*, 217:367–375, 2003.

[41] Athanasios G. Konstandopoulos, M. Kostoglou, E. Skaperdas, E. Papaionnou, D. Zarvalis, and Evdoxia Kladopoulou. Fundamental Studies of Diesel Particulate Filters: Transient Loading, Regeneration and Aging. *SAE:2000-01-1016*, 2000.

[42] Soren Andersson, Claes Akerlund, and Micael Blomquist. Low Pressure EGR Calibration Strategies for Reliable Diesel Particulate Filter Regeneration on HDD Engines. *SAE:2002-01-2780*, 2002.

[43] S. Kamm, M. Koyro, D. Mihelcic, O. Mohler, K.H. Naumann, and U. Schurath. Volatilisation and Surface Oxidation Processes of Soot Aerosol with High NO_2 Concentrations. *EUROTRAC 200 Symposium*, 27-31 March 2000.

[44] Sougato Chatterjee, Raymond Conway, Satish Viswanathan, Micael Blomquist, and Soren Andersson. NO_X and PM Control from a Heavy-Duty Diesel Engines Using a Combination of Low-Pressure EGR and Continuously Regenerating Diesel Particulate Filter. *SAE:2003-01-0048*, 1989.

[45] A.P. Walker, R. Allansson, P. G. Blakeman, M. Lavenius, A. J. Uusimaki, S. Erkfeldt, H. Landalv, B. Ball, P. Harrod, D. Manning, and L. Bernegger. The Development and Performance of the Compact SCR-Trap System: a 4-Way Diesel Emission Control System. *SAE:2003-01-0778*, 2003.

[46] Venkata R. Lakkireddy. The Effect of an Advanced Oxidation Catalytic Converter and a Catalyzed Particulate Filter on the Emissions from a Heavy Duty Diesel Engine. Master's thesis, Michigan Technological University, 2005.

[47] Markus Maly, Michael Claussen, Otto Carlowitz, Peter Kroner, Marco Ranalli, and Stefan Schmidt. Influence of Nitrogen Dioxide Based Regeneration on Soot Distribution. *SAE:2004-01-0823*, 2004.

[48] Edward Bisset. Mathematical Model of the Thermal Regeneration of a Wall-Flow Monolith Diesel Particulate Filter. *Chemical Engineering Science*, 39:1232–1244, 1983.

[49] Ronny Allansson, Andrew P. Walker, Claus Goersmann, Mats Lavenius, Paul Phillips, and Ari J. Uusimaki. The Development and In-Field Performance of Highly Durable Particulate Control Systems. *SAE:2004-01-0072*, 2004.

[50] S. Hashimoto, Y Miyairi, T. Hamanaka, R. Matsubara, T. Harada, and S. Miwa. SiC and Cordierite Diesel Particulate Filters Designed for Low Pressure Drop

and Catalyzed, Uncatalyzed Systems. *SAE:2002-01-0322*, 2002.

[51] H.Oh and James C. Cavendish. Transients of Monolithic Catalytic Converters: Response to Step Changes in Feedstream Temperature as Related to Controlling Automobile Emissions. *Ind.Eng.Chem.Prod.Res.Dev.*, 21:29–37, 1982.

[52] K.W. Lee, L.D. Reed, and J.A. Gieseke. Pressure Drop Across Packed Beds in the Low Knudsen Regime. *Journal of Aerosol Science*, 9:557–565, 1978.

[53] Athanasios G. Konstandopoulos and E. Skaperdas. Microstructural Properties of Soot Deposits in Diesel Particulate Traps. *SAE:2002-01-1015*, 2002.

[54] Farhang Shadman. Kinetics of Soot Combustion During Regeneration of Surface Filters. *Combustion Science and Technology*, 36:183–191, 1989.

[55] P Versaevel, H. Colas, C. Rigaudeau, R. Noirot, G.C. Koltsakis, and A.M. Stamatelos. Some Empirical Observations on Diesel Particulate Filter Modeling and Comparison between Simulations and Experiments. *SAE:2001-01-477*, 2001.

[56] Bernhard Peters. Numerical Simulation of Diesel Particulate Filter during Loading and Regeneration. *ASME Internal Combustion Engine Division*, ICES2003-584, 2003.

[57] Edward Bisset and Farhang Shadman. Thermal Regeneration of Diesel Particulate Monolithic Filters. *A.I.Ch.E*, 31:753–758, 1984.

[58] Arpad B. Palotas, Lenore C. Rainey, Adel F. Sarofim, John B. Vander Sande, and Paolo Ciambelli. Effect of Oxidation on the Microstructure of Carbon Blacks. *Energy and Fuels*, 10:254–259, 1996.

[59] Athanasios G. Konstandopoulos, E. Skaperdas, and Mansour Masoudi. Inertial Contributions to the Pressure Drop of Diesel Particulate Filters. *SAE:2001-01-0909*, 2001.

[60] Athanasios G. Konstandopoulos. Flow Resistance Descriptors for Diesel Particulate Filters: Definitions, Measurements and Testing. *SAE:2003-01-0846*, 2003.

[61] A. G. Konstandopoulos, E. Skaperdas, J. Warren, and Ronny Allansson. Optimized Filter Design and Selection Criteria for Continuously Regenerating Diesel Traps. *SAE:1999-01-0468*, 1999.

[62] A.D.H. Clague, J.B. Donnet, T.K. Wang, and J.C.M. Peng. A Comparison of Diesel Engine Soot with Carbon Black. *Carbon*, 37:1553–1565, 1999.

[63] Karl J. Rockne, Gary L. Taghnon, and David S. Kosson. Pore Structure of Soot Deposits from Several Combustion Sources. *Chemosphere*, 41:1125–1135, 2000.

[64] Steve Arnold, Kevin Slupski, Mark Groskreutz, Gary Vrbas, Rob Cadle, and S.M. Shahed. Advanced Turbocharging Technologies for Heavy-Duty Diesel Engines. *SAE:2001-01-3260*, 2001.

[65] Timothy Jacobs, Dennis Assanis, and Zorn Filipi. The Impact of Exhaust Gas Recirculation on Performance and Emissions of a Heavy-Duty Diesel Engine. *SAE:2003-01-1068*, 2003.

[66] I.S. Abdul-Khalek, D.B. Kittleson, B.R. Graskow, and Q. Wei. Diesel Exhaust Particle Size: Measurement Issues and Trends. *SAE:980525*, 1998.

[67] Imad Abdul-Khalek and David Kittleson. The Influence of Dilution Conditions on Diesel Exhaust Particle Size Distribution Measurements. *SAE:1999-01-1142*, 1999.

[68] I.S. Abdul-Khalek, D.B. Kittleson, and Fred Brear. Diesel Trap Performance: Particle Size Measurements and Trends. *SAE:982599*, 1998.

[69] Athanasios G. Konstandopoulos. An Experimental and Theoretical Study of Ceramic Monolith Traps in Conjunction with a Manganese-Copper Fuel Additive for Diesel Particulate Emissions Control. Master's thesis, Michigan Technological University, 1987.

[70] Arvind Suresh. Cummins Inc. Technical Contact Person. *Private email communication*, 2004.

[71] Paramjot Singh. . Master's thesis, Michigan Technological University, 2005.

[72] Qiang Wei, David B. Kittleson, and Winthrop F. Watts. Single Stage Dilution Tunnel Performance. *SAE:2001-01-2001*, 2001.

[73] A. Carl McDonald. Johnson Matthey Technical Contact Person. *Private email communication*, 2004.

[74] Nishant Singh. Development of a Vehicle Engine Aftertreatment System Simulation Model with Application to the Study of a Controls Design Strategy for Active Regeneration of a Catalyzed Particulate Filter. Master's thesis, Michigan Technological University, 2003.

[75] Johann C. Wurzenberger and Bernhard Peters. Catalytic Converters in a 1D Cycle Simulation Code Considering 3D Behavior. *SAE World Congress: 2003-01-1002*, 2003.

[76] Athanasios G. Konstandopoulos, Margaritis Kostoglou, Paraskevi Housiada, Nickolas Vlachos, and Dimitrios Zarvalis. Multichannel Simulation of Soot Oxidation in Diesel Particulate Filters. *2003-01-0839*, 2003.

Appendix A

Engine Experimental Data

Engine data collected during the engine characterization runs with the newly installed Cummins ISM 2002 engine are presented. Basic engine variables and estimates of friction power were obtained and are shown.

Figure A.1 shows the air flow rate versus BMEP at different speeds. The air flow at 1500 rpm has the highest slope, and at a BMEP of 489 kPa even exceeds the flow rate at 1800 rpm. This is likely because of the turbocharger at that speed, produces a higher boost pressure than at higher speeds.

Figure A.2 shows the A/F ratio at different speeds. A/F ratio decreases at high BMEPs because more fuel is burned per mass of air to produce the higher torque. Also shown for comparison are the A/F at 2100 rpm with the CCRT® in the exhaust line. The decreased A/F ratios are particularly noticeable at higher BMEPs.

Figure A.3 shows the BSFC with BMEP at different speeds with a comparison of BSFC data at 2100 rpm with the CCRT® in the exhaust line. Higher specific fuel consumption is clearly visible even at the lower BMEPs.

Figure A.4 shows the fuel flow rate with power at different speeds. It is clearly seen that the data points, at any given speed, when extrapolated to the Power = 0 line, gives a positive fuel flow rate. This is the fuel required by the engine to
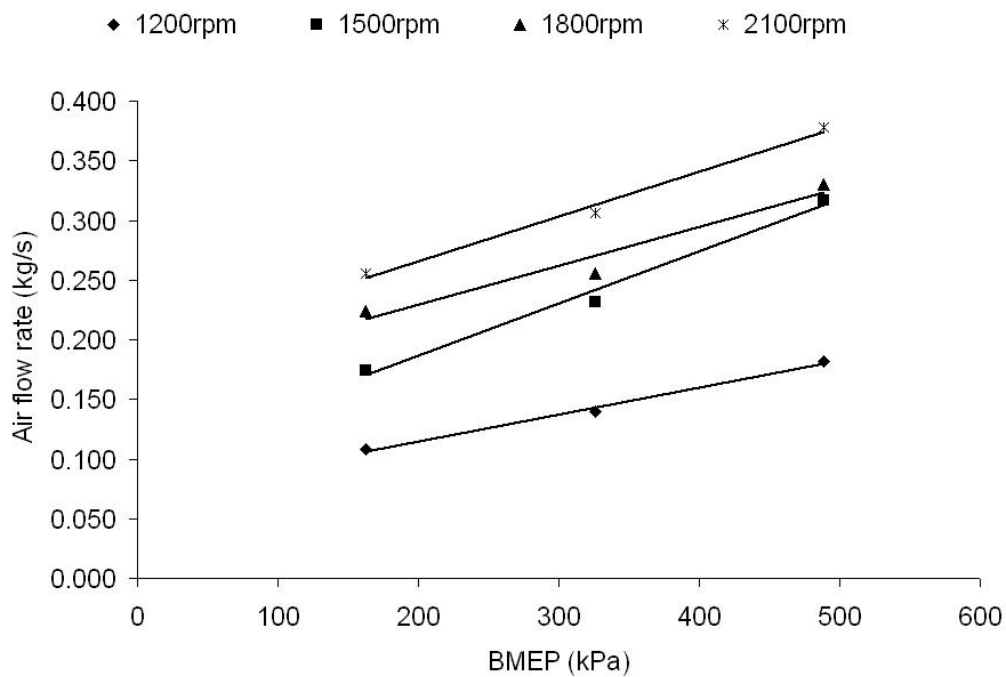
Figure A.1: Air flow rate versus BMEP as a function of engine speed
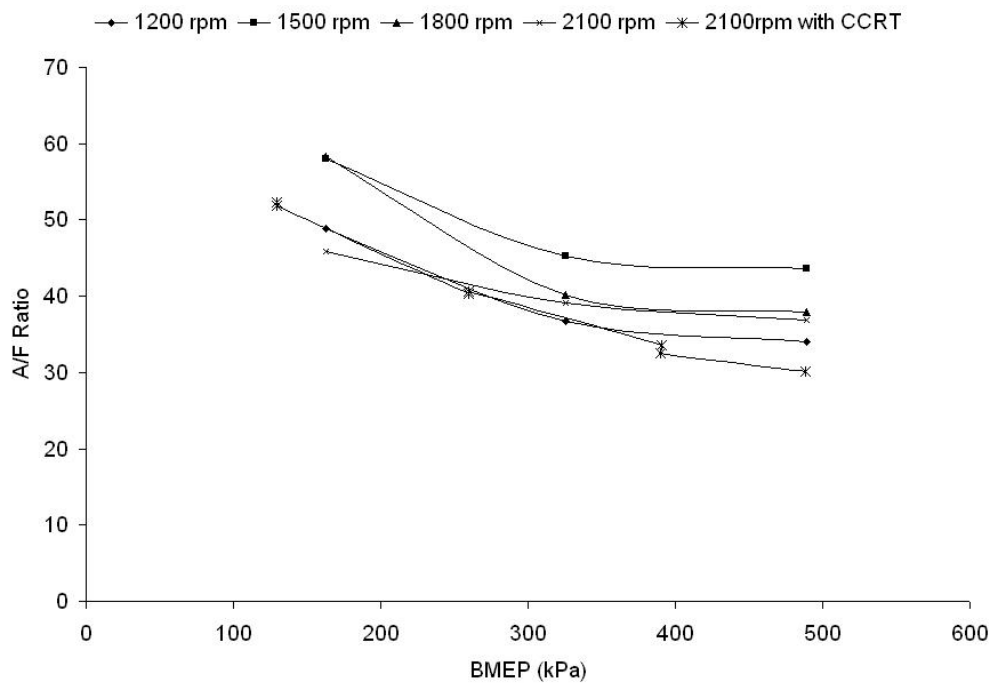
Figure A.2: A/F ratio versus BMEP as a function of engine speed
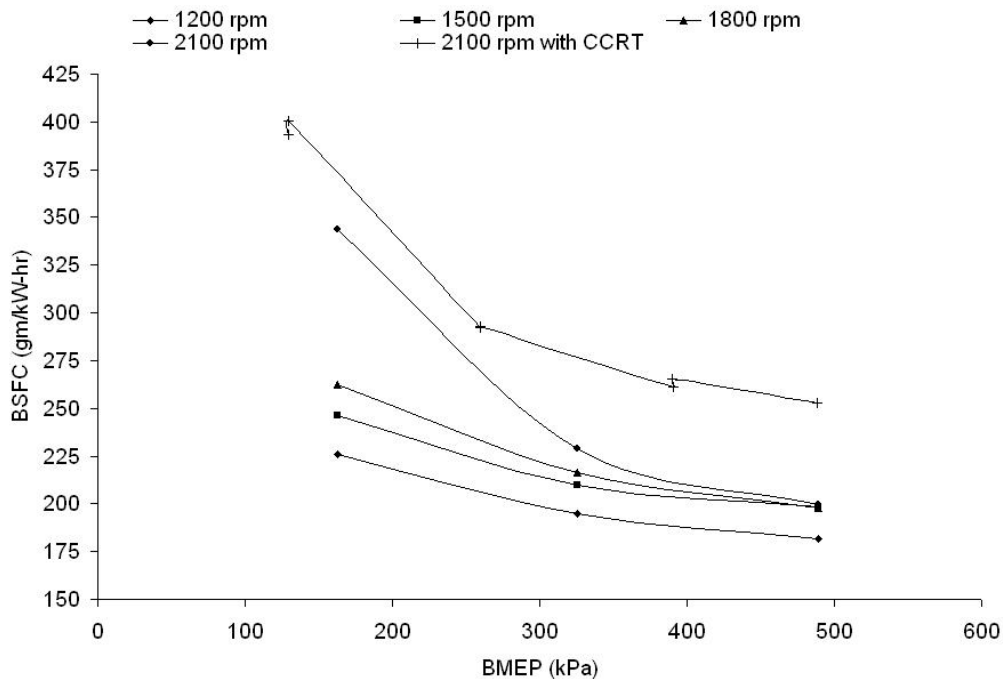
Figure A.3: BSFC versus BMEP as a function of engine speed

produce 0 *brake* power, also called the friction power. This is the power required by the engine to expel exhaust gases, induct fresh air and overcome friction losses. Such plots are also called Willians lines. The friction losses are the intercepts of the linear correlations in Figure A.4. Since friction power increases with speed, probably exponentially, it is interesting to plot the intercepts of the linear correlations of Figure A.4 with engine speed. These results are shown in Figure A.5, where the data are fit with an exponential function with a correlation coefficient of 0.98. An estimate of friction power at any intermediate speed can be obtained from Figure A.5.
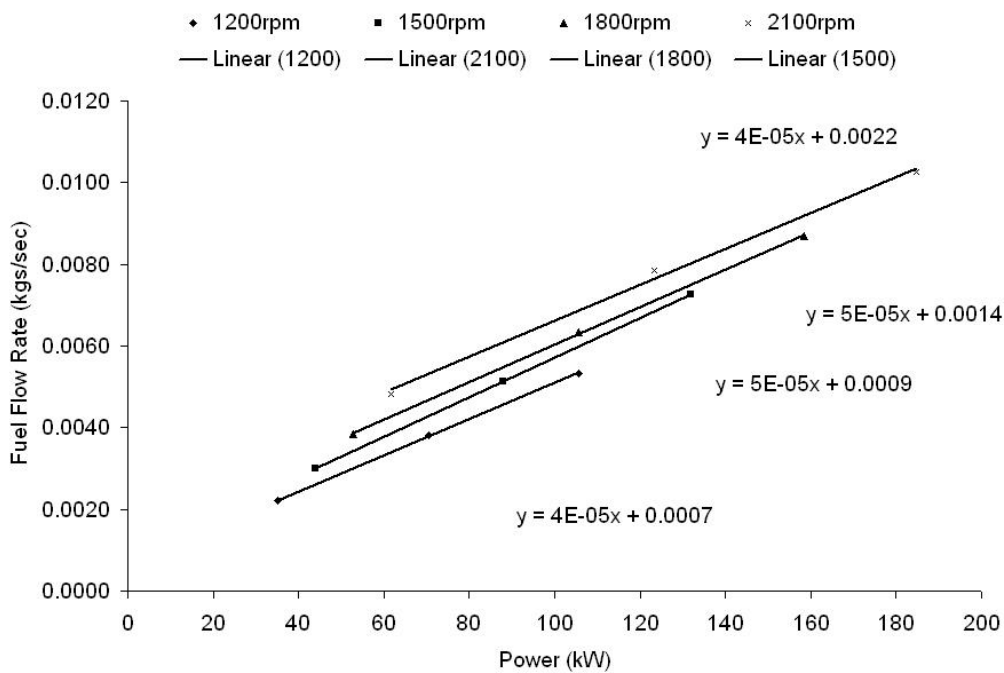
Figure A.4: Fuel flow rate as a function of engine speed
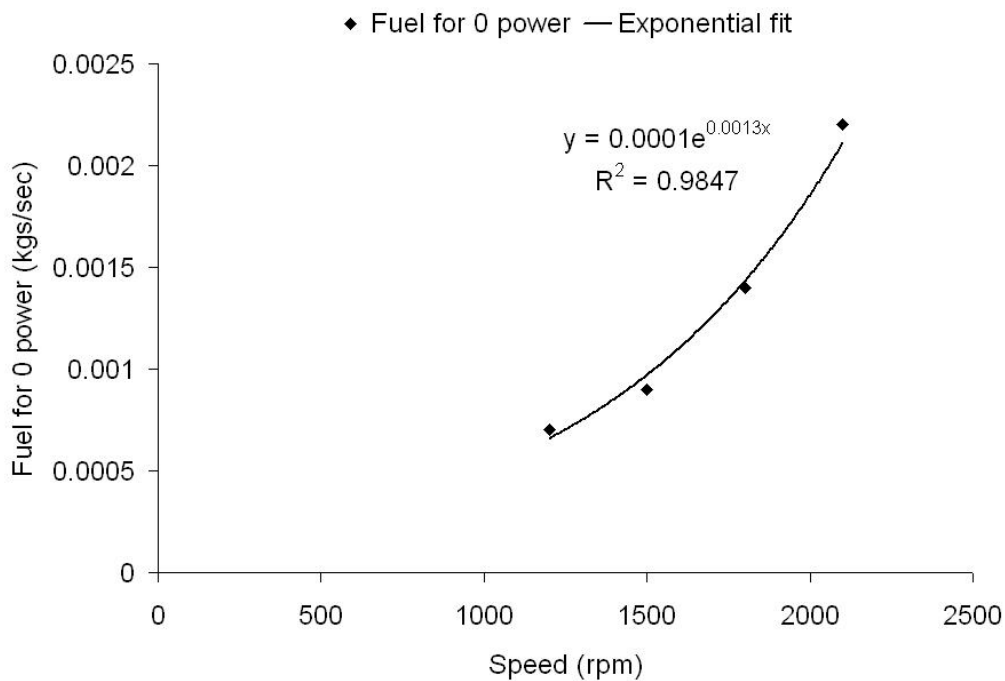
Figure A.5: Friction power correlation

Appendix B

Preparation of Arrhenius Plots

This appendix contains a description of the preparation of Arrhenius plots, which were used to analyze the DOC and CPF model kinetic parameters. Since the varying kinetic parameters of the DOC for gaseous emission oxidation, and for the CPF with oxidation of particulate, are unified by Arrhenius plots to obtain a single set of 'apparent' kinetic parameters, it is instructive to study the logic of such plots.

Recall that for a DOC, the gaseous oxidation kinetics are modeled using modified Arrhenius type functions, described by equation 3.3. The general equation describing the reaction rate kinetics is:

$$K_i = A_i.exp\left(-E_i/\overline{R}T_w\right)$$

where, K_i is the adsorption constant, A_i and E_i are the pre-exponential and activation energies for any of the reaction rates in equation 3.2, and $\overline{R}$ is the universal gas constant.

For the CPF, the thermal, catalytic and NO_2 assisted particulate oxidation kinetics are modeled using modified Arrhenius type functions, described by equations 3.37a, 3.37b and 3.42 respectively. The equations are reproduced below for conve-

nience.

$$k_{th}(T_w) = A_{th}T_w.exp\left(\frac{-E_{th}}{\overline{R}T_w}\right)$$

$$k_{cat}(T_w) = A_{cat}T_w.exp\left(\frac{-E_{cat}}{\overline{R}T_w}\right)$$

$$k_{NO_2}(T_w) = A_{NO_2}T_w.exp\left(\frac{-E_{NO_2}}{\overline{R}T_w}\right)$$

From the above equations, it is clear that the temperature dependent oxidation rates, represented by 'k' or 'K', are Arrhenius functions of temperature with the following form[*]:

$$k_i(T_w) = A_i.exp\left(-E_i/\overline{R}T_w\right) \tag{B.2}$$

where, k_i, A_i and E_i are the reaction rates, pre-exponential factors and activation energies of species i respectively. The subscript 'i' refers to the HCs, CO and NO when one considers the DOC, and to NO_2 and O_2 in the case of the CPF.

In many cases, the activation energies and pre-exponential factors are unknown before model calibration. In other cases, the activation energies are known, but the pre-exponential factors vary with temperature because of diffusion and mass transfer effects, etc. In such cases, model calibration can be done by assuming values of the activation energies (E_i) from the literature. The pre-exponential factors can then be determined on a case-by-case basis by tuning the models to obtain good agreement with experimental data. To obtain 'apparent' model kinetic factors, which do not change with load or temperature, Arrhenius plots are used.

A natural logarithm (LN) of equation B.2 gives the following relation:

$$LN(k_i) = LN(A_i) + LN\left(\frac{-E_i}{\overline{R}T_w}\right)$$

---

[*]The analysis that follows describes the mathematics for Arrhenius-type functions. Modified Arrhenius-type functions can be analyzed by a similar analysis.

$$\Rightarrow LN(k_i) = LN(A_i) + (-1).\left(\frac{-E_i}{\overline{R}T_w}\right)$$

$$\Rightarrow LN(k_i) = LN(A_i) + \left(\frac{-E_i}{\overline{R}}\right)(1/T_w) \tag{B.3}$$

Equation B.3 represents a straight line when $LN(k_i)$ is plotted on the Y-axis against $(1/T)$ on the X-axis. If the data representing $LN(k_i)$ in a temperature range, can be approximated with a straight line with a high linear correlation coefficient (R^2), then the oxidation kinetics in that temperature range can be described by one set of kinetic parameters defined by equation B.3. Plots of this nature are called Arrhenius plots. The slope of the Arrhenius plot gives $(-E_i\overline{R})$ which is the activation temperature, and the intercept of the Arrhenius plot gives $LN(A_i)$, which is the logarithm of the pre-exponential factor. The kinetic parameters determined from the Arrhenius plots stay constant in the temperature range studied.

Appendix C

DOC Model Input and Results

This appendix contains a description of the DOC model input and results obtained. The initial results from the calibration of the kinetics in the DOC model were reduced to a single set of kinetic parameters using Arrhenius plots, the results of which were presented in chapter 5.

The data describing the state of the exhaust gas and the actual volumetric flow rate were input to the DOC model and are shown in Table C.1. The temperatures shown are the average exhaust gas temperatures entering the DOC. For the pressure drop calculation, the atmospheric pressure was assumed to be 101.3 kPa *. For other calculations, the pressure upstream of the DOC (time varying because of the CPF) was taken to be a time average of the upstream DOC pressure. The temperature of the DOC channels was input and was taken to be equal to the time averaged DOC inlet exhaust gas temperature.

The concentrations of gaseous species constituting the exhaust gas were input to the model and are shown in Table C.2. The concentrations of O_2, CO_2, H_2O and N_2 were used to calculate the thermodynamic properties of the exhaust, while the concentrations of HCs, CO, NO and NO_2 were used to calibrate the model kinetics.

---

*Since the pressure in the test cell was not measured during all the experiments, a pressure of 101.3 kPa was assumed

Table C.1: Input to DOC model describing flow conditions

% Load	Temperature (^{o}C)	Pressure (kPa)	Flow rate (act-m^3/sec)
20	280	101.3	0.447
25	305	101.3	0.480
40	340	101.3	0.572
60	415	101.3	0.723
75	460	101.3	0.843

The sum of the concentrations of O_2, CO_2, H_2O and N_2 in Table C.2 is equal to 1.0.

Table C.2: Gaseous species concentrations input to the DOC model

Species ↓/% Load →	20	40	60	75
HC (ppmC)	75	67	61	56
CO (ppm)	185	160	151	145
NO_X (ppm)	182	229	260	281
NO (ppm)	146	200	239	264
NO_2 (ppm)	36	29	21	17
CO_2 (% Vol.)	4.32	5.37	6.53	7.23
H_2O (% Vol.)	5.85	6.89	8.04	8.74
O_2 (% Vol.)	13.48	11.94	10.09	8.85
N_2 (% Vol.)	76.35	75.79	75.34	75.18

To calibrate the model kinetics, activation energies for oxidation of HCs, CO and NO were initially adopted from the work of Triana [6, 7], which were also used previously by references [41, 51]. With these activation energies, the pre-exponential factors needed to predict the concentrations of HCs, CO and NO downstream of the DOC (Table 5.9) were determined are shown in Table C.3.

Table C.3: DOC model kinetic parameters used in the calibration

	CO (K)	HC (K)	NO (K)
Activation temperature	12556	14556	10900
% Load ↓/Pre-exp. factor →	CO (mol-K/cm^2-s)	HC (mol-K/cm^2-s)	NO (mol-K/cm^2-s)
20	1.5E+11	4.0E+10	9.5E+07
25	1.0E+11	4.0E+10	7.0E+07
40	4.2E+10	1.5E+10	3.5E+07
60	1.3E+10	4.0E+09	8.5E+06
80	3.5E+09	2.0E+09	2.6E+06

It can be seen from Table C.3, that there is variation of at least an order of mag-

nitude in the pre-exponential factors for each of the gaseous species shown. However, these parameters were used in the initial calibration of the model and hence their values vary with temperature (load). They were unified to a single set of 'apparent' kinetic parameters which are presented in Figure 5.17 and Table 5.10 respectively.

Appendix D

A Comparison of Kinetics of a DOC in a CRT® and CCRT®

This appendix contains a comparison of the DOC modeling results obtained with the CCRT®, with the results obtained by Triana [6, 7] with a DOC in a CRT®. The details of the DOC used by Triana are listed in [6], while those used in this research are in Table 4.3. Other than catalyst formulations and loadings which were unknown, the most important factor was that, while the diameters and length of the DOCs were the same, the cell density of the DOC used by Triana [6, 7] was 300 cpsi compared with 400 cpsi used in this research.

A comparison of the kinetic parameters are made by means of Arrhenius plots (Appendix B). The experiments of Triana [6, 7] were for a different engine at different loads and speeds, while this research was conducted at different loads at rated speed. Hence the comparison was made in the temperature range encountered in this research, 280 - 465 ^oC. In the following graphs, a comparison of results at different engine speeds are shown and can be identified by the legend in the figures.

A comparison of the Arrhenius plots for the oxidation kinetics of HCs, CO and NO are shown in Figures D.1, D.2 and D.3 respectively. It can be seen that for both

DOCs, the HC reaction rates are very close to each other, and can individually be represented by linear correlations in the entire temperature range at any given speed. Further, for the HC kinetics of Triana, the kinetic factors are very close to each other even at different engine speeds.
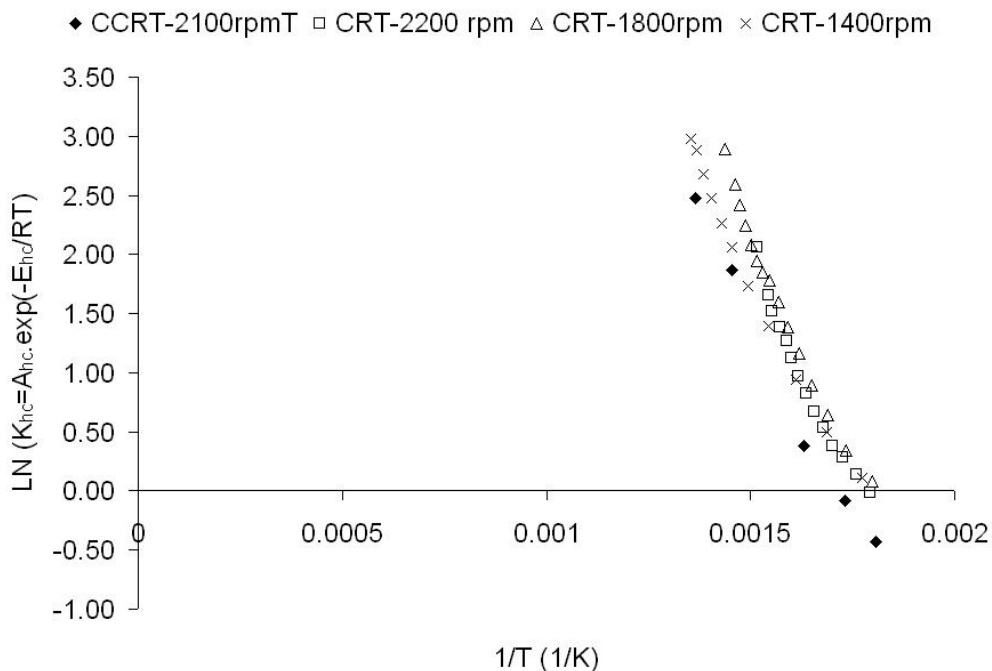
Figure D.1: Comparison of DOC HC oxidation kinetics

Figure D.2 shows that while the CO kinetics of the DOC in the CCRT® can be represented by a straight line as shown in chapter 5, the data of Triana [6, 7] has several regimes for different temperatures, and for different engine speeds unlike the kinetic data of the HC's. The DOC used in this research also had higher reaction rates for CO, because of the complete oxidation of CO at all loads in this research, unlike the research of Triana[6, 7]. The NO oxidation kinetics comparison in Figure D.3 shows a similar trend with the data of Triana[6, 7], with several regimes for different temperatures and for different engine speeds. It is interesting that the NO regime crossover for both DOCs is at a temperature of approximately $390^{o}C$, the temperature window in which NO kinetics move from the kinetically limited regime
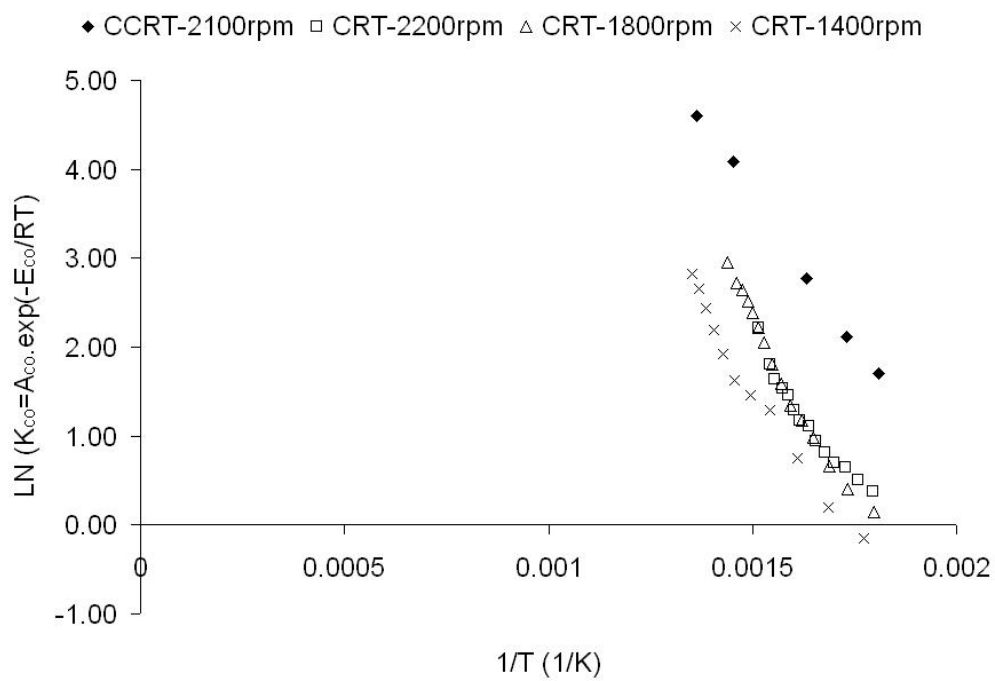
Figure D.2: Comparison of DOC CO oxidation kinetics
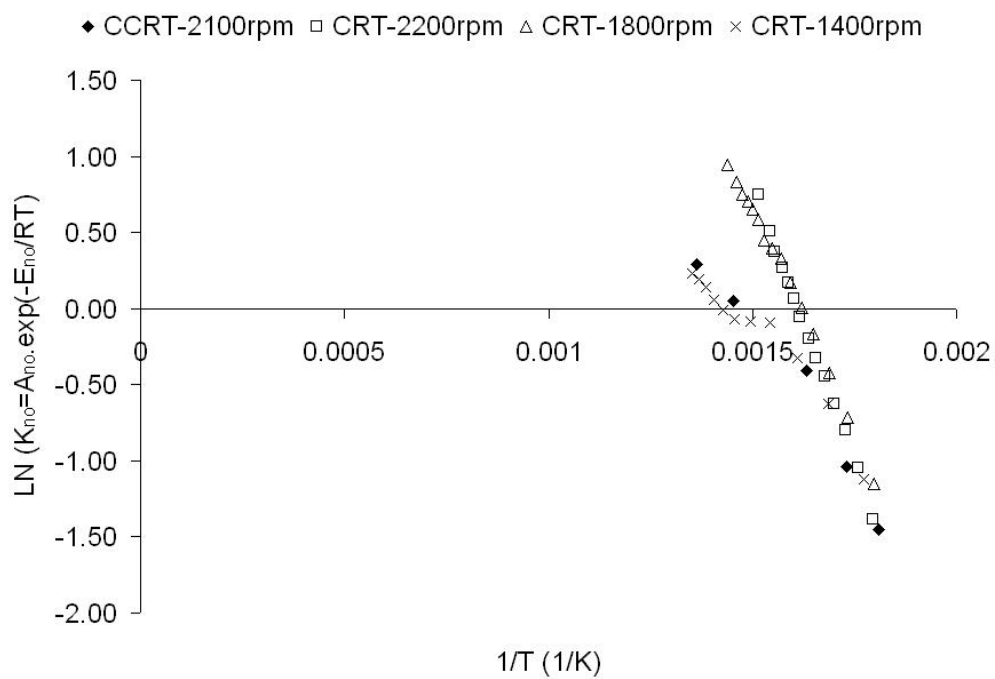
Figure D.3: Comparison of DOC NO oxidation kinetics

to the thermodynamically limited regime (Section 2.1).

One reason for the differences in performance of the DOCs could be because the DOC in this research had a higher cell density, leading to more surface area which increases the contact area with the catalyst and consequently its oxidation efficiency. The differences could also be because of a different catalyst formulation or catalyst loading or both.

Appendix E

Clean Pressure Drop of the CPF

This section describes the determination of the CPF clean pressure drop, and the steep increase in the pressure drop during the first few minutes of the experiment.

The factors which determine the clean pressure drop are CPF inlet exhaust gas flow rate, exhaust temperature, CPF wall temperature and filter wall permeability (equation 3.56). To determine the clean filter wall permeability the clean pressure drop across the CPF, the temperature and flow rate of the exhaust through the CPF a few seconds after the exhaust was diverted from baseline to trapline were needed. These data were obtained from the LabVIEW data acquisition software. Equation 3.56 shows that the clean pressure drop should scale linearly with the actual exhaust volumetric exhaust flow rate and this was verified for both the first and second data points recorded in LabVIEW. A bad linear correlation can be seen in Figure E.1 for both the first and second data points recorded by LabVIEW. It was initially believed that some of this scatter was due to transient measurements by the thermocouples. To check this, the 'clean' pressure drop across the DOC was plotted against the actual exhaust volumetric exhaust flow rates for both the first and second data points recorded in LabVIEW. Figure E.2 shows that both the 'initial' pressure drop during transient inlet temperature regime, and the time averaged DOC pressure drop scale
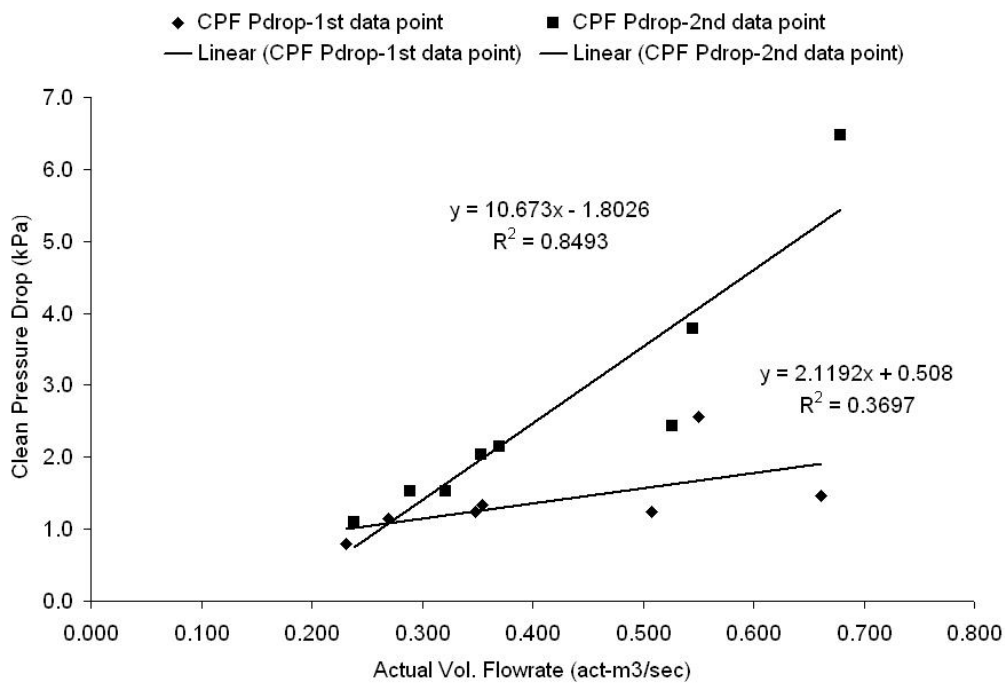
Figure E.1: CPF 'clean' pressure drop versus exhaust flow rate
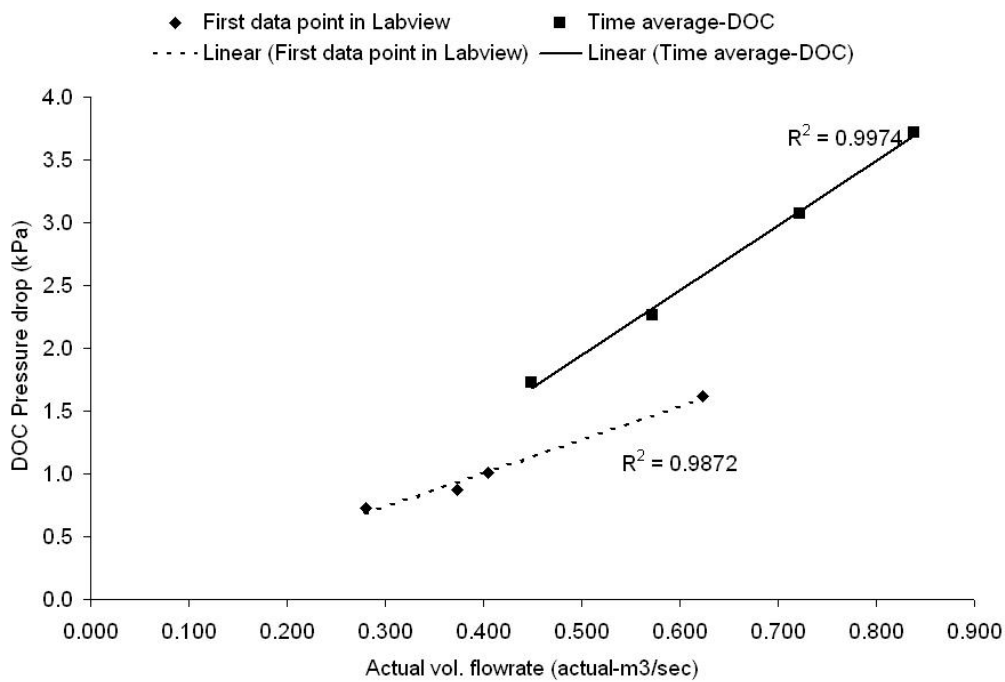
Figure E.2: DOC 'clean' and time averaged pressure drop versus exhaust flow rate

linearly with the actual volumetric exhaust flow rate with a correlation coefficients (R^2) of at least 0.98. Resolving the CPF 'clean' pressure drop issue is critical as it is the first step in the calibration of the CPF model and greatly affects the model determined 'clean' filter wall permeability.

An assumption in Figure E.1 is that the 'clean' filter wall permeability was the same at the start of all the experiments. However, this may not be true with incomplete or improper filter baking which leads to residual PM or ash left in the filter. If the scatter in the CPF 'clean' pressure drop data were indeed due to this, then an accurate determination of the clean filter wall permeability would be impractical. Hence, model calibration was done so that all 'clean' pressure drops were predicted within $\pm$ 0.2 kPa of the experimentally determined value, using one value of the clean filter wall permeability. The variation assumed in the 'clean' pressure drop, $\pm$ 0.2 kPa, is low enough to be a source of experimental error and is not expected to skew the filter wall permeability calibration. Using such an approach, a 'clean' filter permeability of 2.00E-13 m^2 was determined and agrees well with findings of other researchers in references [7, 9, 34, 41] for filters of similar material.

From the pressure drop profiles of the CPF, it was noted that the pressure drop rose very rapidly from low 'clean' pressure drop values of about 1.0 kPa, to pressure drops in the deep bed filtration of greater than 8 kPa. From experimental data analysis, the conclusion was that, after switching the exhaust from the basline to trapline, the thermal inertia of the trapline and the DOC were cooling the exhaust gas before its arrival at CPF inlet. As an example, Figure E.3 shows this phenomenon for the 40% CPF-only characterization experiment. The CPF-inlet temperature can be seen to rise from about 50^oC to over 300^oC in about 200 seconds. Exhaust at a higher temperature has higher viscosity (μ) and decreased density (higher actual volumetric flow rate), which causes a higher pressure drop across the DOC and CPF (Equations 3.4 and 3.58). For example, in the first 120 seconds after 'time=0' for the
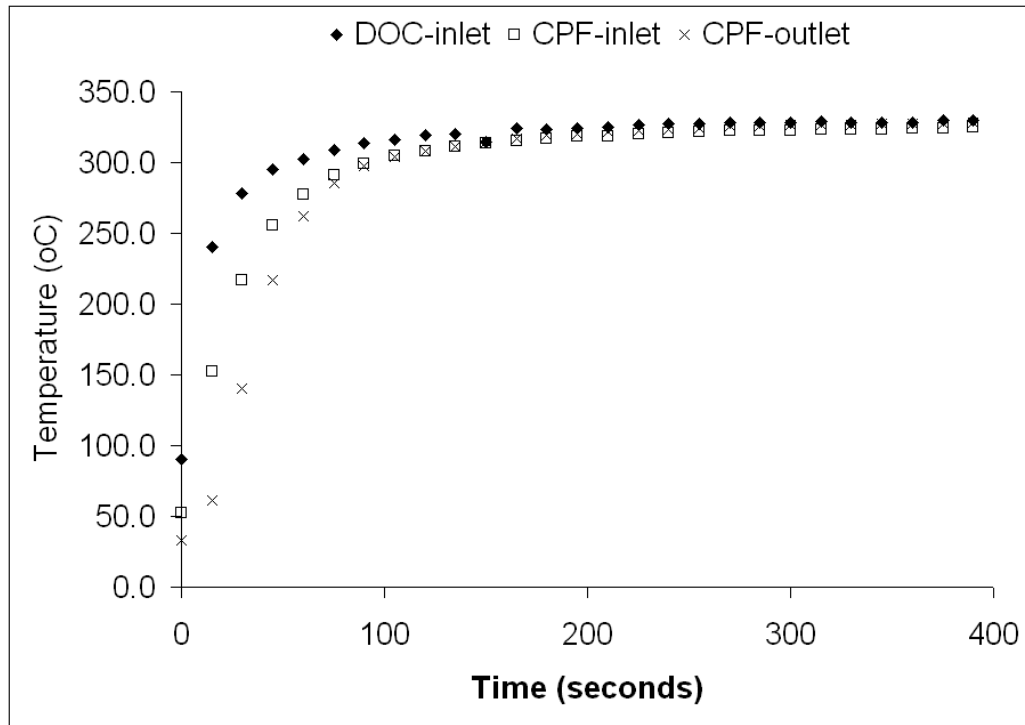
Figure E.3: 40% CCRT®: initial CPF inlet exhaust temperatures

40% CPF-only experiment, the pressure drop rises from 1.3 kPa to about 5.0 kPa. Thus a large part of the initial pressure rise can be attributed to transient density of the exhaust at CPF inlet, and has implications for the clean filter wall permeability calculations. This transient temperature effect also explains why the 'clean' pressure drops even at 60 and 75% loads were only about 1.2 kPa. The 1-D model was hence calibrated in a transient mode, with a variable CPF-inlet temperature taken from the LabVIEW data acquisition system.

Appendix F

Determination of Kinetic Parameters of Particulate Oxidation by NO_2

The data obtained from the characterization experiments in CPF-only and CCRT® configurations were thought to be sufficient to determine the kinetic parameters of the NO_2-assisted particulate oxidation reaction. However significant NO_2 production in the CPF, in both CPF-only and CCRT® configurations meant that the particulate oxidized in these configurations is due to NO_2 entering the filter and due to NO_2 being produced in the filter. Since, in both configurations, both oxidation mechanisms are active, their independent effects cannot be separated without knowing the effect of either one apriori.

To resolve this issue, the options investigated initially were:

- Assigning the particulate oxidation in the CPF-only configuration to a 'catalytic' reaction with O_2. Then use these parameters to calibrate the CCRT® configuration kinetics.

- Use kinetic parameters for the NO_2-assisted particulate oxidation in CCRT®

configuration from the calibration of reference [7], and attribute all other oxidation activity needed to a 'catalytic' reaction with O_2 in the CPF-only configuration.

- Use kinetic parameters for the NO_2-assisted particulate oxidation in CPF-only configuration from the calibration of reference [7], and attribute all other oxidation activity needed to a 'catalytic' reaction with O_2, and use these factors in CCRT® configuration.

An important test of validity is to use Arrhenius plots (Appendix B) for both the NO_2 and the 'catalyst' effects to select the method that best separates the two effects. However, each of the above approaches mentioned above were abandoned for the reasons given below:

- Assuming NO_2 effect=0 in CPF-only configuration is not entirely true in view of the significant NO_2 generation by the catalyst in the CPF. Even if some of the NO_2 increase across the CPF is due to oxidation in the outlet channels, the NO_2 effect in CPF-only configuration cannot be assumed to be zero.

- Use of the NO_2 factors of Triana [7] brings along with it the uncertainty in determination of those parameters due to scatter in experimental data in that project. Combined with experimental error in measurements at MTU, the determined model parameters could have had large errors.

Due to the deficiencies outlined above, a need was felt to investigate alternative methods for determination of kinetic parameters for the NO_2-assisted particulate oxidation. The inherent inseparability of NO_2 consumption and generation effects from the CPF-only and CCRT® characterization experiments makes the use of other experimental data essential. The best option then is to choose experiments which are highly controlled. Upon a review of literature, it was decided to use the controlled

chemical reactor studies of the transient oxidation of diesel particulate by synthetic gases simulating diesel exhaust. An additional advantage of such experiments is that the simulated exhaust contains water vapor and oxygen in addition to NO_2, which are known to increase reaction rates of NO_2 with particulate [2, 18, 20, 21].

Initially, the experimental data reported by Jacquot et.al. [18] were used, but the resulting kinetic parameters were found to be too 'weak' in oxidizing the particulate matter. This was because the authors only reported the steady state oxidation rates in what is an essentially transient process. Finally, the data of Setiabudi et.al [21] was used for the determination of the kinetic parameters for particulate oxidation by NO_2. An advantage of their data was that the O_2 concentrations in the simulated exhaust was 10%, a good average of those measured during the CCRT® characterization experiments (chapter 5, [46]).

To model the data of Setiabudi et.al [21], the 1-D CPF code was modified to model the conditions present in the reactor studies. With the resulting code, the model parameters were changed iteratively to best fit the data available. The results are shown in Figure F.1. The kinetic parameters extracted from this study for the NO_2-assisted particulate oxidation are shown in Table F.1. These values were used to model the oxidation of particulate by NO_2 entering the particulate filter. Any further oxidation needed to make the model agree with experimental results was attributed to NO_2 production by the catalyst in the CPF, with the limitation that model predicted CPF-outlet NO_2 concentrations do not exceed the experimentally measured concentrations.

Table F.1: Results from the TPO calibration

Kinetic parameters extracted from TPO calibration		
Activation energy	Temp. order	Pre-exponential factor
0.73E+08 (J/kmole)	0.5	1.0 (m/s-$K^{0.5}$)
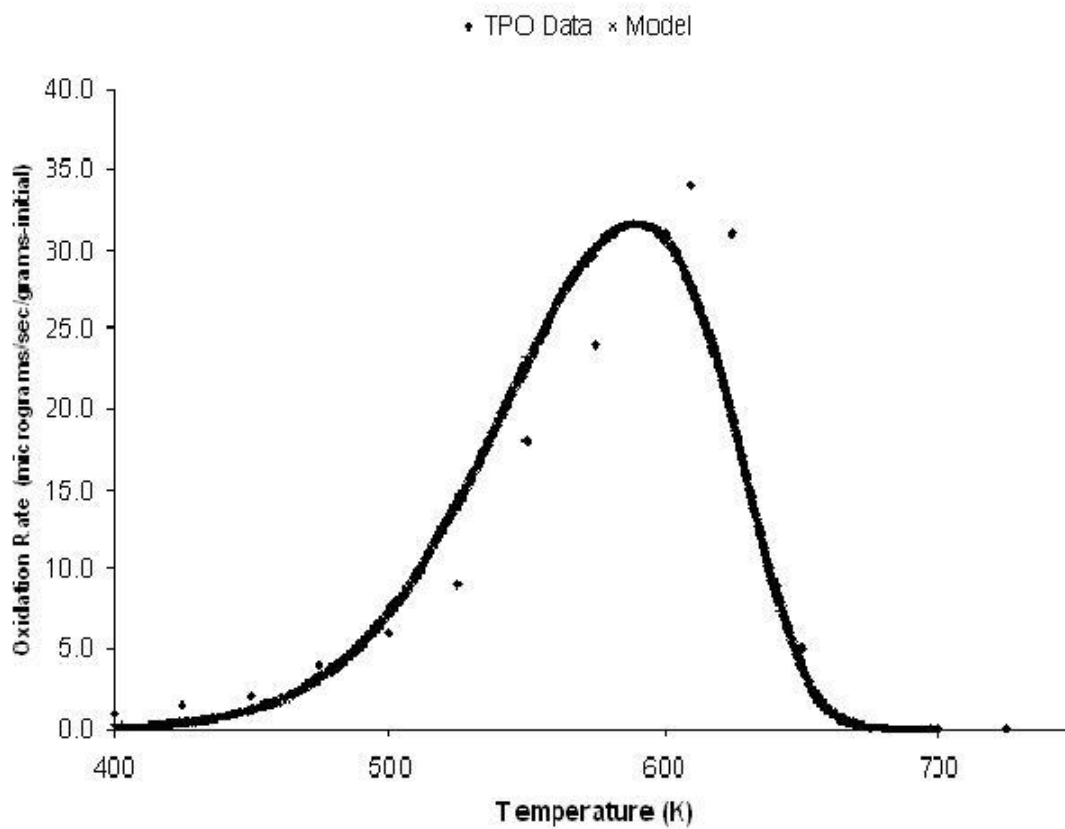
Figure F.1: Results from transient TPO experiment simulation - diesel particulate with 10% O_2 in simulated exhaust (Experimental data of [21])

Appendix G

Additional CPF Model Results

In this Appendix, additional CPF modeling results at the 40 and 60% loads in CPF-only and CCRT® configurations are presented.
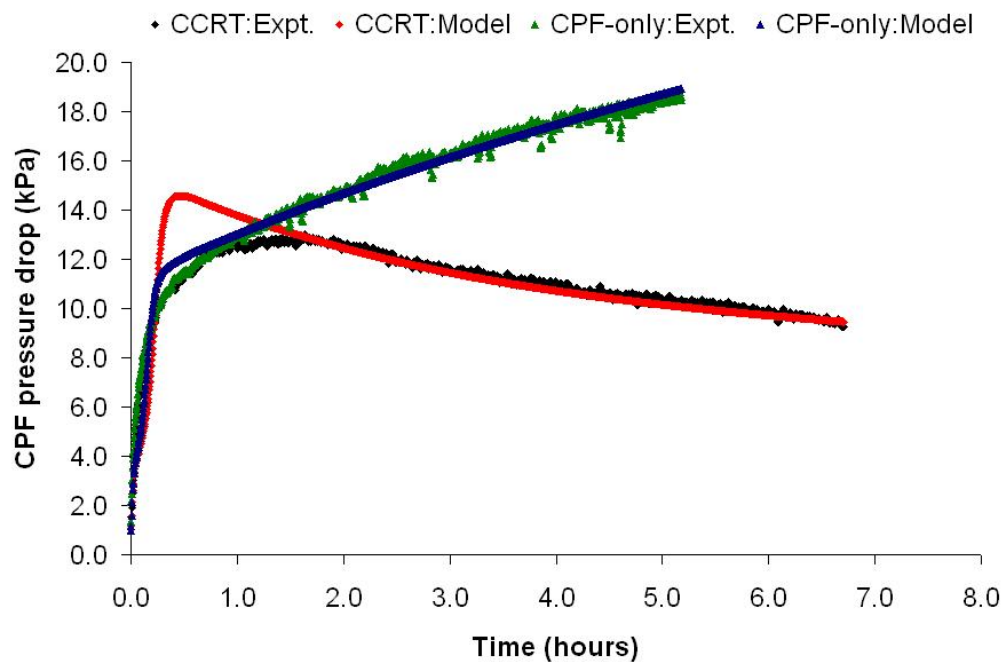
Figure G.1: 40% load pressure drop: experimental and model results
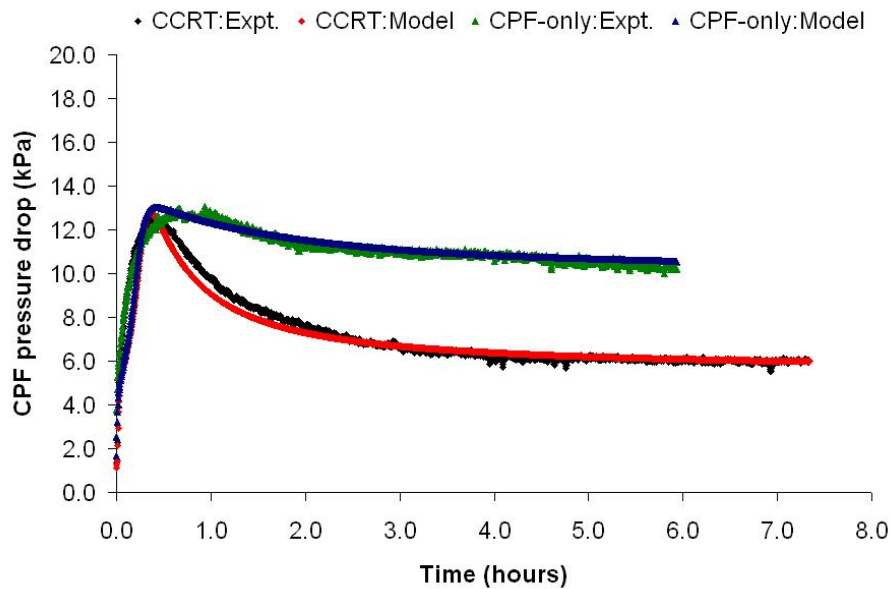
Figure G.2: 60% load pressure drop: experimental and model results
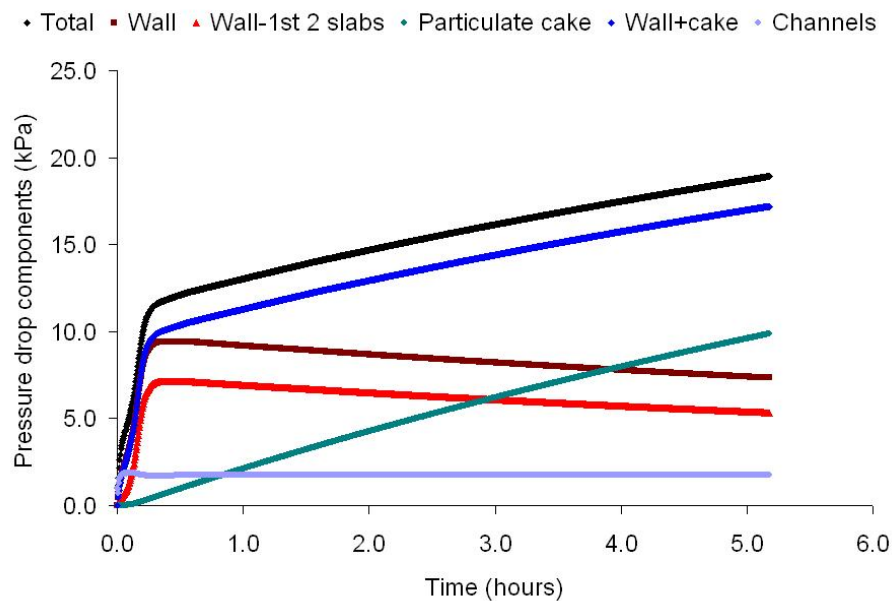
Figure G.3: 40% CPF-only pressure drop components
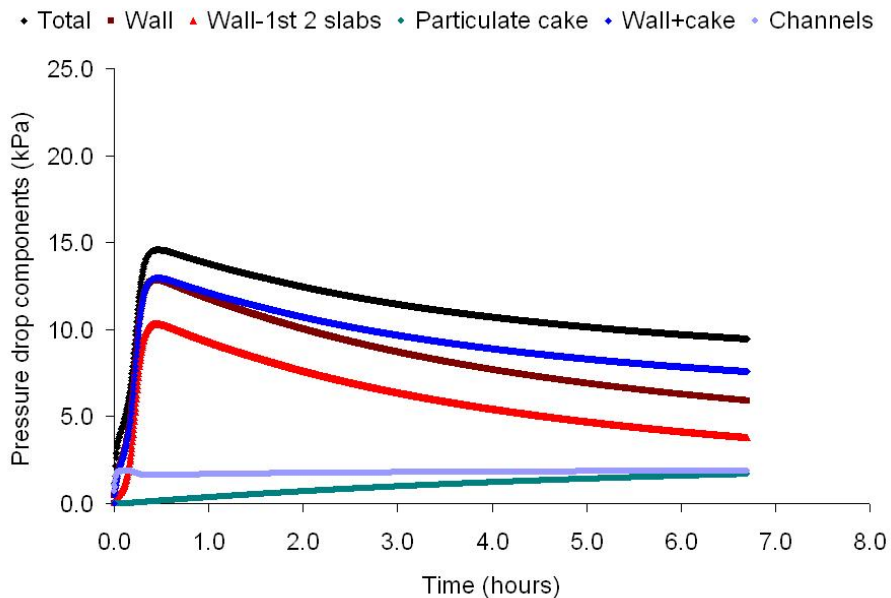
Figure G.4: 40% CCRT® pressure drop components
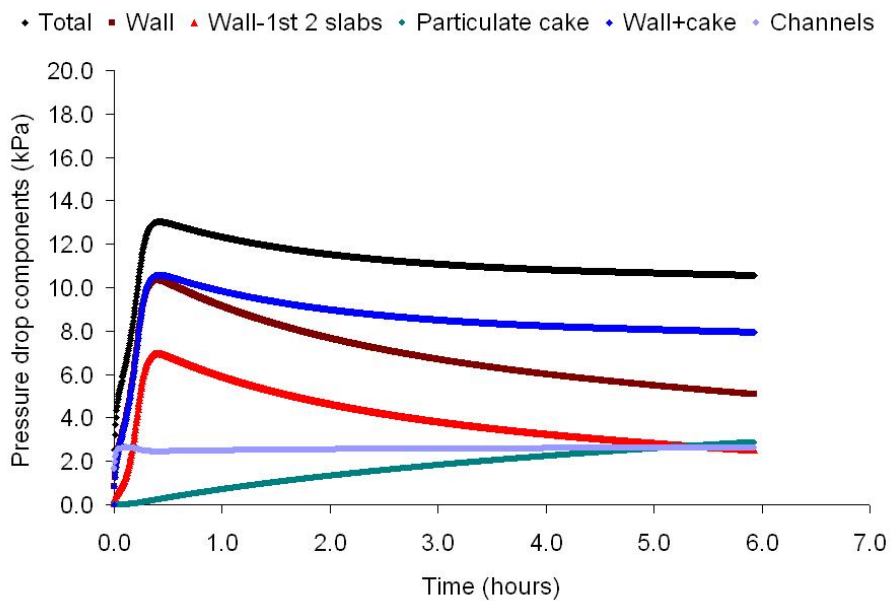
Figure G.5: 60% CPF-only pressure drop components
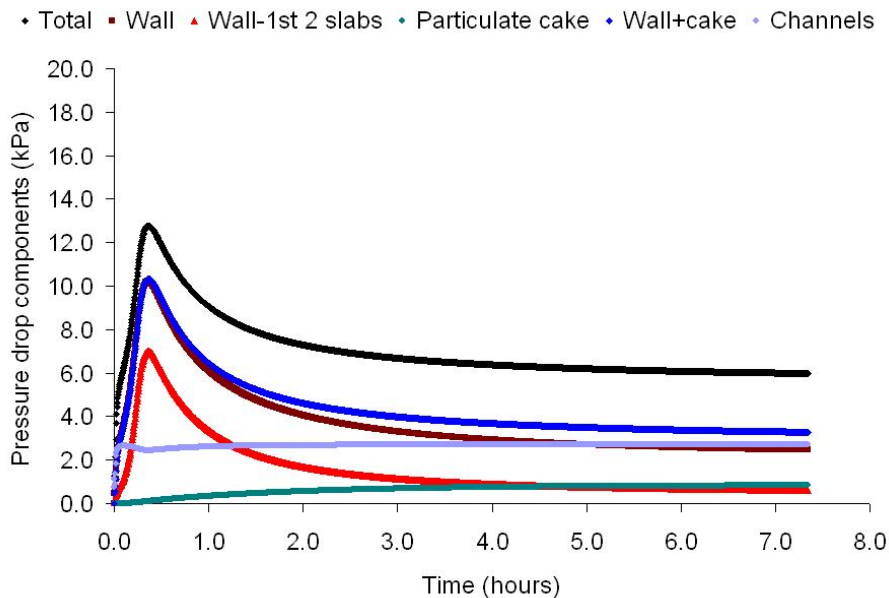
Figure G.6: 60% CCRT® pressure drop components
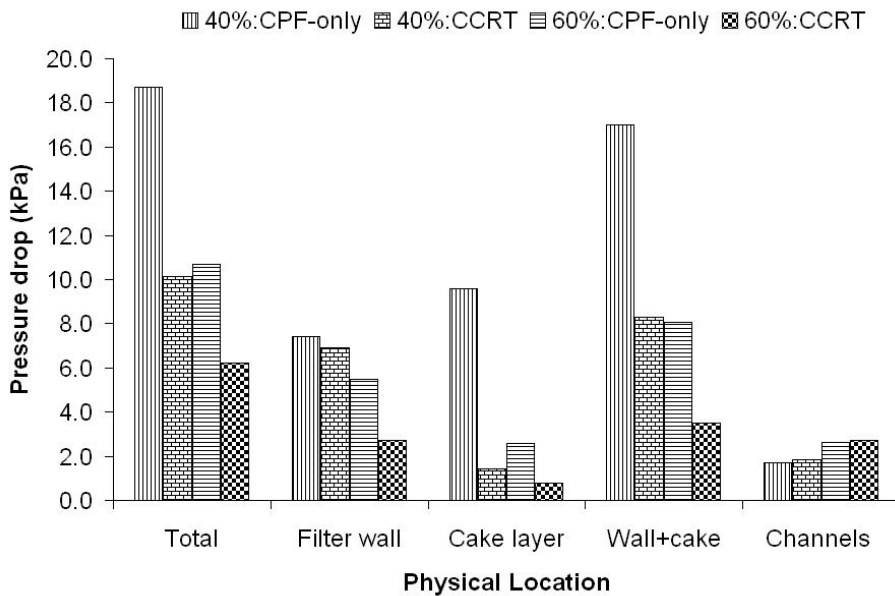
Figure G.7: 40 and 60% loads: pressure drop components after 5 hours of loading
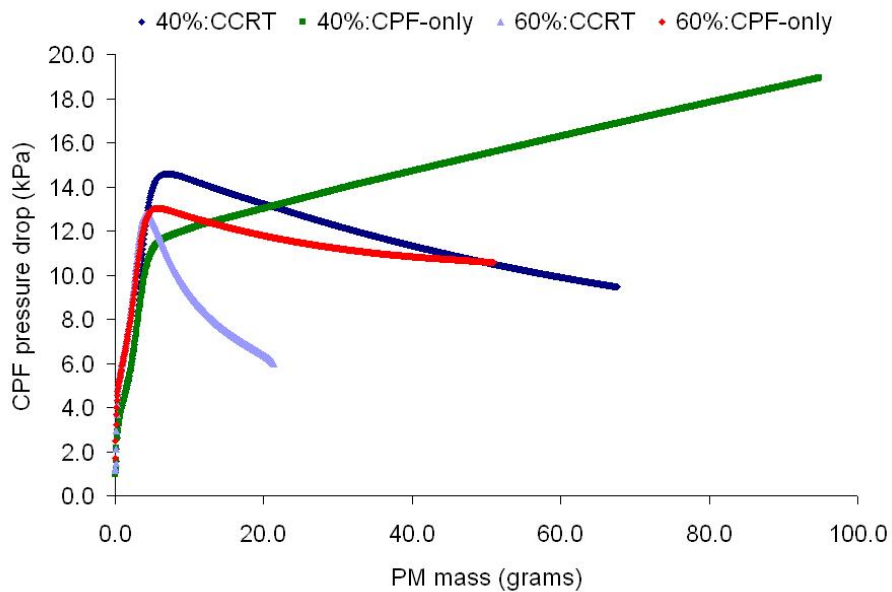
Figure G.8: 40 and 60% loads: pressure drop versus particulate mass
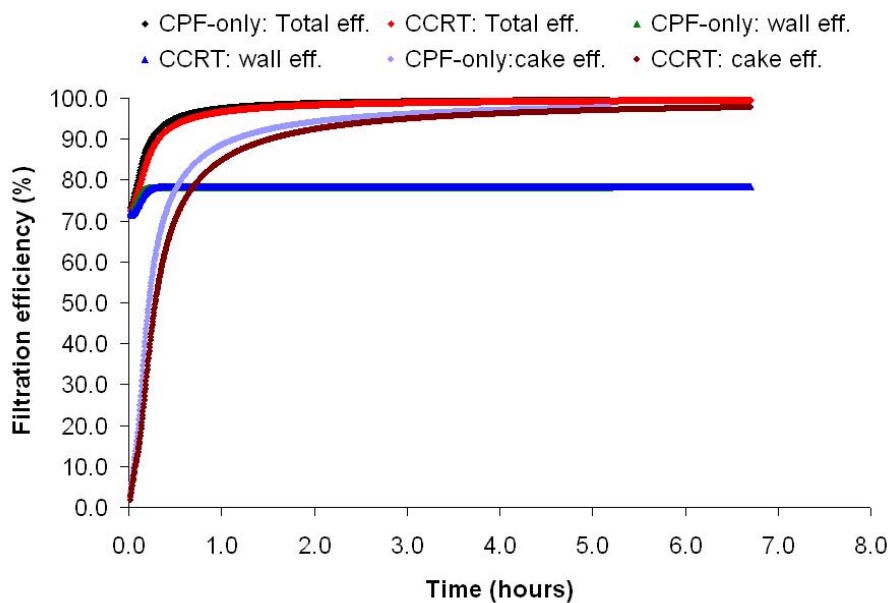
Figure G.9: 40% load: Comparison of filtration efficiencies in CPF-only and CCRT® configurations
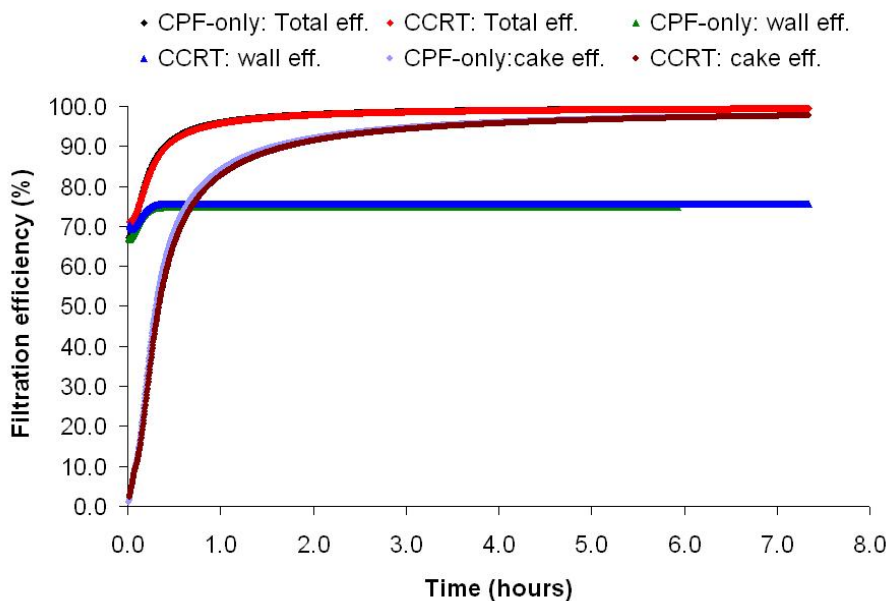
Figure G.10: 60% load: Comparison of filtration efficiencies in CPF-only and CCRT® configurations
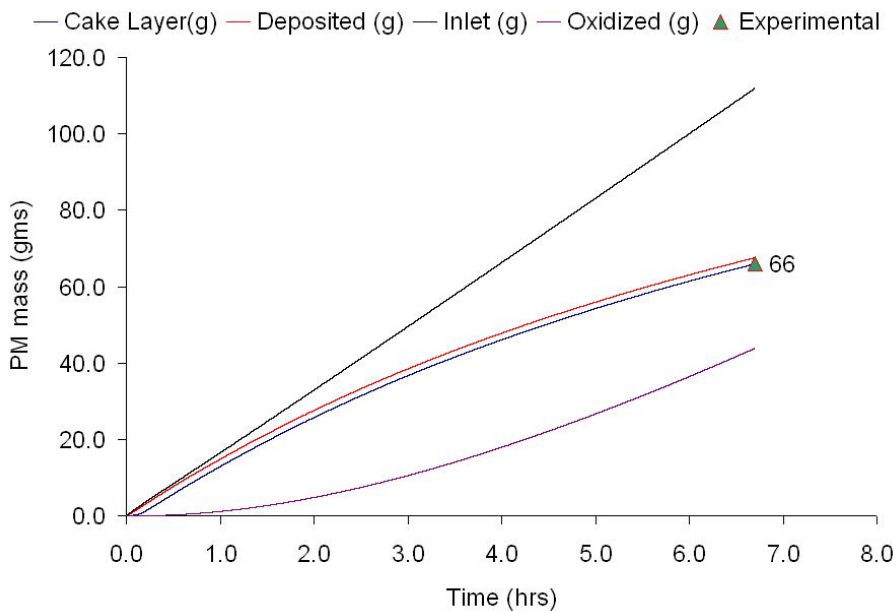
Figure G.11: 40% CCRT®: PM mass evolution with time
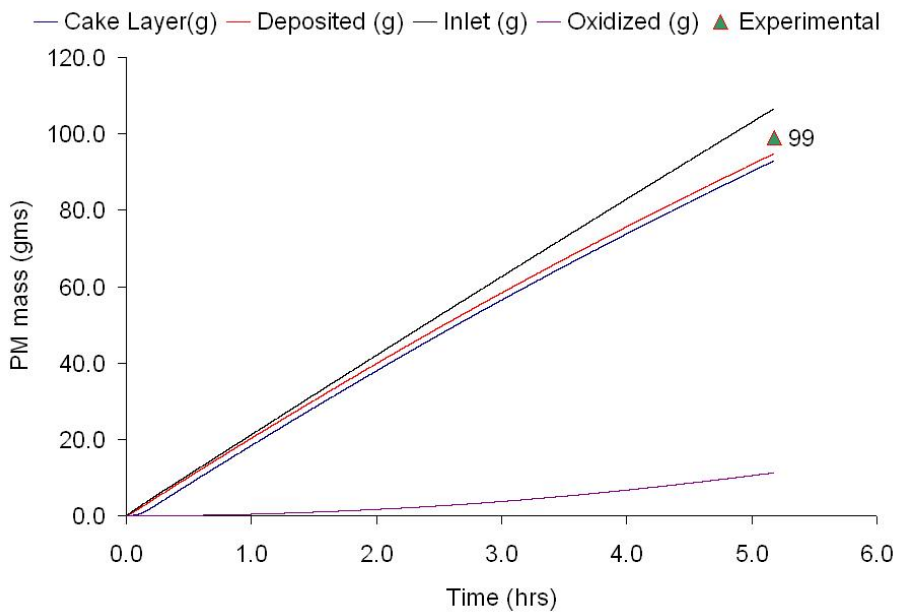
Figure G.12: 40% CPF-only: PM mass evolution with time
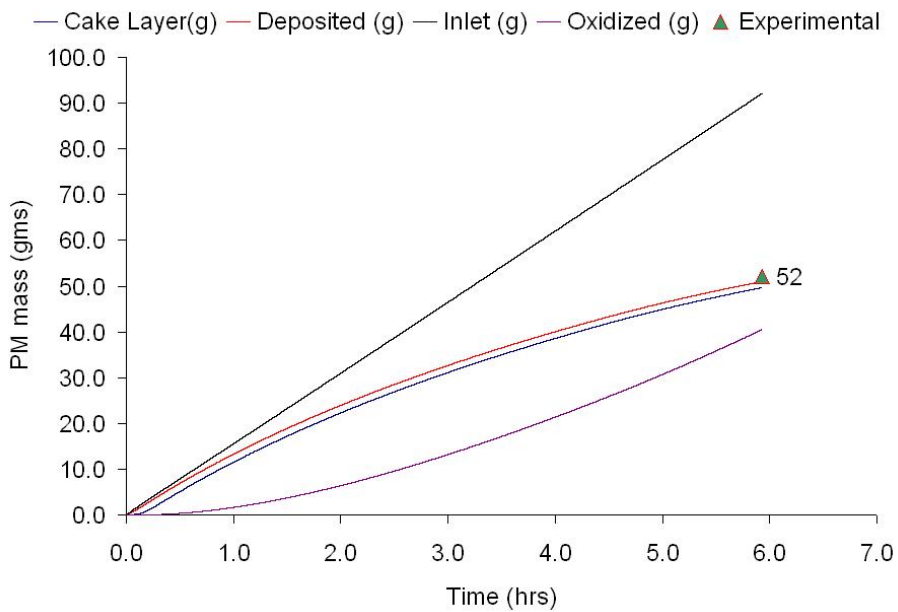
Figure G.13: 60% CPF-only: PM mass evolution with time
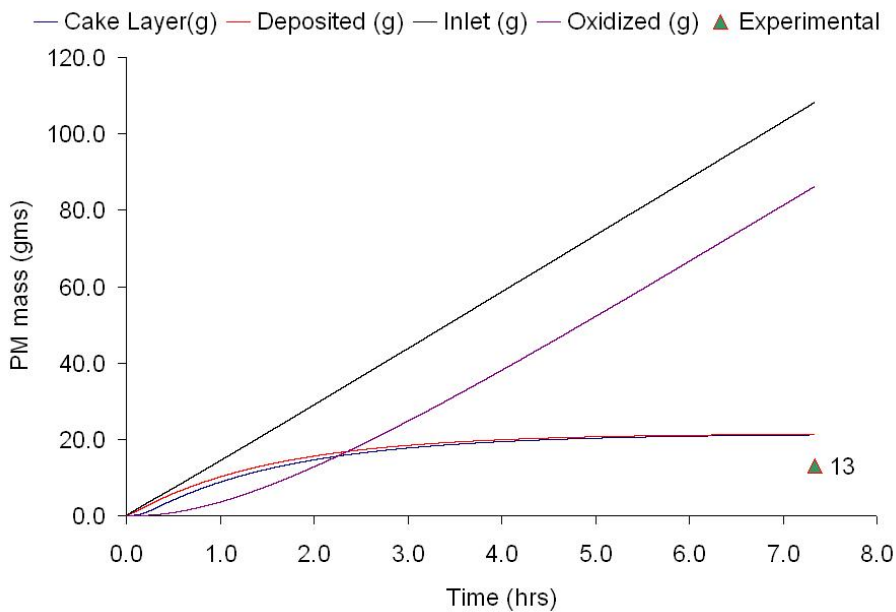
Figure G.14: 60% CCRT®: PM mass evolution with time
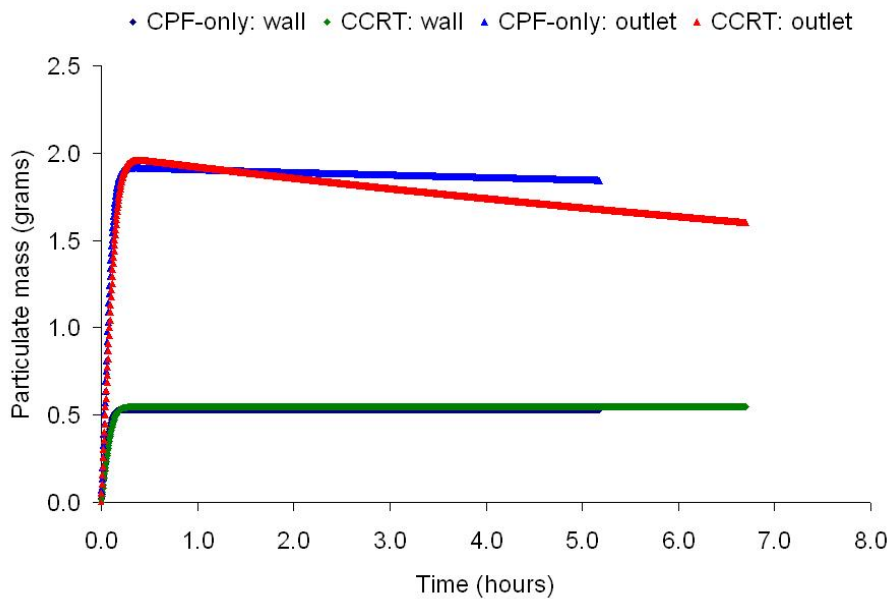
Figure G.15: 40% load: comparison of outlet PM and mass in filter wall
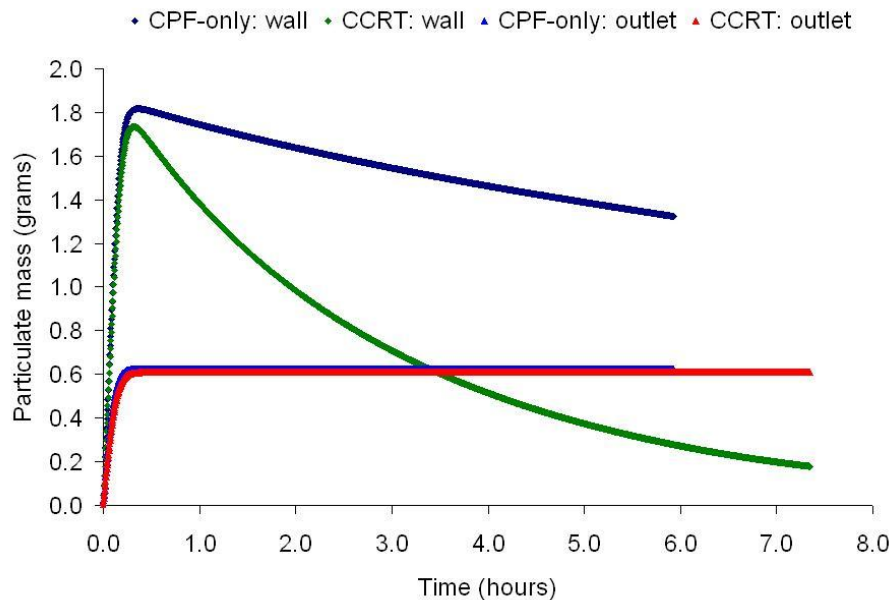
Figure G.16: 60% load: comparison of outlet PM and mass in filter wall
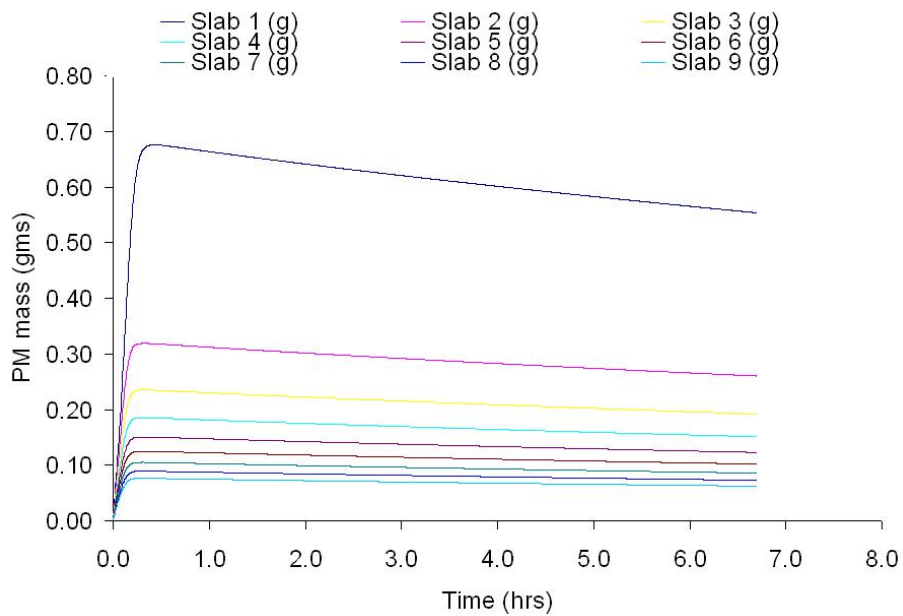
Figure G.17: 40% CCRT®: particulate mass in the wall with time
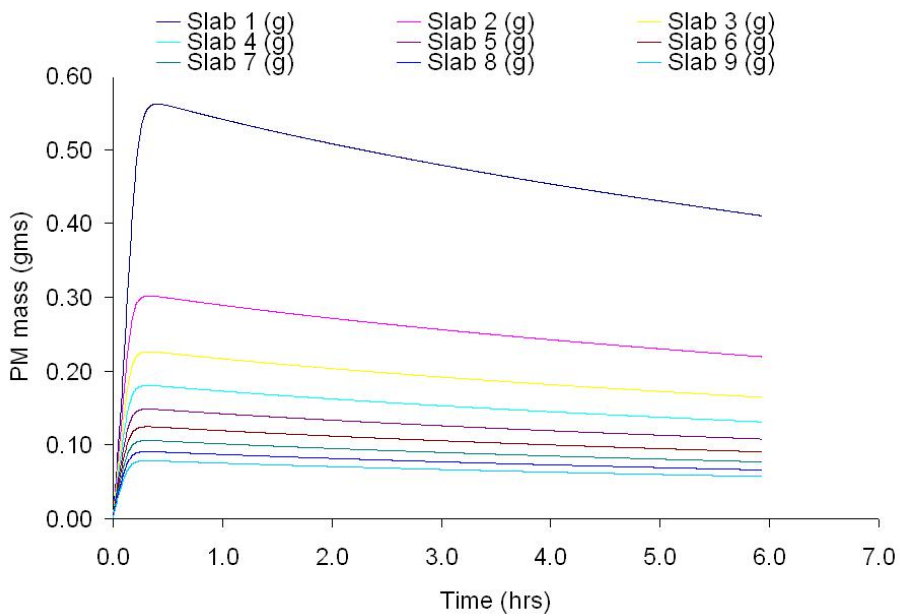
Figure G.18: 60% CPF-only: particulate mass in the wall with time
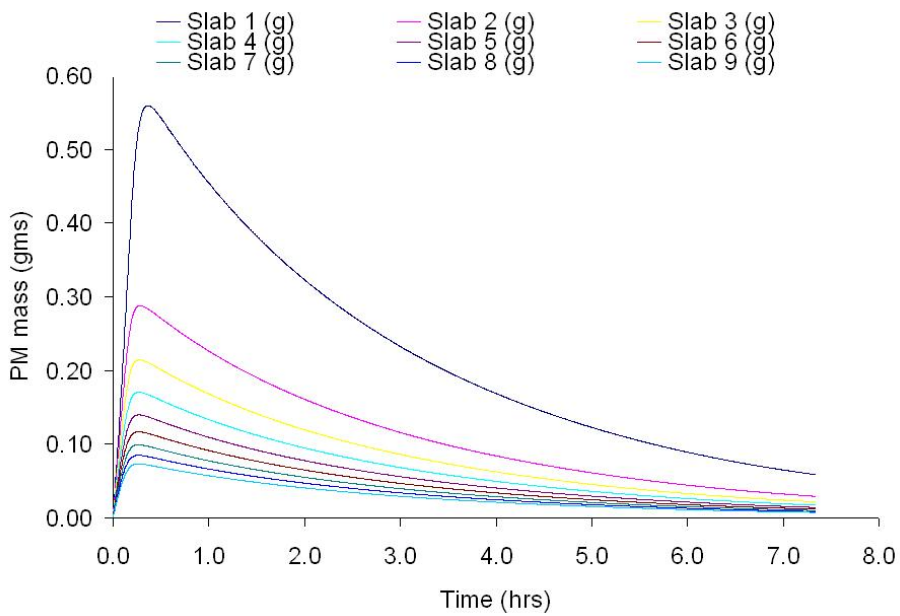
Figure G.19: 60% CCRT®: particulate mass in the wall with time
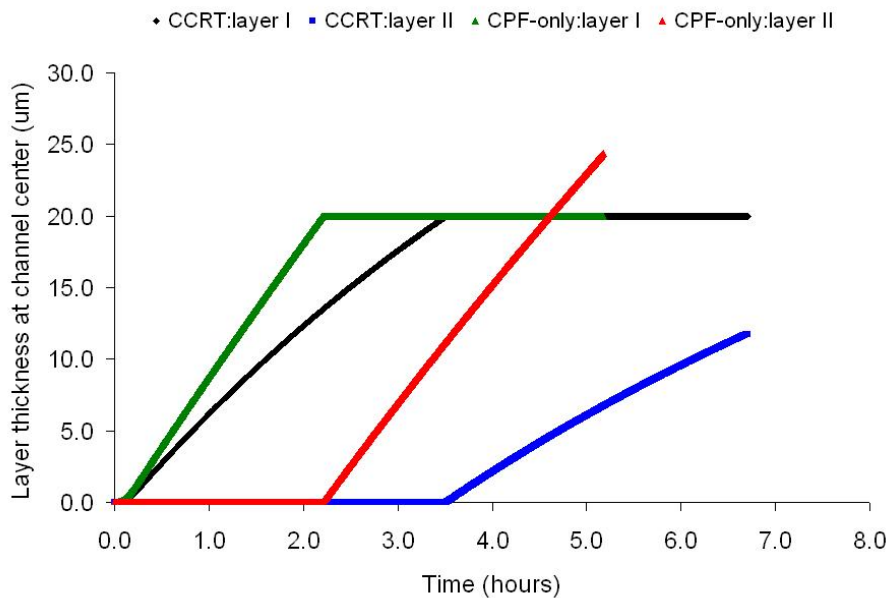
Figure G.20: 40% Load: comparison of particulate layer thickness with time
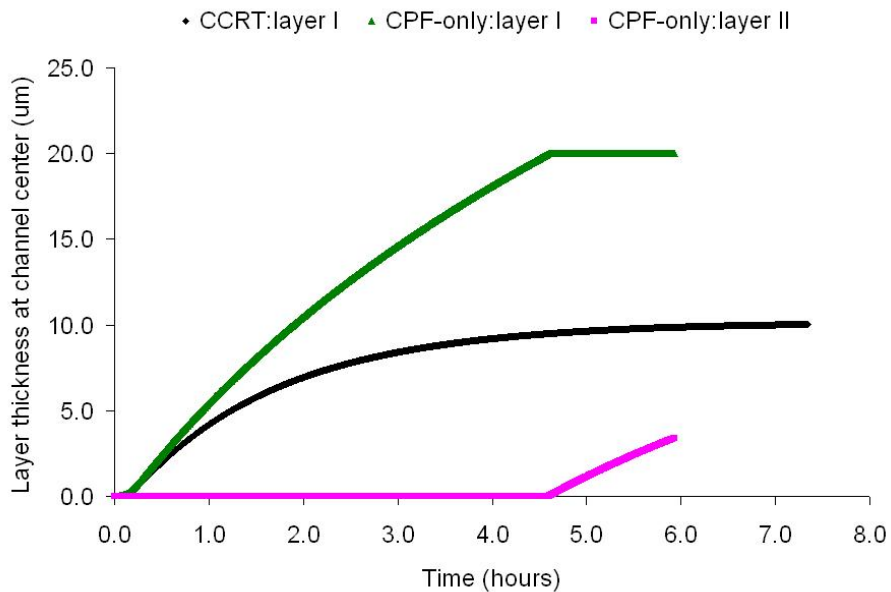
Figure G.21: 60% Load: comparison of particulate layer thickness with time
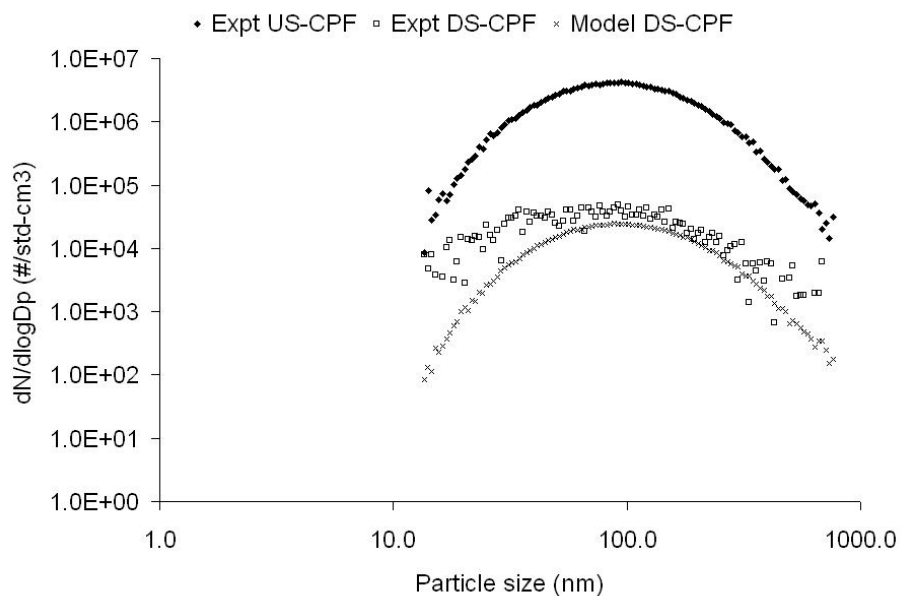
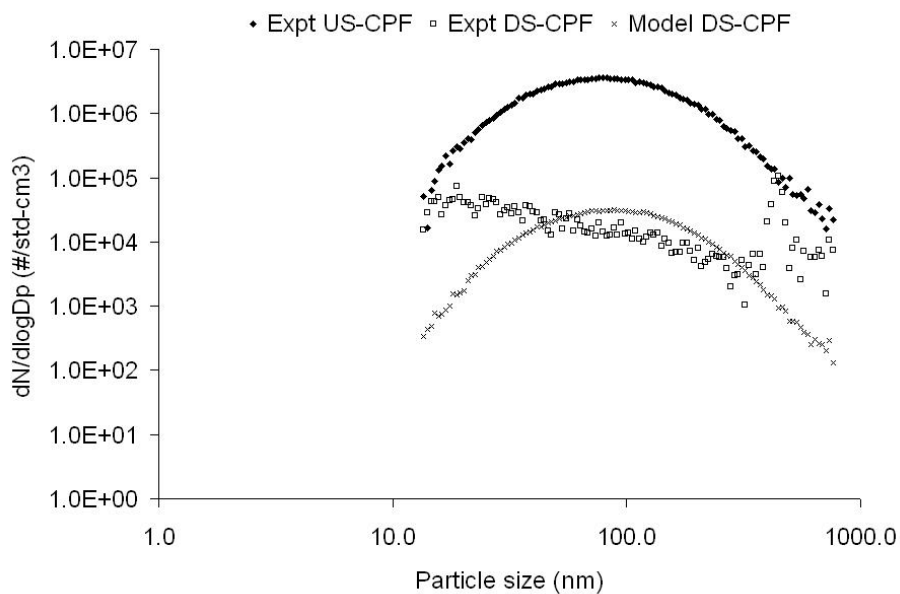Figure G.22: 40% CPF-only: particle size distribtion comparison

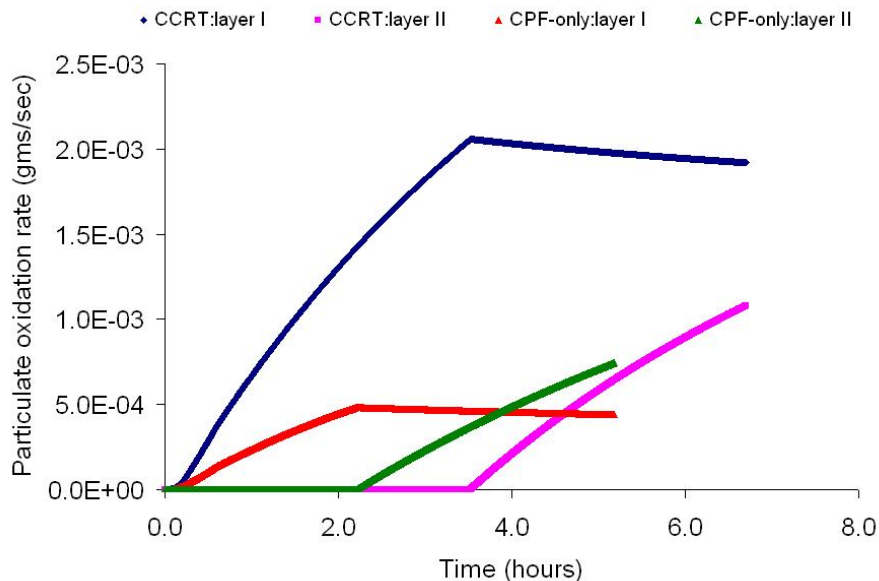Figure G.23: 60% CCRT®: particle size distribtion comparison

Figure G.24: 40% Load: comparison of particulate oxidation rate by location
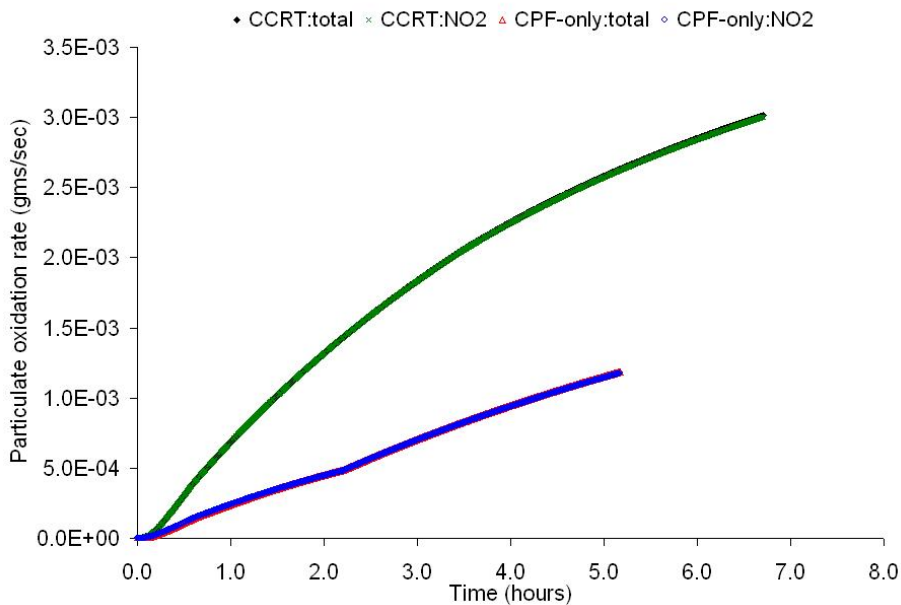

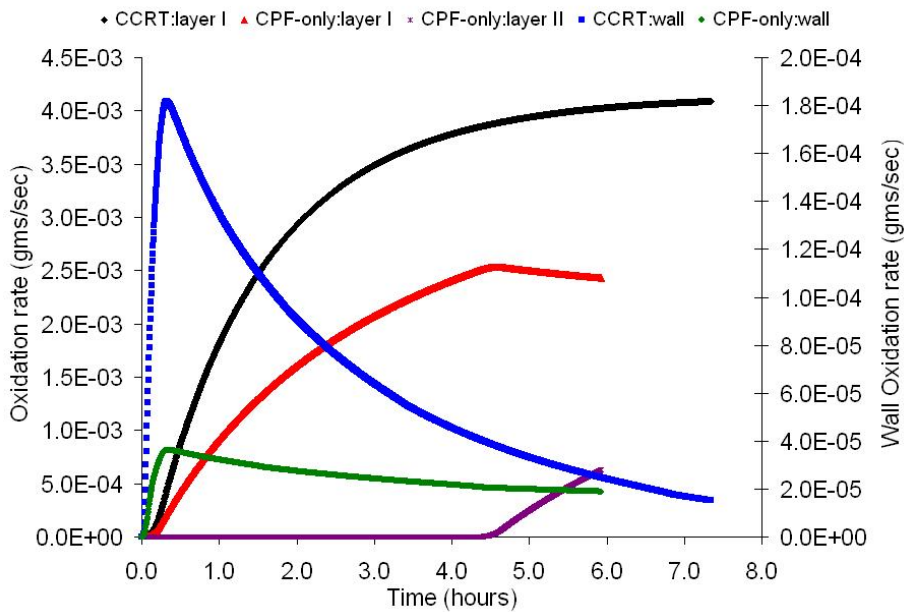Figure G.25: 40% Load: comparison of particulate oxidation rate by type

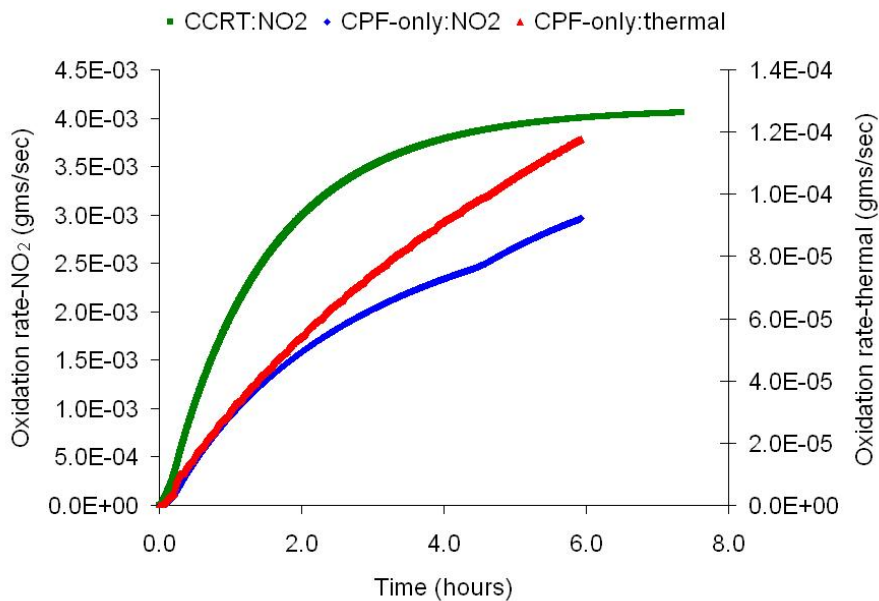Figure G.26: 60% Load: comparison of particulate oxidation rate by location

Figure G.27: 60% Load: comparison of particulate oxidation rate by type

Appendix H

Arrhenius Plots for NO$_2$ Kinetics in the Wall

An Arrhenius plot study of the particulate oxidation kinetics by NO$_2$ in the filter wall is described in this Appendix.

While the NO$_2$ kinetic parameters for particulate oxidation in the cake layer remained constant with load and NO$_2$ concentrations, the NO$_2$ kinetic* parameters in the filter wall changed with both load and NO$_2$ concentrations respectively (Table 5.15). Both tables are shown below for convenience.

Table H.1: Kinetic parameters for the PM cake used in the CPF model

| Oxidation Mechanism	Act. Energy	Temp. Order	Pre-exp factor
Thermal Oxidation	1.497E+08 (J/kmole)	1.0	1.0 (m/s-K)
NO$_2$ oxidation	0.73E+08 (J/kmole)	0.5	1.0 (m/s-K$^{0.5}$)

To verify if the NO$_2$ pre-exponential parameters for particulate oxidation in the wall could be represented by one 'apparent' activation energy and pre-exponential factor, Arrhenius plots were made using the method described in Appendix B. The

---

*Although the NO$_2$ pre-exp factor for the wall is labeled 'kinetic', it has very little effect on the total PM mass oxidized, because there is very little PM, about 3 grams present in the filter wall. Instead, it is used to calibrate the pressure drop curve, because PM oxidation in the wall has a large impact on the pressure drop. The reader should note here that the kinetic parameters for PM oxidation with O$_2$ (thermal) in the filter wall were the same as for the PM cake.

Table H.2: Wall pre-exp and NO_2 production factors used in the CPF model

	Wall NO_2 pre-exp. factor (m/s-$K^{0.5}$)		CPF NO_2 production factor (1/s-K^3)	
% Load	CPF-only	CCRT®️	CPF-only	CCRT®️
20	1.0	0.2	40000	28000
40	0.1	0.15	3000	3500
60	0.12	0.38	400	750
75	0.30	0.55	145	175

Arrhenius plot for both the CPF-only and CCRT®️ configurations is shown in Figure H.1. The result is a surprisingly good degree of fit with a correlation coefficient of at least 0.98. The derived 'apparent' kinetic parameters for NO_2-assisted PM oxidation inside the filter wall are shown in Table H.3. The results are for a Arrhenius type
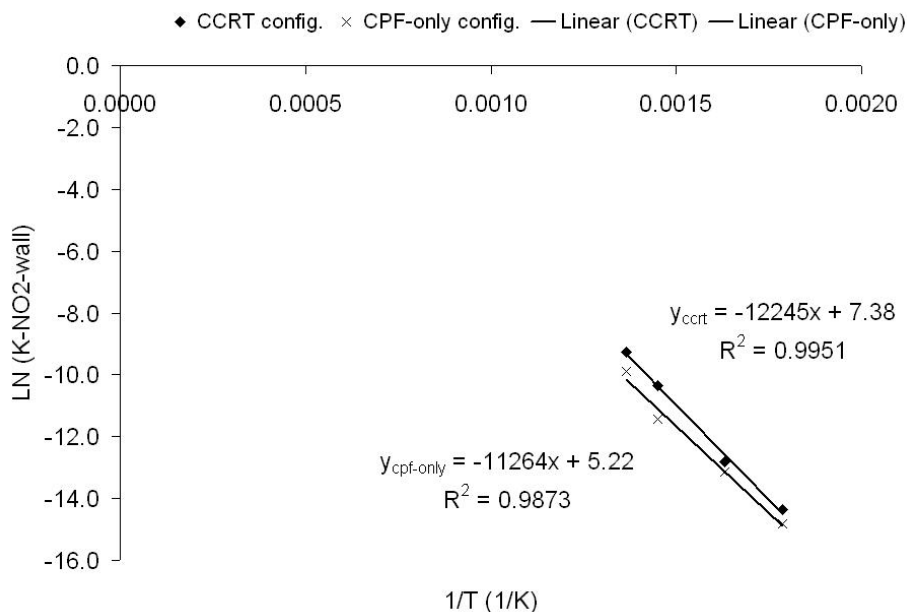
Figure H.1: Arrhenius plots for NO_2-assisted PM oxidation in the wall

Table H.3: Apparent NO_2 kinetics in the wall

Configuration	Activation Energy (J/kmole)	Pre-exponential factor (m/s)
CCRT®️–all loads	1.02E+08	1603.6
CPF-only – all loads	0.93E+08	184.9

equation, as opposed to the modified Arrhenius-type functions used for oxidation in the particulate cake layer (Table 5.14). The estimated activation energies are close

to reactor study determined values of reference [41], possibly because the oxidation in the micro-meter sized pores of the filter wall reduce the influence of diffusion and mass transfer, thus making the particulate oxidation truly kinetically limited. A correlation for the CPF-only configuration was also determined even though the low NO_2 concentrations in this configuration make the pre-exponential factor more amenable to inaccuracies due to the low oxidation rates involved. The conclusion of this study is that the variability in the NO_2 pre-exponential factor for the filter wall is eliminated and the number of unknown model parameters is further reduced.